An Experimental Study of Elastic Electron Scattering from Fluorocarbon Radicals

School of Chemical and Physical Sciences
Faculty of Science and Engineering

Flinders University
South Australia

Jessica R. Brunton B.Sc.(Nanotechnology)Hons.

Thesis submitted for the fulfilment of the degree of
Doctor of Philosophy

January 2011

Contents

Declaration

I certify that this thesis does not incorporate without acknowledgment any material previously submitted for a degree or diploma in any university; and that to the best of my knowledge and belief it does not contain any material previously published or written by another person except where due reference is made in the text.

……..……..

Jessica R. Brunton

Summary

This thesis reports the first measurements of elastic electron scattering differential and integral cross sections for the trifluoromethyl radical (CF_3) for incident electron energies in the range 7-50eV. In order to make those measurements, it was necessary to first measure elastic cross sections for electron scattering from iodotrifluoromethane (CF_3I), in that case over the 10-50eV energy range, and so those results are also presented. This thesis also includes an experimental investigation of low energy (2-20eV) elastic electron scattering from difluoromethylene (CF_2), another important radical species.

Chapter 1 consists of some general information about the CF_2, CF_3 and CF_3I species, including an overview of the previous work undertaken in order to better understand their scattering behaviour. It also incorporates details about the present motivation for measuring electron scattering phenomena from each of them, along with the definitions and general importance of both differential and integral cross sections.

Chapter 2 presents the particulars of the apparatus that was employed for these measurements. It includes a summary of the design and operation for the three main components of the apparatus, including the pyrolytic assembly, the electron spectrometer and the current time of flight mass spectrometer.

Chapter 3 contains information pertaining to the experimental methods employed in this study. It includes details relating to our electron scattering data collection and analysis methods. This chapter also incorporates details related to the *in situ* production of both CF_2 and CF_3, and information about extracting CF_3 cross sections from the direct measurements of those for "mixed species" gas beams.

Chapter 4 details our present results, beginning with the low energy elastic differential and integral cross sections for electron scattering from CF_2. We then move on to present the differential and integral cross sections of CF_3I, a necessary precursor study towards our ultimate goal of investigating electron collisions with CF_3. Thereafter we present our "mixed" beam differential cross sections (DCSs), followed by our extracted CF_3 DCSs and integral cross sections (ICSs). All of our results, where possible, are compared with the results from current theoretical investigations; including some so recent that they have not yet been published.

The main findings of this work are summarised in chapter 5, along with a couple of possible future directions this research might take. Lastly, unpublished theoretical differential cross section data for atomic and molecular iodine, vital for this current work, are presented in the appendices.

Acknowledgements

This project was made possible by the valuable input of many people from both Flinders University and around the world, and it is my pleasure to acknowledge them here:

Firstly I would like to thank my supervisor Professor Michael Brunger. He has not only made the last four years very productive, but also very enjoyable. It has been a privilege to work for him and his guidance throughout this project has been invaluable. I would also like extend my thanks to Dr. Todd Maddern who served as my co-supervisor from January 2007- March 2009, not only for sharing his practical knowledge but for sharing his passion for science and his tenacious attitude towards problem solving.

Dr Leigh Hargreaves was completing his PhD on this experiment as I began mine, and then returned to work part time at Flinders University from February-December 2010. I would like to thank Leigh for showing me the ropes and for his continued support throughout this project.

Furthermore, both the Flinders University Mechanical workshop and the Electronics workshop have been invaluable throughout the course of my PhD. Their technical expertise and experience has been without equal. Bob Northeast, Bill Drury, Wayne Peacock, Mike Mellow, Bruce Gilbert and Greg Hewitt, thank you all for going above and beyond.

Travelling further afield, I would like to extend my gratitude to Professor Mu Tao Lee and Associate Professor Márcio Bettega for providing us with their theoretical cross sections for elastic scattering from CF_2 and CF_3I respectively, so that we could compare them with our data.

I would also like to thank Dr Carl Winstead and Professor Vincent McKoy who have been associated with our research for several years. Their theoretical cross sections and useful advice have improved the quality of this thesis.

I would also like to extend my gratitude to Professor Klaus Bartschat and Dr Oleg Zatsarinny, along with Professors Gustavo García and Fernando Blanco, for providing us with cross sections central to the completion of this project.

I would like to thank the Centre for Antimatter-Matter Studies and its director Professor Steve Buckman for giving me the opportunity to present my work at various conferences throughout my candidature.

Finally, I would like to thank my family for being so supportive of me over this four year period, and for preventing me from losing touch with the world outside the laboratory.

Chapter 1 — Introduction

"Electron driven processes abound in practically every area of our experience"[1]. It is by studying these electron driven processes that we increase our understanding of the behaviour of the world around us. Using atomic and molecular physics (ATMOP) data inputs such as electron impact cross sections, transition probabilities and chemical reaction rates, researchers have been able to model important processes that occur in our atmosphere[2-4] and other planetary atmospheres[5, 6]. ATMOP underpins our understanding of a range of natural phenomena, from lightning storms to the earth's aurora, as well as normal everyday items like fluorescent lights and flat panel displays[1].

Modern technologies like mobile phones and computers are becoming increasingly integrated into our everyday lives. As these technologies are dependent on microelectronics, we need to better understand the processes involved in the production of large scale microelectronic circuitry[7, 8]. So, in order to increase our understanding of the dynamics of this important manufacturing process, we use ATMOP to study many of the individual cross sections for the processes involved.

1.1 Cross Sections: Definitions and their Importance

Since the pioneering work of Arnot[9] and others[10] in the 1930's, cross sections have provided us with a quantitative way of studying the interaction scattering dynamics between particles under various conditions. Scattering phenomenon can also be used to study the energy-level structure of atoms and molecules along with

finding the location of any resonances[11]. There are many different types of cross sections, depending on the type of interaction being studied, some of these include; differential and integral cross sections for electron impact excitation and ionization, momentum transfer cross sections, total cross sections and dissociative electron attachment cross sections. However, the focus of our current work is on the measurement of electron impact differential and integral cross sections for elastic scattering.

The differential cross section (DCS) represents the time-independent probability of a particle, with initial nominal impact energy E_0, scattering from a target species, at an angle $\overline{\Omega}(\overline{\theta}, \overline{\phi})$, after undergoing a scattering process n [12]. Depending on the type of interaction, the incident particles' resultant energy (E_n), can be either the same as it was before the interaction $(\mathrm{E}_0 = \mathrm{E}_n)$, or changed as a result of the interaction $(\mathrm{E}_0 \neq \mathrm{E}_n)$. In the case where there is no nett exchange of energy between the particle and the target species, (i.e. $\mathrm{E}_n = \mathrm{E}_0$), the scattering process is described as being *elastic*, while all other processes $(\mathrm{E}_n \neq \mathrm{E}_0)$ are described as being inelastic. We note that in practice no measured molecular cross section is really purely elastic, as a small amount of energy is always generally exchanged between the projectile and the molecular target, resulting in the excitation or relaxation of the molecular target's rotational modes in its ground vibrational level of its ground electronic state. Changes in energy this small are usually not resolvable experimentally, and so in most practical situations they are ignored[13], and the cross section is described as being a "rotationally averaged elastic" value. Furthermore it should be noted that for our current electron spectrometer (see

section 2.4), lower order vibrational excitation is also unresolvable, thus all the elastic cross sections presented here are also vibrationally averaged. However, at least for the situation away from resonance enhancement, vibrational cross sections are typically several orders of magnitude lower than those for elastic scattering[12] so this doesn't represent a significant concern for this study.

A DCS is usually represented as follows [11, 14]:

$$\sigma(\mathrm{E}_0, \theta, \phi) = \frac{d\sigma(\mathrm{E}_0, \theta, \phi)}{d\Omega}. \tag{1.1}$$

Although as most practical experiments have cylindrical symmetry the more familiar representation

$$\sigma(\mathrm{E}_0, \theta) = \frac{d\sigma(\mathrm{E}_0, \theta)}{d\theta} \tag{1.2}$$

is often used.

For any given impact energy an integral cross section (ICS) can found by integrating the DCS (equation 1.1) over all scattering angles ($0° \leq \theta \leq 180°$, $0° \leq \phi \leq 360°$) as follows:

$$Q(\mathrm{E}_0) = 2\pi \int_0^{\pi} \sigma(\mathrm{E}_0, \theta) \sin\theta d\theta. \tag{1.3}$$

These ICSs are generally plotted as a function of electron impact energy where they can often reveal unique structures for a given species [14].

Resonant interactions between a target and that of the incident electrons can result in strong fluctuations (i.e. a pronounced amplification in the cross section magnitude with energy) in the ICS. These interactions occur when the incident

electron is temporarily captured by the target species and are most common at low energies, where the velocities of the incident electrons and the targets' valence electrons are comparable[15]. Due to the temporary capture of the incident electron by the target species, resonances are often known as "temporary negative ions" (TNI)[16, 17].

In general there are two main types of resonances, those where the energy of the TNI lies below the parent state's energy and those where the TNI energy lies above the parents state's energy. The first of these resonances are commonly referred to by three interchangeable terms: Type 1 resonances, Feshbach resonances and closed channel resonances[17]. These resonances occur very close to the top of the potential well and are often a result of *s*-wave scattering. When the TNI energy lies above that of the neutral species the resonances are called shape resonances, also known as Type 2 resonances or open channel resonances. These resonances can be thought of as occurring when the electron is trapped close to the target as a result of a penetrable barrier created by the angular momentum of the electron. As these resonances are caused by an angular momentum induced barrier they occur for *p*-, *d*- and *f*-waves, but not *s*-waves as they have $l = 0$ [17]. In general shape resonances are shorter lived then Feshbach resonances which results in them having a larger energy width[17].

The energy and width of resonances depends critically on the correlation between the impacting electron and the target[18-21]. For theoretically calculated DCSs, this correlation is heavily dependent on the accuracy of the description of the targets'

structure, normally the quality of the basis set used to describe the target, the targets' ground state dipole moment and it's dipole polarisability. So not only will an ICS reveal the energies and widths of any resonances directly; but the level of agreement shown between the experimental and theoretical cross sections can be used as a gauge of the robustness of the theoretical description of the target species, and the importance of some of the physicochemical species traits on the resultant scattering dynamics.

When the scattering dynamic is dominated by dipole interactions (moment and polarisability), as is the case for the species studied in this work, the elastic DCSs tend to be considerably enhanced in the forward direction[21] (where $\theta \leq 20°$). Due to this enhancement, the forward angle DCS data plays a major role in the overall magnitude of the ICS. However forward angle DCSs are difficult to measure due to the mechanical limitations of most spectrometers including the current spectrometer (see section 2.4.1) and interference from the incident electron primary beam. Similar mechanical limitations also restrict our ability to measure backward angle scattering data to $\theta > 135°$. Therefore an extrapolation procedure (see section 4.2.2 for details) must be performed to extend our measured DCSs to $0°$ and $180°$ before the ICS can be determined. This extrapolation procedure increases the overall uncertainty on the ICS result. Thus we compare both our experimentally measured DCSs with all the theoretical DCS results available, as well as doing the same for the ICSs; and so maximise our ability to gauge the level of agreement between the various theories and our experiments. This in turn allows

us to comment on the validity of some of the physics and chemistry of the approximations made in making those calculations.

The measured elastic CF_2 and CF_3 DCSs and ICSs presented in this thesis represent an important step forward for the electron scattering community, as not only are they the first such elastic measurements preformed with these radical species, they are also the first for electron interactions with species produced *in situ* via pyrolysis. While these measurements certainly provide a comparison for testing models used by theorists, they will also benefit other sections of the atomic and molecular physics community. For example this includes assisting modellers of complex systems to make more informed choices about the cross sections they use, when predicting the behaviour of those systems (e.g. plasmas), and in turn improve the accuracy of those models. This can be transparently seen in the following kinetic equations (1.4-1.6), which link the energy distribution function (f) of the electrons, ions, photon and neutrals in the plasma to the reaction rate coefficients (k) and number densities (N); ultimately expressing their behaviour in terms of cross sections [22, 23]. The variables represented in equations 1.4-1.6 are listed in table 1.1.

$$\frac{df(\vec{v},\vec{r},t)}{dt} = -\vec{v}\cdot\nabla_x f(\vec{r},\vec{v}) - \frac{q\vec{E}(\vec{r},t)}{m_e}\cdot\nabla_v f(\vec{r},t) + \left(\frac{\partial f(\vec{v},\vec{r},t)}{\partial t}\right)_c \tag{1.4}$$

$$k_{ij}(\vec{r},t) = \int_0^\infty f(\varepsilon,\vec{r},t)\left(\frac{2\varepsilon}{m_e}\right)^{\frac{1}{2}}\sigma_{ij}(\varepsilon)d\varepsilon \tag{1.5}$$

$$\frac{dN_k(\vec{r},t)}{dt} = \sum_{i,j}(\pm)n_e k_{ij}\,(\vec{r},t)N_j \rightarrow v_k(\varepsilon) = \left(\frac{2\varepsilon}{m_e}\right)^{1/2}\sigma(\varepsilon)dN_k \tag{1.6}$$

Table 1.1: A list of the variables in equations 1.4-1.6

f	Electron* energy distribution function
$\vec{v}$	3 dimensional velocity vector
$\vec{r}$	3 dimensional position vector
∇_x	Spatial gradient
∇_v	Velocity gradient
t	Time
$k_{ij}(\vec{r},t)$	Electron impact rate coefficient for the electron impact process from state *i* to state *j* in a species
m_e	Electron mass
ε	Energy
$\sigma_{ij}(\varepsilon)$	Cross section for impact process ij occurring at energy ε
n_e	Number density of electrons
N_j	Number density of particles in state *j*
$N_k(\vec{r},t)$	Spatial and temporal particle number density in state *k*
$\left(\frac{\partial f(\vec{v},\vec{r},t)}{\partial t}\right)_c$	How the electron energy distribution function changes over time due to the effect of collisions

*Note that equation 1.4 can also be used to describe the energy distribution of ions and neutral species, in which case m_e becomes the mass of the ion or neutral species.

1.2 Plasma Processing

Plasma processing plays a critical role in many of today's world wide industries as diverse as waste management, textiles, telecommunications, defence, biomedicine and lighting[7, 13]. The plasma processing industry is also expected to play an essential role in emerging technologies including carbon based electronics and solar cell manufacturing to name but a couple[13], thus plasma processing is not only highly relevant today, but it is expected to become even more widespread in the future.

The electronics industry is perhaps one of the foremost among those reliant on plasma processing, which is used for the manufacture of very large-scale integrated (VLSI) microelectronic circuits (or chips)[24]. According to the Semiconductor Industry Association, in 2006, worldwide sales of microelectronics components were worth US$247.7 billion[13]. Considering the obvious importance of plasma processing and in particular the manufacture of VLSI microelectronic circuits, one might assume that plasma processing is a well understood technique, however, this is not the case[25]. Indeed all of the current plasma processes used are done so without a complete understanding of the chemical and physical properties of the plasmas involved, making the processing control largely phenomenological[13]. Acknowledging this industry-limiting lack of understanding of plasma processing, a US National Research Council Board report[8] concluded that "A clear research imperative in the next decade will therefore be to increase our knowledge of the chemical and physical interaction in such plasmas of electrons, ions and radicals with neutral species".

Traditional feedstock gases for plasmas involved in microelectronic production include CF_4, C_2F_6, C_3F_8 and c-C_4F_8 [26]. These chemical species are broken up through a series of inelastic collisions to form ions, neutrals and radicals including CF, CF_2 and CF_3. It is the radical species in particular whose behaviour within the plasma is not well understood, yet these species are responsible for much of the surface etching, due to their extremely reactive natures[25, 27]. As these radicals' properties include large dipole moments and dipole polarisabilites, and, in the case of CF_3, an open shell structure, it is predicted[28] that they will have relatively large

low energy electron collision cross sections. Hence, even in small concentrations, the presence of these radicals might have a profound effect on the overall behaviour of the plasma discharge[19, 28].

Trifluoroiodomethane, is considered to be a 'next generation' plasma processing feedstock gas[18, 29-32] as it is possible to dissociate CF_3I by electron impact[33, 34]. Thus, inside a plasma reactor, CF_3I can be used as a ready source of CF_3, CF_2 and CF radicals. CF_3I's C-I weak bond can also be broken by UV light[18, 32], leading to CF_3I having an atmospheric lifetime in the order of hours to days[35, 36], contrasting with CF_4, which is expected to linger in the atmosphere for some 50,000 years[32]. Hence the global warming potential of CF_3I is significantly lower than that of many current commercial feedstock gases, making it attractive to an industry that still regularly vents these gases into our atmosphere. This attractiveness follows as the Koyoto Protocol requires that strong greenhouse gases must be replaced by alternative compounds[13, 36]. This agreement thus adds to the utility of CF_3I as a replacement plasma feedstock gas as it has global warming potential that is only 1-5 times that of CO_2[29]. In contrast, CF_4 has a global warming potential some 6500 times that of CO_2[37]. While there is some concern about the effect of iodine on ozone in the stratosphere[35], it is considered unlikely that ground based CF_3I emissions will be able to reach that atmospheric layer due to the ready photolysis of CF_3I, and the water solubility of the products[32].

1.3 Previous Work

We note that there have been extensive spectroscopic studies of both CF_2[38-42] and CF_3[43-53]. However, in a major contrast to our present study, these previous works did not require a significant abundance of the radical species to be present, nor did they require the absence of other species. When considering the number of previous studies on the cross sections of these radicals, we find the literature to be sparse at best. We also note that our group is the only one to have published any experimental measurements of the electron impact elastic cross sections for these radical species [19, 20, 54].

In 1993, motivated by the importance of radicals involved in plasma processing, Tarnovsky and Becker[55] measured the electron impact ionisation cross sections for CF_x (x=1,2,3) radicals. To date, we believe they are the only group to have attempted such measurements. These measurements were undertaken using fast (3-3.5 kV) neutral beams of radicals crossed with an electron beam of variable energy. The ions created as a result of the electron-neutral radical collisions were focused onto the entrance plane of a hemispherical analyser and detected by a channel electron multiplier (CEM)[55]. In this way (see their paper[55] for further details) they were able to measure the electron-impact ionisation cross sections from threshold to 200eV for the three (CF_x, x=1,2,3) fluorocarbon radicals.

Deutsch *et al.*[56] published theoretical electron impact ionisation cross sections from threshold to 200eV, for 32 molecular species, including the CF_x (x=1,2,3) series

of radicals, using the Deutsch-Märk (DM) formalisation. In 2002, further theoretical electron impact ionisation cross sections for CF_x (x=1,2,3) were published by Huo *et al.*[57] using a simplified version of the improved binary-encounter-dipole model (siBED) model. The siBED model used the Born cross section, instead of the dipole Bethe cross section employed in the earlier BED model, to represent the long range dipole interaction between the target and incident electron. This more sophisticated treatment of the dipole interaction, in the siBED model, is believed to be the reason why the siBED results are the only ones to agree with the experimentally measured cross sections[57]. Note that the experimentally measured CF_2 and CF_3 150eV electron impact ionisation cross sections, that are directly relevant to this work, are discussed in more detail later in section 3.2.1.

The current published work that is most relevant to our present investigation includes: Lee *et al*.'s study of e + CF_2 elastic DCSs and ICSs using the Iterative Schwinger Variational method (ISVM) with the distorted wave (DW) approximation[27] and Diniz *et al.*'s elastic e + CF_3 DCSs calculated within the Schwinger Multichannel (SMC) approach carried out in the static exchange (SE) approximation[58]. Also relevant to the present work is the extensive series of studies undertaken by Rozum *et al.* into e + CF_x (x=1,2,3) collisions[7, 21, 25, 32, 59]. Although we make no direct comparison to their momentum transfer cross sections (MTCS), we also note Lee *et al.*[27] included them in their investigation of e + CF_2 collisions [27] from 0.1-500eV. Apart from their elastic cross sections, Rozum *et al.* also published excitation cross sections for the six lowest lying electronic energy states of CF_2, for C-F bond lengths ranging from 1.8-3.5a_o[25], as well as a similar

investigation into e + CF collisions[7]. These are noted here for completeness. Because of their importance to the plasma physics community, Rozum *et al.* also published an article in 2006 summarising the then current e + CF_x (x=1,2,3) scattering work along with their previous CF_3I and C_2F_4 electron impact cross sections[32]. It should thus be clear that available data on the systems connected to this thesis are very limited.

The possibility of using CF_3I as a source of CF_x (x=1,2,3) radicals in plasma processing has led both experimentalists and theorists to undertake a variety of studies on e + CF_3I collision cross sections. Those data sets were compiled by Christophorou and Olthoff[29] and more recently summarised by Rozum *et al.*[32]. The CF_3I investigations most relevant to our current work were the experimental elastic DCSs of Kitajima *et al.*[60] and Cho *et al.*[36], and the SMC-SE elastic DCSs, ICSs and momentum transfer cross sections (MTCSs) of Bettega *et al.*[18].

Other relevant CF_3I work that we utilise later in this thesis, includes the total cross section results of Kawada *et al*.[31] and the corresponding complex optical method calculations of Joshipura *et al*.[61]. We note also the CF_3I electron impact ionisation cross section measurements from Jiao *et al.*[62] and Onthong *et al*.[63], and the theoretical ionisation cross sections from Joshipura *et al.*[64].

1.4 The Scope of the Current Investigation

Motivated by the interest in the electron impact elastic DCSs and ICSs of CF_2 and CF_3, because of their importance to plasma processing, and noticing the complete

lack of experimental data, we embarked on our current investigation. This investigation began with the building and subsequent commissioning of a unique apparatus designed to be able to produce beams of radicals *in situ* that were suitable for electron collision studies. Details of the early stages of this process can be found in the doctoral thesis of Hargreaves[65]. This current investigation follows on immediately from the work of Hargreaves[65]. This section now gives a brief overview of the rationale and scope of the current investigation, including details about the publications that have resulted from the measurements made as part of this work.

In 2008 we published a collaborative work[19] containing the first measured elastic DCSs and ICSs for e + CF_2 scattering, with electron impact energies of 30, 40 and 50eV, along with the Schwinger Multichannel method (SMC) calculations of Winstead and McKoy in both the static exchange (SE) and static exchange plus polarisation (SEP) approximations. Those measurements were also compared with the earlier results of Lee *et al*.[27] that were calculated using the Iterative Schwinger Variational method (ISVM) with the distorted wave (DW) approximation. This paper[19] was closely followed by an article in Measurement Science and Technology where we reported both the elastic 25eV e + CF_2 DCS along with a detailed description of the present apparatus[54]. The results of these comparisons (from 25-50eV) have been detailed previously in the doctoral thesis of Hargreaves[65], thus we will only briefly summarise them later in section 4.1. of this thesis. A subset of these e + CF_2 elastic DCSs also appeared in a recent review article on low energy lepton scattering[66].

Rozum *et al*.[25], Lee *et al*.[27] and Winstead and McKoy[19] all found shape resonances in their elastic e+CF_2 ICSs, but disagreed on the energy at which these resonances occurred and their respective energy widths. We therefore continued our e + CF_2 studies to lower electron impact energies (2-20eV)[20] in order to see if we could find any experimental evidence to support the existence of the predicted resonances. This work is discussed in section 4.1.2 of this thesis. Furthermore, we note that at the lower energies the level of agreement between the available theoretical results became worse as dipole scattering interactions became increasingly influential. So we also aimed to ascertain which theoretical description most adequately represented the low energy elastic interaction dynamics of the e + CF_2 system. The discussion of these results is also contained later in section 4.1.

On completion of our low energy CF_2 investigation, our attention shifted to measuring the elastic DCSs and ICSs of CF_3, so that we would ultimately be able to make a comparison with the SMC-SE work of Diniz *et al*.[58] and the UK polyatomic R-matrix results of Rozum *et al*. [21, 32]. However due to our method of producing CF_3 radicals for our electron collision studies (see section 3.3.2), our CF_3 elastic cross sections ultimately depended upon a knowledge for the elastic collision cross sections of C_2F_6, I, I_2 and CF_3I (see sections 3.4.1 and 3.4.2 for details). Thus our first port of call in achieving our aim of investigating the CF_3 radical was filling a gap in the literature in regard to the available low energy CF_3I elastic DCS data.

We note that while Kitajima *et al*. overall reported a quite extensive range of DCSs between 1.5-60eV, they only reported specific results at 10eV, 20eV and 60eV in

the intermediate energy range[60]. So part of the rationale for our CF_3I study came from wanting to increase our knowledge of e + CF_3I elastic scattering processes within the 10eV-60eV gap. Also, by filling in this 10eV-60eV gap for the e + CF_3I elastic DCS, we cleared up part of puzzle for our ultimate study on elastic e + CF_3 collisions over this energy range.

By undertaking e + CF_3I elastic DCS measurements between 10-50eV at 5eV energy intervals (see section 4.2) we were also able to produce detailed ICSs to compare with the only other available CF_3I theoretical ICSs from Bettega *et al.* [18]. Note that these ICSs are in fact probably more important (than the DCSs) to the plasma modelling community[67].

Subsequent to the publication of our elastic e + CF_3I DCSs and ICSs[67], another group, Cho *et al*.[36], also published corresponding DCSs, ICSs and MTCS measurements over an electron impact energy range of 5-50eV. This work[36] was a part of their investigation into the fluorination effects on the cross sections of CF_3Cl, CF_3I and CF_3Br. We discuss all our e + CF_3I DCSs and ICSs results in conjunction with those from Bettega *et al.*[18, 68], Kitajima *et al.* [60] and Cho *et al.* [36] in section 4.2.2 of this thesis.

Having completed our elastic CF_3I DCSs and ICSs electron impact investigations (see section 4.2) our focus shifted back to studying the e + CF_3 elastic scattering dynamics. For the reasons detailed in sections 3.3.2 and 3.4, we then measured DCSs from molecular beams, formed from the pyrolysis of the parent CF_3I,

containing, amongst other species, CF_3 radicals. The measurement of the DCSs of these "mixed" molecular beams (see section 4.3) was very recently published in the journal of Plasma Sources Science and Technology[69]. However, we note here that these cross sections also represent the first such measurements for mixed molecular beams that correspond, to first order, to what you might find in a plasma reactor. As these DCSs are the first of their kind, there are no other measurements or calculations that we can compare them against. They nonetheless represent another crucial step towards determining cross sections for the CF_3 radical.

By using the measured elastic DCSs of CF_3I[36, 67], and C_2F_6[70], in conjunction with the theoretical elastic DCSs of atomic iodine[71] and molecular iodine[72] (see section 3.4.1), and our "mixed" beam DCS measurements, and a knowledge of the composition of the "mixed" beam, we were able to extract elastic DCSs for CF_3. From these DCSs corresponding ICSs were then also subsequently determined in the usual method[73]. These cross sections are compared against the previously published work of Diniz *et al*.[58] and Rozum *et al.* [21], as well as the currently unpublished CF_3 elastic scattering cross sections from Blanco and García[72] and Winstead and McKoy[74] and constitute section 4.4 of this thesis.

1.5 General Information about the Target Species

As this project consists of studies of the elastic electron impacts on CF_2, CF_3I and CF_3, some basic information is presented about each one of these target species.

Also included is some specific information, such as their ground state dipole moment, that is expected to play a significant role in our measurements.

1.5.1 General Information - CF_2

Difluoromethylene (CF_2) is a tri-atomic species consisting of two fluorine atoms each bound to a central carbon atom. In its $^1A_1$ ground state[75] and at equilibrium, CF_2 has C-F bonds have lengths of 1.3Å[76] and a F-C-F bond angle of 104.8°[76] as determined by absorption microwave spectroscopy. This results in CF_2 having overall C_{2v} symmetry (see figure 1.1). CF_2 has a bent rather than linear configuration because of the presence of two unpaired bonding electrons, so although CF_2 is often referred to as a radical species it is more accurate to describe CF_2 as a carbene[75].

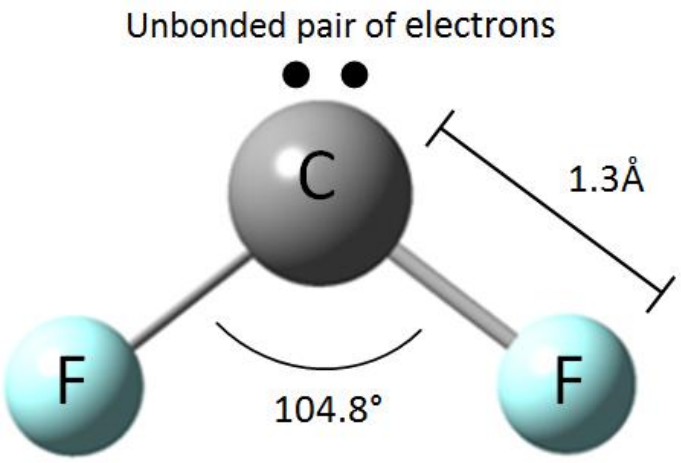

Figure 1.1: A schematic diagram depicting the ground state equilibrium geometry of CF_2, showing bond lengths, the F-C-F bond angle and the location of the unbonded valence electrons.

We are most concerned with the dipole properties of CF_2, as they play an important role in the elastic electron interactions with CF_2. Russo *et al*. have calculated the

ground state permanent dipole moment of CF_2 to be 0.44D[75], which agrees well with the measured value 0.469 ± 0.026D from Kirchhoff *et al.*[77]. The dipole polarisability (α) of CF_2 is not a well understood quantity, with the NIST database listing 113 values for the polarisability of CF_2 calculated using various methods and basis sets[78]. These reported values range from 4.51a_0^3 to 16.84a_0^3 with 86 of them lying between 8-14a_0^3. In addition, to the best of our knowledge, there are no experimental values of α available for this molecule. Note that this polarisability is quite considerable when compared with that of gas phase water 9.67 a_0^3 [79], indicating that the CF_2 target molecular charge is quite diffuse and as a consequence should play an important role in the scattering dynamics. The influence of both the ground state dipole moment of CF_2 and CF_2's dipole polarisability on the elastic electron interactions will be discussed later in sections 4.1.1 and 4.1.2.

Furthermore we note here that CF_2 has a first ionisation energy of 11.44 ± 0.03eV, thus we are unable to directly detect it in our time of flight mass spectrometer, (see section 2.5 for further details). The implications of our inability to detect CF_2 are discussed in detail in section 3.3.1.

Finally we note that the 150 eV electron impaction ionisation cross section of CF_2 is $1.78 \times 10^{-20} m^2$, as measured by Tarnovsky and Becker[57].

1.5.2 General Information - CF_3

The trifluoromethyl radical (CF_3) consists of three fluorine atoms each bound via single bonds to a central carbon atom. At equilibrium, each C-F bond has a length of 1.318Å[45] while each F-C-F bond angle is 110.76°[45]. CF_3 has a trigonal pyramidal molecular geometry due to the presence of a single unbonded valence electron attached to the carbon atom, causing CF_3 to adopt C_{3v} symmetry (see figure 1.2).

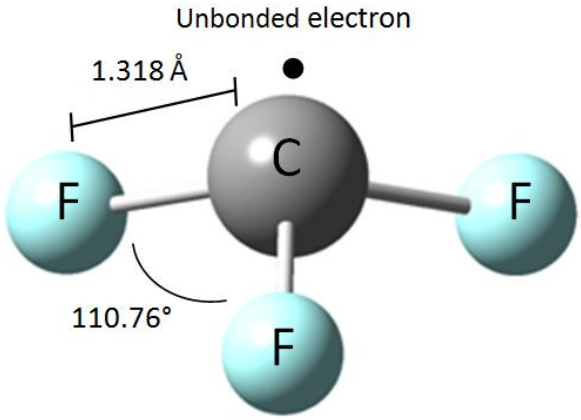

Figure 1.2: A schematic diagram depicting the ground state equilibrium geometry of CF_3, showing bond lengths, the F-C-F bond angle and the location of the unbonded valence electron.

We are again most interested in the dipole properties of CF_3. The ground state dipole moment of CF_3 was measured by Butkovskaya *et al.*[80], who found it to be μ=0.43$\pm$0.07D. As was the case with CF_2, the dipole polarisability of CF_3 is a quantity that has only ever been determined theoretically; with NIST listing 117 values[78]. These values, calculated using various methods and basis sets, range from 5.81-19.52a_0^3, with 86 values between 9-15a_0^3 of which 31 values lie between 12-13a_0^3. The effect of both the dipole moment and polarisiability of CF_3 on its elastic electron interactions is discussed later in sections 4.4.1 and 4.4.2.

The ionisation energy of CF_3 has been determined by 12 different groups [55, 81-91] using a variety of methods including electron impact ionisation and photoelectron spectroscopy, and leading to values ranging from 8.5 ± 0.8eV[55] to 9.8 ± 0.2[91]. Thus, as the ionisation energy of CF_3 is less than 10.48eV, we will be able to detect it in our TOFMS using 118nm photons as an ionisation source. Unfortunately there are no available photoionisation cross sections for CF_3 at 118nm, so in order to determine our post-pyrolysis beam composition (section 3.3.2) we use the corresponding electron impact ionisation cross section which is 0.026$Å^2$ at 10.5eV[55]. We expect this value, as determined experimentally by Tarnovsky and Becker, to be a reasonable approximation to the photoionisation cross section at this energy. Lastly, in order to set an absolute scale to our measurements (see sections 3.1.2 and 3.2.1 for details as to how this is accomplished), we require the electron impact ionisation cross section of CF_3 at 150eV. This was also measured by Tarnovsky and Becker and found to be $2.3 \times 10^{-20} m^2$ (to within 25%)[55].

1.5.3 General Information - CF_3I

Iodotrifluoromethane (CF_3I) belongs to the C_{3v} point group and consists of three fluorine atoms and one iodine atom, all of which are bonded to a central carbon atom (see figure 1.3). The presence of the large iodine atom forces the molecule into a trigonal pyramidal geometry, with an optimised umbrella angle of 108.55°, as determined by Ajitha *et al.*[92] using the complete active space self consistent field (CASSCF) theory. At equilibrium, each C-F bond is 1.344Å[18] long while the C-I

bond measures 2.101Å[18]. The F-C-F bond angle has been determined to be 107.6°[18].

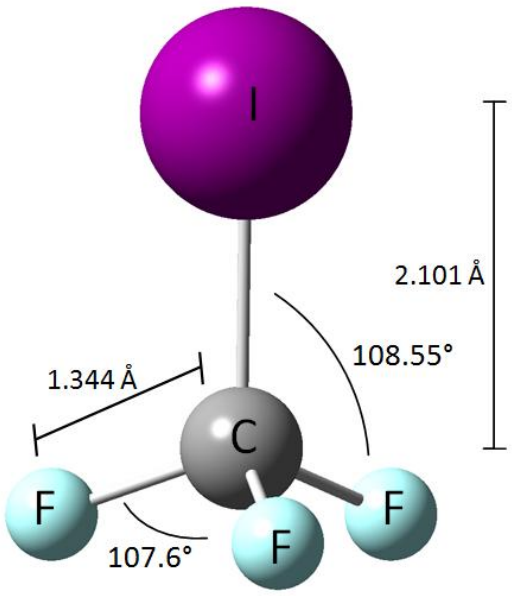

Figure 1.3: A schematic diagram depicting the ground state equilibrium geometry of CF_3I, showing its bond lengths and bond angles.

CF_3I has a ground state dipole moment of $\mu = 1.048\mathrm{D}$ [93], and a dipole polarisability of $\alpha = 52.42a_0^3$ [94], the largest among our current target species. The effect of both CF_3I's dipole moment and dipole polarisability on its elastic electron interactions is discussed later in sections 4.2 and 4.3.

In order to set an absolute scale to our DCS measurements, using our present normalisation method, we require the electron impact ionisation cross section of CF_3I at 150eV. This was calculated by Antony *et al.* [95] who found it to be $8.58 \times 10^{-20}\mathrm{m}^2$ (within 2%).

Furthermore, as CF_3I is used not only as a target of interest but as a precursor to the production of CF_3 radicals via flash pyrolysis (see section 3.3.2), so we also require knowledge of its ionisation energy and photoionisation cross section at 10.48eV. The ionisation energy of CF_3I has been measured multiple times using photoelectron spectroscopy[96, 97] photoionisation mass spectroscopy[86, 98, 99] and electron impact studies[100-102]. From these studies the ionisation energy is taken to be 10.28 ± 0.07[103]. Thus we expect to be able to detect CF_3I in our TOFMS. The photoionisation cross section of CF_3I at 10.48eV (118nm) that we used to determine our beam composition post-pyrolysis was $0.502 \times 10^{-20} m^2$, as determined by Martín *et al*.[104] using their molecular quantum defect orbital (MQDO) calculations.

Chapter 2 — The Apparatus

The apparatus used to measure the current differential cross sections has been described in great detail elsewhere[54, 65] Nonetheless, for the purpose of completeness, a description of this apparatus is included here. In particular, modifications that have been made since the publishing of those earlier works [54, 65] are highlighted.

2.1 Basic Overview of the Apparatus

The apparatus consists of three main systems; a pulsed gas nozzle; an electron spectrometer; and a time of flight mass spectrometer (TOFMS), with all these components being mounted in successive adjoining high vacuum chambers (see figure 2.1).

Each of the chambers was fabricated from non magnetic stainless steel (type 316) and they were all mounted on a common rail (see figure 2.2). This configuration ensured that the chambers could be unbolted and separated horizontally in order to allow internal access. Neoprene o-rings were used throughout as seals between the various chambers, while a combination of neoprene o-rings and copper gaskets were employed to seal the many feed-throughs associated with this apparatus.

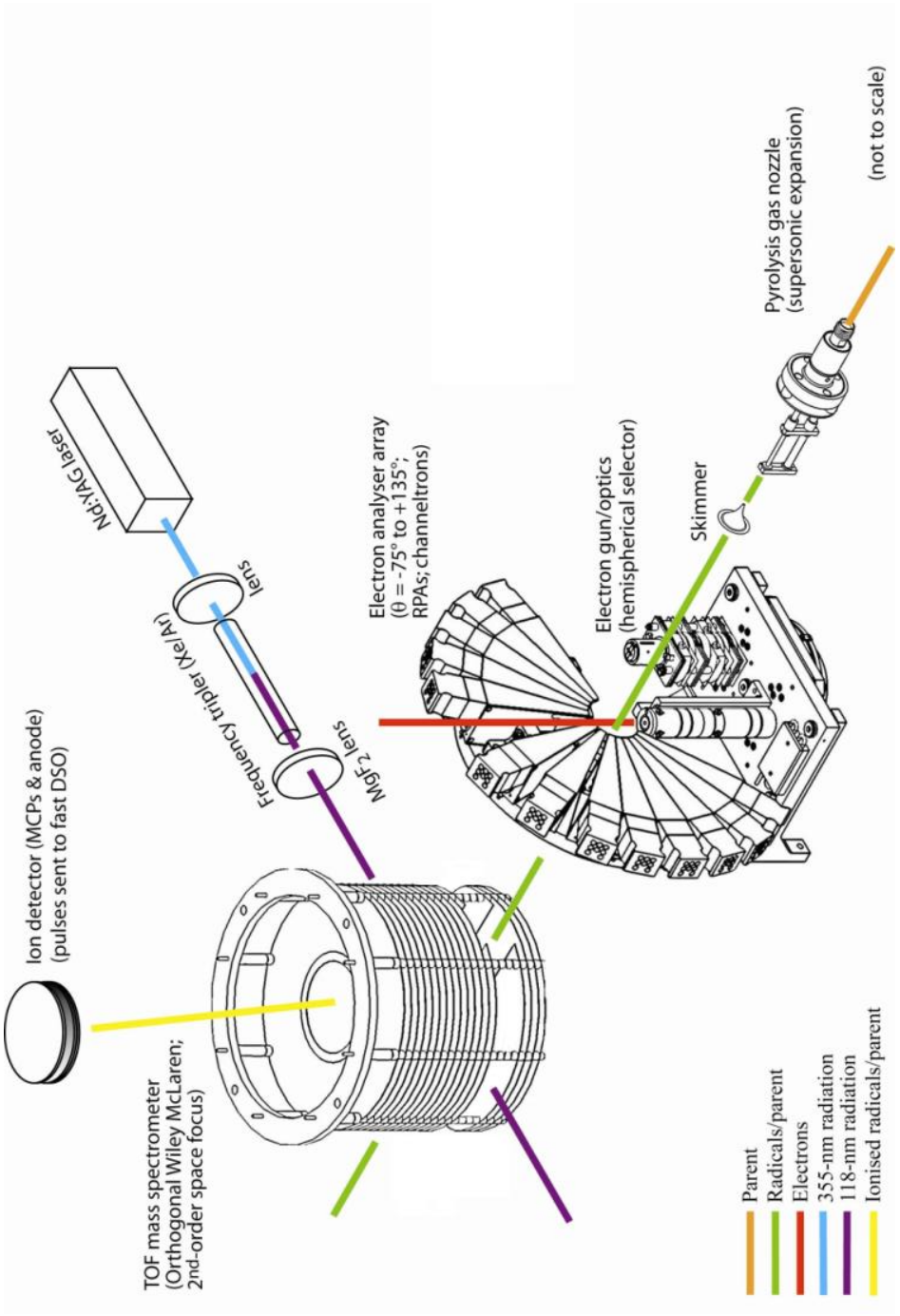

Figure 2.1: A Schematic diagram showing the main components of the present apparatus. All these components reside in high-vacuum chambers (see text for details).

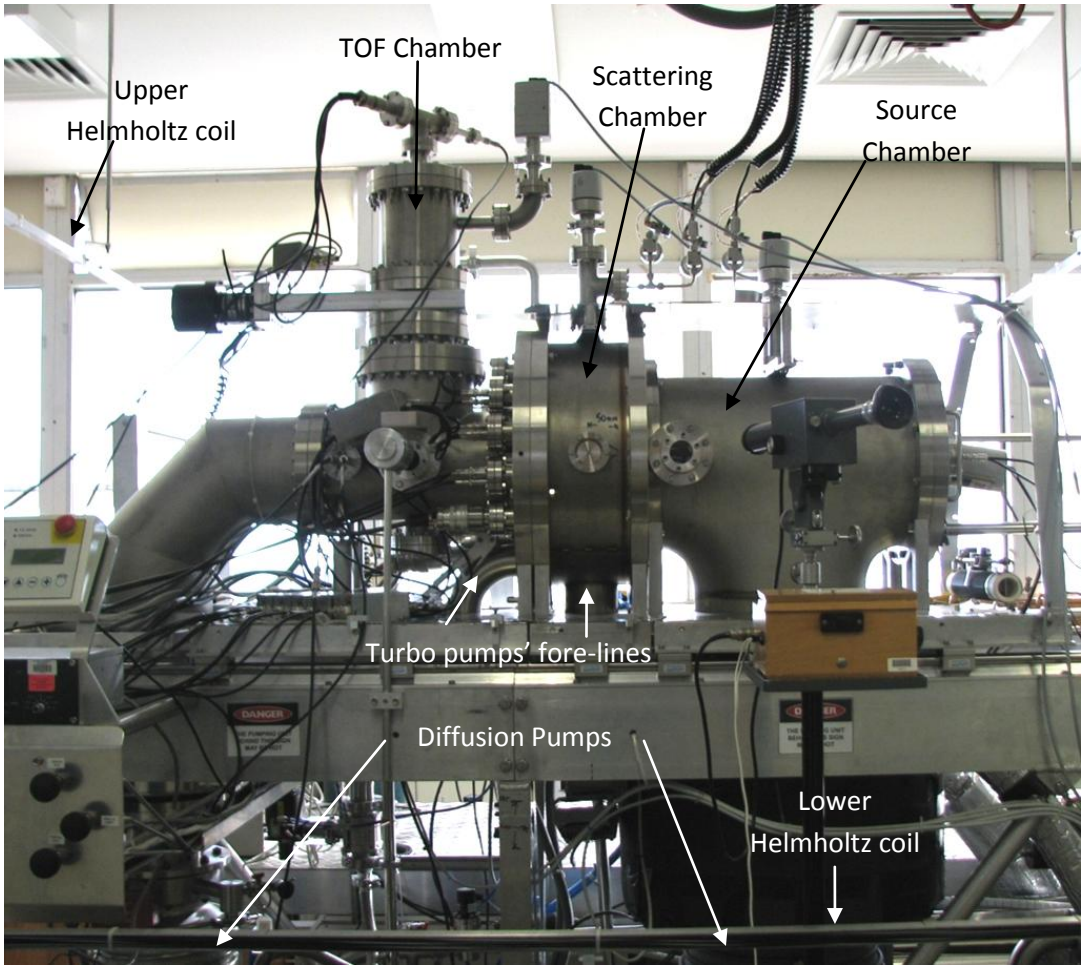

Figure 2.2: A photograph of apparatus. This photograph hints at the scale and complexity of this system.

The first chamber, referred to as the "source chamber" contained the pulsed gas nozzle (General Valve Series 9), through which various gases were introduced to the system. For experiments involving the production of radicals a pyrolytic assembly was additionally mounted to the face of this pulser. The source chamber was pumped on by a 10 inch diffusion pump (Varian VSH10) with a maximum pumping speed of 5,300 L/s (air). That diffusion pump was backed on by a two stage rotary vane pump (Balzers DUO 060A).

The source chamber was separated from the second chamber, referred to as the "scattering chamber", by a gold plated skimmer (Beam Dynamics Inc., diameter 1.5mm). The scattering chamber housed the electron spectrometer; which in turn consisted of an electron monochromator and an array of thirteen retarding potential analysers (RPAs) mounted radially about the electron interaction region. We note that each of these RPAs incorporated a channel electron multiplier (Sjuts KBL 210). In this configuration the electron interaction region was located at a fixed position of 5.4 cm upstream of the skimmer

The scattering chamber was evacuated by a turbo-molecular pump (Pfeiffer TPU 261 PC) with a maximum pumping speed of 190 L/s (N_2). The electron monochromator was itself housed in a differentially pumped sub-chamber within this scattering chamber. This sub-chamber was pumped on by a second turbo-molecular pump (Pfeiffer TMU071P) with a maximum pumping speed of 33 L/s (N_2). Both these turbo molecular pumps shared a common backing pump (Pfeiffer DUO 10 C).

A 30 mm orifice separated the scattering chamber from the final chamber that housed a time of flight mass spectrometer (TOFMS). The TOF chamber was pumped on by a 6 inch diffusion pump (VHS6 BOC Edwards Diff Stack), which was backed on by an Alcatel (2033CP+) rotary backing pump. The ionisation region of the TOFMS was located at a fixed position of 33.8 cm upstream of the interaction region.

The possible backstreaming of oil between the diffusion pumps and their respective backing pumps was minimised using glycol charged cold fingers, with an operating temperature of -30^{o}C. Cold traps mounted above each diffusion pump minimised the presence of any diffusion pump oil in the source and TOF chambers. These cold traps were maintained at approximately -55^{o}C using chilled recirculated methanol, which was sourced from a 50L reservoir that was cooled to approximately -80^{o}C using a custom built two stage recirculating methanol chiller (Thermoline Scientific).

Perfluorinated oils were chosen for use in all of the pumps, as the system would come into contact with highly reactive species. Specifically, YH VAC Fomblin 25/6 inert vacuum pump oil was employed to charge all three backing pumps while both diffusion pumps were charged with VH VAC 25/9. Finally F3 oil was used in both turbo-molecular pumps.

Recirculating water was used to cool both the diffusion pumps and the Pfeiffer TPU261PC turbo-molecular pump, while the Pfeiffer TMU071P turbo-molecular pump was air cooled.

The source, scattering, and TOF chamber pressures were each monitored by compact full range gauges (Pfeiffer PKR 251). Compact Pirani pressure gauges (Pfeiffer TPR 281) were further used to monitor the pressure of the backing lines of each diffusion pump, and the backing line common to both the turbo molecular pumps. All these Pfeiffer pressure gauges were read by a six input maxi-gauge control unit (Pfeiffer TPG 256A). The electron monochromator sub-chamber's

pressure was recorded by a series 274 Bayard-Alpert nude ion gauge with a Granville-Phillips 307 vacuum gauge controller.

A programmable logic controller (PLC) was used to operate all the pumps, pneumatic valves and internal electronics. It also monitored the chamber pressures, diffusion pump temperatures, cold trap temperatures and for water circulation. The hierarchy of interlocking on the PLC was designed to allow it to shut down the all of the components of the apparatus in the event of any fault conditions being detected.

A set of square-section Helmholtz coils, powered with 7.5V at 1.8A using a trio-regulated DC power supply (Electrix PR-652), were configured in the manner shown in figure 2.2, and were used to counter the vertical component of the Earth's magnetic field. The scattering chamber was also lined with a stress annealed metal alloy (Co-Nectic), such that the entire chamber was encased in a closed non-magnetic metal surface, in principle preventing the entry of any external magnetic fields. In addition, where possible, current carrying wires were mounted in pairs. This was undertaken so that the current travelling in one wire was equal and opposite to the current travelling in the other wire, thereby negating any magnetic fields. All these precautions resulted in a residual magnetic field in the scattering chamber of less than 5 mGauss in each direction, as measured by a digital magnetometer (Meda, μMag series), and less than 1 mGauss around the hemispherical selector.

The electron monochromator and analyser array were mounted inside grounded stainless steel shielding, in order to prevent electric field penetration into the interaction region. The wires mounted outside these shields were also completely encased in grounded Al-foil as an additional precaution.

2.2 The Gas Handling System

The gas handling system (GHS) was a lattice-like network of predominantly ¼ inch stainless steel tubing, with swagelok connections. It contained: eleven screwed-bonnet needle valves (Nupro, JN series); seven solenoid actuated valves (24V DC SMCXSA1-125) with a shared controller (custom built by the Flinders University Electronics Workshop); two variable leak valves (Granville-Phillips Series 203); and two metering valves (Nupro, BM series). A picture of the GHS is shown in figure 2.3.

The GHS could accommodate up to four gas cylinders at any one time although only two were needed during an experiment; each gas used for experimentation was routed from its respective bottle to the solenoid actuated pulsed nozzle. The pressure behind the nozzle was controlled by one of the two variable leak valves while a precision Baratron pressure gauge (MKS 690A12TRC) displayed and recorded that pressure.

The GHS could be evacuated using the rotary pump (DUO 060A) backing pump, after this backing pump was isolated from the VHS10 diffusion pump's exhaust line.

The GHS also contained three additional volumes (two 26L and one 1L) that could be used to make various gas mixtures. A fourth detachable 10mL volume allowed for the vapourisation and subsequent introduction of species that were liquids at room temperature into the apparatus. These extra volumes were not needed during the course of this project.

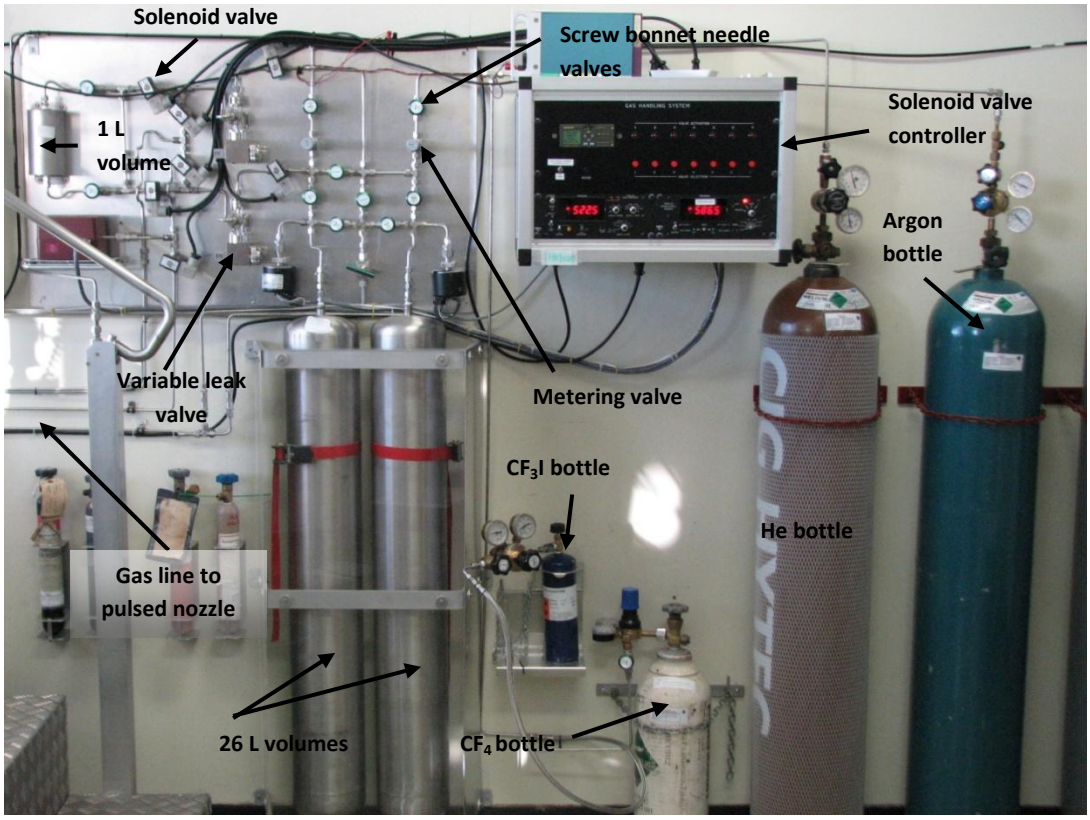

Figure 2.3: A picture of the gas handling system of the present apparatus.

2.3 Solenoid Actuated Pulsed Nozzle

A solenoid actuated pulsed nozzle (Granville Phillips series 9), set to a normally closed configuration, used a Teflon poppet held by a spring to create a seal with the nozzle's faceplate. On application of a voltage (typically 440V) the spring recoiled and pulled the poppet away from the faceplate allowing gas to flow through. For all

of the research presented here this nozzle was pulsed at 10 Hz using a custom built (Flinders University Electronics Workshop) pulsed nozzle driver.

The two internal wires that connected the pulser to its driver were wrapped around each other, such that the electromagnetic fields produced by the pulsing voltages were created in opposite directions and so minimised the overall field present. The pulser housing itself was shielded using Al-foil. External to the chamber, RG58 shielded cables transmitted the pulser voltages from the driver to the relevant feedthrough.

2.3.1 The Pyrolytic Assembly

The pyrolytic assembly was mounted onto the front of the pulsed nozzle valve, such that the gas admitted into the system passed through a heated silicon carbide tube (SiCT) before it passed through the rest of the apparatus (see figure 2.1). The heated SiCT supplied the energy needed to break bonds within the molecules of interest and thus created the radicals to be studied.

The pyrolytic assembly was built “in-house” (Flinders University Mechanical Workshop) and was based on a design published in 1994[105]. This assembly was conveniently mounted directly onto the face of the pulsed nozzle. Pyrolysis occurred within a resistively heated silicon carbide tube (Hexaloy SE) with a length of 37 mm, an inner diameter (ID) of 1 mm, and an outer diameter (OD) of 3mm. The alternating current that was used to heat this tube was connected using titanium

electrodes with graphite contacts, these electrodes also served to support the tube. An aluminium oxide tube (OD 3 mm, ID 2 mm) of 30 mm length was mounted to the face of the pulser and connected to the SiCT via a custom made graphite adapter. The aluminium oxide tube ensured that the heated SiCT and pulser face were electrically and thermally insulted. A stainless steel heat shield with a diameter of 38 mm was mounted between the SiCT and the mounting plate to reduce the possibility of any radiative heating of the pulser by the heated tube. The entire assembly was kept rigid by a support ring, spring mounted in front of the SiCT. Figure 2.4 shows a schematic diagram and a photograph of the pyrolytic assembly that illustrates some of the features just described.

A custom built (Flinders University Electronics Workshop) power supply (40V, 7A) connected to a mains power outlet (240 V, 50 Hz), via a Variac transformer (Regavolt 71A 0-275V 6A), enabled the nozzle power and thus temperature to be controlled. An ammeter (Keithley 197), connected in series, monitored the current flow while a multimeter (Fluke 77), connected in parallel, monitored the assembly's voltage.

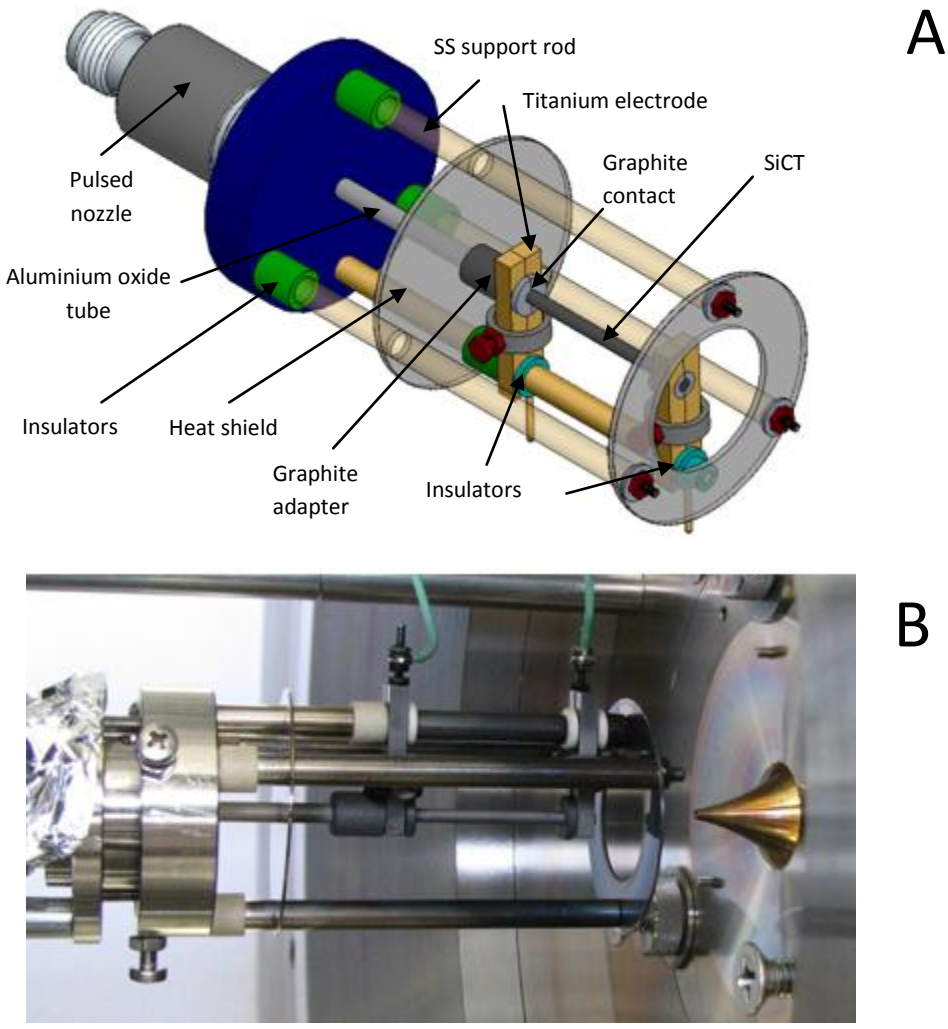

Figure 2.4 A: A schematic diagram of the current of Pyrolytic assembly including its main features. This figure is drawn to scale and was produced using the SolidWorks educational CAD software. B: A photograph showing the pyrolytic assembly *in situ.*

2.3.2 Striking the Silicon Carbide Nozzle

The 37 mm SiCT had an initial resistance of 8.2 MΩ and so was unable to conduct enough current for resistive heating. However, unlike most metals, the resistance of silicon carbide decreases with increasing temperature. Hence the SiCT was heated under vacuum, using a tungsten (W) filament, until the resistance of the tube had decreased to a point where it could conduct enough current for resistive heating. This process was called “striking”.

The striking and subsequent annealing of the SiCT was undertaken in a separate cylindrical vacuum chamber to that of our scattering apparatus. This was undertaken as the striking process would coat the walls of the vacuum chamber with a thin film of carbon, that would be liberated from the SiCT's surface. During the striking and initial annealing process the SiCT was therefore mounted as shown in figure 2.5, and was connected to the same custom built 7A, 40V AC power supply noted previously.

The tungsten filament was created from 0.25 mm thick wire that was wrapped around the SiCT, as also shown in figure 2.5A. The tungsten filament was connected to a 60A, 50V power supply (Sorensen SRL 40-50) using 2.2 mm diameter copper wires. The "striking" vacuum chamber was then evacuated by a turbo molecular pump (Pfeiffer TPU 520 L/s N_2) and a Balzers-Pfeiffer backing pump (DUO 016B), to a pressure of 1×10^{-7}Torr as measured by an ion gauge (IKP 020 Balzers Penning gauge).

Once this pressure was attained the tungsten filament was heated to approximately 1500^{o}C, as measured with an optical pyrometer (figure 2.5B). Over the course of several hours of heating the SiCT began to conduct 32.7 Watts AC (1A, 32.7V), indicating that the resistance of the tube had decreased to 32.7 Ω. The configuration was now left like this for 2 hours, during which time the SiCT underwent the initial stage of a permanent irreversible change to its microstructure called annealing. After the initial annealing period both the W-filament and the SiCT were turned off and allowed to cool to room temperature, where the measured

resistance of the SiCT was found now to be 24kΩ. From this point onward the SiCT was able to conduct enough current for it to potentially resistively heat the nozzle to temperatures up to 1500^{o}C.

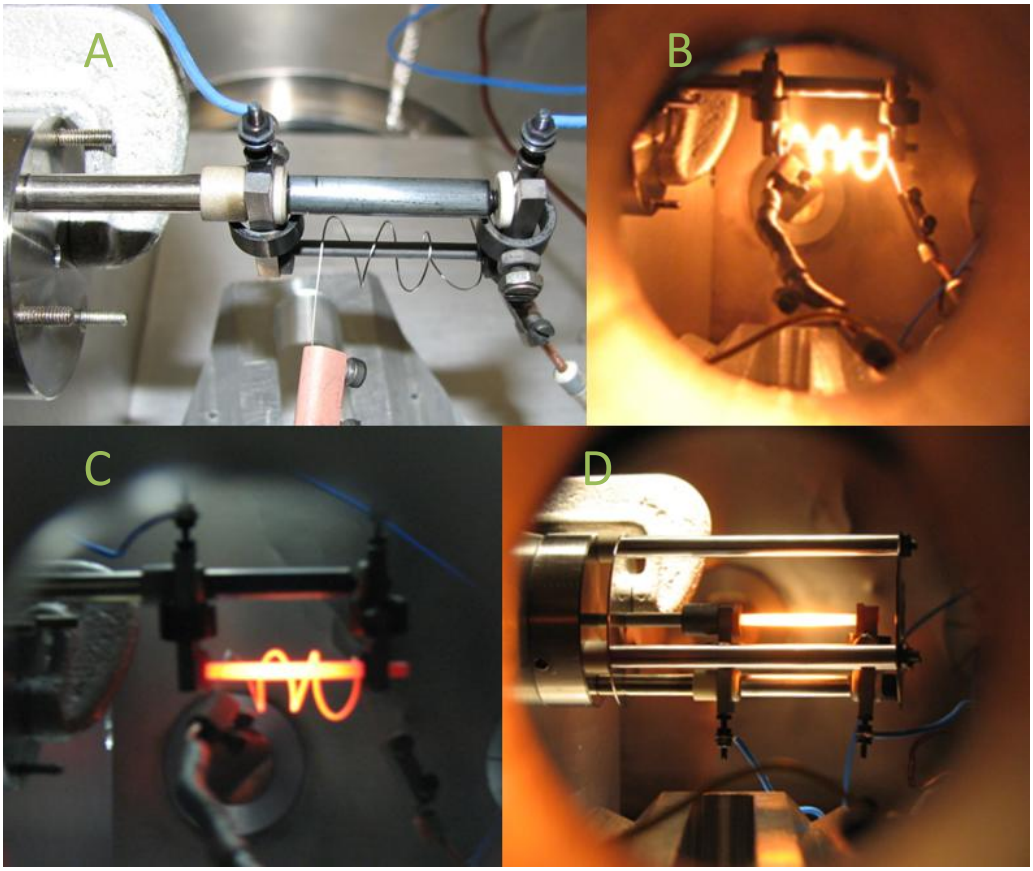

Figure 2.5 A: A photograph depicting the SiCT mounted for striking; B: A photograph showing the W-filament heating the SiCT; C: A photograph showing the SiCT during the initial annealing process; D: A photograph depicting the SiCT after successful striking and annealing and without the W-filament.

The negative resistivity coefficient of the SiCT did, however, effect the tubes operation. Indeed each time the SiCT was re-heated the resistance dropped further causing more current to flow. This in turn resulted in an increase in the temperature that further caused more current to flow and so on. Thus it was always necessary to increase the tube temperature in a slow and controlled fashion. Clauberg *et al* [105], for example, put a 100 W light globe in series with their SiCT in order to limit

the current flow; this was not found to be necessary in our case provided the tube power and temperature were monitored.

Each time the SiCT tube was heated, the annealing process continued, although in a less dramatic fashion than for the initial period. This continued annealing resulted in the resistance of the SiCT decreasing with use, as illustrated in figure 2.6. This decrease in the resistance of the SiCT necessarily caused a corresponding increase in the amount of current required to reach the operating temperature (1200^{o}C for CF_2 radical production), as is shown in figure 2.7.

While the custom made AC power supply was capable of delivering more than the 6A of current required, to maintain 1200^{o}C after 140 hours of operation, the lowered resistance of the SiCT began to cause other problems. For example when the SiCT reached a resistance of 2.5Ω, after almost 120 hours of operation, its resistance became comparable to that of the graphite contacts; which began to glow cherry red, indicating that they were heating to a temperature of 800^{o}C. As graphite has a positive resistivity coefficient, and thus has a resistance that increases with temperature, this heating affect become more apparent as the SiCT operating time increased. After 140 hours of operation the original SiCT was retired as the graphite contacts were now heating to approximately 1000^{o}C causing a slight bending of the titanium electrodes and concerns about the overall integrity of the pyrolytic assembly. This SiCT in fact lasted some forty hours longer than the quoted lifetime[105] for such a system.

A second SiCT of 36.6mm length was struck in the same fashion as already described, and it was used for the pyrolysis of CF_3I (see later). Its lower operating temperatures (see section 3.3.2) resulted in a considerable slowing of the ongoing annealing process, and as such this nozzle is expected to have an operational lifetime of upwards of two hundred hours.

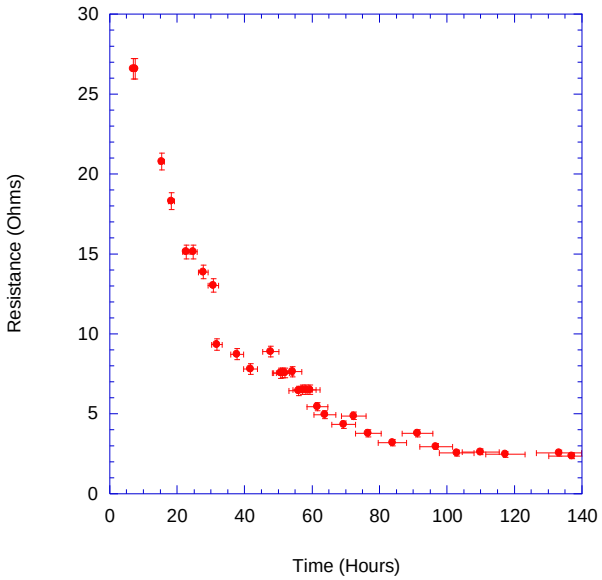

Figure 2.6: Plot of the resistance of the SiCT, at an operating temperature of 1200°C, as a function of the SiCT operating time.

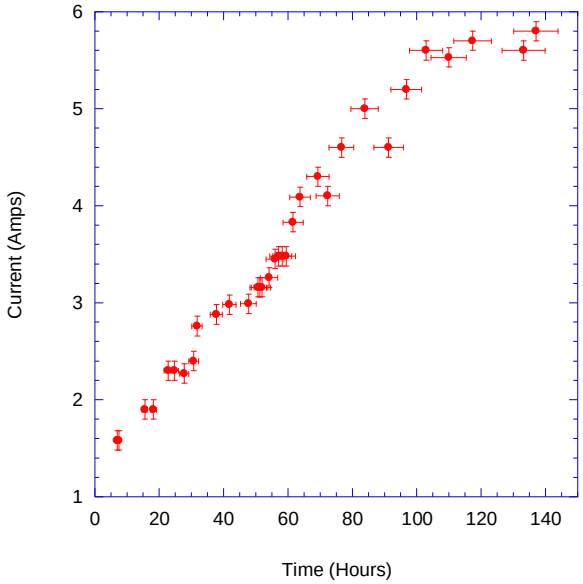

Figure 2.7: Plot showing the current required to maintain the SiCT at an operating temperature of 1200°C, as a function of the SiCT operating time.

2.4 The Electron Spectrometer

The electron spectrometer, consisting of an electron monochromator and an array of analysers, was completely constructed at the Australian National University. That initial design was, however, modified significantly with most of these changes being detailed in Hargreaves[65].The electron monochromator was used as the electron source for all the present scattering experiments, and was capable of producing an electron beam with an adjustable energy between 2eV and 50eV with a theoretical energy resolution of 60 meV (see equation 2.2). The retarding potential analyser (RPA) array consisted of thirteen wedges mounted radially around the interaction region, with each of these wedges containing a channel electron multiplier. This array of CEMs was used to detect the number of scattered electrons present at each angle.

A detailed description of the electron spectrometer can be found in Hargreaves' thesis[65] published in 2008, so that only a summary of its major features will be presented here. Since that description the spectrometer has undergone three modifications. Two of these modifications were made to each of the thirteen RPA wedges, while the third, the inclusion of an extra collimating aperture, was made to the electron spectrometer. These changes and the rationale for making them are detailed shortly.

2.4.1 Electron Monochromator

2.4.1.1 Construction, Wiring and Operation

The purpose of the electron monochromator is to transport, focus and collimate electrons emitted by a filament onto the interaction region (IR). To assist in this deflectors are incorporated into its design. While these deflectors perform no focussing action, they do help steer the beam through the various collimating apertures of the electron monochromator. The monochromator also has the purpose of significantly narrowing the energy width of the electrons emitted by the filament. The electron monochromator ultimately produces a stable, well collimated beam of electrons at the IR for our scattering experiments.

The monochromator consisted of four main parts; an aperture lens stack that guided the electron beam to the entrance of a hemispherical selector; the hemispherical selector that narrowed the energy width of the electron beam; the cylindrical lens stack that guided the electron beam from the hemispherical selector to the interaction region; and two concentric Faraday cups that monitored the final electron beam current. The design of all the electron optic elements was based on both the tables in Harting and Read[106] and its charged-particle-optics (CPO-3D) code that can be commercially purchased from Scientific Instrument Services Inc., an Authorized CPO Distributor[107]. Figure 2.8 shows a 3D cutaway schematic of the electron monochromator that indicates its main features, while the dimensions (element separation and aperture size) of the elements that comprise this monochromator are shown in figures 2.9-2.12.

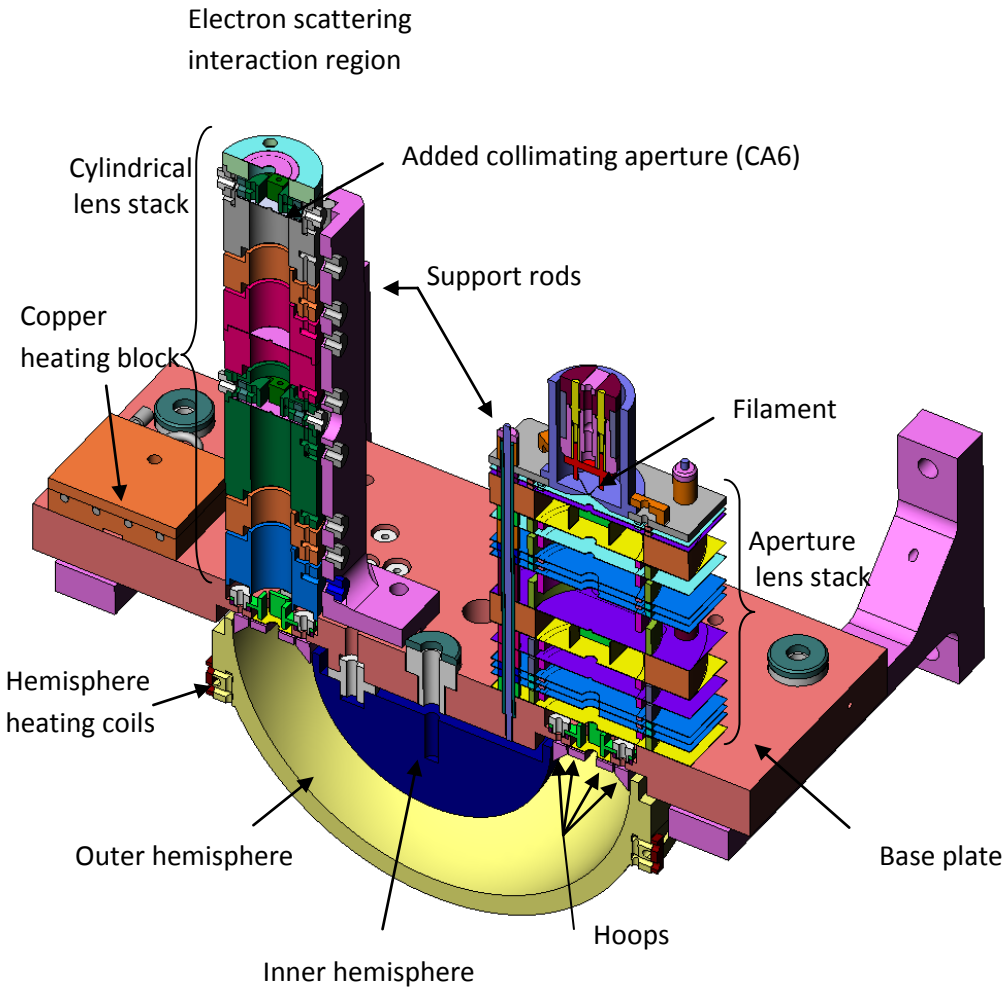

Figure 2.8: A cutaway schematic diagram of the components of the present electron monochromator indicating its mounting. This figure was produced using the Solid Works educational CAD software.

The electrons were supplied by thermionic emission from a thoriated tungsten filament, mounted in a triode configuration at the top of the aperture lens stack (see figure 2.9). Once drawn through a Pierce extraction element, the electrons passed through a grid, three sets of deflectors, two collimating apertures and two multi-element lenses before reaching the entrance plane of the hemispherical selector. Typical operating potentials for all these elements are given later in table 2.1. Note that all these voltages are referenced to the cathode potential, which ultimately corresponds to the energy you wish the electrons to have as they enter the interaction region.

The lens elements and deflectors in the aperture stack were fabricated from rectangular sheets of titanium (0.2mm thick), with apertures of various sizes punched into their middle (see figure 2.9). Interlocking concentric titanium cylinders, of various heights, were spot welded onto the top and bottom of those flat titanium pieces. These cylinders completely encased the electron beam and so shielded it from any external electric fields, or insulating surfaces that might lead to charging effects and beam instability. Three stainless steel rods mounted inside ceramic sheaths ran the length of the aperture stack that, in conjunction with the ceramic spacers, held the aperture stack in place on top of the base plate.

The inner and outer hemispheres with radii of r_{inner} = 30mm and r_{outer} = 50mm, were mounted beneath the base plate immediately after the third set of deflectors (see figure 2.10). Four hoops (H1-H4 in figures 2.10 and 2.11) contained within the hemispheres, kept the electric field as uniform as possible around the hemisphere

entrance and exit planes[108]. A photograph of the interior of the hemispherical selector indicates hoops 1-4, is shown later in figure 2.11. The pass energy of the hemispheres (E) was typically set at 2eV or 3eV for this project. The optimal energy resolution (ΔE) of the current spectrometer was determined using equation 2.1, from Read *et al.*[109],

$$\Delta E \approx E\left(\alpha_{\frac{1}{2}}\frac{r_s}{L_s}+\beta_{\frac{1}{2}}\theta^n\right) \quad (3.2\ (2.1)\ ) \tag{2.1}$$

where E represents the "pass energy" of the hemispheres, r_s is the radius of the beam at the entry into the hemispherical selector, L_s represents the straight line distance between the entry and exit apertures of the hemispheres, θ represents the pencil angle of the electron beam entering the hemispherical selector, while $\alpha_{\frac{1}{2}}$, $\beta_{\frac{1}{2}}$ and n are functions of the type of selector, the type of apertures used and the ratio of $\beta_{\frac{1}{2}}\theta^n$ to $\alpha_{\frac{1}{2}}\frac{r_s}{L_s}$. We note that the pencil angle θ often is very close to zero, as in an ideal scenario lens 2 collimates the electron beam before it enters the hemispherical selector. Given that $n = 2$ [109] and $\beta_{\frac{1}{2}} \ll \alpha_{\frac{1}{2}}$[109] we assume $\beta_{\frac{1}{2}}\theta^n \approx 0$. Thus equation 2.1 is rewritten as follows:

$$\Delta E \approx E\alpha_{\frac{1}{2}}\frac{r_s}{L_s}. \tag{2.2}$$

Using equation 2.2 and a "pass energy" of 2eV, $\alpha_{\frac{1}{2}} \sim 1.6$ [109] and the following geometry $r_s = 1.5\text{mm}$, $L_s = 80\text{mm}$, we estimate the lower limit of the current spectrometer's resolution to be approximately 60meV.

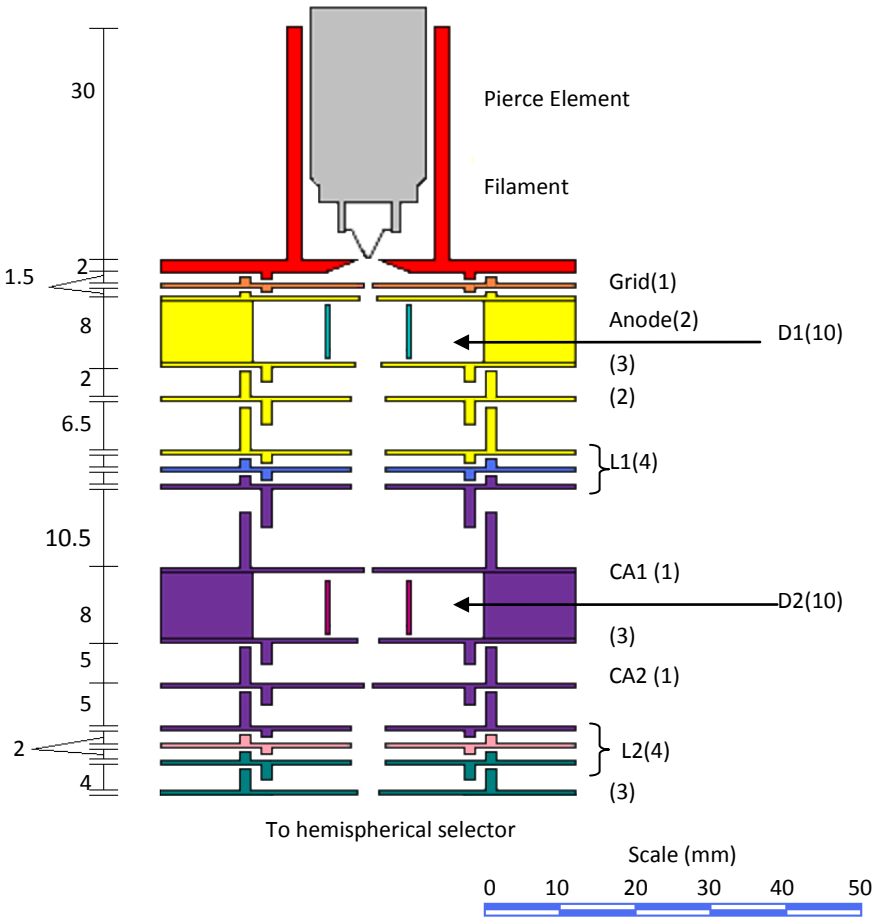

Figure 2.9: A schematic diagram of the aperture lens stack of the present electron monochromator, which indicates its characteristic dimensions drawn to scale. All dimensions are given in mm. Like colours indicate common electrical potentials. The acronyms are defined as L = lens element, CA = collimating aperture, D = deflector set. Numbers in parenthesis indicate the diameter of each circular aperture or in the case of the deflectors, the distance between parallel plates. All titanium plates are 0.2mm thick. See text for further details.

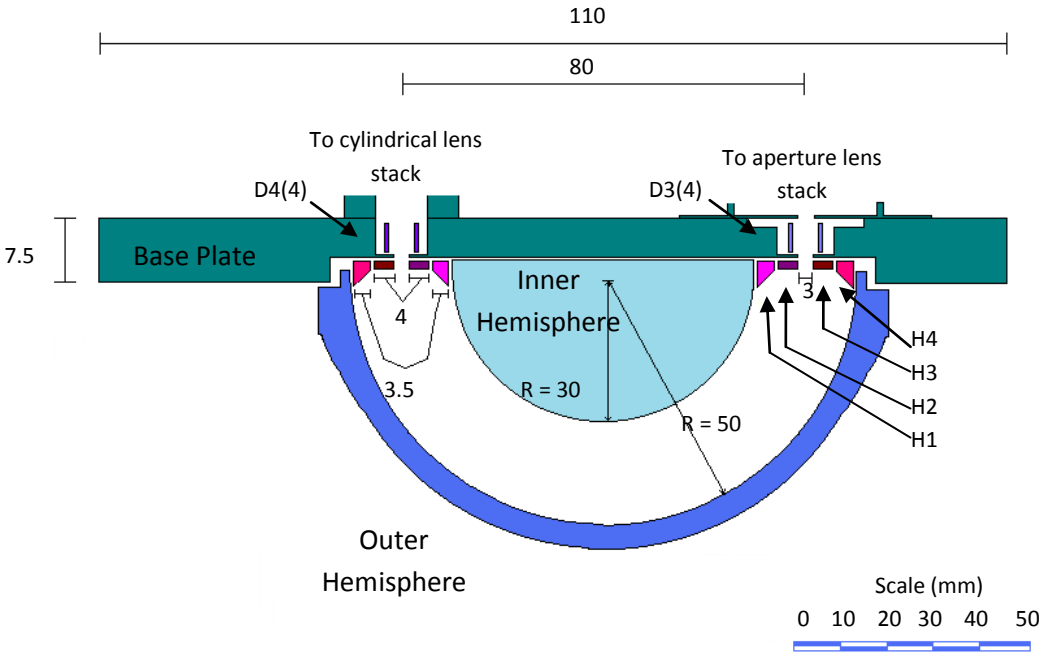

Figure 2.10: A schematic diagram of the current hemispherical energy selector of the present electron monochromator, which indicates its characteristic dimensions drawn to scale. All dimensions are given in mm. Like colours indicate common electrical potentials. D=deflector set, the numbers in parenthesis indicate the distance between parallel plates of the deflectors. See text for further details.

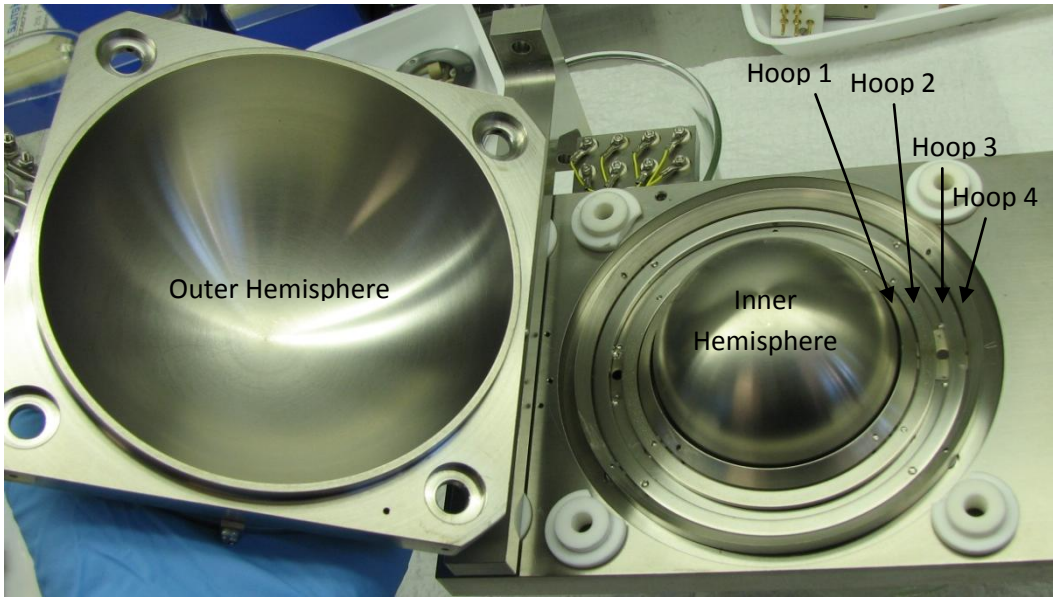

Figure 2.11: A photograph showing the interior of our hemispherical energy selector. Note the field correction hoops on the right of the figure.

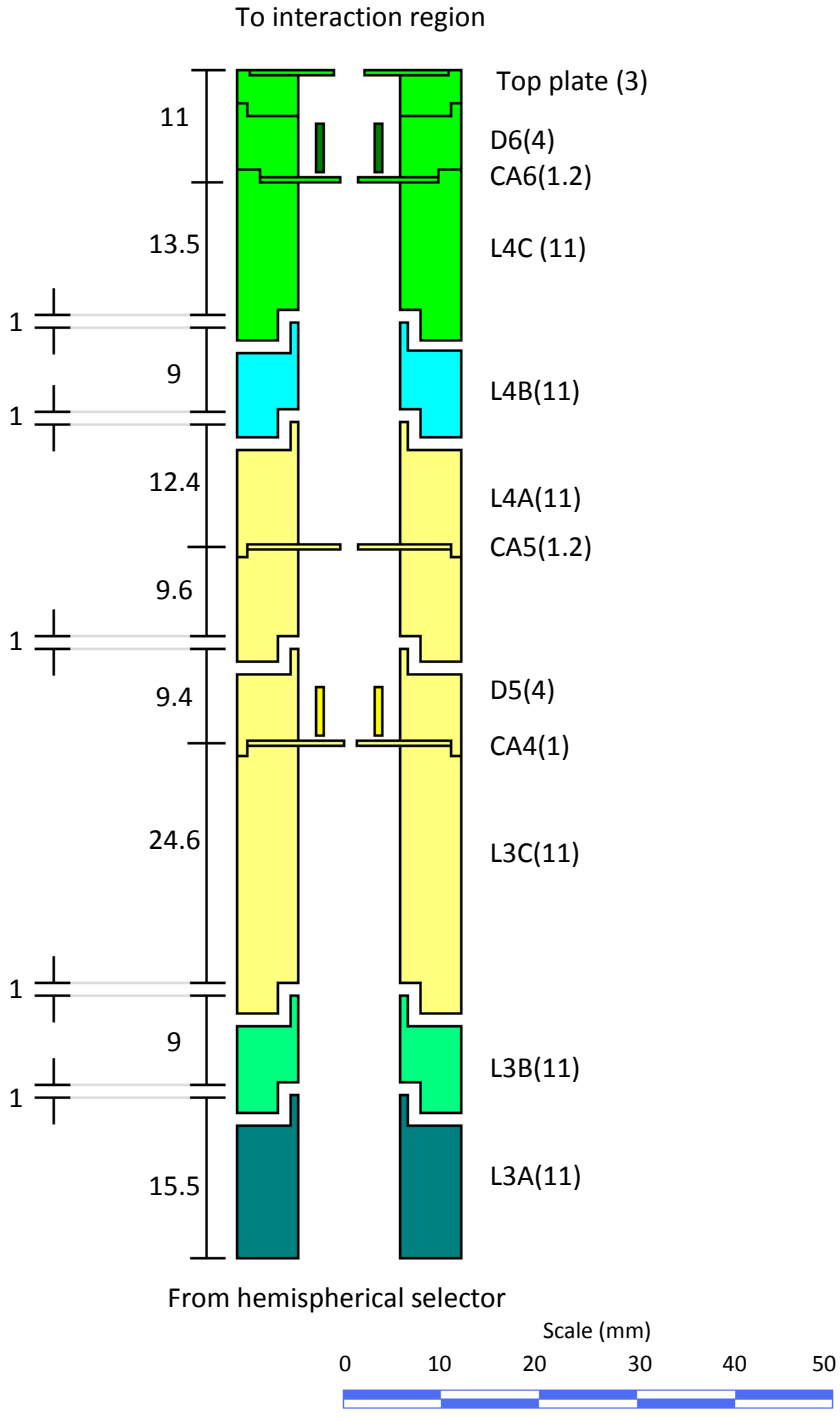

Figure 2.12: A schematic diagram of the cylindrical lens stack of the present electron monochromator, which indicates its characteristic dimensions drawn to scale. All dimensions are given in mm. Like colours indicate common electrical potentials. The acronyms are defined as L = lens element, CA = collimating aperture, D = deflector set. Numbers in parenthesis indicate the diameter of each circular aperture or in the case of the deflectors, the distance between parallel plates. See text for further details.

Finally the cylindrical lens stack consisted of two multi-element lenses, some further collimating apertures and three deflectors, all of which were again manufactured from titanium (figure 2.12). All these components were attached to a common support that secured them to the base plate as shown in figure 2.8. Typical operating potentials for the elements in this lens stack can also be found below in table 2.1.

Element	Potential (Volts)
Cathode	40
Pearce Element	-1.9
Grid	3.7
Anode /L1A	67.75
Lens 1B	268.3
Lens 1C / Lens 2A	48.85
Lens 2B	14
Lens 2C	3
Inner Hemisphere	6.13
Hoop 1	3.87
Hoop 2	3.38
Hoop 3	2.61
Hoop 4	2.29
Outer Hemisphere	1.8
Lens 2C/ Lens 3A	3
Lens 3B	8.1
Lens 3C	41.26
Lens 4A	41.26
Lens 4B	126.9
Lens 4C	0

Table 2.1: Typical operating potentials for elements in the electron monochromator, operating with a 40eV electron beam and a 3 eV pass energy.

Since the thesis of Hargreaves[65] in 2008, a collimating aperture (CA6) was added at the entry plane to the sixth set of deflectors. This aperture limited the penetration of the electric fields created by lens elements 3C, 4A or 4B from interfering with the performance of those final deflectors. The overall performance of the electron monochromator in terms of its focussing capability subsequently

improved considerably, increasing the lower limit of the incident electron energy range from 20 eV down to 2 eV.

Two stainless steel (type 310) concentric Faraday cups (FC) were mounted 40mm away from the last element of the electron monochromator, and monitored the electron current using two auto-ranging picoammeters (Keithley 485). The inner FC had a diameter of 1.25 mm while the outer cup had a diameter of 4 mm, both cups had knife edges to minimise any possible back scattering of electrons into the interaction region.

The electron monochromator was powered by custom-built (Australian National University Workshop) rack mounted power supplies, these were interfaced with a desktop PC and controlled using a purpose built Labview virtual instrument[54].

As noted previously all the electron-optic elements except lens 4C were floated on the cathode potential (beam energy). In practice this enabled the beam energy to be changed with only minor adjustments then being required for the other elements in the monochromator, to transport and refocus the electrons. Lens 4C, being the last element in the monochromator and the only element with a direct line of sight to the interaction region, was grounded. The lens elements immediately above and below a given set of deflectors shared the same power supply, which was also used to float the respective deflector pairings. A schematic diagram depicting the electronic circuitry for the monochromator is shown in figure 2.13.

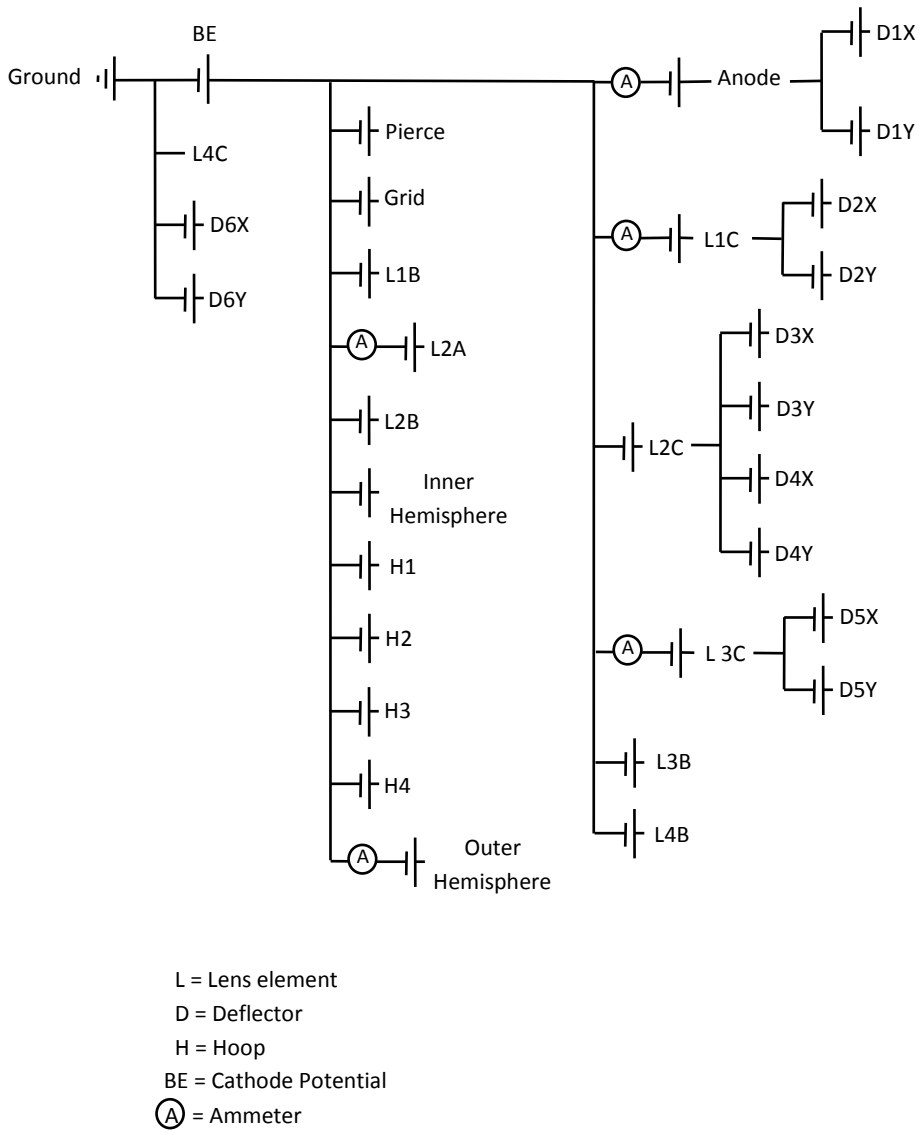

Figure 2.13: Schematic diagram depicting the electronic circuitry for the present monochromator potentials.

2.4.1.2 Monochromator Cleaning Procedure

Each time the chamber was opened to atmosphere it was vented using dry nitrogen, in order to prevent water vapour condensing on the interior surfaces. After closing and subsequent evacuation of the chamber, the electron spectrometer

was baked to approximately 110^{o}C, for a period of up to 24 hours, using a resistively heated copper block attached to the base plate and a heated copper coil positioned around the outer hemisphere (see figure 2.8). A 12W Halogen light sat behind the monochromator, near the top of the cylindrical aperture stack, and was used to provide additional heat during baking. K-type thermocouples were employed to monitor the temperature of the base plate and lens 4C during baking.

The electron monochromator was periodically removed from the vacuum chamber and disassembled for cleaning. Thin film build up was removed from the lenses and collimating apertures using 30 micron fibre optic paper followed by a final polish with 10 micron fibre optic paper. After polishing, all these small parts were cleaned in a sonic bath filled with ethanol and then dried in a 100^{o}C oven before reassembly. The larger parts of the monochromator assembly were simply washed with ethanol before drying.

2.4.1.3 Tuning the Monochromator

The power supplies for all the elements within the monochromator were interfaced with a PC and controlled using a purpose built Labview virtual instrument. This meant that only the voltage on one element could be varied at any one time (using the computer's mouse), and so the on-going process of optimising the electron gun current was tedious. Retuning of the monochromator to account for any voltage drifts and/or surface charge effects was also tedious. For these reasons an auto-tuning Labview virtual instrument (vi) was created by Maddern and Hargreaves[65]

which was similar to that described by Howell *et al*.[110], in that they also used the Nelder-Mead simplex. Full details of this vi can be found in Hargreaves[65], with a précis of that description being given immediately below.

The Nelder-Mead simplex is used to create an irregular simplex in n-dimensional Euclidean space with n+1 vertices. The simplex then calculates the value of a function f(x), with n dependant variables at each vertex, and compares these values to the previous values; subsequently one or more of the vertices is moved using one of four basic operations (reflect, expand, subtract, shrink). The value of f(x) at each point is then recalculated and the process continues with the simplex progressing through Euclidean space towards the minimum value of f(x), or until the simplex has reached a predetermined size known as the convergence.

In the case of the electron monochromator, up to twelve elements can be selected at any one time; becoming the n variables of f(x). The measured current on a chosen ammeter (either the Faraday cup or an ammeter in series with an electrostatic lens within the electron monochromator) was used as the value of f(x), and thus the electron beam current was increased by minimising the measured (negative) current. As the simplex was only capable of finding local minima and required a measurement of f(x) that was negative and non-zero, it was necessary that some electron current (0.1 nA) be present before the auto-tuning process would work.

In general, with the assistance of the auto-tuning virtual instrument, it was possible to reach the monochromators' maximum electron current, for a given electron beam energy, in less than half an hour. For electron energies of between 20-50 eV, typically currents of 5 nA were measured with approximately 70% of that current measured on the inner FC. For lower energies of 10-20eV, currents of ~1 nA were typically recorded with between 30-50% of that current being measured on the inner FC. For energies below 10eV electron currents of ~0.5 nA were achievable.

2.4.2 Analysers

2.4.2.1 Construction, Wiring and Operation

The interaction region was surrounded by thirteen grounded stainless steel wedges, each housing a channel electron multiplier (Dr. Sjuts) mounted behind a retarding potential analyser (RPA). These wedges were mounted (see figure 2.14) at the following angles (θ): -75^{o}, -60^{o}, -45^{o}, -30^{o}, -15^{o}, 20^{o}, 40^{o}, 60^{o}, 75^{o}, 90^{o}, 105^{o}, 120^{o}, and 135^{o}. Due to there being a limited number of available channel electron multipliers (CEMs), this resulted in the -60^{o} and -75^{o} degree wedges being unused for the course of the present experiments. A schematic picture of the wedge arrangement around the interaction region is shown in figure 2.14. Note that a grounded stainless steel housing was fitted over the back of the wedges creating a continuously grounded shield that stopped any electric fields from these analysers penetrating into the interaction region.

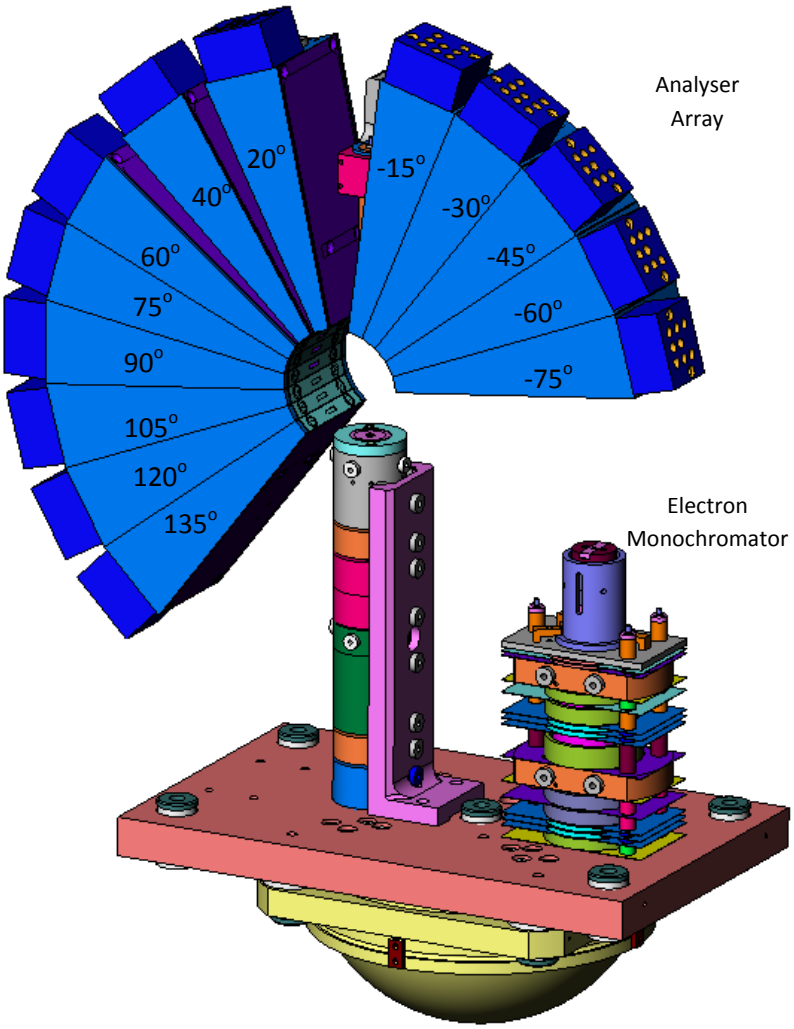

Figure 2.14: A schematic picture illustrating the analysers arrangement around the interaction region. Also show are the angles, relative to the $\theta=0^{o}$ scattering angle, at which its wedges are mounted.

Each wedge in figure 2.14 contained an identical RPA "set-up" with all the respective elements sharing common power supplies across the wedges. These power supplies were similar to those for the electron monochromator and were controlled using the same Labview interface. A schematic which is representative of all of the RPAs is shown in figure 2.15, while photographs highlighting the main physical features of each wedge are given in figure 2.16.

The four major grounded apertures (CA1-4) in the RPAs were originally designed with rectangular slits that were 6mm wide and 1 mm high. These openings were subsequently reduced to in size by the addition of 1mm diameter laser cut titanium apertures to their fronts.

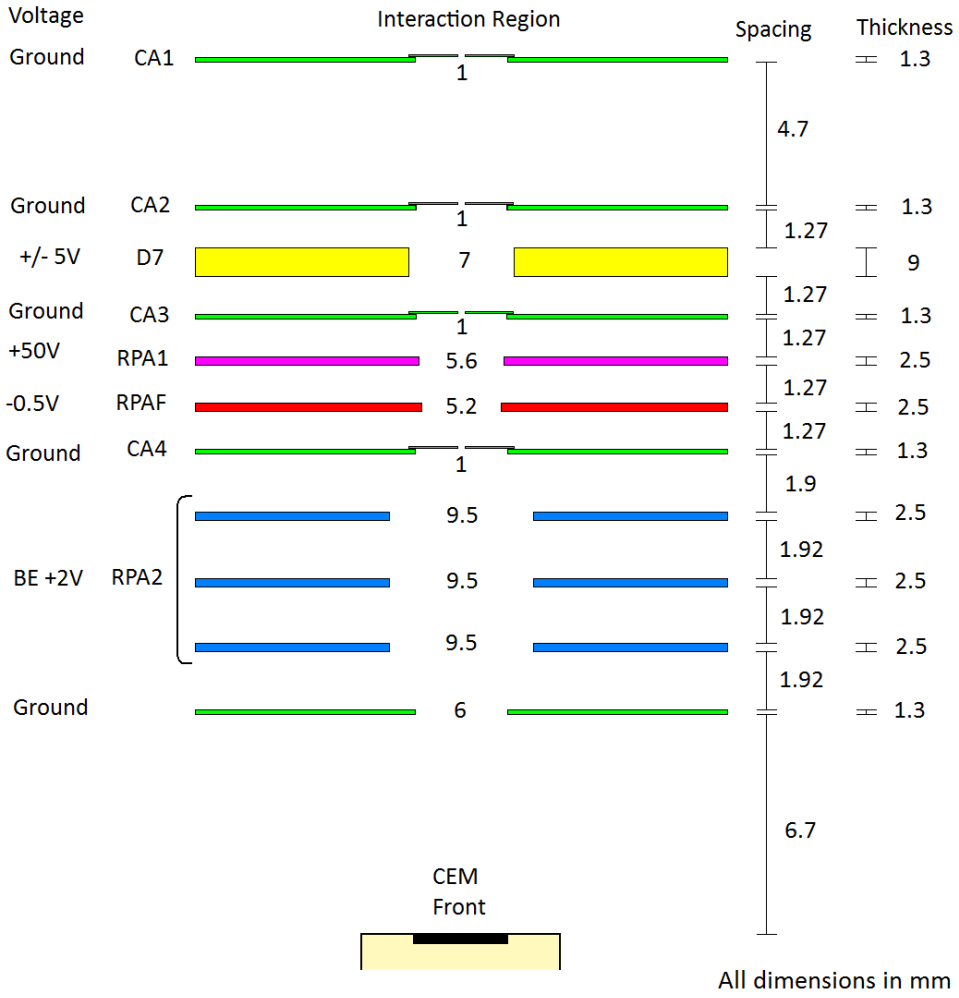

Figure 2.15: A schematic diagram depicting one of the present retarding potential analysers. Relevant dimensions e.g. spacing between elements, thickness of the elements and aperture diameters, as well as the potentials on these optic elements, are given. Acronyms are as defined previously: BE= beam energy; CA = collimating aperture; RPA = retarding potential analyser; RPAF = retarding potential analyser filter; and D = deflector set.

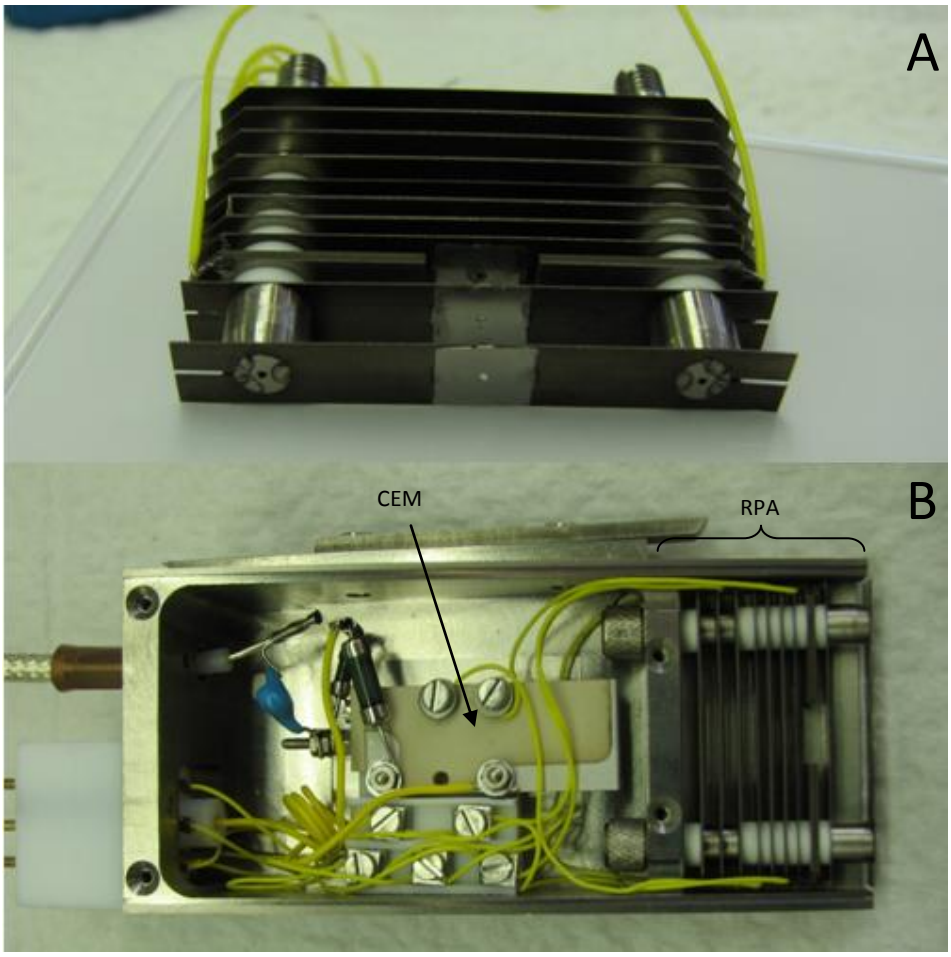

Figure 2.16 A: A photograph of the RPA lens array (looking from the IR towards its CEM), B: A photograph of the inside of one the wedges showing its CEM and RPA lens array (IR is to the right of the picture).

The voltages applied to the rear of the CEMs were supplied by using three channels of a four channel high voltage (HV) power supply (Dansfysik N1130). The CEMs at 15^{o} and 20^{o} each had their own individual HV channels, so that the potential applied could be adjusted independently. All the remaining CEMs were supplied by a common high voltage power rail. The HV for 15^{o} and 20^{o} was set to 1.9kV and 2.06kV, respectively, while the other CEMs were operated at HVs between 2.28kV-2.36kV throughout the course of the current experiments.

20 MΩ and 1 MΩ glass coated resistors (Ohmite, RX Hi-Meg) separated the high voltage supplies from the respective CEM backs and CEM anodes. In each case 220pF capacitors decoupled the CEM transient signal from the relevant high voltage line. Note that the front of each CEM was connected to a common 100V power rail. A circuit diagram showing the wiring and pulse "pick-off" configuration for each of the CEMs is given in figure 2.17.

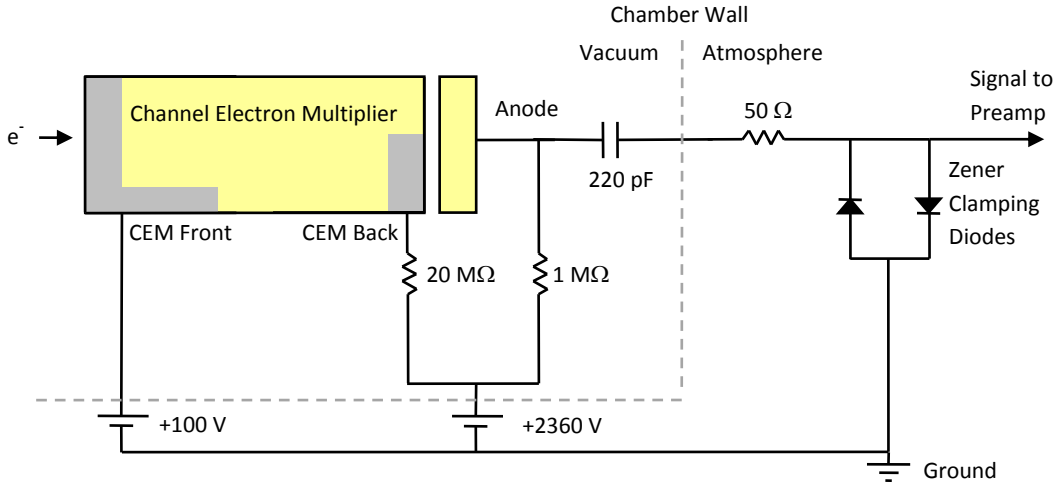

Figure 2.17: A circuit diagram depicting the CEM wiring and pulse "pick-off" configuration.

2.4.2.2 Signal Processing

After decoupling from the high voltage line, the electron scattering signals progress as negatively going pulses that ranged in magnitude from 15-80mV with a full width at half maximum of 8 ns. A typical output signal pulse is shown in Figure 2.18. These signal pulses were next sent to custom made (Flinders University Electronics Workshop) preamplifiers, via a 50 Ω resistor and a pair of Zener clamping diodes (see figure 2.17). Each pair of clamping diodes served to protect its preamplifer

from any "over-voltage" (>10V) spikes, while each resistor protected the preamplifer from any "over-current" spikes. The preampliers now transformed all of the negatively going pulses, that had a magnitude greater than an adjustable discriminator level, into square wave transistor-transistor logic (TTL) pulses (magnitude +4 V, pulse width of 295 ns). At this stage the TTL pulses from each CEM were split into two and fed into twenty individual counters contained across BNC2121 devices as detailed in table 2.2. The BNC2121 devices were subsequently connected to four National Instruments high speed counter-timing cards (NI-DAQ 6602) that were interfaced with a PC.

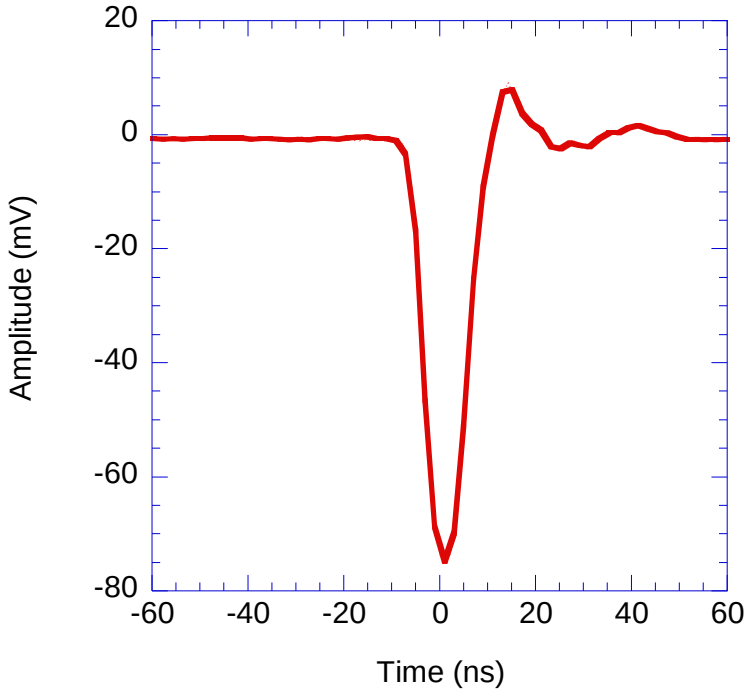

Figure 2.18: A trace depicting the typical signal output from one of the CEMs. This data was taken from the CEM located at $\theta = 40^{o}$.

Labview Channel	Scattering Angle (Degrees)	Gross Count window	Background Count window
0	-30	Device 2 / counter 0	Device 2 / counter 1
1	-15	Device 2 / counter 2	Device 2 / counter 3
2	20	Device 2 / counter 4	Device 2 / counter 5
3	40	Device 2 / counter 6	Device 2 / counter 7
4	60	Device 3 / counter 0	Device 3 / counter 1
5	75	Device 3 / counter 2	Device 3 / counter 3
6	90	Device 3 / counter 4	Device 3 / counter 5
7	105	Device 3 / counter 6	Device 3 / counter 7
8	120	Device 4 / counter 0	Device 4 / counter 1
9	135	Device 4 / counter 2	Device 4 / counter 3
10	-45	Device 4 / counter 4	Device 4 / counter 5

Table 2.2: Configuration of the BNC2121 devices 2-4.

A fourth BNC2121 device, device one, was used to sense the master timing pulse (MTP) that was in turn sent by a custom built (Flinders University Electronics Workshop) 6 channel master timing control. Device one was also used to control the pulser enable commands, along with enable commands for each of the timing windows, and to set the length of each timing window.

Another purpose built Labview virtual instrument was then used to receive and record these TTL pulses, as well as to adjust the timing windows in which the signals were collected.

Prior to their amplification, the very fast low-magnitude signal pulses were particularly susceptible to interference by electronic noise, which in turn was influenced by cable length. In order to reduce cable length the decoupling capacitors, that were originally mounted at a distance of 40 cm from the CEM, were moved into the back of each wedge (see figure 2.16). This resulted in an overall reduction in exterior signal cable length of approximately 30 cm and reduced noise

on all the channels. The entire cable length of each signal channel was shielded by a grounded braid with 50Ω impedance matched connections where necessary.

2.5 Time of Flight Mass Spectrometer

The time of flight mass spectrometer (TOFMS) was mounted in the third and final vacuum chamber (see figures 2.1 and 2.2) downstream from the electron spectrometer, and was used to monitor the initial molecular beam purity and also the fractional composition of the molecular beam after pyrolysis. Its design was based on a paper published by Wiley and McLaren in 1955[111].

Positive ions with a charge of $+1.6*10^{-19}$ C were created from the molecular beam using single photon ionisation, with 118 nm photons supplied via an orthogonally intersecting laser beam (see later). These ions were created within a uniform electric field and hence they all experienced a common force; this force caused ions of different masses to accelerate to different velocities. After the initial acceleration period the ions were allowed to drift in a field free region, thus allowing the lighter (and so faster travelling) ions to overtake the slower moving (heavier) ions.

A detector (see next section) was mounted at the end of the field free region and recorded the ion signal as a function of ion arrival time at the detector. As the force experienced by the ions was known, as is the relationship between mass and arrival time, it was possible to resolve the ion signal as a function of mass.

The TOFMS was fabricated from a published design[111] and incorporated second-order space focusing. Second order space focusing improves the resolution of the TOFMS as it ensures that all ions with the same mass, created at the same instant arrive at the detector at the same time regardless of their initial position. Thus the resolution of the TOFMS becomes independent of the volume of the ionisation region. This is particularly important for this project as the molecular beam has quite a large diameter (approximately 2 cm) in the TOFMS ionisation region. The combination of second-order space focusing and a long drift region resulted in the present TOFMS having a resolution of better than 1 amu[65].

2.5.1 TOFMS Construction and Wiring

The TOFMS was constructed from circular stainless steel (SS) sheets with a diameter of 160mm and a thickness of 0.5 mm. These circular sheets were mounted concentrically on eight grounded SS rods that were encased in Teflon, with ceramic spaces holding the plates 5.08 mm apart. A pair of 40 mm microchannel plates (MCPs) with a timing anode, were mounted in a chevron configuration, 439.6 mm above the ionisation region, and were employed to detect positive ions. A schematic diagram of the present TOFMS, indicating its main design components and configuration is given in figure 2.19.

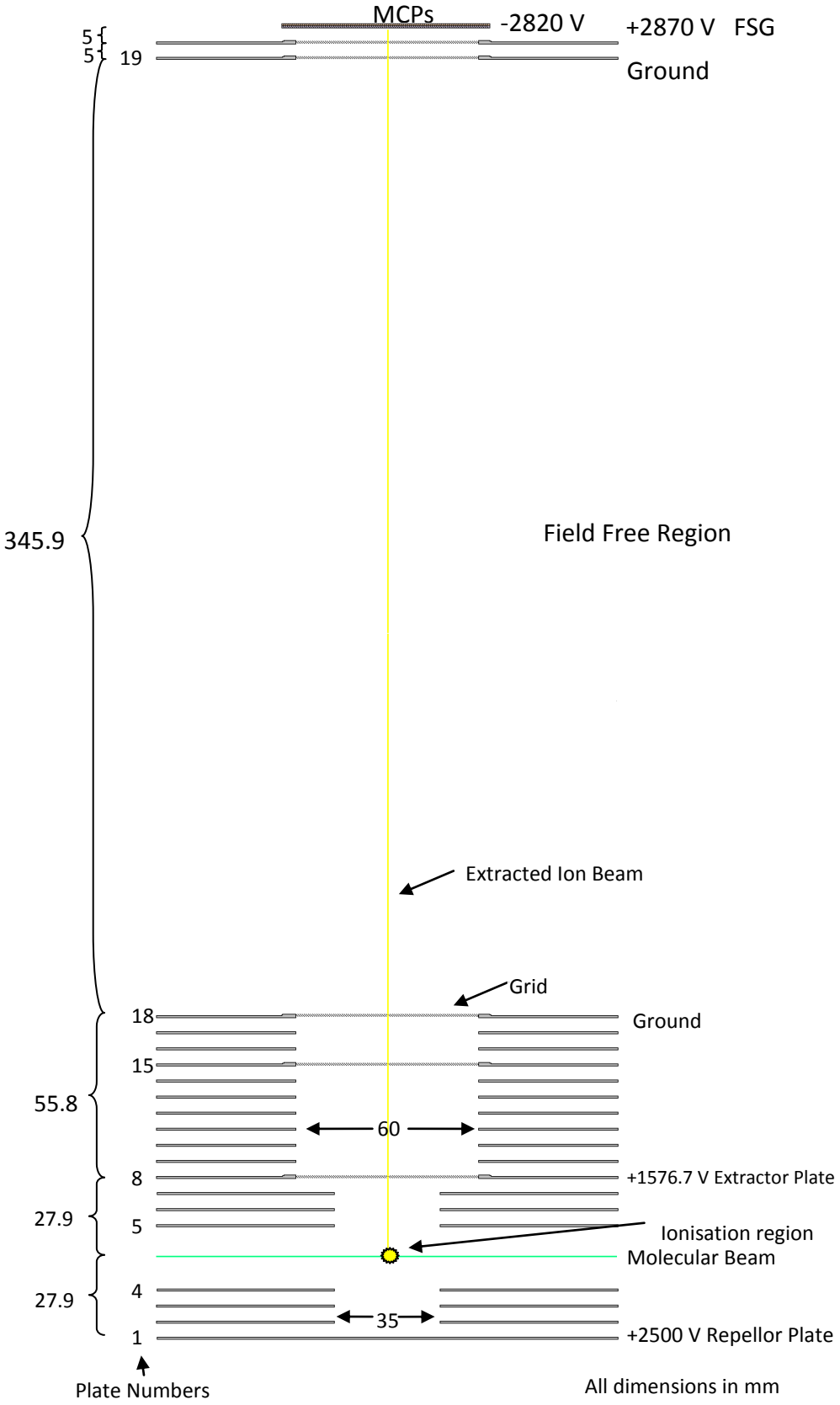

Figure 2.19: TOFMS Schematic diagram showing its main design components and potentials. All of the dimensions are in mm.

The ionisation region (see figure 2.19) was located centrally between the first and eighth SS plates inside a uniform, 1654.66 NC^{-1}, electric field. The bottom (first) plate, known as the repellor plate, sat at a potential of 2500 V while the eighth plate (see figure 2.19), known as the extractor plate, sat at a potential of 1576.7 V. Both these plates were "powered" by 415B Fluke high voltage power supplies.

In order to keep the TOFMS electric field as uniform as possible, six further plates were placed between the extractor and repellor plates. Note that all these plates were connected using a chain of 1 MΩ resistors (Ohmite, RX Hi-Meg) that acted as a voltage divider, with plates 4 and 5 being connected using four 1 MΩ resistors. Plates 2-4 had central concentric 35 mm diameter holes to allow for the passage of the ions; while plates 5 and 6, immediately above and below the ionisation region, each had a 35 mm wide central strip removed so as not to interfere with the passage of the molecular beam through that ionisation region. Ten additional plates were mounted above the extractor plate, plates 9-18, in figure 2.19, with each having 60 mm wide central holes that allowed for the passage of the ions. Plates 9-18 were also linked using the 1MΩ resistor chain. The 18^{th} plate was grounded, marking the beginning of the 345.9 mm length field free region. High transmission mesh was spot welded over the orifices in plates 8, 15, 18 and 19 in order to prevent field-fringing effects around the central holes. The 19th plate was mounted at the end of the field free region, behind which a field suppression grid (FSG) and the MCPs were mounted (again see figure 2.19).

The field suppression grid was made from the same high transmission mesh as was used elsewhere in the TOFMS. Typically it sat at a potential of -2870 V, which was provided by a 412B Fluke power supply. The MCPs sat at a potential of -2820V and were "powered" by the fourth channel of the Dansfysik N1130 supply that was also used for the CEMS. Ion signals received by the MCP timing anode were sent to an oscilloscope (LeCroy Waverunner 6050), where they were averaged over one thousand laser shots and displayed as ion voltage as a function of ion-MCP arrival time. These plots were finally saved as data files and transferred to a PC where they could be interpreted. A circuit diagram for the MCPs and anode ion detection system is shown in figure 2.20.

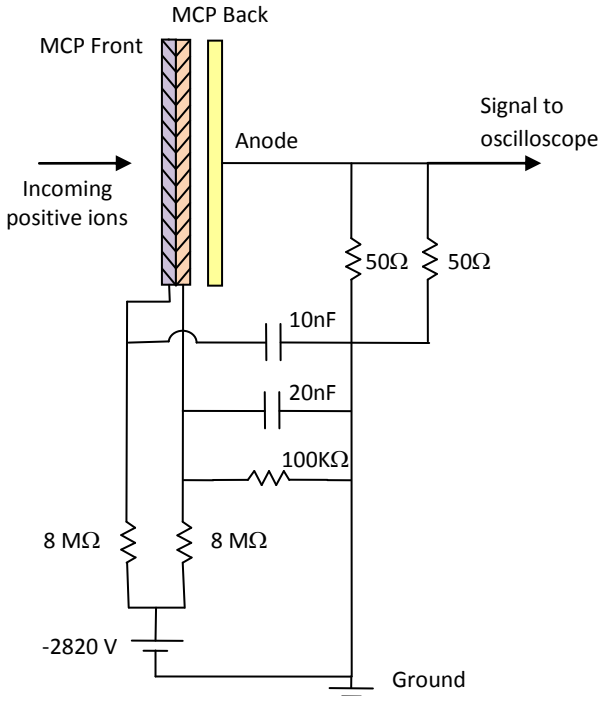

Figure 2.20: Circuit diagram showing the wiring for the TOFMS MCPs and anode ion detector.

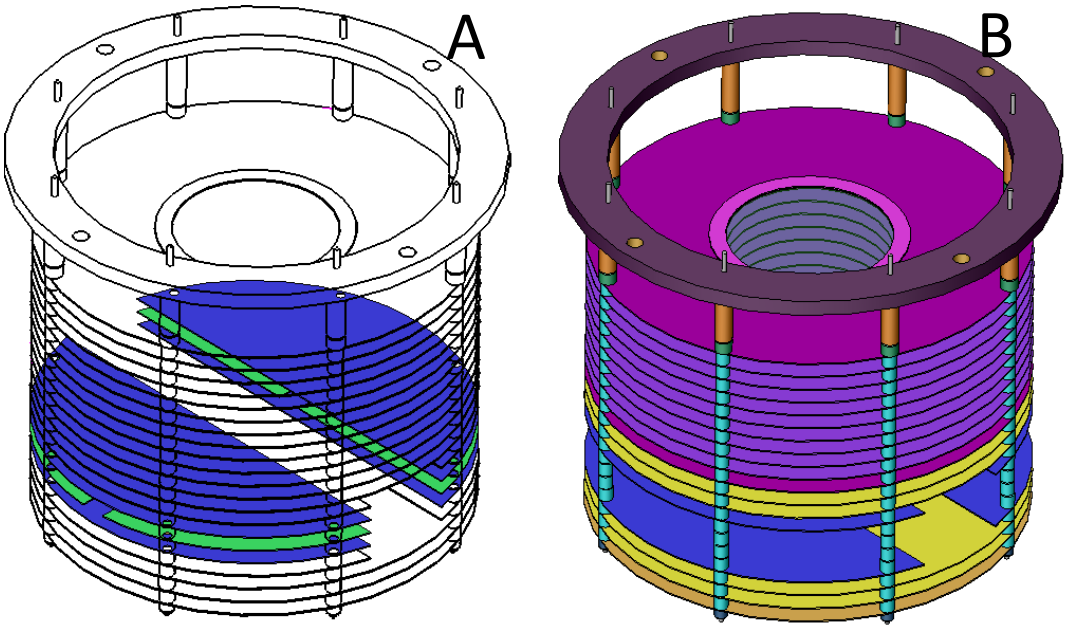

Figure 2.21: Schematic diagrams illustrating A: Original TOFMS plate configuration, B: The current TOFMS plate configuration.

Originally there were three additional plates mounted around the ionisation region, as shown in figure 2.21A. These plates were subsequently removed, however, as they were being ablated by the diffuse 355 nm radiation (see next section) around the ionisation region. This diffuse 355 nm radiation had the unfortunate and unwanted effect of causing background peaks in the TOFMS spectrum. The present TOFMS configuration is shown in figure 2.21B.

2.5.2 Ionisation Source: The Nd:YAG Laser/ Frequency Tripling

118 nm photons (10.48 eV) were used as the ionisation source for the TOFMS; these photons were obtained by three successive stages of frequency addition of the fundamental wavelength (1064 nm) of a Q-switched neodymium-doped yttrium aluminium garnet Nd:YAG (Quantel Brilliant B) laser. Two commercially purchased

(Quantel) sum frequency generation units were attached to the front of this laser. The first unit produced the second harmonic of the Nd:YAG laser (532nm) arising from the units' nonlinear response to the fundamental (1064 nm) frequency[112]. Second harmonic generation (SHG) can be thought of as a process that destroys two photons with a given wavelength and produces one photon with half the original wavelength (and double the original frequency)[113], in this case two 1064 nm photons produced one 532 nm photon. The second unit used sum frequency generation (SFG) to produce light with a wavelength of 355 nm. SFG is the more general case of SHG whereby the two input photons have different frequencies and the resultant photons' frequency is the sum of these two frequencies[113]. In this case the addition of one 1064 nm photon and one 532 nm photon, produced one 355nm photon. The laser beam was then directed to a custom built (Flinders University Mechanical Workshop) gaseous frequency tripling medium using two mirrors. This medium used a third order non-linear effect to triple the frequency of the laser beam[113], using the addition of three 355 nm photons to produce one photon of 118 nm, the ninth harmonic of the Nd:YAG laser.

The gaseous frequency tripling medium was housed in a 373 mm long stainless steel tube with a volume of 0.134 L. The laser beam entered this tube through a planar-convex MgF_2 lens before being directed into the ionisation region through a biconvex MgF_2 lens. The laser beam then exited the chamber via a UV grade fused silica window, and was finally terminated in a custom made (Flinders University Mechanical Workshop) beam stop. The laser pathway described above is also shown schematically in figure 2.22.

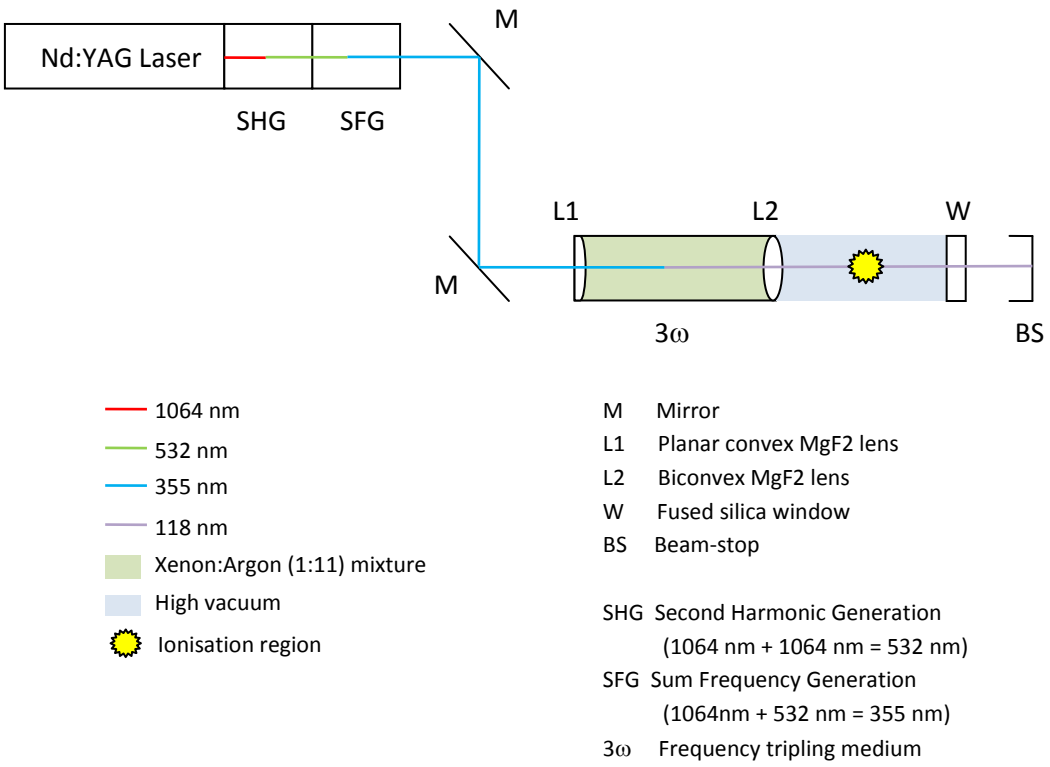

Figure 2.22: The Nd:YAG laser pathway employed in the present studies.

A separate gas handling system was used to fill the custom built frequency tripling tube while a baratron pressure gauge (Pressure transducer type 122A, MKS Instruments) was employed to set and monitor the pressure inside that tube. Hargreaves[65] determined that a total pressure of 55 mbar, and a ratio of xenon to argon of 1:11, produced the most efficient frequency tripling medium.

The nonlinear effects utilised to create the harmonic frequencies were in fact not 100% efficient, so that as no optical filters were used in the beam path the laser beam contained a mixture of the 1064 nm photons, 532 nm photons, 355 nm photons and 118 nm photons. The 1064 nm and 532 nm photons were not considered to be a problem in the ionisation region of the TOFMS, as with energies of 1.2 eV and 2.3 eV respectively they were unable to ionise most gases using single

photon ionisation; and they were too diffuse to create multiple photon ionisation. In an attempt to make the 355 nm photons more diffuse the frequency tripling tube was reduced in length by 2.3 cm (from its original length of 30cm), thus shifting the 355 nm focal point of the biconvex MgF_2 lens. The result of this modification was a reduction in the background peaks, produced by the ionisation of pump vapours by the 355 nm photons, from 10 mV to less than 0.5 mV. This modification took place after the publication of the work of Maddern *et al*[54] and the thesis of Hargreaves[65], and so has not been previously noted.

2.5.3 TOFMS Operation

The Nd:YAG laser's flash lamp and Q-switch were set to "external sync", and were controlled by channels five and six of a custom built (Flinders University Electronics Workshop) six channel master timing control with a Labview interface. Note that the "master timing pulse" occupied channel one of this timing control, while the nozzle's "pulser fire" command was controlled using channel two. Channels three and four were not used in any of the present experiments. The power of the Nd:YAG was set by varying the time delay between the flash lamp and the Q-switch, which was set to 400μs for all of the present experiments.

The current TOFMS was used to determine the temporal profiles of the molecular beams used in this study, as well as to determine the fractional composition of pyrolysed molecular beams. The temporal profiles of the molecular beams were obtained by mapping the effect of varying the delay between the "pulser fire" command and the laser's Q-switch on the average the signal received by the MCPs

(at the corresponding mass of the main component of the molecular beam), over 1000 laser pulses. Note that the power of the laser was maintained throughout each experiment by maintaining a constant time delay between the flash lamp and the Q-switch. An example of a typical plot of MCP signal vs the time delay between the "pulser fire" and "Q-switch fire" commands is shown below in figure 2.23, where the temporal length of the molecular beam is taken to be 1500 μs.

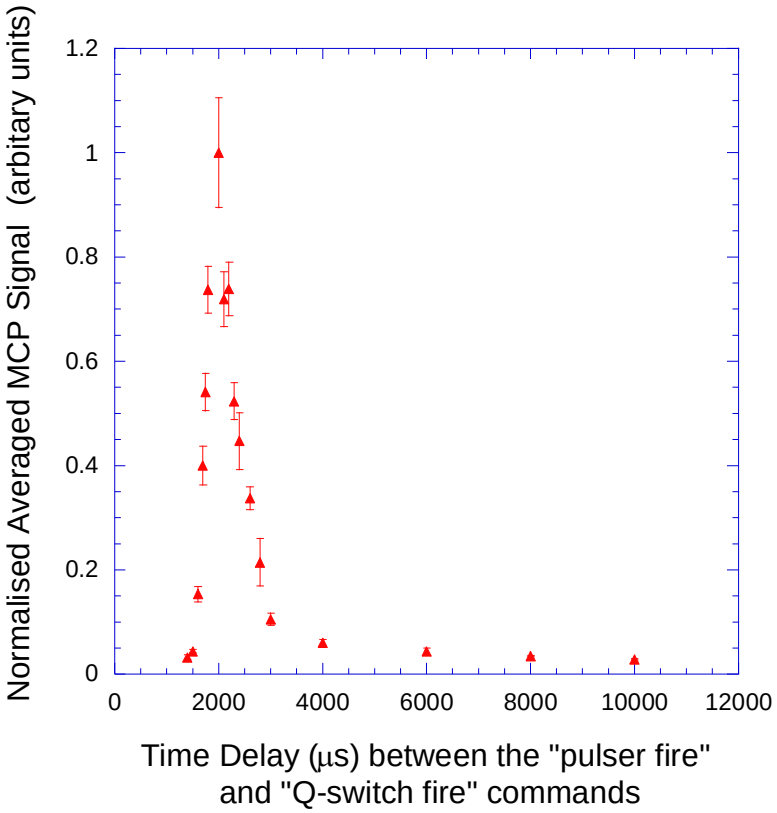

Figure 2.23: A typical plot of normalised MCP signal, averaged over 1000 laser shots, as a function of the time delay (in μs) between the "pulser fire" and the "Q-switch fire" commands. This particular plot represents the measurements made from a room temperature CF_3I molecular beam, with a stagnation pressure of 430mbar, expanded through a 0.5mm nozzle orifice, and with a nozzle-skimmer separation distance of 8cm.

During fractional decomposition investigations, the time delay between the "pulser fire command" and the laser's Q-switch was set such that the laser fired when the molecular beam in ionisation region was at its most dense. Then, for a particular

pyrolysis temperature the peak height in mV and corresponding time stamp were recorded. These time stamps were then converted into their corresponding masses (using the following relationship:$mass(amu) = 1.3024t^2(\mu s)$), and the pryrolysis products were identified. As 118 nm photons were used as the ionisation source for the TOFMS, it was necessary (when pyrolysis produced a mixed species beam) to correct for each species' 118 nm photon-ionisation cross section; this was achieved by dividing each peak by its species photo-ionisation cross section, as obtained from the literature. As the TOFMS was only sensitive to species with ionisation energies less than 10.48 eV, it was also necessary to know the likelihood of any "undetectable" pyrolytic products before the fractional composition of the "mixed" molecular beam could be determined. This is discussed in more detail in sections 3.3 and 3.4.

Chapter 3 — Experimental Methods

3.1 Determining Absolute Values – The Normalisation Technique

3.1.1 The relationship between scattered count rates and cross sections

To appreciate why a normalisation technique is used in measuring the differential cross sections presented in this study, it is first necessary to discuss the relationship between the number of scattered electrons and the DCS for a particular scattering process. This generic relationship, after a background correction, is shown in equation 3.1[11]:

$$N_n\left(\overline{\mathrm{E}_0}, \overline{\mathrm{E}_n}, \overline{\Omega}\right) = \int_{\mathrm{r}} \int_{\mathrm{E}_0} \int_{\mathrm{E}_n} \int_{\Omega} \rho(\mathbf{r}) f(\mathrm{E}_0, \mathbf{r}) \xi(\mathrm{E}_n, \mathbf{r}) \frac{d^3\sigma(\mathrm{E}_0, \mathrm{E}_n, \Omega)}{d\mathrm{E}_n d\Omega} d\Omega d\mathrm{E}_0 d\mathrm{E}_n d^3\mathrm{r}\,. \quad (3.1)$$

Here N_n is defined as the number of scattered electrons detected per second at the nominal (average) solid angle $\overline{\Omega}(\overline{\theta}, \overline{\phi})$ and with an energy of $\mathrm{E}_n = \mathrm{E}_0 - \Delta\mathrm{E}$, where E_0 represents the impact electron energy and $\Delta\mathrm{E}$ is the energy loss corresponding to scattering process n. $\rho(\mathbf{r})$ is defined as the density distribution of the target molecules, $f(\mathrm{E}_0, \mathbf{r})$ is taken to be the energy and spatial distribution of the incident electron flux and $\xi(\mathrm{E}_n, \mathbf{r})$ is the response function of the detector when detecting electrons of energy E_n scattered by a target molecule at position $\mathbf{r}$. The geometry for a typical crossed beam experiment is shown in figure 3.1[11].

Provided that the energy resolution of the apparatus and the angular range of the detector are both narrow in comparison to the energies and angles over which the differential cross section changes significantly, and it is possible to integrate over the energy loss profile for excitation into a discrete energy state n; then

$\mathrm{DCS}_n(\overline{\mathrm{E}_0}, \overline{\Omega})$ can be used as an accurate representation of the cross section at $\overline{\mathrm{E}_0}$ and $\overline{\Omega}$. Thus it is possible to rewrite equation 3.1 as equation 3.2[12]:

$$N_n(\overline{\mathrm{E}_0}, \overline{\mathrm{E}_n}, \overline{\Omega}) = \mathrm{DCS}_n(\overline{\mathrm{E}_0}, \overline{\Omega}) \int_{\mathrm{r}} \int_{\mathrm{E}_0} \int_{\Omega} \rho(\mathbf{r}) f(\mathrm{E}_0, \mathbf{r}) \xi(\overline{\mathrm{E}_n}, \mathbf{r}) d\Omega d\mathrm{E}_0 d^3\mathrm{r} \,. \tag{3.2}$$

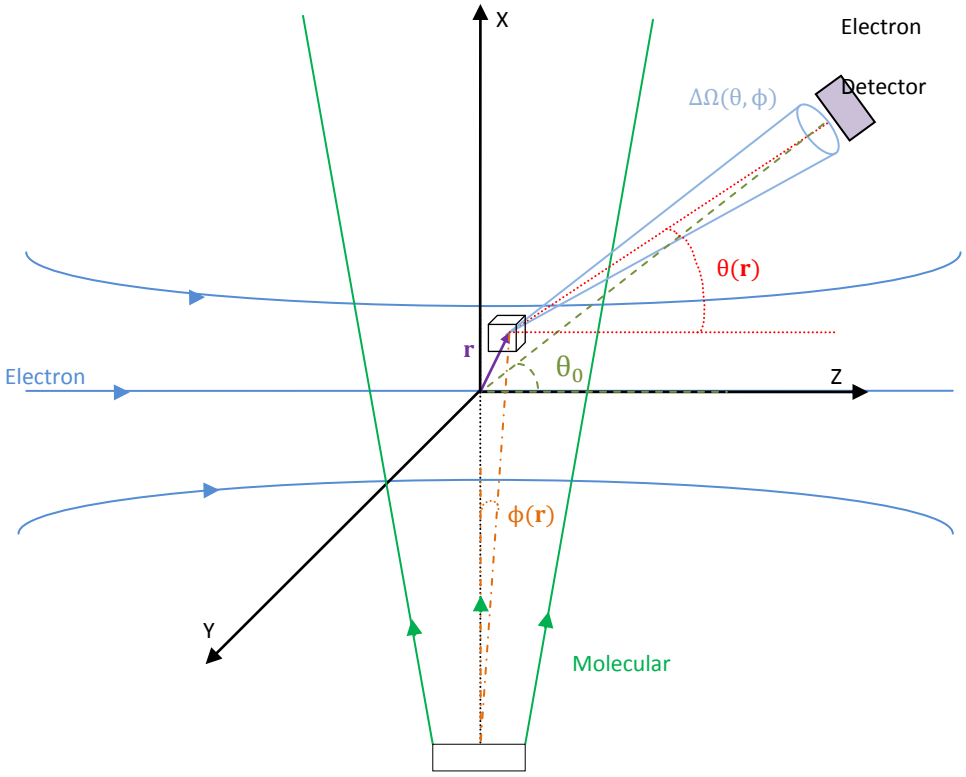

r is the position of the target molecule,

θ_0 is the mounting angle of the detector,

$\Delta\Omega(\theta, \phi)$ is the solid angle subtended by the electron detector,

$\theta(\mathbf{r})$ is the angle made between the detector, target molecule and axis of the electron beam,

$\phi(\mathbf{r})$ is the angle between the axis of the molecular beam and the particle at position **r**.

Figure 3.1: Geometry used in a typical effusive flow crossed beam experiment, figure reproduced from J. C. Nickel et. *al*.[11].

Equation 3.2 can be further simplified by assuming that the energy distribution of the electrons is independent of $\mathbf{r}$, i.e. $f(\mathrm{E}_0, \mathbf{r}) = \mathrm{I} f(\mathrm{E}_0) f(\mathbf{r})$, where I represents the magnitude of the incident electron beam current[12]. In addition the detector response can be taken to be dependant only on the energy of the detected electrons and not on the position of their respective scattering events $(\mathbf{r})$, i.e. $\xi(\overline{\mathrm{E}_n}, \mathbf{r}) = \xi(\overline{\mathrm{E}_n})$. Equation 3.2 can now be rewritten as equation 3.3:

$$N_n(\overline{\mathrm{E}_0}, \overline{\mathrm{E}_n}, \overline{\Omega}) = \mathrm{DCS}_n(\overline{\mathrm{E}_0}, \overline{\Omega})\mathrm{I} \int_{\mathrm{r}} \int_{\mathrm{E}_0} \int_{\mathrm{E}_n} \int_{\Omega} \rho(\mathbf{r}) f(\mathrm{E}_0) f(\mathbf{r}) \xi(\overline{\mathrm{E}_n}) d\Omega d\mathrm{E}_0 d\mathrm{E}_n d^3\mathrm{r}\,. \quad (3.3)$$

It is now possible to separate the integrals in equation 3.3 into those dependent on energy and those dependent on angle, as shown in equations 3.4 and 3.5 respectively:

$$\mathrm{C}(\overline{\mathrm{E}_n}) = \int_{\mathrm{E}_n} \int_{\mathrm{E}_0} f(\mathrm{E}_0) \xi(\overline{\mathrm{E}_n}) d\mathrm{E}_0 d\mathrm{E}_n, \quad (3.4)$$

$$\widetilde{\mathrm{V}}_{\mathrm{eff}}(\theta, \phi) = \int_{\mathrm{r}} \int_{\Omega(\mathrm{r})} \rho(\mathbf{r}) f(\mathbf{r}) d\Omega(\theta, \phi) d^3\mathrm{r}\,. \quad (3.5)$$

$\widetilde{\mathrm{V}}_{\mathrm{eff}}(\theta, \phi)$ is known as the scattering volume and describes the volume of the intersection of the molecular and electron beams within the view cone of an electron detector. This can be further simplified as in most scattering experiments molecules are randomly orientated, thus $\widetilde{\mathrm{V}}_{\mathrm{eff}}(\theta, \phi)$ becomes $\widetilde{\mathrm{V}}_{\mathrm{eff}}(\theta)$, where:

$$\widetilde{\mathrm{V}}_{\mathrm{eff}}(\theta) = 2\pi \int_{\mathrm{r}} \int_{\theta'(\mathrm{r})} \rho(\mathbf{r}) f(\mathbf{r}) \sin\theta'(\mathbf{r}) d\theta'(\mathbf{r}) d^3\mathrm{r}. \quad (3.6)$$

By combining equations 3.4 and 3.6 with equation 3.3 the following expression is obtained:

$$N_n\left(\overline{\mathrm{E}_0}, \overline{\mathrm{E}_n}, \overline{\theta}\right) = \mathrm{DCS}_n\left(\overline{\mathrm{E}_0}, \overline{\theta}\right)\mathrm{IC}\left(\overline{\mathrm{E}_n}\right)\widetilde{\mathrm{V}}_{\mathrm{eff}}(\theta). \quad (3.7)$$

The effective scattering volume, $\widetilde{\mathrm{V}}_{\mathrm{eff}}(\theta)$, can in principle be calculated explicitly (as was done by Brinkman and Trajmar in 1981[114]), provided one is able to accurately determine the density distribution and flux for both of the intersecting beams. However, even if the current apparatus allowed for these measurements to be undertaken on both beams, one would still require the energy dependent term $\mathrm{C}\left(\overline{\mathrm{E}_n}\right)$ for each CEM in order to explicitly evaluate the absolute differential cross section. This is a far from trivial matter as, in general, $\mathrm{C}\left(\overline{\mathrm{E}_n}\right)$ would be quite a complex function and would be unique for each of the 11 CEMs employed in our measurements.

A common feature of most beam-beam scattering apparatus is the use of a single detector mounted behind a rotatable hemispherical analyser. As the same detector is used throughout a measurement, the function $\mathrm{C}(\overline{\mathrm{E}_n})$ remains constant. In this way it is possible to obtain relative scattering intensities as functions of incident energy, scattering angle or energy loss. Only these relative scattering intensities are required to determine the energy level structure of atoms and molecules, the location and types of resonances, and the coherence and correlation parameters, so that most of the information obtained from crossed beam experiments from the 1930's until the 1970's was measured and reported in this relative scattering intensity form[11].

If an absolute cross section was required there were various indirect approaches to make the relative data absolute. Some of these approaches included using a phase-shift analysis to determine the absolute value of a cross section for a particular scattering process at a particular angle and impact energy; then determining the correction factor for this point and applying it to the rest of the differential cross section [115]. However, this technique would only produce a reliable result if the impact energy was below the first inelastic threshold and was low enough that only the contribution from a few partial waves was required. This procedure was also difficult to apply to highly polarisable targets[115]. Other approaches were also used[115], although those techniques were again somewhat limited, with some requiring accurate information about the targets' integral cross sections over a wide range of energies, while others were only applicable for cases of small momentum transfer (K). In 1975 Srivastava *et al.* [116] outlined a new method, called the relative flow method (RFM) for producing absolute scattering measurements. The RFM compares the amount of scattering from an unknown target gas to that from a reference gas (with a known absolute DCS for the scattering process). The ease at which the RFM enables the measurement of absolute cross sections has resulted in a wealth of absolute cross section measurements to be available in the literature today.

For several reasons, including the use of multiple CEMs (see section 2.4.2) in conjunction with a pulsed supersonic molecular beam, none of these earlier normalisation techniques were applicable for the current experiment. Thus a new normalisation method was required here. The new normalisation technique

developed for this experiment, although applicable to all gated skimmed supersonic sources, was called the skimmed supersonic relative density method (SSRDM). This technique was based on the well established RFM, but adapted to take into account a molecular beam formed from a skimmed supersonic source rather than an effusive flow from a single capillary or a capillary array [117].

Although atomic hydrogen is the simplest atom, in 1980 Register *et al.* [115] proposed that (for the RFM) helium should be used as a calibration standard and this is still the most common reference species used today. Experimentally, helium is easier to work with than hydrogen and still possesses a simple enough atomic structure for accurate theoretical investigations. Indeed helium's elastic DCS is regarded to be known e.g. to within 1-3% for energies less than 19eV[118] and to within 7% for energies up to 1000eV[119].

The RFM requires that the experimental conditions be largely identical for both gases for each fixed value of E_0 and θ. It also requires that the mean free paths of the molecules in each of the target and reference beams are identical, so that their distribution functions will also be largely identical [11, 12, 116]. This technique also specifies that the energy E_0 and flux $f(\mathbf{r})$ of the impact electron beam be the same for both gases. Traditionally the RFM has mainly been applied to elastic scattering processes (when $\Delta\mathrm{E} = 0$), so that from this point on we concern ourselves only with the elastic scattering process. Hence the subscript n is replaced with 0.

Provided the conditions for the RFM are met, equation 3.7 can be re-written as equation 3.8 using the superscripts U and R to denote the "unknown" and reference gases:

$$\frac{N_0^{\mathrm{U}}(\overline{\mathrm{E}_0},\theta)}{N_0^{\mathrm{R}}(\overline{\mathrm{E}_0},\theta)} = \frac{DCS_0^{\mathrm{U}}(\overline{\mathrm{E}_0},\theta)\mathrm{I}^{\mathrm{U}}\mathrm{C}^{\mathrm{U}}(\overline{\mathrm{E}_0})\widetilde{\mathrm{V}}_{\mathrm{eff}}^{\mathrm{U}}(\theta)}{DCS_0^{\mathrm{R}}(\overline{\mathrm{E}_0},\theta)\mathrm{I}^{\mathrm{R}}\mathrm{C}^{\mathrm{R}}(\overline{\mathrm{E}_0})\widetilde{\mathrm{V}}_{\mathrm{eff}}^{\mathrm{R}}(\theta)}. \tag{3.8}$$

As the electron detector response function $\xi(\overline{\mathrm{E}_0})$ is independent of the target species it will be the same for both species provided that the same electron detector is used for a particular angle. Now, if the electron flux remains constant during the collection of scattering signal from both the unknown and reference species then $\mathrm{C}^{\mathrm{U}}(\overline{\mathrm{E}_0}) = \mathrm{C}^{\mathrm{R}}(\overline{\mathrm{E}_0})$. Thus regardless of the complexity of the actual instrumental energy dependence function $\mathrm{C}(\overline{\mathrm{E}_0})$, it can be cancelled out from equation 3.8. This is a tremendous advantage for the current apparatus as not one but eleven different detector response functions would have been required otherwise!

In our case $f(\mathrm{E}_0)$ and $f(\mathbf{r})$ are monitored by taking successive measurements of the scattering signal, for both the reference and unknown species while conserving the focus of the electron monochromator. These successive recordings also minimise any difference in CEM response $\xi(\overline{\mathrm{E}_0})$, as, over time the internal surface of a CEM degrades, effecting its gain characteristics.

Terms I^{U} and I^{R}, in equation 3.8, refer to the measured electron current during the scattering undertaken on the unknown target and reference gases respectively.

These quantities are measured directly using two concentric Faraday cups (as discussed previously in section 2.4.1.1). Our procedure for the measurement of $N_0^{\mathrm{R}}\left(\overline{\mathrm{E}_0},\theta\right)$ and $N_0^{\mathrm{U}}\left(\overline{\mathrm{E}_0},\theta\right)$ is detailed later in section 3.2. Now only the $\widetilde{\mathrm{V}}_{\mathrm{eff}}^{\mathrm{R}}(\theta)$ and $\widetilde{\mathrm{V}}_{\mathrm{eff}}^{\mathrm{U}}(\theta)$ terms must be determined in order to derive the unknown DCS.

It is when the effective scattering volume $\widetilde{\mathrm{V}}_{\mathrm{eff}}(\theta)$ is defined that our new normalisation method really starts to differ from the established RFM.

In the RFM the pressures behind the capillary array for both the reference and unknown gases are set such that their mean free paths are identical and thus the two beams would also share the same spatial distribution. By defining the target density function as:

$$\rho(\boldsymbol{r}) = n_b n(\boldsymbol{r}), \tag{3.9}$$

where n_b represents the total number of molecules in the beam and $n(\boldsymbol{r})$ is the distribution of the beam, then provided that the mean free paths of the molecules in each of the gas beams are identical, their distribution functions will be equivalent i.e. $n^R(\boldsymbol{r}) = n^U(\boldsymbol{r})$. Thus a ratio of $\frac{n_b^R}{n_b^U}$ would be equal to the ratio of $\frac{\widetilde{\mathrm{V}}_{\mathrm{eff}}^{\mathrm{R}}}{\widetilde{\mathrm{V}}_{\mathrm{eff}}^{\mathrm{U}}}$, thereby further simplifying equation 3.8.

The relationship between the number of particles in each beam has been related to the flow rate and mass of the respective gases through the capillary or capillary array by Nickel *et al*.[11], and was found to be:

$$\frac{n_b^U}{n_b^R} = \frac{F^U\sqrt{m^U}}{F^R\sqrt{m^R}}, \tag{3.10}$$

where F denotes the flow rate of each gas and m the gases respective masses. In practice the ratio of the flow rates and masses is determined, in a separate series of measurements, by creating a calibration curve of this ratio as a function of the ratio of the driving pressures, over a range of those driving pressures. That range of driving pressures is dictated by the need to match the mean free paths of the two gases at the entrance of the capillary, maintain a mean free path greater than or equal to the diameter of the capillary and by the need to operate in the Clausing flow regime[11].

By combining equations 3.9 and 3.10, with equation 3.8, one obtains the now familiar relative flow equation for an effusive gas source:

$$DCS_0^{\mathrm{U}}\left(\overline{\mathrm{E}_0},\theta\right) = DCS_0^{\mathrm{R}}\left(\overline{\mathrm{E}_0},\theta\right)\frac{N_0^{\mathrm{U}}\left(\overline{\mathrm{E}_0},\theta\right)}{N_0^{\mathrm{R}}\left(\overline{\mathrm{E}_0},\theta\right)}\frac{\mathrm{I}^{\mathrm{R}}}{\mathrm{I}^{\mathrm{U}}}\frac{F^R\sqrt{m^R}}{F^U\sqrt{m^U}}. \tag{3.11}$$

3.1.2 Skimmed Supersonic Relative Density Method (SSRDM)

In the current apparatus the gas under investigation flows into the interaction region not as an effusive flow, but as a pulsed skimmed supersonic molecular beam. In this case the target density function cannot be expressed as shown previously in equation 3.9, and thus equations 3.10 and 3.11 also need to be discarded.

Instead one must consider the configuration shown in figure 3.2, which is a representation of what occurs inside the current apparatus[117]. Here the gas jet is

shown entering the source chamber from a nozzle and undergoing a supersonic expansion. During this expansion the velocity of the flow increases while the internal energy of the molecules decreases. Initially the flow is collisional, although the continued expansion results in a transition from this collisional flow regime to a regime of free molecular flow. The quitting surface, x_q, is considered to be the boundary between these two flow regimes. Once particles have passed beyond the theoretical quitting surface and into the region of free molecular flow, all of their thermodynamic properties remain fixed. Under these circumstances their properties are suffixed with the word 'terminal', to indicate that there will be no further change. The particles are also often considered to be 'frozen' in that regime.

Figure 3.2 also illustrates the expansion "streamlines"; these originate in the stagnation source and travel outwards tracing lines of constant enthalpy. The atoms/molecules involved in the expansion do not necessarily travel along these streamlines, however, it is usual to express a particle's velocity as a ratio of the component of velocity parallel to these streamlines divided by the velocity component that is perpendicular. This ratio is known as the speed ratio, S.

The approximate location of the quitting surface can be calculated using equation 3.12:

$$x_q \approx d\left(\frac{S_\infty}{C_1}\sqrt{\frac{2}{\gamma}}\right)^{\frac{1}{\gamma-1}}, \tag{3.12}$$

where d is the nozzle diameter, S_∞ is the terminal speed ratio, C_1 is a terminal speed ratio constant (C_1=3.232 (monoatomics)[120], $C_1 = 3.606$ (diatomics)[120] or $C_1 = 3.971$ (polyatmoics)[120]) and γ is an adiabatic constant defined as:

$$\gamma = \frac{f + 2}{f}. \tag{3.13}$$

Here f is the number of degrees of translational, rotational and vibrational freedom for each atom/molecule.

For hypersonic expansions, i.e. those where the speed ratio S is greater than five, the ideal intensity distribution $I(\phi)$ of a collimated free jet, both on-centreline and off-centreline, is given by equation 3.16[121]. This intensity distribution requires that the skimmer is placed upstream of the quitting surface.

$$I(\phi) = I_0 J(\phi), \tag{3.16}$$

where I_0 is the centreline intensity and $J(\phi)$ is the distribution function of particles:

$$J(\phi) = \frac{1}{2\pi} \int_0^{2\pi} \left[e^{-S_\infty^2 \sin^2(\phi)} \right]_{\phi_1 \max(\theta,\phi)}^{\phi_1 \max(\theta,\phi)} d\theta. \tag{3.17}$$

Here we note that the θ and ϕ in equation 3.17 are illustrated in figure 3.2 and S_∞ is again the terminal speed ratio. S_∞ can be estimated to within 10% accuracy for polyatomic molecules using the following relationship[122]:

$$S_\infty \approx 5.4(P_i d)^{0.32}, \tag{3.18}$$

where the stagnation pressure, P_i , is measured in Torr and d is the diameter of the nozzle as measured in centimetres.

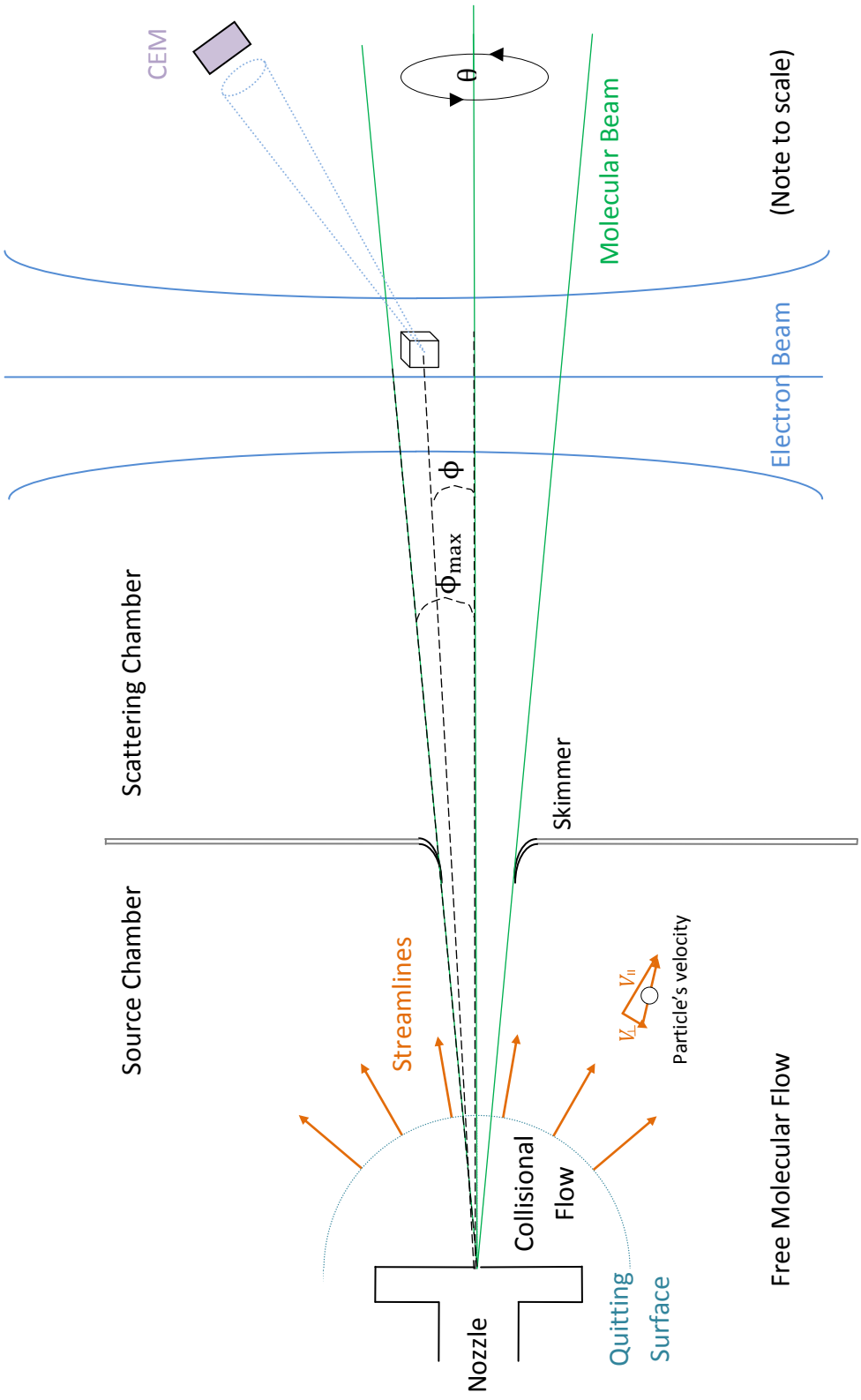

Figure 3.2: Schematic diagram of a skimmed supersonic jet entering the source chamber and passing through to the interaction region. See text for further details.

By matching the stagnation pressures and nozzle diameters, provided both the reference gas and unknown gas were polyatomic molecules, we are able to match the terminal speed ratios of the gases, and hence match their density distributions. This is similar to how the RFM uses the matched mean free paths of each gas, in order to obtain a matched density distribution. Now instead of measuring flow rates to determine the ratio of the number of particles in each beam, as shown in equation 3.10, we determine the centreline intensity I_0 of each gas jet in the scattering chamber. I_0 is in practice measured using a relationship determined by Götte *et al*[122] and expressed by equation 3.19:

$$\mathrm{I}_0 = \frac{\Delta \mathrm{p} \mathrm{S}_{\mathrm{eff}} \mathrm{L}^2}{\mathrm{A} k_B \mathrm{T}_{\mathrm{Scatt}}}, \tag{3.19}$$

where $\Delta \mathrm{p}$ is the difference in pressure between the baseline pressure and the average pressure during an experimental run, and $\mathrm{T}_{\mathrm{Scatt}}$ is the temperature of the scattering chamber (in all cases this temperature was taken to be 298 K). The cross sectional area of the collimated gas beam in the reaction plane, at a distance L from the expansion nozzle, is denoted in equation 3.19 by A; provided the distribution functions are the same for the reference and unknown gases, this area A will also be the same for both gases. $\mathrm{S}_{\mathrm{eff}}$ is the effective pumping speed. In the first incarnation of SSRDM this effective pumping speed was theoretically calculated[117], however later it was considered a more rigorous approach to actually measure this pumping speed. This follows as a combination of four different pumps (two turbomolecular pumps and two diffusion pumps) are involved in evacuating the various chambers of the present apparatus (see section 2.1)[65, 67].

In a similar fashion to the combination of equations 3.9 and 3.10 with equation 3.8, equation 3.14 is combined with 3.8 to produce equation 3.20:

$$\frac{N_0^{\mathrm{U}}(\overline{\mathrm{E}_0},\theta)}{N_0^{\mathrm{R}}(\overline{\mathrm{E}_0},\theta)} = \frac{DCS_0^{\mathrm{U}}(\overline{\mathrm{E}_0},\theta)\mathrm{I}^{\mathrm{U}}\mathrm{C}^{\mathrm{U}}(\overline{\mathrm{E}_0})}{DCS_0^{\mathrm{R}}(\overline{\mathrm{E}_0},\theta)\mathrm{I}^{\mathrm{R}}\mathrm{C}^{\mathrm{R}}(\overline{\mathrm{E}_0})}\left(\frac{\mathrm{I}(\phi)}{\nu_\infty \mathrm{L}^2}\right)^{\mathrm{U}}\left(\frac{\nu_\infty \mathrm{L}^2}{\mathrm{I}(\phi)}\right)^{\mathrm{R}}. \tag{3.20}$$

Equation 3.20 is now rearranged, with equations 3.15 and 3.16 used to expand the expressions for ν_∞ and $\mathrm{I}(\phi)$, to become:

$$DCS_0^{\mathrm{U}}(\overline{\mathrm{E}_0},\theta) =$$

$$\left(\frac{N_0^{\mathrm{U}}(\overline{\mathrm{E}_0},\theta)}{N_0^{\mathrm{R}}(\overline{\mathrm{E}_0},\theta)}\right)\left(\frac{\Delta \mathrm{pS}_{\mathrm{eff}}\mathrm{L}^2}{\nu_\infty \mathrm{L}^2 \mathrm{A} k_B \mathrm{T}_{\mathrm{Scatt}}\mathrm{J}(\phi)}\right)^{\mathrm{R}}\left(\frac{\nu_\infty \mathrm{L}^2 \mathrm{A} k_B \mathrm{T}_{\mathrm{Scatt}}\mathrm{J}(\phi)}{\Delta \mathrm{pS}_{\mathrm{eff}}\mathrm{L}^2}\right)^{\mathrm{U}} DCS_0^{\mathrm{R}}(\overline{\mathrm{E}_0},\theta) \tag{3.21}$$

Note that in equation 3.21 the ratio of the electron currents has been suppressed, effectively being incorporated into the scattered count rates, while the terms C^{U} and C^{R} have cancelled out. Now, as the density distributions $\mathrm{J}(\phi)$ are matched when the same stagnation pressure is used for both gases, these functions can also be cancelled out. Similarly, the areas A, Length L, temperature of the scattering chamber $\mathrm{T}_{\mathrm{Scatt}}$ and Boltzmann's constant k_B can further be cancelled out. Equation 3.21 can thus be rewritten as equation 3.22:

$$DCS_0^{\mathrm{U}}(\overline{\mathrm{E}_0},\theta) = \left(\frac{N_0^{\mathrm{U}}(\overline{\mathrm{E}_0},\theta)}{N_0^{\mathrm{R}}(\overline{\mathrm{E}_0},\theta)}\right)\left(\frac{\Delta \mathrm{pS}_{\mathrm{eff}}}{\nu_\infty}\right)^{\mathrm{R}}\left(\frac{\nu_\infty}{\Delta \mathrm{pS}_{\mathrm{eff}}}\right)^{\mathrm{U}} DCS_0^{\mathrm{R}}(\overline{\mathrm{E}_0},\theta). \tag{3.22}$$

In equation 3.22 the ratio of the terminal velocities is calculated using equation 3.15, and becomes equation 3.23:

$$\frac{\nu_{\infty}^{U}}{\nu_{\infty}^{R}} = \frac{\sqrt{\frac{2k_B T_i}{m^U}\left(\frac{\gamma^U}{\gamma^U - 1}\right)}}{\sqrt{\frac{2k_B T_i}{m^R}\left(\frac{\gamma^R}{\gamma^R - 1}\right)}}. \tag{3.23}$$

Provided that the initial stagnation temperature T_i is the same for both the reference and unknown gas, equation 3.23 can be simplified to become equation 3.24:

$$\frac{\nu_{\infty}^{U}}{\nu_{\infty}^{R}} = \sqrt{\frac{m^R}{m^U}\left(\frac{\gamma^U}{\gamma^U - 1}\right)\left(\frac{\gamma^R - 1}{\gamma^R}\right)}. \tag{3.24}$$

Now as all the terms contained on the right hand side of equation 3.22 can be either directly measured or theoretically calculated, the unknown elastic differential cross section can be determined, without having to explicitly calculate any detector efficiency functions or effective scattering volumes.

3.1.3 The preferred reference gas - CF_4

The reference gas used for all the present work was tetrafluoromethane (CF_4), rather than the usual RFM choice of helium. While the uncertainty in the known differential cross sections for CF_4 did introduce larger uncertainties than would have been the case with helium (20% as opposed to 1-7%), there were several factors that made CF_4 the better choice.

SSRDM requires the measurement of the change in pressure between the “gas on” and “gas off” conditions, and the ability to measure the effective pumping speed in

order to determine the centreline intensity as defined by equation 3.19. It was discovered that attempting to use helium as a reference gas resulted in a very small pressure rise between the "gas off" and "gas on" conditions, indeed in practice sometimes this pressure rise was so small as to be indistinguishable from the background pressure. Suffice to say that this small pressure rise led to difficulties in measuring a reproducible value for it, in part number due to the relevant pressure gauge resolution capability. This small pressure rise also resulted in a very quick return to the background pressure level once gas pulsing had stopped, making the measurement of the effective pumping speed difficult due to a lack of data points. Section 3.2.1 contains a detailed discussion of our measurement procedure for both the change in pressure Δp and the effective pumping speed S_{eff}.

Tetrafluoromethane also has the advantage of being stable at the pyrolysis temperatures used for the production of both CF_2 and CF_3. This facet also allowed the initial nozzle temperature to be the same for both the reference gas and the unknown target gas. While helium was certainly not unstable at these same temperatures, its resultant expansion meant a lower density gas jet in the interaction region, making experimental run times considerably longer. Being able to maintain the pyrolytic nozzle temperature for both gases also meant that it was not necessary to wait for the nozzle to cool down between experimental runs, allowing for quicker overall experimental throughput. Using the same nozzle temperature further meant that it was not necessary to know the exact temperature of the SiC tube, so long as the temperature remained unchanged throughout each experiment. This was advantageous as the emissivity of the SiCT, a

number required to determine the tube's absolute temperature, was quoted by the manufacturer with no indication of it's accuracy.

Finally, being a polyatomic, CF_4 is predicted to behave similarly to the "unknown" target polyatomic gases during a supersonic expansion. This follows as it is molecular structure, rather than actual chemical composition, that is the driving force in the dynamics of such an expansion[120].

The experimental measurements of the elastic electron differential cross sections for CF_4, by Boesten *et al.* [123], were used as the reference DCS as shown in equation 3.22. This data set provided elastic DCSs for the following electron impact energies (eV); 1.5, 2, 3, 5, 6, 7, 8, 9, 10, 15, 20, 35, 50, 60 and 100. For the energies we studied where a reference DCS was not available, a result was interpolated (from graphs of cross section vs energy at each angle) from the existing CF_4 data set. Of course this method would have been flawed if there were any significant resonant responses over this energy range. Fortunately the SMC calculations of Huo[124] show only three broad (>18eV energy width) resonances occurring over a 10 eV range where the measured DCS are broadly spaced. A narrower (4.1eV width) resonance was found at 6.6eV[124], but considering this resonance lay in an area where data for the elastic DCS of CF_4 were available it did not affect any of our interpolations. These broad resonances caused the ICS to be almost completely featureless, for electron impact energies greater than 15eV, as also predicted by Varella *et al.* [125]. Hence in this case the interpolations of the CF_4 DCS are

expected to produce valid cross sections to be used for the normalisation of the present electron scattering data.

Boesten *et al.* [123] did not measure the elastic DCS of CF_4 at four of the angles studied in the current work, specifically 45^o, 75^o, 105^o and 135 ^{o}. In these cases the average of the DCS at adjacent angles was used for our normalisation purposes.

3.2 Experimental Procedures

3.2.1 Measuring the change in pressure and the effective pumping speed

As discussed in section 2.1 the pressure of the scattering chamber was read by a compact full range gauge (Pfeiffer PKR 251), which was logged using a Labview interface at a frequency of 10 Hz. A typical graph of the pressure as a function of time is shown in figure 3.3. Note that graphs such as this were logged after electron scattering counts had been recorded.

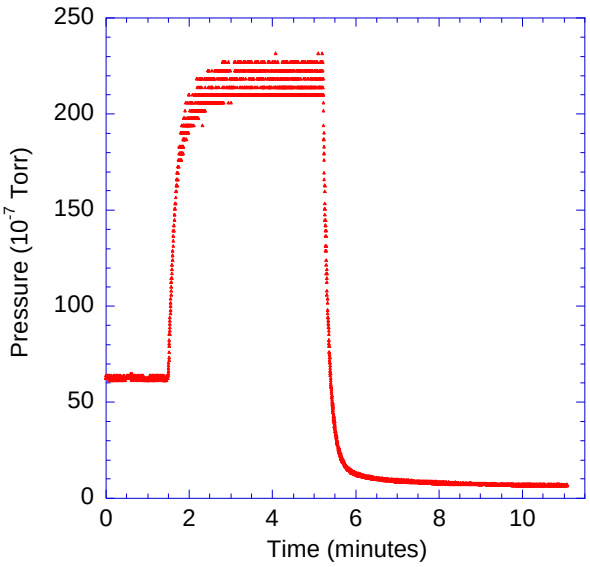

Figure 3.3: A graph of the pressure measured in the scattering chamber as a function of time, for a hot CF_3I mixture.

Figure 3.3 shows five distinct regions. The first region from $0 \leq t < 2$mins shows a constant pressure of $6.2*10^{-6}$ Torr, this is the pressure with the pyrolysed CF_3I mixture pulsing into the apparatus while all pumps are evacuating the chamber. Region 2, $2 \leq t < 3$ mins shows a large increase in pressure, this is a result of the gate valve above the smaller of the two diffusion pumps (VHS6) closing (see figure 2.2 showing the diffusion pumps). In region 3, $3 \leq t < 5$mins, the pressure in the scattering chamber once again stabilises, this time with a value of $2.18*10^{-5}$ Torr. When $t \approx 5$mins, the pulsed nozzle driver is turned off, resulting in a rapid decrease in pressure as seen in region 4, $5 \leq t < 5.5$mins. Finally in region 5, $t > 5.5$mins, the pressure in the scattering chamber once again stabilises, this time with a value of $7.5*10^{-7}$ Torr.

The "gas on" and "gas off" pressures are taken to be the average value from regions 3 and 5 respectively, with the uncertainty on each value taken to be the standard

deviation of the mean value, which is usually in the order of 1%. The difference between these measured "gas on" and "gas off" values is Δp^*. This pressure difference is then corrected to take into consideration for the total ionisation cross section of each particular gas species measured, using equation (3.25):

$$\Delta p = \frac{\Delta p^* Q_{N_2}^{ion}}{Q_{target}^{ion}}, \tag{3.25}$$

where Δp^* is the measured pressure difference, Q_{target}^{ion} represents the total ionisation cross section at 150 eV for the target species (either the reference or "unknown" gas) and $Q_{N_2}^{ion}$ is the ionisation cross section for nitrogen (the gas used for the calibration of the pressure gauge) at 150 eV. Finally Δp is the corrected pressure.

As in the final calculation of the differential cross sections (see equation 3.22) only the ratio of the corrected pressures $\Delta p^R/\Delta p^U$ is required, the ionisation cross section of nitrogen is in fact cancelled out. Table 3.2 thus summarises the electron impact ionisation cross sections at 150 eV (the potential of the pressure gauge cathode), for each of the species used in this work. When the gas beam contained a mixture of gases an average ionisation cross section was used. This cross section was determined by the addition of the ionisation cross sections for each species weighted using their proportion in the beam.

Species	Q_{150eV}^{ion} (x10^{-20}m^2)	Reference
CF_2	1.78 (25%)	[57]
CF_4	5.71 (2%)	[95]
CF_3I	8.58 (2%)	[95]

CF_3	2.3 (25%)	[57]
C_2F_6	8.95 (2%)	[95]
I_2	9.32(2%)	[126]
I	4.85(2%)	[126]

Table 3.1: Summary of available electron impact ionisation cross sections at 150eV for the species considered in this work.

The effective pumping speed, S_{eff}, was determined by using the relationship shown in equation 3.26[67]:

$$P(t) = P(0)\exp\left(-t\frac{S_{eff}}{V}\right), \tag{3.26}$$

where P is the measured pressure as a function of time, V is the volume of the chamber, while the time $t = 0$ corresponds to when the pulsed nozzle is switched off. Therefore a plot of $\ln(P(t))\ vs\ t$ should produce a straight line graph with a slope of $\frac{-S_{eff}}{V}$, with an example of such a plot being shown in figure 3.4. The uncertainties in the slopes were calculated using a linear regression, and were typically between 2-4%.

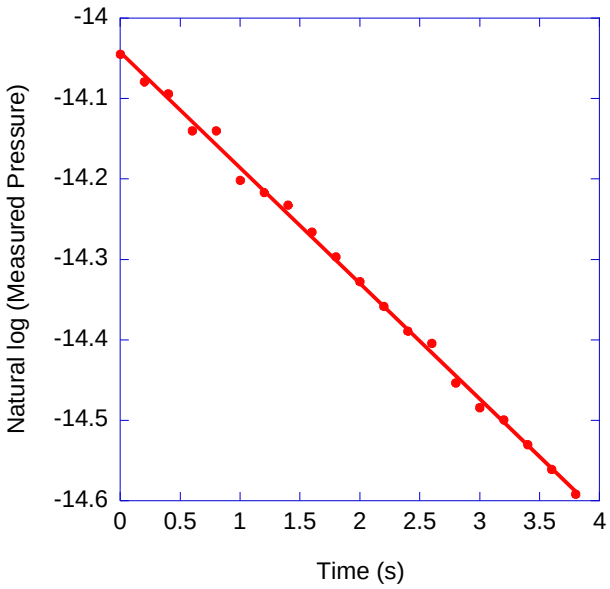

Figure 3.4: Typical plot of the natural log of the scattering chamber pressure as a function of time (red ●), with the nozzle closed at t=0. Here after pulsing CF_4 with a stagnation pressure of 280 mbar. A linear trend line (red ——) has been fitted to these data points. A similar plot for the relevant "unknown" gas would also be measured in practice.

Note that as only the ratio of the effective pumping speeds of the "unknown" and reference gases is required, it was not actually necessary to calculate the total volume of the chamber.

3.2.2 Measuring the Electron Scattering Signals

The CEMs detected scattered electrons continuously during operation and fed those signals to a purpose built Labview virtual instrument, by the route described earlier in section 2.4.2.2.

This virtual instrument logged the counts received during two completely adjustable data collection time windows; scattered counts received outside these timing windows were discarded. The first counting window, called the "gross count

window" was open when a molecular beam was present in the interaction region, and thus it contained counts from electrons scattered from both the molecular beam and from background gases. The second window, called the "background window", opened and closed while the interaction region was "vacant" and thus recorded only electron scattering signal due to the background gases present in the scattering chamber.

In order to properly adjust the timing windows it was necessary to ascertain when a molecular beam was and was not present in the electron scattering interaction region. The first step of this process involved determining the temporal length of the molecular beam using the TOFMS as detailed previously in section 2.5.3. The second step of the process involved using the information just obtained from the TOFMS to determine the outer limits of the time over which a molecular beam could be present in the electron scattering interaction region. By considering the molecular beams' arrival time and departure time in the TOFMS ionisation region, along with the distance between the ionisation region and the interaction region (33.8cm), the outer bounds of the molecular beams' arrival and departure time in the interaction region was calculated. Once the limits of the molecular beams presence in the interaction region were known, the third and final step of this process involved varying the time delay between the "pulser fire" command and the opening of the gross count window (with the proviso that the gross count window remained within these limits). For each "pulser fire"-"gross count window" delay, the true scattering signal (see equation 3.28) was recorded (at a particular angle and for a particular incident electron energy), with the largest amount of true

scattering signal taken to correspond to the optimal "pulser fire"- "gross count window" delay time. Note that for each "pulser fire"-"gross count window" delay background scattering was also recorded, with the background window length and delay remaining fixed for each optimisation.

The current elastic differential and integral cross section investigations employed the use of various stagnation pressures, nozzle-skimmer separation distances, nozzle operating temperature and gas species and as such the electron scattering timing windows were different in each case. Table 3.3 lists the physical conditions and subsequent electron scattering timing windows for each of the configurations used in the present investigation.

Table 3.2: Details of the production method, physical conditions and subsequent electron scattering timing windows for each of the various species used in the present investigation.

Species of Interest	CF_2	CF_3I	CF_3
Production Method	Pyrolysis	Not applicable	Pyrolysis
Pyrolysis temperature	1200^oC	-	817^oC
Parent Molecule	C_2F_4	-	CF_3I
Physical Conditions			
Nozzle Diameter	2.0 mm	0.5 mm	2.0 mm
Nozzle-Skimmer separation	4.5 cm	8.0 cm	2.5 cm
Stagnation pressure	280 mbar	430 mbar	530 mbar
Scattering Windows			
Gross count window delay	1900 μs	1700 μs	3000 μs
Gross count window time	5000 μs	1500 μs	9000 μs
Background count window delay	60000 μs	60000 μs	15000 μs
Background count window time	5000 μs	10000 μs	80000 μs

*Note the distance between the skimmer and the interaction region was fixed at 5.4cm, while the distance between the interaction region and the TOFMS ionisation region was fixed at 33.8cm.

Each of the ten gross count windows and background count windows were populated for a given amount of time (called the bin-length), after which the number of counts each had accumulated was recorded and the counters were reset to zero in order to begin the process again. At the beginning and end of each bin the electron monochromator current along with the stagnation pressure and scattering chamber pressure were also recorded, so that any changes in their conditions could be properly taken into account.

Each experimental run consisted of a number of successive bins. Both bin-length and run length were highly variable across data sets, as they were dependant on the number of scattered electrons received. This in turn depended on the amount of the incident electron flux, molecular flux in the interaction volume, CEM responses and the elastic differential cross section. In general bin-lengths varied from five minutes to fifteen minutes while run times varied from 2 to 4.5 hours. Each experiment typically consisted of two experimental runs, one run using the gas under investigation and one run using a reference gas, in all cases the reference gas used was CF_4 (as discussed in section 3.1.3). Note that many experiments were preformed before a final DCS data set was arrived at for a given species at a given energy.

Scattering data were analysed "on-the-fly" by another purpose build Labview vi. This virtual instrument determined the amount of "true" electron scattering received (C_s) by each successive bin using the following formula:

$$C_s = \frac{\frac{C_G}{T_G} - \frac{C_B}{T_B}}{\frac{I_{Start} + I_{End}}{2}}, \tag{3.27}$$

where C refers to the number of electron counts recorded in a count window, T denotes the length of a count window and the subscripts G and B refer to the gross count window and the background count window respectively. I_{Start} refers to the measured current of the incident electron beam on the Faraday cup at the start of the bin, similarly I_{End} is the corresponding current measured at the end of the bin.

The number of "true" scattered electron counts, ($\dot{N}_e$), received during a run containing 'n' bins, was taken to be the mean of the number of scattered electron counts (C_s), received in each bin as defined in equation 3.27. By dividing the total run time for a particular gas into a series of successive bins, it made it possible to take into consideration both the statistical variation of $\dot{N}_e$ and the pulse by pulse variation of the molecular beam. Note that $\dot{N}_e$ is dependent on both the scattering angle θ and the nominal impact energy E_0, and is defined as:

$$\dot{N}_e(\mathrm{E}_0, \theta) = \frac{\sum_n C_{sn}}{n}. \tag{3.28}$$

The uncertainty in $\dot{N}_e$ ($\Delta\dot{N}_e$) was taken to be the true error of the mean as shown in equation 3.29:

$$\Delta\dot{N}_e = \frac{stdev(\dot{N}_e)}{\sqrt{n}}, \tag{3.29}$$

where $stdev(\dot{N}_e)$ is the standard deviation of the number of scattered electron counts and 'n' is the number of bins in the run. The data analyser vi also calculated

and displayed the percentage uncertainty ($\%\dot{N}_e$), for each scattering angle, as shown in equation 3.30:

$$\%\dot{N}_e = \frac{\Delta\dot{N}_e}{\dot{N}_e} \times 100. \tag{3.30}$$

Runs were typically terminated when the uncertainty on each of the channels decreased to below 5%. Occasionally a run might be terminated when most of the channels had an uncertainty below 5%, but the amount of time required for the remaining channels' uncertainties to decrease below 5% would make the overall run time longer than five hours. As each experiment consisted of at least two runs, if the first run lasted more than five hours the experiment could potentially run for over eleven hours in a given day. In our case experiments could not be run overnight as the stagnation pressure behind the nozzle had to be monitored and adjusted manually to ensure it remained within $\pm$ 5mbar of its set valve. Also, as the electron monochromator current into the Faraday Cups was explicitly used to calculate the number of scattered counts recorded in each successive bin (equation 3.27), it was important that this current remained constant for each experiment, so runs were always measured consecutively. Consecutive runs also limited any variation in the CEM responses, so all experiments were completed within the same day. With as many experiments as needed being performed before the final differential cross section was arrived at.

On the odd occasion the number of gross counts recorded, C_G, did not exceed the number of background counts recorded C_B, by enough of a margin to make the resultant number of "true" signal counts, C_s, statistically distinguishable from

background levels. An inability to resolve C_s from the background, for a given angle and electron impact energy for either the "unknown" molecular beam under investigation or the reference beam, resulted in an inability to calculate $\dot{N}_e$ and hence the differential cross section at that point.

3.3 The Production of radicals *in situ* via vacuum flash pyrolysis

3.3.1 Producing CF_2 radicals

Tetrafluoromethane (C_2F_4) (99% purity ABCR) was used to produce the CF_2 radicals. This was achieved via the pyrolytic decomposition of C_2F_4, in which the dominant reaction is the schism of the carbon-carbon double bond and the production of CF_2[127]:

$$C_2F_4 \xrightarrow{heat} 2CF_2. \tag{3.31}$$

C_2F_4 has an ionisation potential of 10.12±0.01 eV[89] and as such is detectable in our TOFMS, as it can be ionised by the 118 nm (10.48 eV) photon source that the TOFMS utilises. However CF_2, having an ionisation potential of 11.5±0.4 eV [55], cannot be ionised by this photon source and is therefore undetectable in the current configuration of the TOFMS. Hence the existence of CF_2 as a product of the pyrolysis of C_2F_4 is inferred rather than directly measured as detailed below.

The optimum temperature for the pyrolysis of C_2F_4 was determined by slowly increasing the temperature of the pyrolytic nozzle while pulsing C_2F_4. At each nozzle

temperature the average C_2F_4 peak height over 1000 laser shots (as measured by the TOFMS) was recorded; the uncertainty on the measurement was taken to be the standard deviation of this mean. The time delay between the pulser fire and laser fire command was set such that the laser fired during the maximum density of C_2F_4 molecules in the ionisation region for each gas pulse. A plot of the results from such an experiment is shown in figure 3.5.

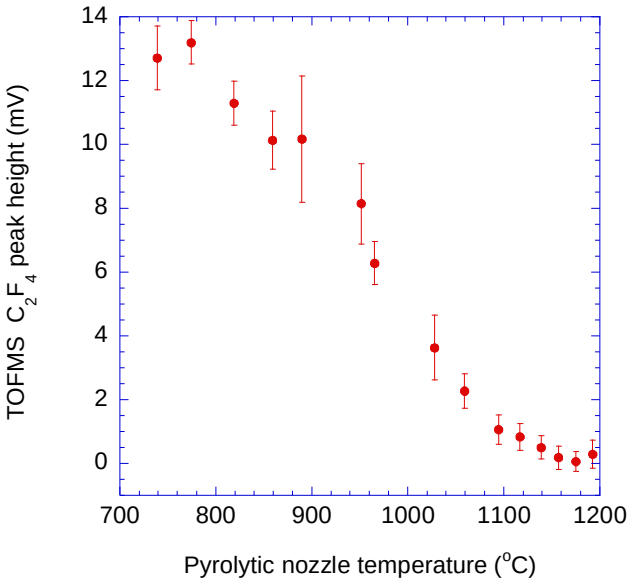

Figure 3.5: C_2F_4 signal height in mV, as measured by the TOFMS, as a function of pyrolytic nozzle temperature in degrees Celsius. The C_2F_4 stagnation pressure was 400mbar, the nozzle skimmer separation 4.5 cm, while the Nd: YAG fire delay was 2100μs from the nozzle 'pulser fire' command.

The pyrolytic nozzle's temperature was monitored using an optical pyrometer with a tungsten filament. The emissivity of the SiCT was taken to be 0.95, as quoted by the manufacturer (Hexaloy), and this constant was used to scale the measured temperature to our absolute values. Hexaloy did not allude to the accuracy of this emissivity coefficient, so the absolute values quoted for the temperatures might still be considered as being only somewhat an approximate figure. Having said that,

there is no problem with the accuracy of the relative temperatures, or with maintaining the pyrolytic nozzle at a constant temperature.

From figure 3.5 it can be seen that the onset of C_2F_4 pyrolysis occurs between 773^{o}C and 818^{o}C, with no detectable C_2F_4 signal remaining by 1200^{o}C. These temperatures are in reasonable agreement with previously published data of Snelson [127] and Pottie[128], who both used a temperature of 1300^{o}C for the complete pyrolysis of C_2F_4 to form CF_2 radicals. Cameron and Kable[129] reported different temperatures for both the onset of pyrolysis (~630^{o}C) and complete pyrolysis (~830^{o}C), although again there is some doubt over the absolute scale of those temperatures.

Nonetheless, without the ability to directly detect CF_2, all that can be determined with absolute surety from the results in figure 3.5 is that an increased nozzle temperature results in a decrease in the amount of C_2F_4; not that this reduction in C_2F_4 necessarily results in the production of CF_2. For this reason the experiment was repeated, so that we also simultaneously monitored the amount of true electron scattering with those results being shown in figure 3.6. Note that the electron scattering counts were recorded in the detector at a scattering angle of 75°, with the incident electron beam energy being 40 eV.

Figure 3.6 indicates that even when there is no C_2F_4 detected in the TOFMS, there is still a molecular beam in the apparatus, as there are true electron scattering counts being received by the 75° CEM detector.

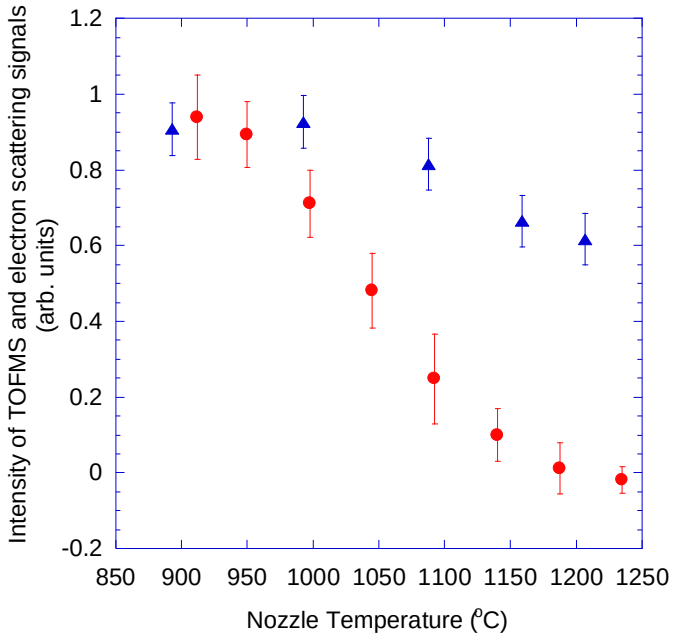

Figure 3.6: Normalised C_2F_4 average peak height average (red ●), normalised true electron scattering signal (blue ▲), (recorded at 75°, with an electron impact energy of 40eV) as a function of pyrolytic nozzle temperature measured in degrees Celsius. The C_2F_4 stagnation pressure was 280mbar

We investigated whether CF radicals or CF_3 radicals were also produced (both species being detectable in the TOFMS with ionisation energies of 9.4±0.4 eV[55] and 8.5±0.4 eV[55] respectively) and found no evidence for the presence of either species. We thus concluded that there was no pyrolytic pathway for the production of those species and that there was also no secondary pyrolysis of CF_2 occurring. Indeed as no mass peaks other than for C_2F_4 were detected in the TOFMS spectrum, as the pyrolytic nozzle temperature was increased, it was concluded that the products of this pyrolysis were comprised solely of species that could not be ionised by 118nm photons.

Snelson[127] reported the formation of both CF_3 and CF_2, along with C_2F_6, C_3F_6 and C_4F_8 (both linear and cyclic), as a result of the (incomplete) pyrolysis of C_2F_4 at

500°C. It was postulated that the C_2F_6 was formed by the addition of two CF_3 radicals, C_3F_6 was formed by the addition of a CF_2 radical to C_2F_4, while C_4F_8 was produced by the dimerisation of C_2F_4. However, as the temperature increased, the amount of both the C_3 and C_4 species decreased, most likely due to the increasing instability of C_2F_4. As we detect no CF_3 present in our molecular beam we consider the production of C_2F_6 highly unlikely. Similarly, we also consider the presence of CF_4 unlikely as its production requires several steps; some involving the presence of the CF_3 radicals that we have established are not present.

For these reasons we conclude that for the conditions in our experiment the only possible product forming as a result of pyrolysis of C_2F_4, is CF_2. Furthermore, in a move similar to that of Cameron and Kable[129], we limit the temperature of the pyrolytic nozzle by setting it just above the point of complete C_2F_4 pyrolysis (1200°C), to ensure that there are no secondary pyrolytic reactions.

3.3.2 Producing CF_3 radicals

Iodotrifluoromethane (CF_3I), purchased from Oakwood Products (South Carolina, USA), with a reported purity of 99%, was used as a CF_3 radical source. CF_3I was pulsed through the apparatus with a stagnation pressure of ~300 mbar while the pyrolytic nozzle temperature was increased from room temperate to 950°C. Note that 500 laser shot averaged time-of-flight (TOF) spectra were recorded throughout these measurements. Background signal was also recorded by adjusting the laser timing to fire between the molecular pulses; these backgrounds were then

subtracted from all of the respective spectra. Typical results, in the range 740°C – 900°C, from this process are given in figure 3.7. From these spectra the onset of CF_3I pyrolysis was found to be ~740°C, with complete pyrolysis occurring at ~1000°C. Unlike the pyrolysis of C_2F_4, the pyrolysis of CF_3I resulted in the production of multiple species, as evidenced by mass peaks at 69amu, 127amu and 254amu along with the CF_3I mass peak at 196amu. The heights of these peaks varied with changing pyrolytic nozzle temperature, indicating that the beam composition is temperature dependent.

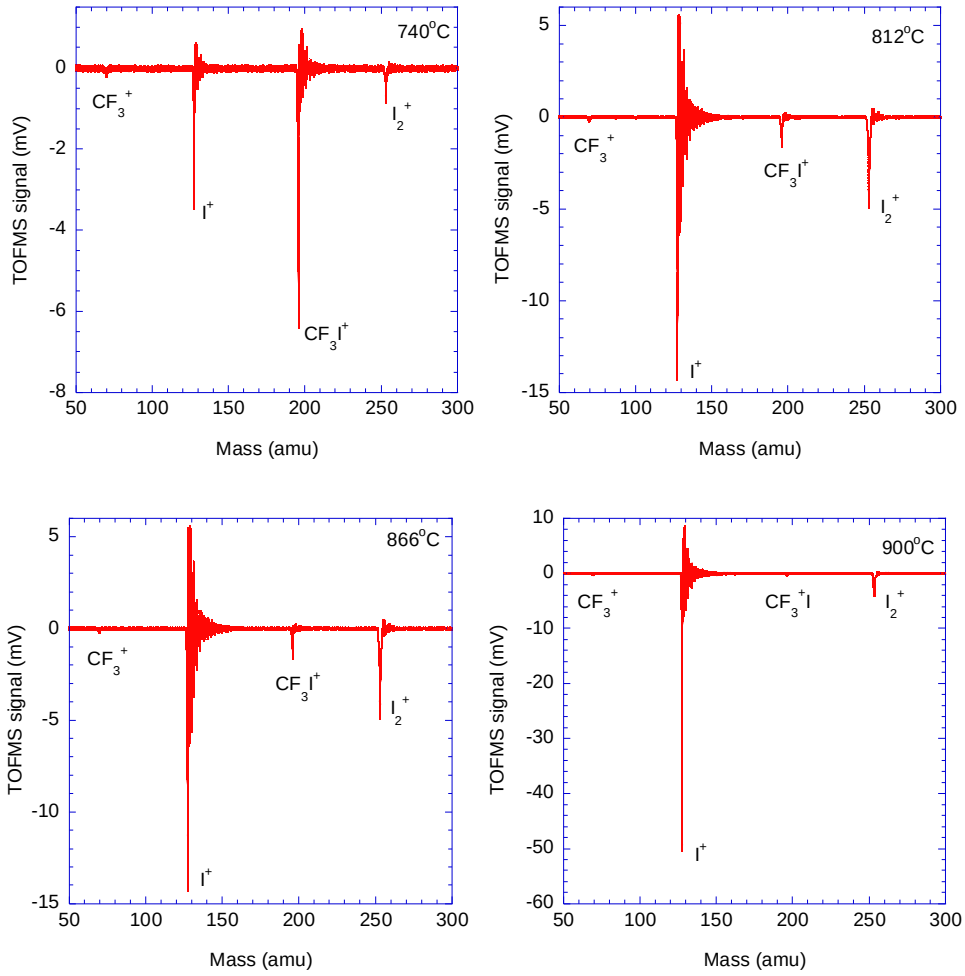

Figure 3.7: Recorded TOF spectra for the pyrolysis of CF_3I for various pyrolytic nozzle temperatures including; 740°C, 812°C, 866°C and 900°C. Experimental conditions: 500 laser shot averaging, 300mbar CF_3I stagnation pressure, background subtractions were performed.

Each peak measured in the TOF spectra was subsequently scaled according the 118nm photon impact ionisation cross section of the relevant species, to give an actual measure of the relative number densities of the respective species in the mixed beam, with the cross sections being used listed in table 3.4. The photon impact ionisation cross section for CF_3 at 118 nm is unknown at this time, so the electron impact ionisation cross section was employed instead; we expect this to be a reasonable approximation at this energy. Examples of the present scaled spectra are shown in figure 3.8.

Table 3.3: 118 nm photon impact ionisation cross sections for CF_3, CF_3I, I_2 and I.

Species	$Q^{ion}_{118\ nm}$ (x$10^{-20}m^2$)	Reference
CF_3	0.026*	[55]
CF_3I	0.502^{+}	[104]
I_2	0.552	[130]
I	0.74	[130]

*10.5eV Electron impact cross section
$^{+}$Photionisation cross section at 11eV

As the spectra shown in figure 3.8 were collected over a period of several hours, the absolute peak heights of the species in each cannot be directly compared because the laser power may have drifted somewhat over this time. However one can clearly see that the amount of CF_3I decreases as more and more of it undergoes pyrolysis, until ~900°C where almost all traces of CF_3I are gone and the pyrolysis is almost complete. The 900°C TOF spectrum shows a considerable amount of atomic iodine which must have been produced by the C-I bond breaking in CF_3I. The schism of this C-I bond should result in an equal amount of CF_3 radicals and atomic iodine being produced, yet this is not apparent from the 900°C TOFMS trace. The only explanation for these "missing" CF_3 radicals is that they must have undergone subsequent reactions, producing fluorocarbons that are not detectable with the

current TOFMS configuration. So we are forced to refer to the literature to determine those likely additional products for the pyrolysis of CF_3I.

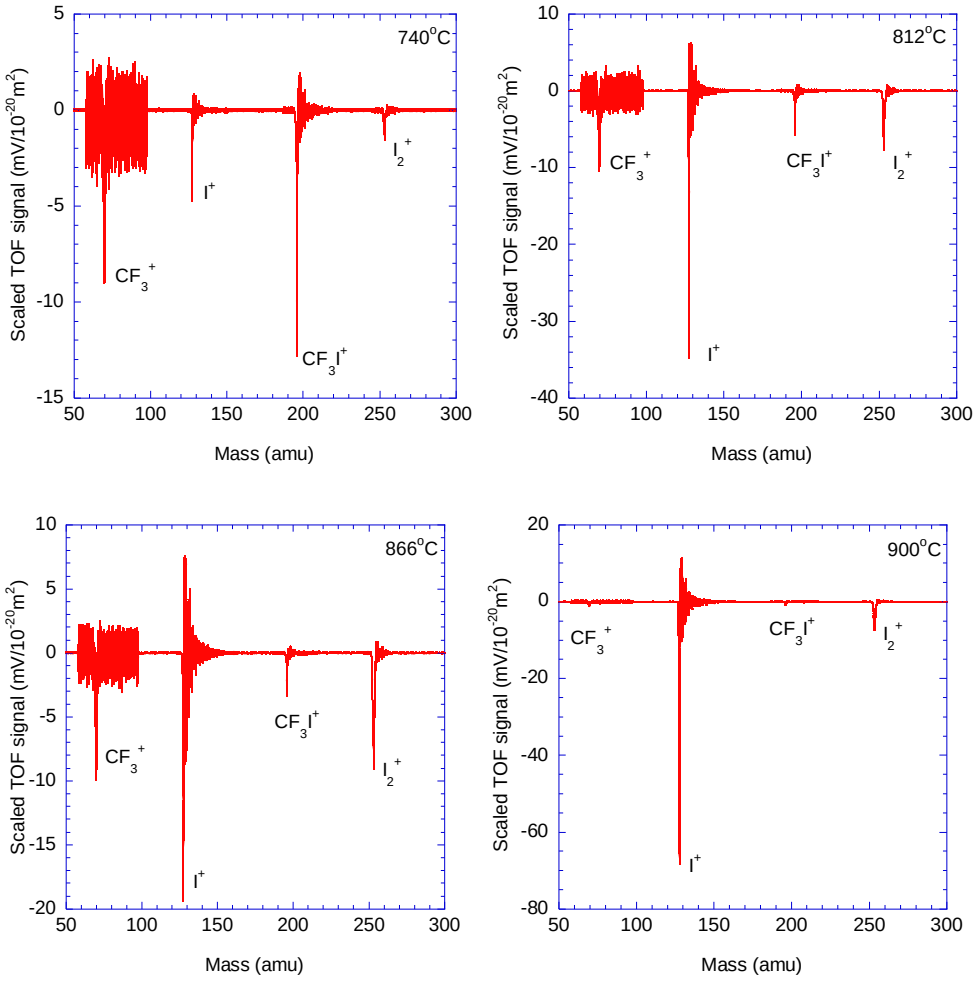

Figure 3.8: CF_3I pyrolysis products for various pyrolytic nozzle temperatures including; 740°C, 812°C, 866°C and 900°C. Each mass peak has been scaled using the photon impact ionisation cross sections of the relevant species. A 300mbar stagnation pressure for CF_3I, 500 laser shot averaging, and backgrounds being subtracted from each spectrum should also be noted.

Snelson[127] reports that the primary reaction in the pyrolysis of CF_3I was the breaking of the weak C-I bond, with secondary reactions occurring between iodine atoms to form molecular iodine, and between CF_3 radicals to form C_2F_6 [127]:

$$\begin{aligned} CF_3I &\xrightarrow{heat} CF_3 + I, \\ 2I + M &\longrightarrow I_2, \\ and \quad 2CF_3 &\longrightarrow C_2F_6. \end{aligned} \tag{3.32}$$

Note that a third body "M" acts in the iodine recombination reaction, this body can be either the SiC tube wall or another constituent of the gas mixture that serves to assist in the conservation of momentum of the collision. In figures 3.7 and 3.8 we clearly observe the products of the result of both the broken C-I bond and the re-combination of atomic iodine to form molecular iodine. Considering that the collision rate within the 37mm pyrolytic tube is sufficient to allow for the recombination of atomic iodine, it is highly likely that CF_3 radicals are also reacting with each other to produce C_2F_6. C_2F_6, which has a first ionisation threshold of 14.6eV[131], is undetectable with our present TOFMS configuration. Furthermore C_2F_6 is stable at the temperatures used in the pyrolysis of CF_3I, so once formed there would not be sufficient energy to break that molecule apart.

Snelson[127] also reports the combination of CF_3 with unreacted CF_3I to form CF_2I and CF_4 ($CF_3I + CF_3 \rightarrow CF_2I + CF_4$), followed by the breakdown of CF_2I to form CF_2 and atomic iodine ($CF_2I \rightarrow CF_2 + I$). Had any CF_2I been present in the molecular beam it would have been able to be detected by our TOFMS, as it has an ionisation energy of less than 10.48 eV[132] and a significant photoionsation cross section at 118nm. The absence of any CF_2I makes the presence of any CF_2 or CF_4 very unlikely in our current configuration.

Hence the undetected fluorocarbon that must be present in our system, in order to conserve the mass of CF_3 post-pyrolysis, is identified to be C_2F_6. The amount of C_2F_6 is now calculated by considering the total number of iodine atoms to be equal to the total number of CF_3 radicals, with the iodine atoms appearing in the TOF

spectrum as either I ions or I_2 ions, while the CF_3 radicals either appear as CF_3 ions or not at all. This leads to the following relationship:

$$\#Ions_{CF_3} + 2 \times \#Ions_{C_2F_6} = \#Ions_I + 2 \times \#Ions_{I_2}. \quad (3.33)$$

Equation 3.33 is now simply rearranged to find the number of C_2F_6 ions that would have been detected by the TOFMS if 118 nm photons were able to ionise it:

$$\#Ions_{C_2F_6} = \frac{\#Ions_I + 2 \times \#Ions_{I_2} - \#Ions_{CF_3}}{2}. \quad (3.34)$$

Note that the 'number of ions' for I, I_2 and CF_3 are taken from the area of the corrected peaks in the measured TOF spectra:

$$Peak\ area = \#Ions = \frac{gross\ peak\ area\ - background\ area}{\mathrm{Q}^{\mathrm{ion}}_{118\,\mathrm{nm}}}, \quad (3.35)$$

where the gross peak area is the area measured when the molecular beam is present in the system and the background peak area is the area measured between the molecular beam pulses (this was achieved in practice by adjusting the delay between the laser fire command and the pulser fire command). $\mathrm{Q}^{\mathrm{ion}}_{118\,\mathrm{nm}}$ has been defined previously.

The areas of the peaks were used rather than simply the peak height as the widths of the respective peaks varied somewhat, with the molecular iodine peak being noticeably broader than the others. The number of unseen C_2F_6 'ions' was then calculated for each spectra using the relationship expressed in equation 3.34.

The total number of ions present in each spectrum was then determined and the composition of the molecular beam in each case was then calculated by subsequently working out the percentages of each species present. Namely,

$$\#Ions\ per\ spectrum = \#Ions_{I_2} + \#Ions_{CF_3} + \#Ions_I + \#Ions_{C_2F_6} + \#Ions_{CF_3I}, \quad (3.36)$$

$$\%_{species} = \frac{\#Ions_{species}}{\#Ions\ per\ spectrum} \times 100. \quad (3.37)$$

The uncertainty on each measured area was taken to be the standard deviation of the mean area, while the overall uncertainty on the area was the quadrature sum of those individual uncertainties. Hence the overall uncertainty on the total number of ions present in each spectrum was calculated using the quadrature sum of each of the individual uncertainties for each ion species present.

An experiment was therefore conducted to determine the change in beam composition as a function of temperature, with those results being presented graphically in figure 3.9 and in tabular form in table 3.5. From these results it can be seen that the maximum concentration of CF_3 radicals (22.86 %) occurs at a pyrolytic nozzle temperature of ~808°C. While increasing the nozzle temperature past 836°C results in a more complete pyrolysis of CF_3I, it also results in a sharp increase in the production of C_2F_6. This increase in C_2F_6 is interpreted to be the result from the presence of a higher concentration of CF_3 radicals in the pyrolytic tube, resulting in more collisional recombination of that radical. At pyrolytic nozzle temperatures below 820°C it is, however, considered that the CF_3 radicals are buffered somewhat by the other species present in the beam and prevented from forming C_2F_6.

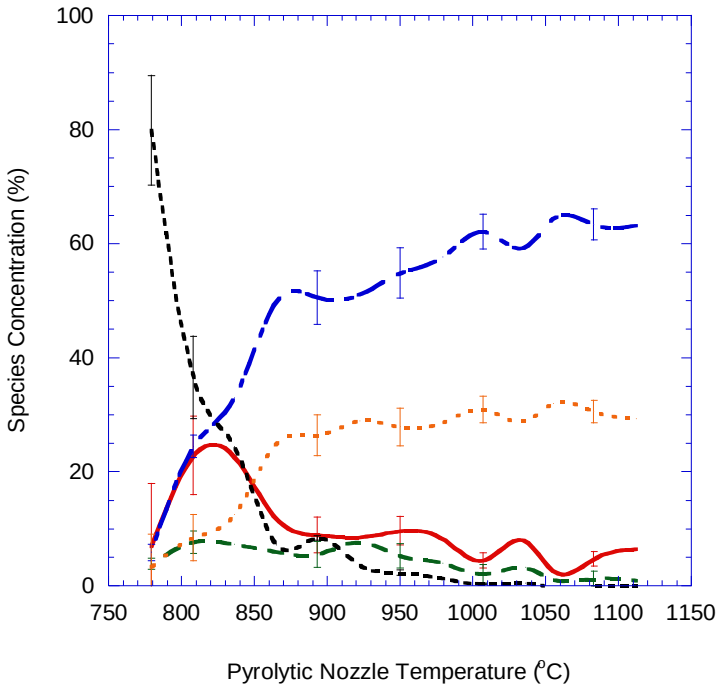

Figure 3.9: Species concentration in our "mixed" molecular beam as a function of pyrolytic nozzle temperature, for the pyrolysis of CF_3I. Here we denote CF_3 (red ——), I (blue – — – —), I_2 (green — —), CF_3I (black – – – –) and C_2F_6 (orange ·····).

Temperature °C	$\%CF_3$	%I	$\%CF_3I$	$\%I_2$	$\%C_2F_6$
779	6.98±11.00	5.91±1.42	79.89±9.60	3.88±0.99	3.34±5.63
808	22.86±6.83	24.46±1.97	36.54±7.20	7.67±2.01	8.47±4.09
836	22.68±4.85	33.02±2.18	24.49±3.10	7.32±1.47	12.49±3.03
865	11.76±4.44	49.91±3.96	7.26±2.04	6.00±4.25	25.08±5.19
893	8.94±3.11	50.60±4.64	8.46±0.39	5.58±2.25	26.41±3.58
922	8.53±2.11	51.10±3.15	3.69±0.23	7.70±1.43	28.98±2.37
950	9.67±2.52	54.85±4.41	2.30±0.47	5.29±2.16	27.88±3.33
979	8.27±1.11	57.70±3.58	1.31±0.21	4.00±1.60	28.71±2.46
1007	4.48±1.29	62.15±3.09	0.37±0.16	2.09±1.62	30.92±2.33
1036	7.85±1.70	59.40±4.76	0.51±0.17	3.23±1.33	29.01±2.86
1055	2.63±1.71	64.37±4.86	-0.17±0.46	1.15±1.37	32.02±2.92
1083	4.76±1.26	63.39±2.67	-0.05±0.06	1.29±1.34	30.61±1.99
1112	6.51±0.81	63.22±3.85	0.08±0.06	0.92±0.98	29.28±2.20

Table 3.4: Species concentration in our "mixed" molecular beam as a function of pyrolytic nozzle temperature, for the pyrolysis of the CF_3I using a stagnation pressure of 530mbar.

Another experiment to document the concentration of the CF_3 radicals as a function of the CF_3I stagnation pressure, for a given pyrolytic nozzle temperature, was undertaken. For this experiment the pyrolytic nozzle temperature was set at 817°C with the CF_3I stagnation pressure varied between 50 mbar – 600 mbar in 50 mbar

intervals. The laser-pulsed nozzle delay time for both gross and background data collection were set to be the same as in the previous experiment, that was designed to investigate species concentration as a function of nozzle temperature. Similarly, the number of ions and percentage concentration for each species were also calculated using the method detailed previously. The results from this investigation are shown both graphically (see figure 3.10) and in tabular form (see table 3.6).

From figure 3.10 and table 3.6 it can be seen that the percentage of CF_3 radicals present in the molecular beam, as a result of the 817°C pyrolysis of CF_3I, is largely invariant to the stagnation pressure of CF_3I. The stagnation pressure that produced the largest total number of detectable ions and the largest number of detectable CF_3 ions was 500 mbar, while the CF_3 concentration peaked at 600 mbar. It was thus decided to conduct the electron scattering experiments using a stagnation pressure of 530mbar and a pyrolytic nozzle temperature of 817°C, which was considered to be a suitable compromise between a molecular beam containing the largest possible percentage of CF_3 radicals and the overall density of the molecular beam.

The beam composition and related uncertainties for a 530 mbar CF_3I molecular beam pyrolysed at 817°C was now measured in the same manner as previously described. In an effort to reduce the uncertainties related to the beam composition, the measurement was conducted using the maximum number of laser shots (1000) and repeated six times. The results from these measurements appear in table 3.7. Using these results the weighted mean and associated uncertainty for each species

present in the "mixed" molecular beam was now determined; these concentrations are tabulated in table 3.7.

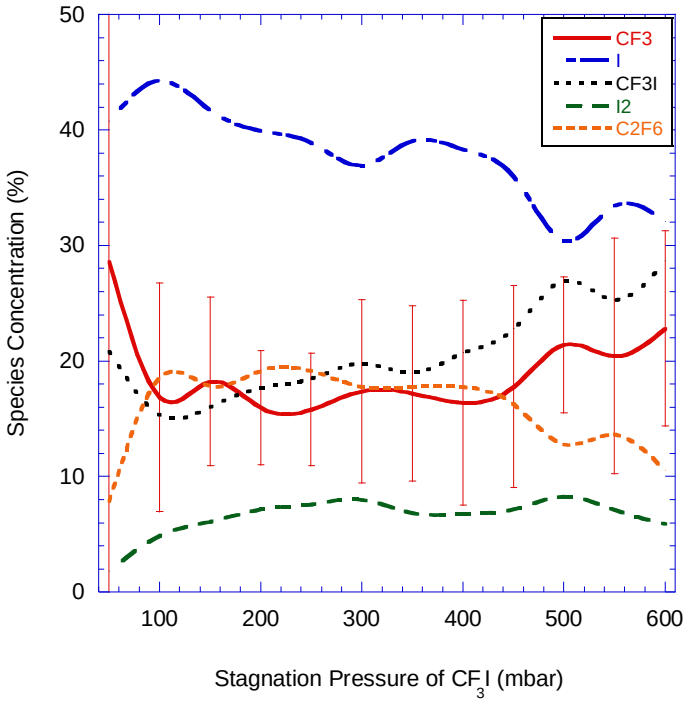

Figure 3.10: Species concentration as a function of CF_3I stagnation pressure, for a pyrolytic nozzle temperature of 817°C. Again we denote CF_3 (red ——————), I (blue - - —— - - ——), I_2 (green — —), CF_3I (black - - - - -) and C_2F_6 (orange ·····).

Stagnation pressure of CF_3I (mbar)	$\%CF_3$	%I	$\%CF_3I$	$\%I_2$	$\%C_2F_6$
50	28.61±33.91	40.76±5.26	20.88±4.10	1.84±1.57	7.91±113.89
100	16.87±9.88	44.30±5.29	15.35±2.53	4.88±0.95	18.60±56.21
150	18.23±7.30	41.72±1.92	16.05±1.72	6.12±0.93	17.87±50.66
200	15.96±4.96	39.96±1.42	17.71±1.16	7.18±0.54	19.18±49.40
250	15.82±4.88	38.91±2.63	18.49±2.62	7.62±1.20	19.17±47.40
300	17.40±7.94	36.96±3.30	19.83±4.07	8.01±1.85	17.79±46.61
350	17.23±7.58	39.08±1.76	19.01±1.51	6.88±0.65	17.81±45.17
400	16.39±8.88	38.35±2.71	20.71±2.30	6.78±1.09	17.76±46.13
450	17.77±8.72	35.98±2.89	22.79±2.31	7.18±1.17	16.28±47.62
500	21.41±5.87	30.46±2.39	27.01±2.93	8.30±1.09	12.82±43.70
550	20.44±10.18	33.45±1.06	25.32±5.74	7.14±1.99	13.65±46.25
600	22.82±8.44	32.08±0.82	28.67±3.87	5.90±1.41	10.53±47.79

Table 3.5: Species concentration as a function of CF_3I stagnation pressure, using a pyrolytic nozzle temperature of 817°C.

$\%CF_3$	%I	$\%CF_3I$	$\%I_2$	$\%C_2F_6$
19.56±4.69	31.08±3.81	27.69±5.49	7.96±1.97	13.72±3.40
24.55±3.15	29.35±1.86	27.53±2.53	8.09±1.03	10.49±1.95
24.23±3.62	29.07±2.06	27.45±2.87	8.41±1.21	10.84±2.27
26.82±4.97	30.98±2.75	23.31±3.61	8.41±1.56	10.48±2.93
24.34±4.03	31.10±3.31	23.41±3.49	8.89±1.79	12.26±3.01
24.85±3.43	31.62±3.55	22.69±3.85	8.73±1.96	12.11±2.87

Table 3.6: Repeated measurements of the species concentration of a mixed CF_3I beam, with a stagnation pressure of 530mbar and a pyrolytic nozzle at a temperature of 817°C.

Species	% Concentration
CF_3	24.19±1.56
I	30.03±1.06
CF_3I	25.68±1.36
I_2	8.34±0.59
C_2F_6	11.32±1.06

Table 3.7: The weighted mean of the percentage concentration of each species present in a "mixed" CF_3I gas jet formed using a stagnation pressure of 530mbar and undergoing pyrolysis at 817°C.

3.4 Determining the e + CF_3 elastic DCSs

3.4.1 Extracting CF_3 DCSs from the Measured Multi-component DCSs

"Mixed" molecular beams containing CF_3 were produced via the 817°C pyrolysis of CF_3I, as discussed previously in section 3.3.2. The composition of these multi-component molecular beams was then determined by time of flight mass spectroscopy, again see section 3.2.2 and specifically table 3.8, for the measured composition.

The DCSs for electron impact energies ranging from 5eV-50eV were then measured using the "mixed" molecular gas jets as the target beam, as detailed in section

3.2.2; after which the normalisation procedure, detailed in section 3.1.2, was applied to set an absolute scale to those measurements.

The "mixed" DCSs (σ_{mix}) were assumed to be the sum of each of the constituent species' DCSs, weighted by their respective fractional composition (x). This relationship is expressed below as equation 3.37:

$$\sigma_{mix} = x_{CF_3I}\,\sigma_{CF_3I} + x_{CF_3}\,\sigma_{CF_3} + x_I\,\sigma_I + x_{I_2}\,\sigma_{I_2} + x_{C_2F_6}\,\sigma_{C_2F_6}. \qquad (3.37)$$

Equation 3.37 was now simply rearranged to determine the CF_3 (σ_{CF_3}) DCS as shown in equation 3.38 below:

$$\sigma_{CF_3} = \frac{\sigma_{mix} - x_{CF_3I}\,\sigma_{CF_3I} - x_I\,\sigma_I - x_{I_2}\,\sigma_{I_2} - x_{C_2F_6}\,\sigma_{C_2F_6}}{x_{CF_3}}. \qquad (3.38)$$

Hence to determine the cross sections of the CF_3 radical we must know the remaining DCSs for each of the other species in equation 3.38. Finally, note that it is also implicit in equation 3.38 that to derive the CF_3 cross section we are performing a "difference-type" experiment. These types of experiments are always inherently difficult and are usually associated with quite large experimental uncertainties.

3.4.2 The Elastic DCSs (CF_3I, C_2F_6, I and I_2) used to determine the e + CF_3 DCSs from the measured multi-component DCSs.

This section details the elastic DCSs that were attributed to CF_3I, I, I_2 and C_2F_6 as a part of the process in determining the e + CF_3 elastic DCS from the measured multi-component molecular beam. We note that the values for each of these species DCS changed as the energy of incident electron changed as the scattering angle changed.

The contribution to the mixed-beam cross section made by CF_3I was subtracted using the measured fractional composition (25.68%), multiplied by the experimentally measured CF_3I electron impact differential cross section of Cho *et al.*[36]. This is true for each energy and scattering angle. Note that later, in section 4.2.1, a detailed comparison between our measured e + CF_3I scattering cross sections and those of Cho *et al.* will be made. The decision to use Cho *et al.*'s cross sections, rather than those measured by our present apparatus[67], was made as both data sets were largely consistent with each other but Cho *et al.*'s were reported with a smaller uncertainty (8% as opposed to ∼30%). At one electron impact energy (10eV) our data set does somewhat diverge from that of Cho *et al.*, the influence of this on the elastic DCS for CF_3 is discussed later in section 4.4.1.

Where specific electron impact energies were not provided (e.g. 25 eV), the DCSs were interpolated by averaging the angular data of adjacent electron impact energies (e.g. 20eV and 30eV). This method rests on the assumption that the particular species has no sharp features in it's DCS, such as might be caused by the decay of a shape resonance, over the electron impact energy range of the interpolation. To the best of our knowledge this was the case for all the interpolations that were made throughout the course of the current work. Where cross section data for specific angles (e.g. 75°) at a given energy were not available, the adjacent angles were averaged. As the molecular species on which this technique were employed were all measured using 10° intervals, that revealed only smooth distributions, this angle averaging procedure was considered to be a valid approach.

The elastic cross sections used to account for the electron scattering due to the C_2F_6 component of the mixed beam, were those of Takagi *et al.*[70]. We note that this set was recommended by M. Hoshino *et al.*[14] in their 2008 report for the National Institute for Fusion Science in Japan. These C_2F_6 electron impact DCSs were measured using a conventional crossed beam apparatus at Sophia University in Japan, covering an angular range of 10° - 130° and an electron impact energy range of 2eV-100eV. Further note that they reported overall uncertainties on their measured DCSs of 20%[70].

With the exception of our recently measured atomic iodine electron impact elastic DCS at 50eV[133], there are currently no electron impact elastic differential cross section measurements available for either molecular iodine or atomic iodine. This is due partly to the difficulty of working with iodine in a laboratory setting. For example it is not only a solid, it can also harmfully interact with the various types of hydrocarbon based oils that are commonly used to charge the backing pumps of high vacuum systems. This adds to the ongoing costs associated with the maintenance of these systems, and can also shorten the operating lifetime of the pumps in question. We were able to, at least in part, overcome the problems associated with working with iodine and iodine containing molecules by charging our backing pumps with Fomblin, a non-reactive oil (see section 2.1). However, even with a lower gas throughput than normally required by a conventional spectrometer set up, we still observed a powdery yellow coating on some of the surfaces inside our source chamber. This was a result of the use of CF_3I and the creation of both atomic and molecular iodine during the pyrolysis of CF_3I. Due to the

configuration of our chambers (see section 2.1), this contamination was prevented from spreading to the electron spectrometer, but this would not have been the case in a conventional crossed beam apparatus. Hence experimentalists have generally stayed away from studying these types of targets.

This lack of experimental scattering data, for electron impact on both atomic and molecular iodine, was tackled theoretically by both Bartschat and Zatsarinny[71] and by Blanco and García[72]. The elastic cross sections provided to us by these theorists have yet to be published, and so for the purpose of completeness they are included as appendix A and appendix B at the rear of this thesis. Each of these data sets contains elastic electron DCS data at 1° across an electron impact energy range of 5-50eV.

Bartschat and Zatsarinny[71] preformed a Dirac *B*-Spline R-Matrix (DBSR) calculation[134] to determine the e + I elastic scattering cross sections, an approach based on a close coupling expansion of the total (projectile + target) wave function. Inside the R-matrix sphere (that is centred on the iodine atom with a radius of $50a_0$) *B*-splines are used as the underlying and effectively complete basis set. The other defining feature of the DBSR method is its ability to describe the target using term dependent sets of one-electron orbitals, thus it was not necessary to impose any orthogonality conditions, which in turn reduced the number of terms necessary in the R-matrix expansion.

These authors include the atomic polarisability in their calculation by adding five pseudo-states that are coupled with the two ground physical states (J=3/2, 1/2) of iodine. By doing this they obtain polarisabilities of $35.2a_0^3$and $36.6a_0^3$ for each of the physical states. These polarisabilities are in excellent agreement with the structure-only calculations of Fleig and Sadlej [135], that predict $\alpha = 34.6a_0^3$ and $\alpha = 31.5a_0^3$. Encouraged by both the rigorous nature of the DBSR calculation, in conjunction with the accurate prediction of iodine's polarisability, this calculation was considered to be the most accurate representation of the true e + I elastic DCS. Hence the DBSR results were used for the subtraction of atomic iodine's contribution from the "mixed" DCSs.

In contrast to the complexity of the DBSR method, the Optical Model Potential method (OMP) used by Blanco and García[72], to determine the elastic e + I DCSs, is quite straightforward. Even though the elastic e + I DCSs of Bartschat and Zatsarinny are chosen over those of Blanco and García[72], to be used for the determination of the CF_3 cross sections from the measured "mixed" DCSs, the OMP calculations of Blanco and García[72] form the basis of their e + I_2 elastic DCSs, which are used in determining the CF_3 DCSs. Thus it is worth noting briefly how the OMP is formulated. The OMP method involves solving the partial wave equation with the real part of the local model potential taken as the combination of a static potential, an exchange potential (from Riley and Truhlar [136]) and a polarisation potential (from Zhang *et al.*[137]). Note that there is also the provision for a complex absorption potential to allow for the computation of inelastic processes, but it is not

used in this case. Relevant general references to this OMP approach can also be found in [138, 139].

Blanco and García[72] calculate electron-molecule scattering using their Independent Atom Model (IAM)[140], in which they compute the electron-atom scattering DCS (using the OMP method) for each atom contained within the molecule and then sum these results together. This is known as the additivity rule (AR). At low energies (<100 eV) molecular cross sections determined using the AR overestimate the true cross sections, due to the AR ignoring the mutual screening of the atomic cross sections by nearby atoms. These screening effects can be approximately corrected for down to electron impact energies of ~10eV[141], by using the so called screening corrected additivity rule (SCAR) [142, 143]. Thus the IAM-SCAR cross section is expressed below in equation 3.39[142, 143]:

$$\sigma_{molecule}^{elastic} = \sum_{i} s_i \ \sigma_i^{elastic}, \tag{3.39}$$

where $s_i, (0 < s_i, < 1)$, are the screening coefficients attributed to each atom and $\sigma_i^{elastic}$ represents the elastic DCS for each atom i. For information about the calculation of these screening terms see reference 142.. Note that this formulation can be further extended to account for polar molecules, but as this is not relevant to our work here we do not discuss this point any further.

As the Blanco and García[72] IAM-SCAR calculations for their e + I_2 elastic DCSs (see appendix B) are dependent on their OMP calculations for the e + I elastic DCSs, a brief comparison between their e + I elastic DCSs and those of the computationally

more rigorous e + I elastic DCSs of Bartschat and Zatsarinny will now be made. Note that the e + I elastic DCSs from both theoretical groups are plotted in figure 3.11, for the electron impact energies of 5 eV, 10eV, 20eV, 30eV, 40eV and 50eV.

Generally, for the electron impact energies in the range of 30eV-50eV, the atomic iodine elastic DCSs from both theoretical groups are in reasonable accord. This is true in terms of both the overall magnitude of each of the DCSs and the predicted structure (see figure 3.12), with the exception of the depths of some of the minima in the angular distributions.

Qualitatively, all the iodine cross sections have large forward angle peaks (most probably as a result of iodine's substantial polarisability), three minima occurring at ∼45°, ∼100° and ∼135°, and moderate secondary backward angle peaks. The main difference between the cross sections from each of the theoretical groups is in the exact location and depth of the predicted minima. This was initially of some moderate concern, given that these minima all occur either at, or very near, angles where we have measured mixed-beam DCSs. However, considering that the SCAR correction used by Blanco and García has the effect of smoothing out the minima predicted in their e + I DCSs for their e + I_2 DCSs, coupled with the relatively small percentage of I_2 present in the mixed molecular beam (8.34%), the calculated IAM-SCAR I_2 cross sections are still in fact expected to be accurate enough for most of our purposes in that 30-50eV range.

The agreement in terms of the shape of the elastic iodine cross sections, from both groups, at an electron impact energy of 20eV, is arguably the worst agreement seen (see figure 3.11) for the entire set of theoretical DCSs; with differences occurring for both the position and depths of the minima.

However, while these differences clearly result in quite different angular characteristics at this energy, it is fortunate to note that the agreement at most of the angles where we have our CEMs mounted is nonetheless fair. Thus for our purposes we anticipate few problems at 20eV with the derivation of our CF_3 cross section caused by the use of the IAM-SCAR e+ I_2 DCSs.

Lastly, it is interesting to note the level of agreement shown between the two e + I elastic DCSs for electron impact energies of 5eV and 10eV (see figure 3.11), with the only real differences being the depth of the predicted minima. This gives us some hope that the molecular IAM-SCAR calculations below about 10eV, where the threshold for the validity for the SCAR correction is generally held to be[142, 143], could still be valid. We revisit this point later in chapter 4.

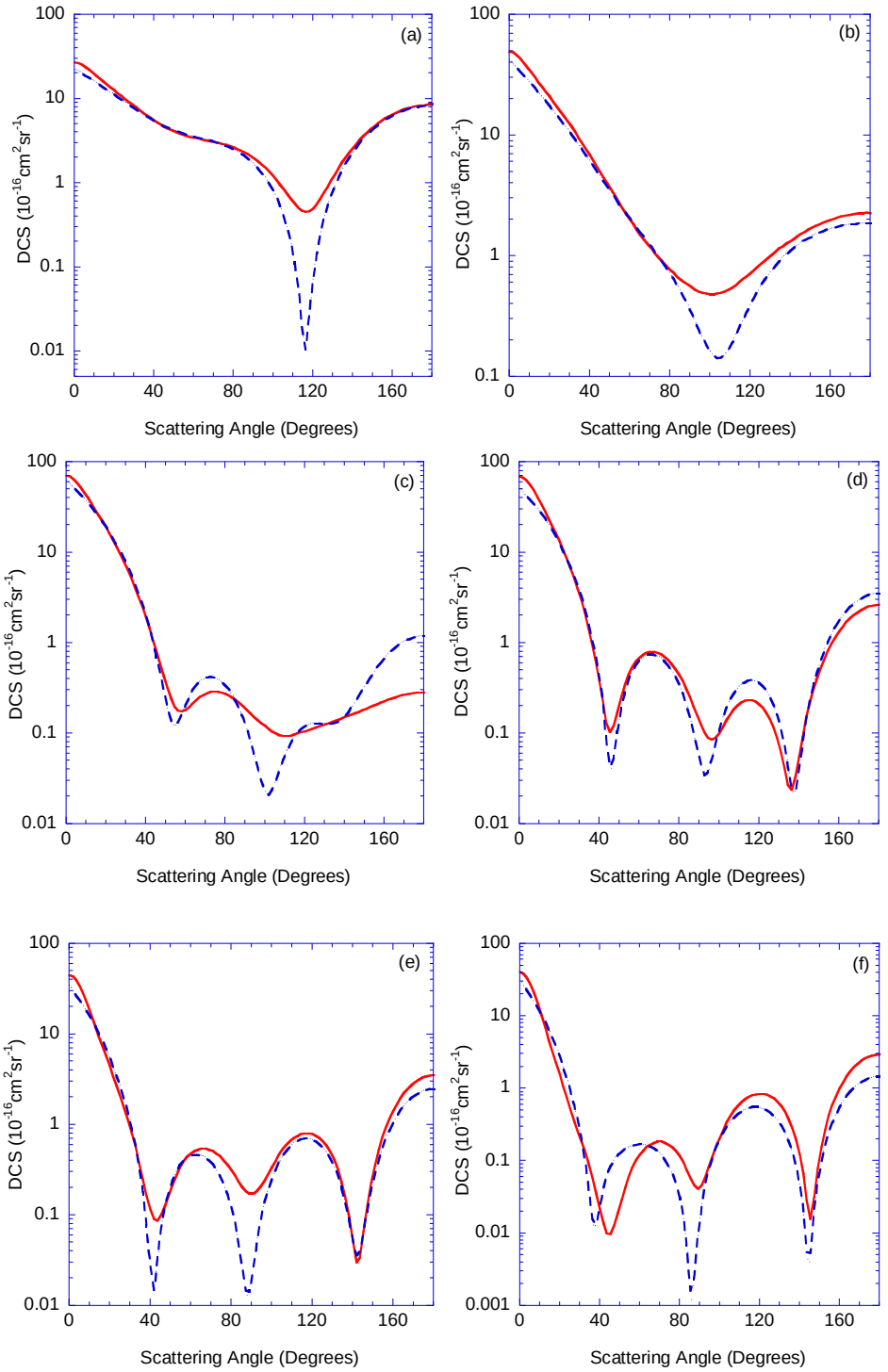

Figure 3.11: The Bartschat and Zatsarinny[144] DSBR elastic DCS (red ———) for e + I scattering are compared with those of Blanco and García[72] (blue – – –) as calculated using the OMP. The electron impact energies are: a=5 eV, b=10 eV, c=20eV, d=30 eV, e=40 eV and f=50 eV.

3.4 Summary of the uncertainties in the measured differential cross sections

The uncertainties described throughout this chapter are now summarised in table 3.9. Ultimately, they were added together in quadrature in order to determine the overall uncertainties on the measured differential cross sections for CF_2 and CF_3I.

Table 3.8: Summary of the uncertainties used in the calculation of the overall uncertainty on the present measured differential cross sections.

Term	Notation	Percentage Uncertainty
Terminal Speed ratio	S_∞	10%
Pressure rise	Δp	~1%
Effective pumping speed	S_{eff}	~2%
Ionisation cross section at 150eV	Q^{ion}_{150eV}	2-25%*
Statistical uncertainty in $\dot{N}_e$	$\Delta\dot{N}_e$	5-10%
Elastic DCS for CF_4	$DCS_0^R(\overline{E_0}, \theta)$	20%

*species dependent term, see table 3.2.

In the case of the mixed beam differential cross sections, the additional uncertainties related to the beam composition were also taken into consideration in order to determine the "pressure drop" and hence set an absolute scale.

Finally for the e + CF_3 elastic DCSs (as calculated from the mixed beam DCSs), the uncertainties taken into consideration were those related to the fractional beam composition as listed in table 3.8 and the uncertainties in the differential cross sections of C_2F_6(20%), I (1%), CF_3I (8%) and I_2(1%). Thus the absolute uncertainties

of the CF_3 (shown as a square for convenience) elastic DCSs were determined using equation 3.42, that is given below:

$$\Delta\sigma_{CF_3}{}^2 = \left(\frac{\partial(\sigma_{CF_3})}{\partial\sigma_{mix}}.\Delta\sigma_{mix}\right)^2 + \left(\frac{\partial(\sigma_{CF_3})}{\partial\sigma_{CF_3I}}.\Delta\sigma_{CF_3I}\right)^2 + \left(\frac{\partial(\sigma_{CF_3})}{\partial x_{CF_3I}}.\Delta x_{CF_3I}\right)^2$$
$$+\left(\frac{\partial(\sigma_{CF_3})}{\partial\sigma_I}.\Delta\sigma_I\right)^2 + \left(\frac{\partial(\sigma_{CF_3})}{\partial x_I}.\Delta x_I\right)^2 + \left(\frac{\partial(\sigma_{CF_3})}{\partial x_{I_2}}.\Delta x_{I_2}\right)^2$$
$$+\left(\frac{\partial(\sigma_{CF_3})}{\partial\sigma_{I_2}}.\Delta\sigma_{I_2}\right)^2 + \left(\frac{\partial(\sigma_{CF_3})}{\partial\sigma_{C_2F_6}}.\Delta\sigma_{C_2F_6}\right)^2 + \left(\frac{\partial(\sigma_{CF_3})}{\partial x_{C_2F_6}}.\Delta x_{C_2F_6}\right)^2$$
$$+\left(\frac{\partial(\sigma_{CF_3})}{\partial x_{I_2}}.\Delta x_{I_2}\right)^2 + \left(\frac{\partial(\sigma_{CF_3})}{\partial x_I}.\Delta x_I\right)^2 + \left(\frac{\partial(\sigma_{CF_3})}{\partial x_{CF_3}}.\Delta x_{CF_3}\right)^2 \quad (3.42)$$

Chapter 4 — Results

4.1 Differential and Integral Cross Sections for CF_2

4.1.1 Electron Impact Elastic Differential Cross Sections

The present apparatus (see chapter 2) has been used to measure elastic DCSs for the electron scattering from CF_2 (see chapter 3), for electron impact energies from 2-50eV. As discussed previously in section 3.3.1, the CF_2 radicals were produced by passing C_2F_4 through a silicon carbide tube heated to 1200°C.

To the best of our knowledge the experimental measurements presented here are unique for the CF_2 radical. These results have been outlined in three papers; the first published in 'The Journal of Measurement Science and Technology' (25eV)[54], the second published in 'Physical Review Letters' (30-50eV)[19] and the final paper published in 'Physical Review A' (2-20eV)[20]. The elastic DCSs for CF_2 over the electron impact energy range of 25-50eV have also been discussed in detail in the doctoral thesis of Hargreaves[65]. For this reason the discussion here will focus on the 2-20eV energy range. These cross sections are listed in table 4.2 and plotted in figures 4.1 – 4.7, where they are compared with all the presently available theoretical calculations. Namely, those calculations made by Winstead and McKoy [20, 74], Lee *et al.* [27, 145] and Rozum *et al.* [21].

Rozum *et al.* calculated the elastic DCSs of CF_2 using the UK polyatomic R-Matrix code. Their calculations were restricted to electron impact energies below 10eV due the range of electronic states included in the computations. Note that (in brief) the R-Matrix method involves splitting the coordinate space into two regions separated

by a sphere centred at the centre of mass of the molecule. The sphere's radius is set such that it completely encloses the electron charge cloud of the molecule, typically resulting in a radius of $10a_0$[21]. The interaction between the molecule and the incident electron is then treated differently in the inner and outer regions.

Inside the sphere the incident electron is considered to be in the same environment as the molecule's electron charge cloud. As the incident electron is indistinguishable from the molecular electrons, all electrons here are treated as an electron complex[21]. Furthermore, due to the proximity of the incident electron to the molecule, it is necessary to consider the full multi-centred interaction between the electron complex and the system including electron correlation and electron-electron exchange. These particular interactions are modelled using various quantum chemistry methods[21]. Rozum *et al.* describe the system wave function(Ψ_k^{N+1}) in the inner region, for a molecule with N associated electrons, as shown below in equation 4.1[21]:

$$\Psi_k^{N+1} = A \sum_I \Psi_I^N (x_1, \dots, x_N) \sum_j \xi_j(x_{N+1}) a_{Ijk} + \sum_m \chi_m (x_1, \dots, x_N, x_{N+1}) b_{mk}. \tag{4.1}$$

Here A is the anti-symmetrization operator allowing for exchange to take place, x_N is the spatial and spin coordinate of the N^{th} electron, ξ_j is a continuum orbital spin coupled with the scattering electron, and a_{Ijk} and b_{mk} are variational coefficients. The first summation runs over all the configuration interaction (CI) target states and gives rise to terms known as 'target + continuum' configurations. The second

summation runs over the configurations χ_m, where all electrons are placed in the target molecular orbitals.

The description of the system wave function in the outer region is somewhat simpler, as the incident electron and the electrons associated with the molecule are considered far enough apart to be treated separately. Thus in this case electron correlation and exchange effects are considered negligible[59, 146]. In this region, however, the long range effects of the dipole moment and polarisability of the molecule become important[7].

Rozum *et al.* utilised the 6-311G* Gaussian basis set for their CF_2 calculations, as they reported that it gave "a satisfactory compromise between the singlet–triplet energy gap and dipole moment"[25]. They also considered smaller basis sets including the double zeta plus polarisation (DZP), 6-31G, 6-311G and triple zeta (TZ). However they all gave a poorer representation of the target's properties, particularly for the ground state dipole moment.

Complete active space configuration interaction (CASCI) wave functions were additionally used by Rozum *et al.,* with the molecular orbitals represented by state-averaged pseudo-natural orbitals obtained from all single and double configuration interaction calculations for all target stages[25]. By doing this Rozum *et al.* were able to satisfactorily represent the intrinsic molecular properties of CF_2, including calculating a ground state dipole moment for the radical of 0.448D[25]. This agrees

well with both the value 0.44D[75] calculated by Russo *et al.,* and the experimental value of 0.469 ± 0.026D of Kirchhoff and Lide[77].

Both Winstead and McKoy and Lee *et al.* used variations of the Schwinger variational method[147], in order to calculate elastic differential cross sections for the CF_2 radical. Lee *et al.* solved the Lippmann-Schwinger equation using an iterative procedure called the Iterative Schwinger Variational Method (ISVM) within a distorted wave (DW) approximation [27, 148]. Lee *et al.*'s calculation considered static, exchange and polarisation effects. On the other hand Winstead and McKoy calculated two sets of CF_2 elastic differential cross sections using the Schwinger Multichannel method (SMC), one set using the static and exchange approximations (SE) and the other set using the static, exchange and polarisation approximations (SEP)[19, 20].

The most significant difference between the methods of Winstead and McKoy and Lee *et al.* lies in the description of the scattering potential, in particular the description of the potential due to polarisation. Lee *et al.* used an optical potential, the real part of which comprises the static and exchange contributions obtained exactly from a Hartree-Fock self consistent-field (HF–SCF) target wave function[27] and a correlation-polarisation approximation determined using a parameter free model potential from Padial and Norcross[149]. While Lee *et al.* have the provision for including the absorption potential (as the imaginary part of a complex optical potential) it was not used in this case. This was because the calculated magnitude of this absorption potential was much less than its real counterpart[27]. Furthermore,

Lee *et al.* used a first-Born-approximation (FBA) to account for CF_2's long range dipole interaction potential[27].

The SMC-SEP calculation of Winstead and McKoy took into account exchange and polarisation effects in their description of the interaction potential V, but did not include the permanent dipole moment of CF_2 or a correction for dipolar scattering[20].

A detailed description of the formulation of the SMC method can be found in references [150, 151]. Briefly the SMC method defines the scattering amplitude $\left[f_{\vec{k}_i,\vec{k}_f}\right]$ as shown below in equation 4.2, while the notation in this equation is defined in table 4.1[18].

$$\left[f_{\vec{k}_i,\vec{k}_f}\right] = -\frac{1}{2\pi}\sum_{m,n}\left\langle S_{\vec{k}_f}\middle|V\middle|\chi_m\right\rangle (d^{-1})_{mn}\left\langle\chi_n\middle|V\middle|S_{\vec{k}_i}\right\rangle, \tag{4.2}$$

where:

$$d_{mn} = \langle\chi_m|A^{(+)}|\chi_n\rangle \tag{4.3}$$

and

$$A^{(+)} = \frac{\hat{H}}{N+1} - \frac{\left(\hat{H}P + P\hat{H}\right)}{2} + \frac{(VP+PV)}{2} - VG_P^{(+)}V. \tag{4.4}$$

Table 4.1: Details of the notation used in equations 4.2-4.4.
See reference [18] for more details.

$\lvert S_{\vec{k}_{i,f}}\rangle$	Is the solution of the unperturbed Hamiltonian H_0, and is the product of a target state and a plane wave.
V	Is the interaction potential between the incident electron and the electrons and nuclei of the target molecule.
$\lvert\chi_m\rangle$	Is a set of $(N+1)$- electron Slater determinants used in the expansion of the trial wave function.
$\hat{H}$	Is the total energy E, minus the full Hamiltonian of the system ($\hat{H} = E - H$), where $H = H_0 + V$.
P	Is the projection operator onto the open channel space target eigen function.
$G_P^{(+)}$	Is the free Green function projected onto the P space.

Figures 4.1, 4.2 and 4.3 present the measured elastic electron DCSs for scattering from CF_2, for 20eV, 18eV, 16eV, 15eV, 14eV and 12eV, along with the available SMC-SE[20, 74], SMC-SEP[74] and ISVM+DW[27, 145] results where applicable. In general it is clear from these CF_2 DCSs that they are all strongly peaked at the more forward scattering angles (below 50°). As discussed in more detail later, we believe this observation can be explained by the permanent dipole moment that CF_2 possesses and the significant magnitude of its dipole polarisability. These CF_2 elastic DCSs from 12-20eV also feature a broad shallow "dip" in their angular distributions from $\sim 40° - 120°$, followed by a moderately increasing (in magnitude) DCS as you go to more backward scattering angles.

At 20eV the CF_2 theoretical DCSs all reproduce the general qualitative behaviour of the measurements, with the shape agreement between the SMC-SE[74] being almost perfect (see figure 4.1). However, even taking into consideration the experimental uncertainties, all the theories (SMC-SEP[74], SMC-SE[74] and ISVM+DW[27]) over estimate the cross section magnitude by almost a factor of two. Considering the ICS (see section 4.1.2) we observe that all the theories predict the existence of a shape resonance at around this energy, which is not experimentally found. This, at least in part, may explain this disagreement. As the electron impact energy decreases to 16eV (see figure 4.2), the agreement between both the magnitude and shape for the measured CF_2 elastic DCS and the SMC-SE[20] theory is now found to be very good. This indicates that the scattering description offered by this theory at that energy is physical. A similar level of accord (not quite as impressive) is also found at 15eV and 14 eV (see figure 4.3).

For incident electron energies of 14 and 15 eV, we note that there is an unexpected omission in the measured DCS at scattering angles between 40° and 75°. The absence of these data points was not caused by any lack of CF_2 elastic signal, rather these angles coincided with a deep minimum in the CF_4 elastic DCS[123], resulting in a lack of CF_4 elastic signal. Nonetheless, the absence of this data does mean that a more comprehensive description of the level of agreement between theory and experiments at these energies is just not possible.

As the incident electron energy further decreases to 12 eV (see figure 4.3), the agreement between Lee *et al.*'s ISVM+DW and Winstead and McKoy's SMC-SE is almost exact over the angular range of 20°- 80°. Indeed both these calculations also agree well with the shape and magnitude of the measured DCS over this angular range. However, these theories (SMC-SE, SMC-SEP, ISVM+DW) do somewhat over estimate the measured DCSs at the more backward (>100°) angles.

In general the SMC calculation at the SE-level does well in consistently reproducing the shape of the CF_2 elastic DCSs over the energy range of 12-20eV, which is also consistent with the agreement found previously for the 25-50eV impact energy range[19, 54, 65]. Given the complexity of both the experimental measurements and the computations the agreement between the magnitude of the measured and calculated cross sections is also considered to be fairly good over this 20-12eV energy range.

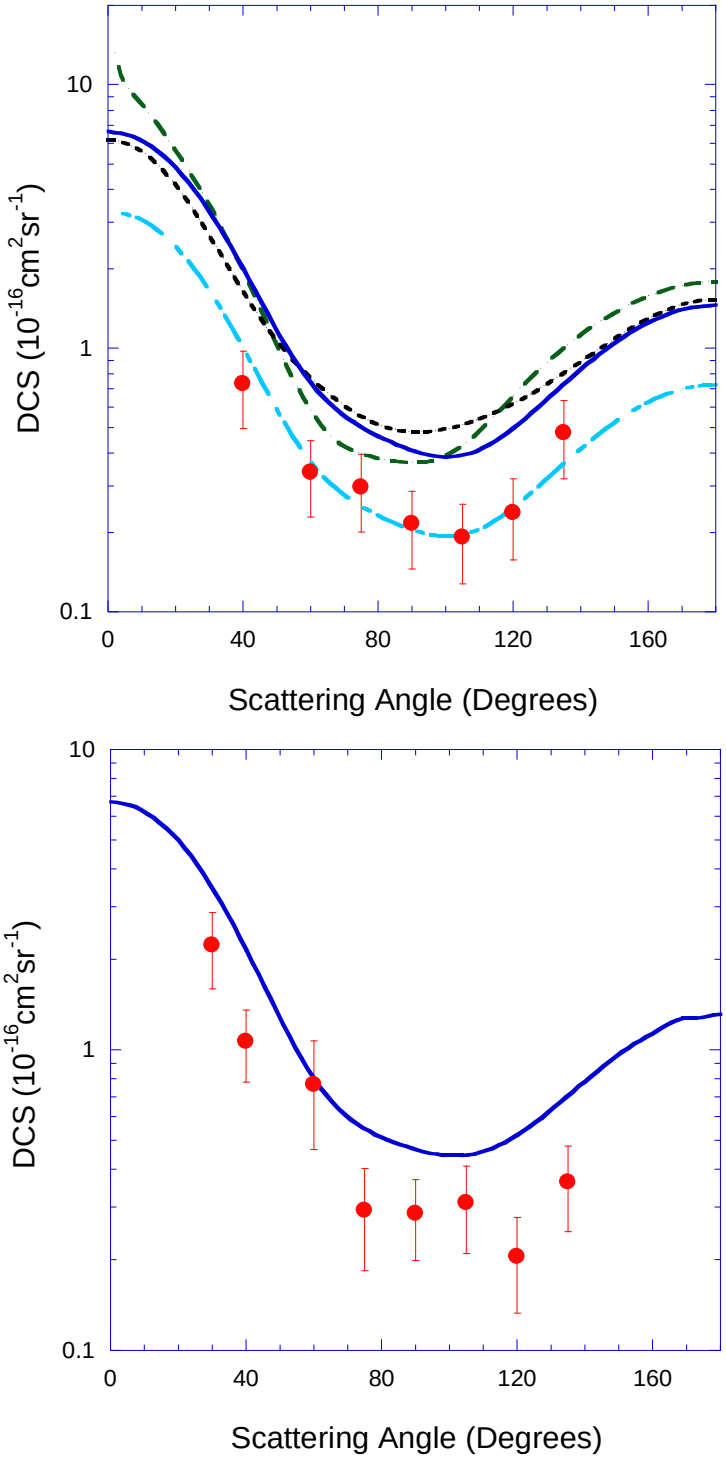

Figure 4.1: Absolute Differential Cross Sections (10^{-16}cm^{2}sr^{-1}) for elastic electron scattering from the CF_2 radical at 20eV (top) and 18eV (bottom). Present data (red ●) are compared against SEP[74] (black - - - - - - -)and SE[74] (blue ———) level calculations along with 0.5* SE[74] (light blue - — - — - —) and the ISVM + DW [145](green — — — —) calculation.

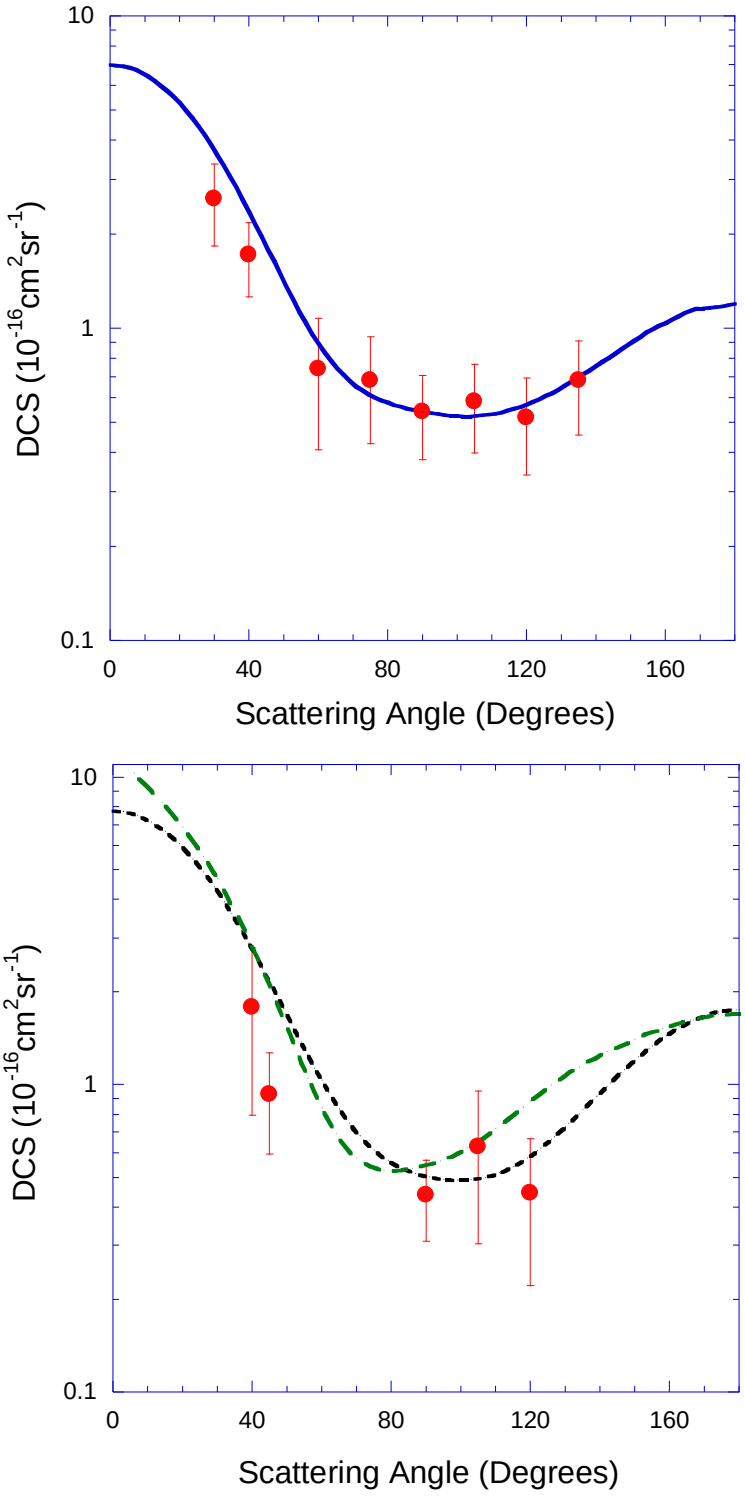

Figure 4.2: Absolute Differential Cross Sections (10^{-16}cm^{2}sr^{-1}) for elastic electron scattering from the CF_2 radical at 16eV (top) and 15eV (bottom). Present data (red ●) are compared against SEP[74] (black – – – – – –) and SE[20, 74] (blue ——) level calculations and the ISVM + DW [145] (green — — — —) calculation.

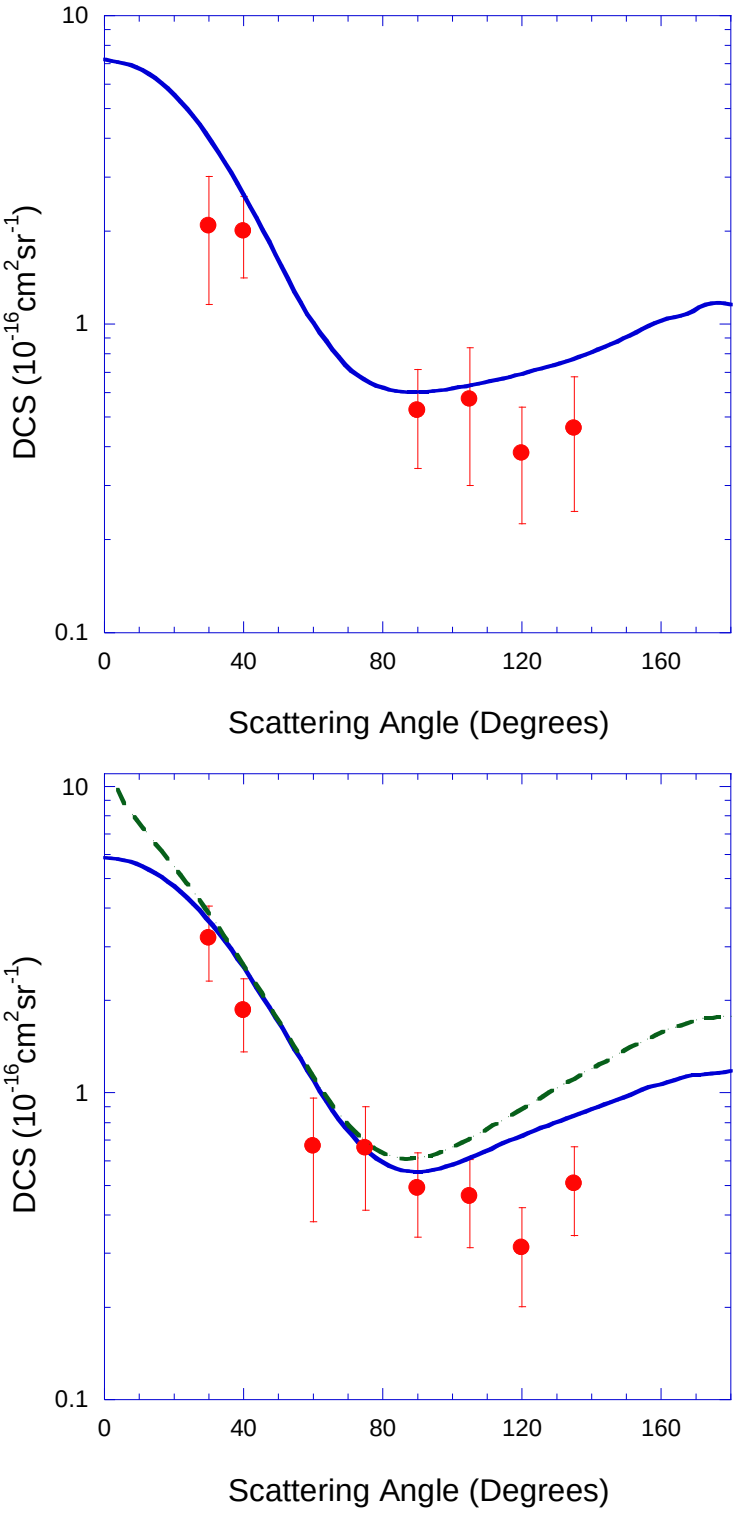

Figure 4.3: Absolute Differential Cross Sections (10^{-16}cm^{2}sr^{-1}) for elastic electron scattering from the CF_2 radical at 14eV (top) and 12eV (bottom). Present data (red ●) are compared against SE [20, 74] (blue ——) level calculations and the ISVM + DW [20, 145] (green – – –) calculation.

In the 2eV-10eV (see figures see figures 4.4-4.7) energy regime it is unfortunate that the angular range of the measured cross sections is somewhat limited, with the most forward scattered electron angle in most cases being 40°. This angular restriction was caused by the more forward detectors (15°, 20° and 30°) saturating when collecting either or both the CF_2 and CF_4 elastic signal. This saturation was due to a combination of the relatively uncollimated nature of our CF_2 gas jet and the field of view of the RPA detectors[20]. As discussed in section 2.4.2.1, an attempt was made to decrease the angular acceptance of these detectors by introducing much smaller apertures throughout the RPA lenses. However, this was only partially successful. Further collimation of our molecular beam was also considered, but was not pursued due to our concern that we would consequently "lose signal" at the larger scattering angles where the cross sections are much smaller. This lack of measured data below 40° precludes a definitive conclusion as to which of the theories does the best job in describing the CF_2 cross section over this energy and angular range. In particular we are unable to comment on the accuracy of the theoretical dipole corrections, which only become significant at scattering angles below about 15°. Notwithstanding this, the general shape and magnitude of the experimental data is apparently best described by the SMC-SEP[20, 74] calculation from 2-10eV.

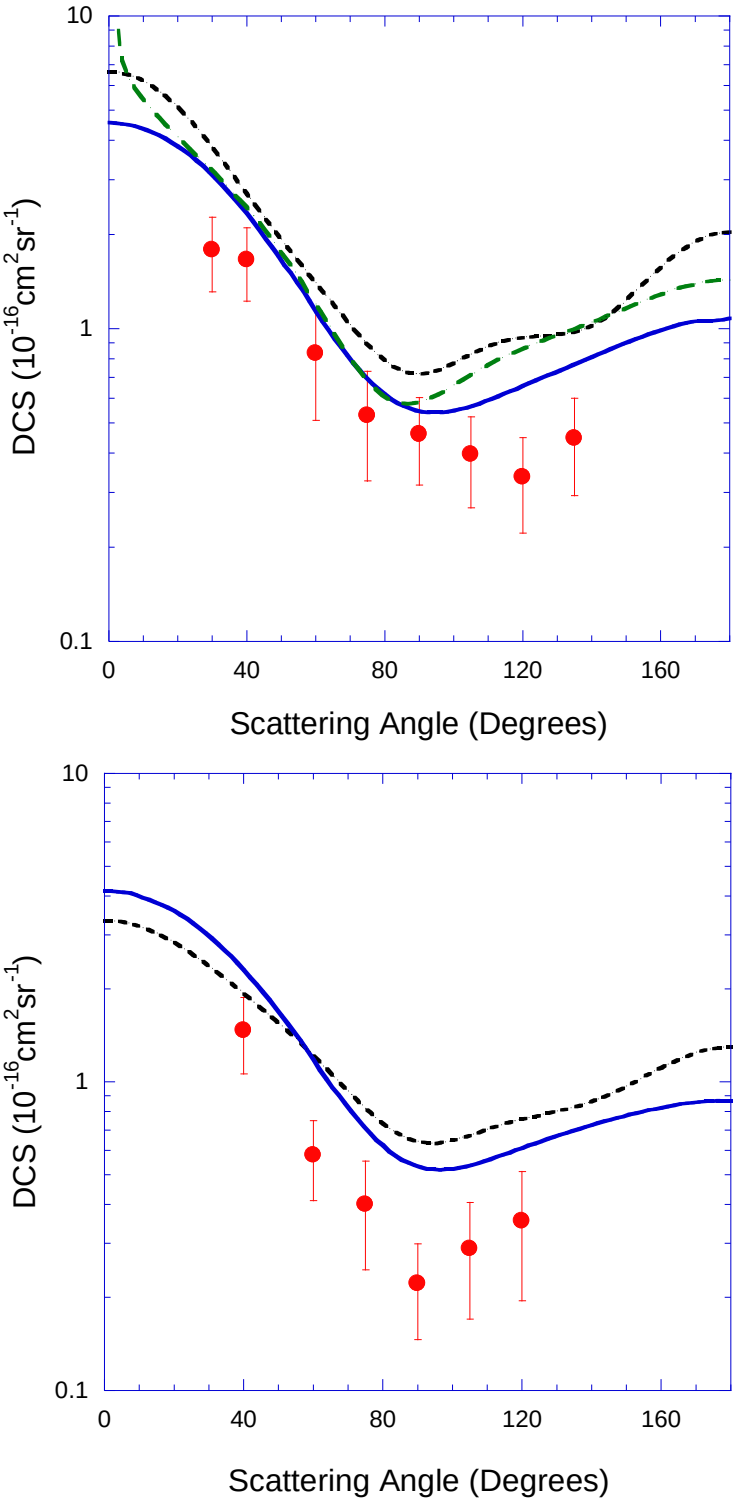

Figure 4.4: Absolute Differential Cross Sections (10^{-16}cm^{2}sr^{-1}) for elastic electron scattering from the CF_2 radical at 10eV (top) and 8eV (bottom). Present data (red ●) are compared against SE [74] (blue ——) and SEP [74] (black - - - - - -) level calculations and the ISVM + DW [27] (green — — — —) calculation.

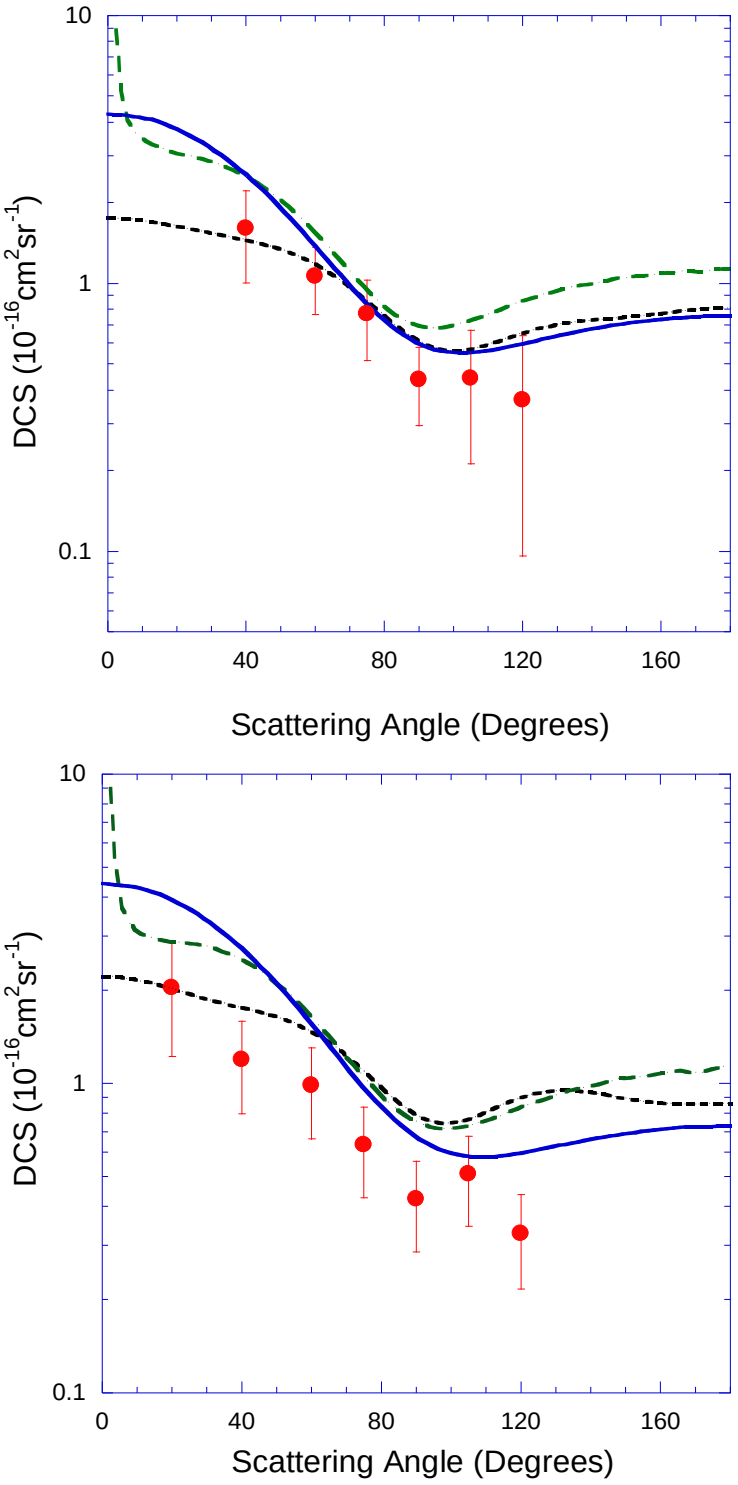

Figure 4.5 Absolute Differential Cross Sections (10^{-16}cm^{2}sr^{-1}) for elastic electron scattering from the CF_2 radical at 6eV (TOP) and 5eV (bottom). Present data (red ●) are compared against SE[20, 74] (blue ——) and SEP[20, 74] (black - - - - - -) level calculations and the ISVM + DW [20, 27] (green — — —) calculations.

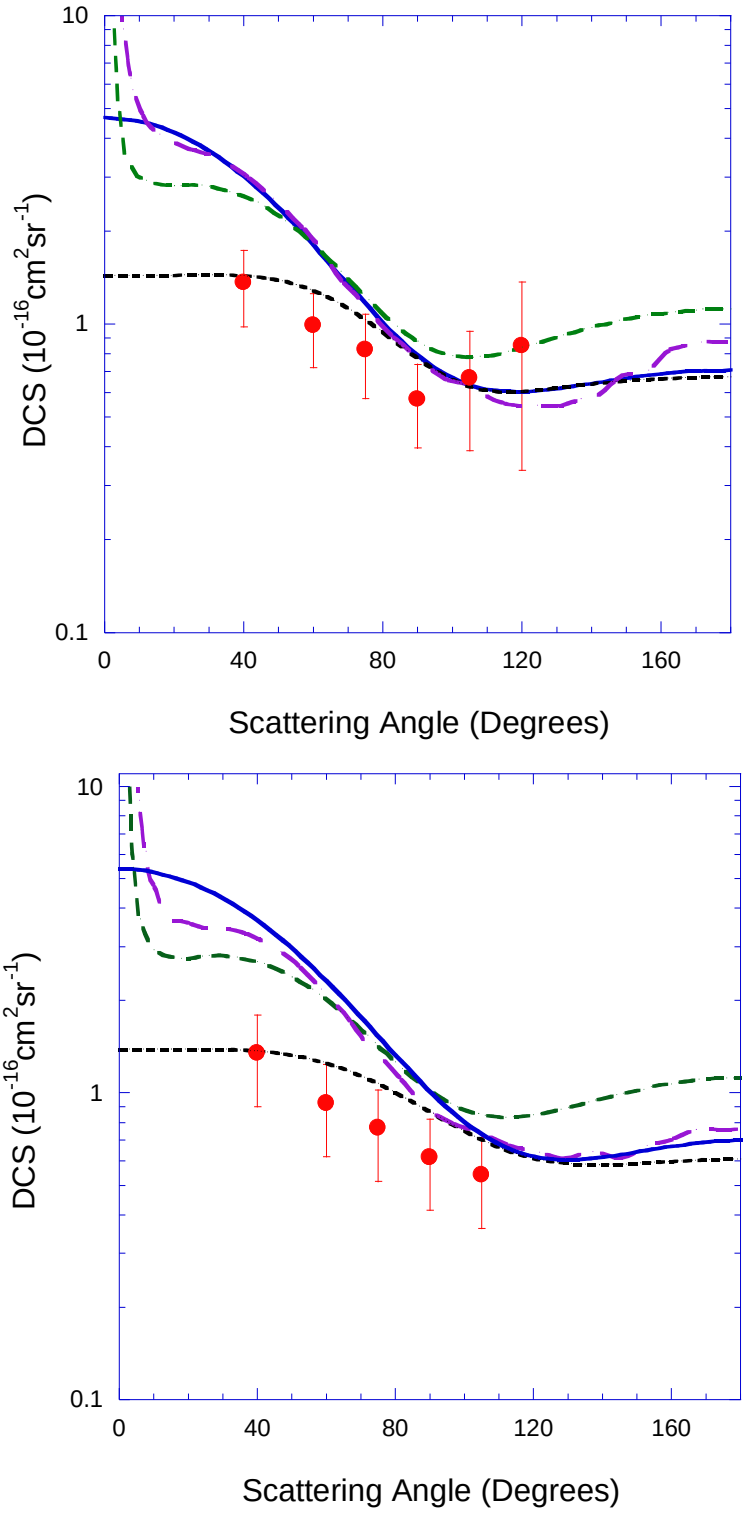

Figure 4.6: Absolute Differential Cross Sections (10^{-16}cm^{2}sr^{-1}) for elastic electron scattering from the CF_2 radical at 4eV (TOP) and 3eV (bottom). Present data [20] (red ●) are compared against SE [20] (blue ——) and SEP [20] (black - - - - - -) level calculations, ISVM + DW [20, 145] (green — — —) and the R-matrix [20, 21] (purple —— ——) calculations.

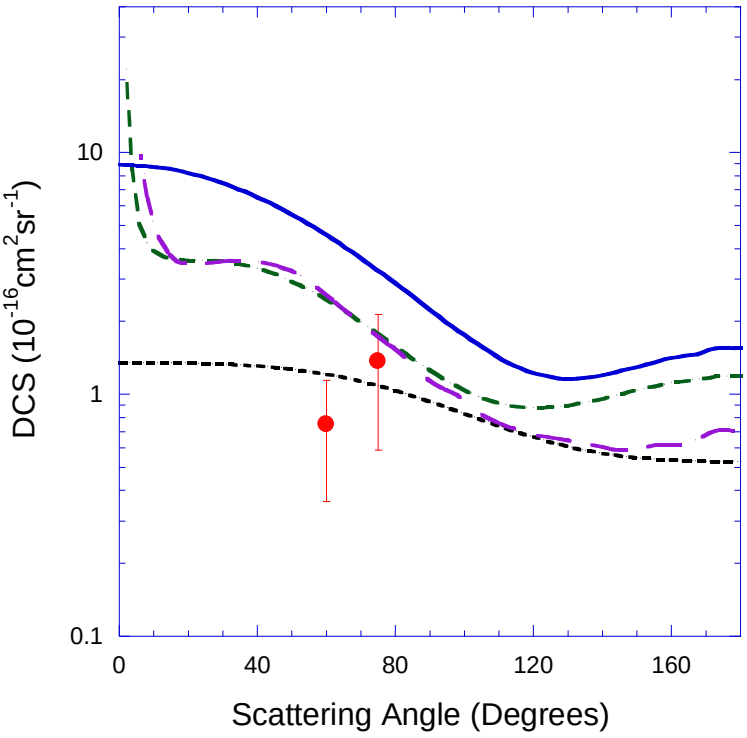

Figure 4.7: Absolute Differential Cross Sections (10^{-16}cm^{2}sr^{-1}) for elastic electron scattering from the CF_2 radical at 2eV The present data [20] (red ●) are compared against SEP[20] (black - - - - - - -)and SE [20] (blue ——) level calculations along with R-Matrix [21] (purple — — — —) and the ISVM + DW [27, 145] (green — — — —) calculations.

At the lower incident electron energies, the differences in the various theories does become more obvious as the scattering events become dominated by long range interactions, and so the description of the permanent dipole moment and in particular the polarisability becomes increasingly important[18]. Note again, as previously stated in section 1.5.1, that, while predicted to play an important role in the scattering dynamics, the dipole polarisability of CF_2 is not a well understood quantity. Nonetheless its importance is precisely what we observe in figures 4.5-4.7, where only the SMC-SEP calculation, which incorporates a very accurate model for the polarisation, can successfully reproduce the middle angle differential cross sections.

Energy (eV)	Scattering Angle									
	20°	30°	40°	45°	60°	75°	90°	105°	120°	135°
2	-	-	-	-	0.28 ±0.27	0.14±0.17	-	-	-	-
3	-	-	1.35±0.45	-	0.93±0.31	0.77±0.25	0.62±0.2	0.54±0.18	-	-
4	-	-	1.26±0.41	-	1.12±0.37	0.8±0.26	0.46±0.15	0.58±0.19	0.88±0.29	-
5	2.04±0.81	-	1.19±0.39	-	0.98±0.32	0.63±0.21	0.42±0.14	0.51±0.17	0.33±0.11	-
6	-	-	1.56±0.41	-	1.03±0.22	0.75±0.16	0.42±0.08	0.43±0.09	0.36±0.11	-
8	-	-	1.47±0.41	-	0.58±0.17	0.4±0.15	0.22±0.08	0.29±0.12	0.35±0.16	-
10	-	1.79±0.48	1.66±0.44	-	0.84±0.33	0.53±0.2	0.46±0.14	0.4±0.13	0.34±0.11	0.45±0.15
12	-	3.19±0.88	1.86±0.5	-	0.67±0.29	0.66±0.24	0.49±0.15	0.46±0.15	0.31±0.11	0.51±0.16
14	-	2.08±0.92	2.00±0.59	-	-	-	0.53±0.19	0.57±0.27	0.38 ±0.16	0.46±0.21
15	-	-	1.79±0.99	0.93±0.34	-	-	0.43±0.13	0.63±0.32	0.44±0.22	-
16	-	2.59±0.76	1.72±0.46	-	0.74±0.33	0.68 ±0.26	0.54±0.16	0.58±0.19	0.52±0.18	0.68±0.23
18	-	-	1.07±0.29	-	0.77±0.30	0.29±0.11	0.29±0.09	0.31±0.1	0.21±0.07	0.36±0.12
20	-	-	0.73±0.24	-	0.34±0.11	0.30±0.10	0.22±0.07	0.19±0.06	0.24±0.08	0.48±0.16

Table 4.2: Experimental elastic differential cross sections of CF_2 for electron impact energies from 2-20eV, in units of $10^{-16}cm^2sr^{-1}$. Note this table is reproduced from Francis-Staite *et. al.* [20].

4.1.2 Electron Impact Elastic Integral Cross Sections

The corresponding elastic ICSs for electron scattering from CF_2 were obtained by extrapolating the present measured DCS, at each energy, to 0° and 180° using a molecular phase shift analysis (MPSA)[73] procedure followed by the standard integration. These ICSs are shown in table 4.3 and plotted in figure 4.8, alongside all the other available theoretical electron impact elastic CF_2 ICSs. Namely the SMC-SE[19] and SMC-SEP[19] level calculations of Winstead and McKoy, the R-matrix calculation of Rozum *et al.*[25] and the ISVM+DW calculation of Lee et al[27]. Note that this comparison between the measured ICSs and the available theoretical calculations orignially appeared in our Physical Review A publication in 2009[20]. Some of the CF_2 ICSs as measured by the present apparatus, also appeared in a Physical Review Letter in 2008[19], with an electron impact energy range of 30-50eV, and in the doctoral thesis of Hargreaves[65] with an energy range of 25-50eV. Therefore the majority of the discussion of the ICSs for this section will focus on the energy range 3-20eV, although for the purpose of completeness the measured ICSs from 25-50eV also appear in both figure 4.8 and table 4.3.

The present measured ICSs have a quoted uncertainty of 45%. This conservative estimate of the uncertainty on that data takes into account the uncertainty on each measured DCS, and the errors associated with the extrapolation of the forward angles to 0° and the backward angles to 180°. We note that all the MPSA extrapolations showed a strong resemblance to the calculated SMC-SE [74] DCSs at energies above 10eV, and the SMC-SEP [74] DCSs at energies below 10eV. This fact

gave us some confidence in the validity of those extrapolations and thus in the ICS data reported here.

From figure 4.8 it can be seen that theoretical cross sections obtained using the R-matrix method[25], the ISVM+DW[27] and the SMC in the SE [19] approximation all predict a significant resonance enhancement, due to the temporary capture of the incident electron, at low (∼0.9-2.2eV) electron impact energies. The SMC calculation in the SEP[20] approximation also predicts a strong low energy resonance occurring at less than 0.1eV, however this resonance is not shown in figure 4.8. The R-matrix calculations of Rozum *et al.* [25] places this low energy resonance at 0.95 eV, with a width of 0.18eV, and identifies it as a $^2B_1$ symmetry resonance arising from the scattering electron temporarily occupying a $3b_1$ orbital[25]. Lee *et al.*'s [27] ISVM+DW calculation also identifies this as a $^2B_1$ resonance, but being somewhat broader (∼0.3eV) and placed it at a slightly higher energy (∼1.6 eV) then the R-matrix result. Finally, the SMC-SE[19] calculation places this same resonance at a higher energy again (∼2.2 eV). Unfortunately, due to limitations in the performance of the current monochromator, we could not produce experimental ICSs that might have been used to clarify these theory results. However, Lee *et al.*[27] comment that the position and width of such low energy resonances is extremely sensitive to the details of the interaction potentials utilised and the manner of accounting for the polarisation. Polarisation, being an attractive interaction potential has the effect of shifting resonances to lower energies. This is consistent with the SMC-SEP and R-matrix calculations capturing most of the polarisation, while the ISVM+DW included less (note that the Lee *et al.*

ground state dipole moment was only half that of the measured value[27] clearly indicating limitations in their target state description). Consistent with our comparison at the DCS level, at low energies our ICSs indicated that the SMC-SEP method provided the best description of the measured data. We thus believe it likely that it would also provide the most accurate information as to the position and widths of this resonance. Further arguments in support of this are now given.

Schwartz *et al.*[152] determined the existence of a stable negative CF_2 anion using photodetachment spectroscopy. This negative anion was found to have an adiabatic electron affinity of -0.18$\pm$0.2eV, and the same $^2B_1$ electronic configuration as the low energy resonance found in the ICS calculations[152]. By placing the $^2B_1$ resonance between ~1-2eV, Rozum *et al.*[25] and Lee *et al.*[27] predict that the energy of the negative anion increases from -0.18$\pm$0.2eV to ~1-2eV as it moves from the anion equilibrium geometry to that of the neutral species. When Winstead and McKoy[20] predict a lower resonance energy in their SMC-SEP calculation, they indicate that the anion is either very nearly bound or actually bound at the vertical geometry. Winstead and McKoy[20] consider a bound or very nearly bound anion a more plausible scenario than neutral CF_2 having an energy 1-2 eV above that of a negative anion, which they cite as further evidence that the $^2B_1$ resonance peak should occur below 0.1eV.

Lee *et al.*[27] also predicted a second much weaker, broader, resonance at 15eV. This they attributed to the $^2B_2$ scattering channel[27]. Winstead and McKoy's SMC-SE and SMC-SEP ICSs also exhibit a peak in this region, although they attribute this

peak to the overlap of a $^2A_1$ resonance centred at 12eV and a $^2B_2$ resonance centred at 13.5eV[20]. There is some experimental evidence in support for the existence of this structure in the ICSs, with the measured ICS data exhibiting a small peak between 8-20eV[20]. However, due to the uncertainties in the measured ICS data, it is not possible to be more specific in this respect. The R-matrix calculation does not extend into this energy range[25], and so no supporting evidence can thus be gleaned from it.

In summary, the measured ICSs are largely consistent with the predictions of the ISVM+DW[27], SMC-SE[19] and SMC-SEP[19] calculations above about 14eV. This is an interesting result, as it suggests that the computationally "cheaper" SE level calculation should be sufficient for application in plasma kinetic studies in which CF_2 is a constituent. Between 8-12eV, however, the measured ICSs sit below all the theoretical calculations while below 6eV the measured ICSs are only consistent with the SMC-SEP[19] calculations (even when taking into consideration the uncertainty on the measured ICS).

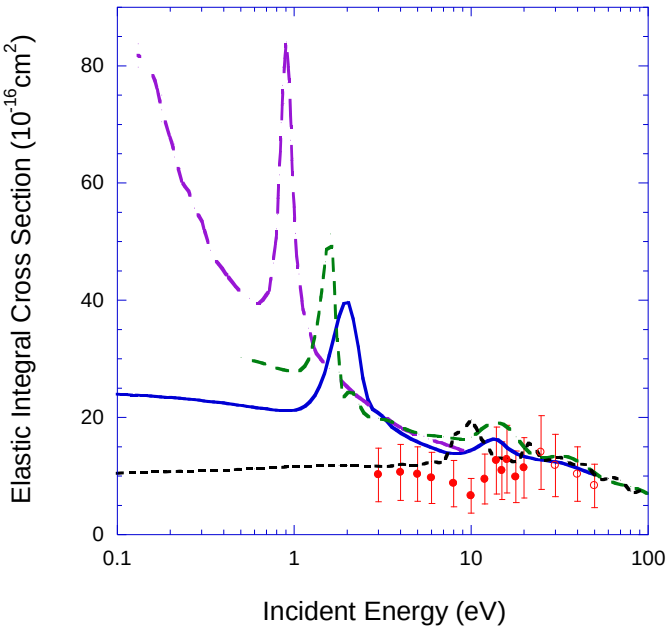

Figure 4.8: Elastic integral cross section (10^{-16}cm^2) for electron scattering from the CF_2 radical. The present data [20] (red ●) is compared against SEP[20] (black – – – – – – –) and SE [20] (blue ——) level calculations, along with the R-Matrix [25](purple — — — —) and ISVM + DW [27, 145] (green — — — —) calculations. Our earlier measured data from 25-50eV are also shown (red ○)[19].

Table 4.3: Experimental elastic integral cross sections of CF_2 for electron impact energies from 3 to 50eV. Table reproduced from Francis-Staite *et al.* [3].

Electron Impact Energy (eV)	ICS (10^{-16}cm^2)
3.00	10.20
4.00	10.60
5.00	10.33
6.00	9.69
8.00	8.70
10.00	6.64
12.00	9.45
14.00	12.66
15.00	10.91
16.00	12.84
18.00	9.85
20.00	11.40
25.00	14.00
30.00	11.80
40.00	10.30
50.00	8.30

Note: Uncertainties in the ICS measurements are in the order of 45%.

4.2 Differential and Integral Cross Sections for CF_3I

4.2.1 Electron Impact Elastic Differential Cross Sections

This section details the present CF_3I elastic differential cross sections measured by the current apparatus with electron impact energies ranging from 10eV-50eV[67]. We note that these measurements were only undertaken because at that time there was no other comprehensive set of elastic DCS for $e + CF_3I$ available in the literature. Such data are a necessary precursor for any attempt in deriving elastic cross sections for $e + CF_3$ scattering, when CF_3 is formed from the pyrolysis of CF_3I. The experimental conditions under which the present CF_3I data were collected have been previously detailed in section 3.2.2 and specifically listed in table 3.3. This data is presented graphically (figures 4.9 - 4.13) and is listed in table 4.4. The present DCSs are compared where possible with the measurements of Kitajima *et al.*[60] and the calculations of Bettega *et al.*[18, 68]. After the measurement and subsequent publication of the present data[67], another experimental group, Cho *et al.*[36], published their measured DCSs for elastic scattering from CF_3I. Where possible the data of Cho *et al.* [36] is also used as a comparison in the discussion that follows.

Kitajima *et al.* used a conventional crossed beam apparatus whereby electrons from a 180° monochromator intersected an effusive molecular beam at right angles; with the scattered electrons detected by a rotatable (-10° to 135°) 180° hemispherical analyser. Kitajima *et al*[60]. quoted the energy resolution of their system, during the CF_3I measurements, to be between 35-40 meV with an angular resolution of $\pm$1.5°.

Cho *et al.* [36] employed a crossed beam apparatus comparable to that of Kitajima *et al.*[60], with a similar monochromator and rotatable analyser. However, Cho *et al.* also utilised a magnetic angle changing device (MAC) based on a design developed by Read and Channing [153]. This device worked by producing a localised magnetic field in the interaction region that was used to change the angles of the various electron trajectories. Thus Cho *et al*. were able to extend the measurement of the elastic differential cross sections to more backward scattering angles (125° - 180°), that would otherwise have been inaccessible due to the mechanical constraints of their electron monochromator.

In order to set an absolute scale to their DCS measurements both Cho *et al.* and Kitajima *et al.* used the traditional relative flow method (RFM) of Srivastava *et al*.[116] with helium as the reference gas. Overall Cho *et al.* presented elastic CF_3I DCS data from 5-50eV, with uncertainties between 8-15%, while Kitajima *et al.* presented data with uncertainties between 15-20%.

Bettega *et al.* calculated the elastic differential and integral cross sections of CF_3I using the Schwinger Multichannel Method, in the static exchange approximation (SMC-SE)[18]. Bettega *et al*.'s approach to calculating the DCSs for CF_3I is similar to that used by Winstead and McKoy[20] when calculating the DCS for CF_2 (see section 4.1.1). The main difference between these two approaches is that Bettega *et al*. approximate the core electrons and protons by a non-local but single particle pseudo-potential (PP). This in turn creates a smoother valence wave function allowing for the use of a smaller basis set in the target expansion, resulting in a

decrease in computing time and the associated cost[154]. For their CF_3I calculations Bettega *et al.* used the PP's of Bachelet *et al.*[155].

Bettega *et al.* did not include a correction due to long range dipole interaction of CF_3I, even though their structure calculations produced a dipole moment of 1.546 D for it. Instead they simply acknowledge that their cross sections are likely to underestimate the true DCS at forward scattering angles by up to 13%[18], which may in fact be a somewhat optimistic estimate.

Considering the relatively strong permanent dipole of CF_3I at 1.048D[18], and its dipole polarisability of $52.42a_0^3$[94]), it is no real surprise that the main feature of the elastic DCSs, from 10-50eV, are their considerable forward-angle peaks. This is well illustrated in figures 4.9-4.13. A small "hump" between ∼50° - 120° is visible for the 10eV and 12 eV (figure 4.9) DCSs, although with increasing energy this feature essentially becomes a shoulder. However by 25eV the CF_3I elastic DCS exhibits almost a completely smooth angular distribution from ∼40 - 150°. With further increasing energy this curve begins to form a dip at ∼100°, that is clearly visible from 30-50eV. All these qualitative features are essentially reproduced by the other measurements and the SMC-SE(PP) calculation.

The experimental results of Kitajima *et al.*[60] and Cho *et al.*[36] are consistent, to within their quoted uncertainties, for all their common angles and energies and in general they are also consistent with the results from Bettega *et al.*'s[18] calculations. The present data are slightly more scattered than that of the other

experimental groups, suggesting that for stable molecules an effusive relative flow approach might be a preferable experimental procedure. However, in general the agreement in terms of both the shape and magnitude, between the present results and the other published work, is considered to be quite fair for energies between 12-50eV.

The present 10eV CF_3I DCS, however, is larger in magnitude than the other data sets at this same energy, at all but two (60° and 75°) of the measured angles (see figure 4.9). On the other hand the data sets of Cho *et al.* and Kitajima *et al.* at this energy are completely consistent with each other from 20° to 150°. As a consequence, this discrepancy at 10eV between the present DCSs and those from the Japanese and Korean groups is a little worrying. Bettega *et al.* predict the existence of an A_1 symmetry resonance to occur in the elastic ICS, centred at around 12eV (see following section). It is likely that had Bettega *et al.*'s ICS calculation included polarisation, this resonance could have shifted to a slightly lower energy (e.g. 10-11eV). This combined with a possible slight mismatch in the true electron impact energy could explain, at least in part, the discrepancy between the present measured DCSs at 10eV and those obtained by the other groups. A detailed study was nonetheless undertaken on the sensitivity of our present 10eV DCS measurements to the conditions under which they were obtained, in all cases, including with the variation of the stagnation pressure, the results were reproducible and entirely consistent with those shown in figure 4.9 and table 4.4. A further analysis of this point will be presented in the next section.

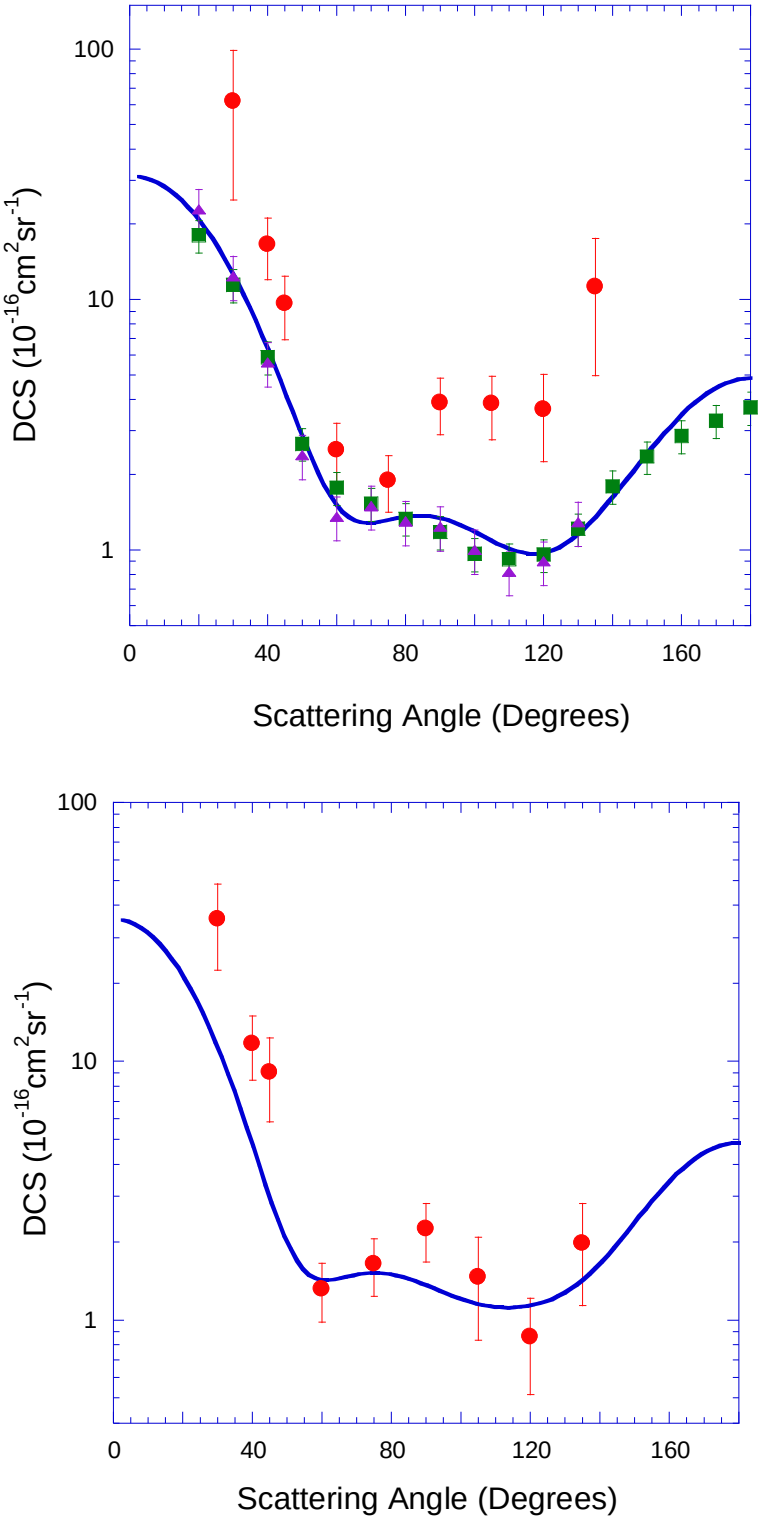

Figure 4.9: Elastic Differential Cross Sections of CF_3I for electron impact energies of 10eV (top) and 12eV (bottom). Present data [67](red ●) are compared against the experimental measurements of Cho *et al.*[36] (green ■) and Kitajima *et al.* [60](purple ▲), along with the theoretical SMC-SE(PP) level calculation of Bettega *et al.* [18, 68] (blue ——).

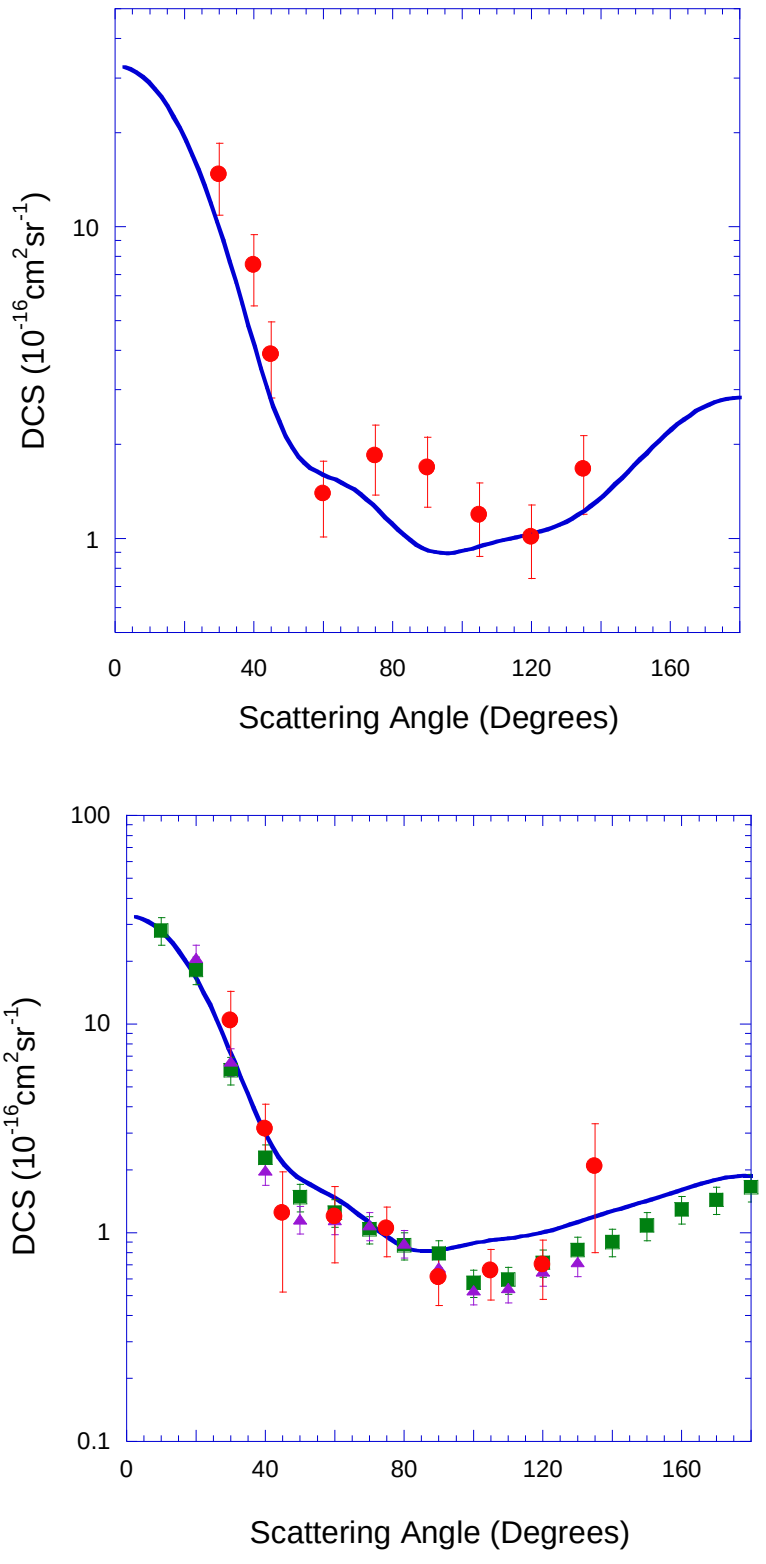

Figure 4.10: Elastic Differential Cross Sections of CF_3I for electron impact energies of 15eV (top) and 20eV (bottom). Present data [67](red ●) is compared against the experimental measurements of Cho *et al.*[36] (green ■) and Kitajima *et al.* [60](purple ▲), along with the theoretical SMC-SE(PP) level calculation of Bettega *et al.* [18, 68] (blue ——).

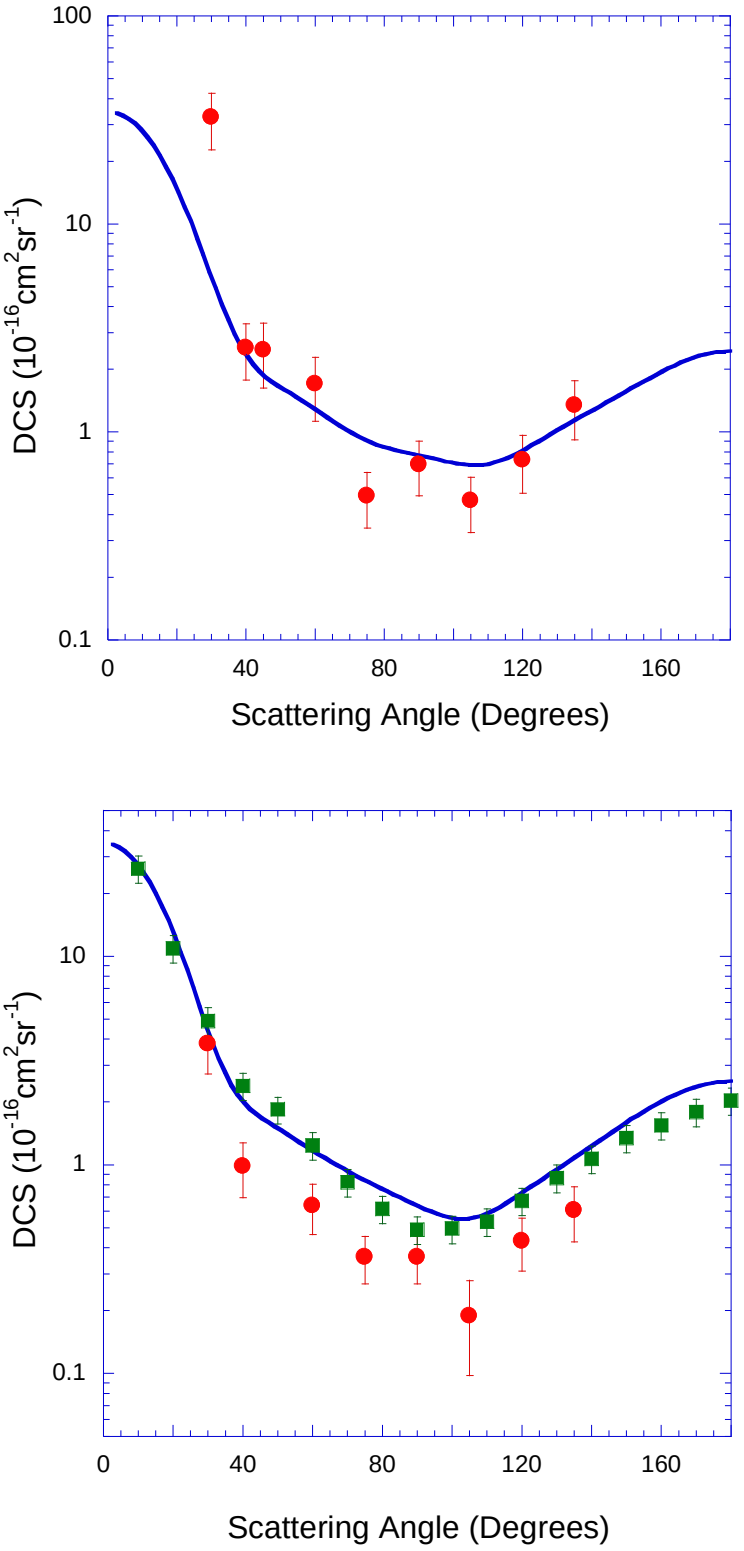

Figure 4.11: Elastic Differential Cross Sections of CF_3I for electron impact energies of 25eV (top) and 30eV (bottom). Present data [67](red ●) are compared against the experimental measurements of Cho *et al.*[36] (green ■) along with the theoretical SMC-SE(PP) level calculation of Bettega *et al.* [18, 68] (blue ——).

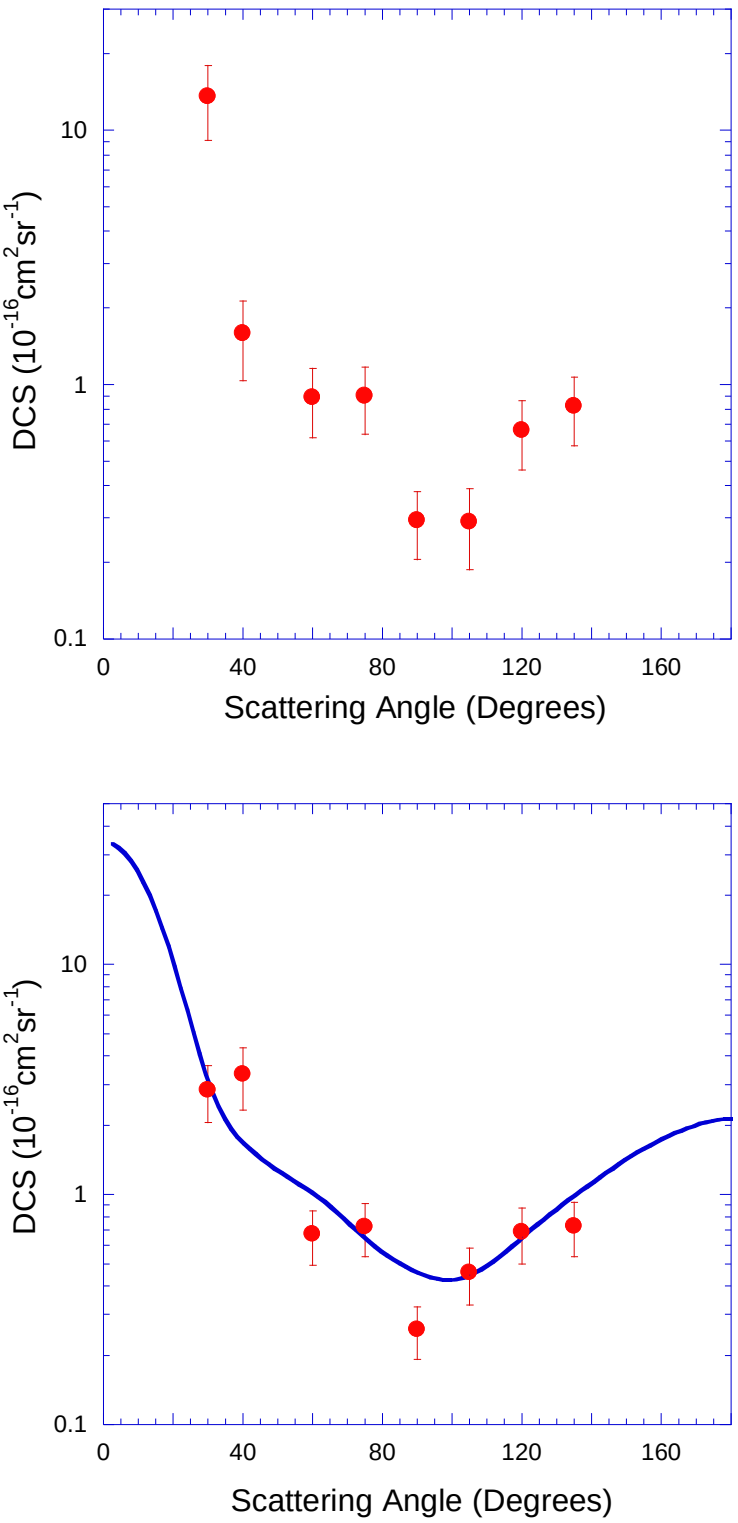

Figure 4.12: Elastic Differential Cross Sections of CF_3I for electron impact energies of 35eV (top) and 40eV (bottom). Present data [67](red ●) are compared against the theoretical SMC-SE(PP) level calculation of Bettega *et al.* [18, 68] (blue ——).

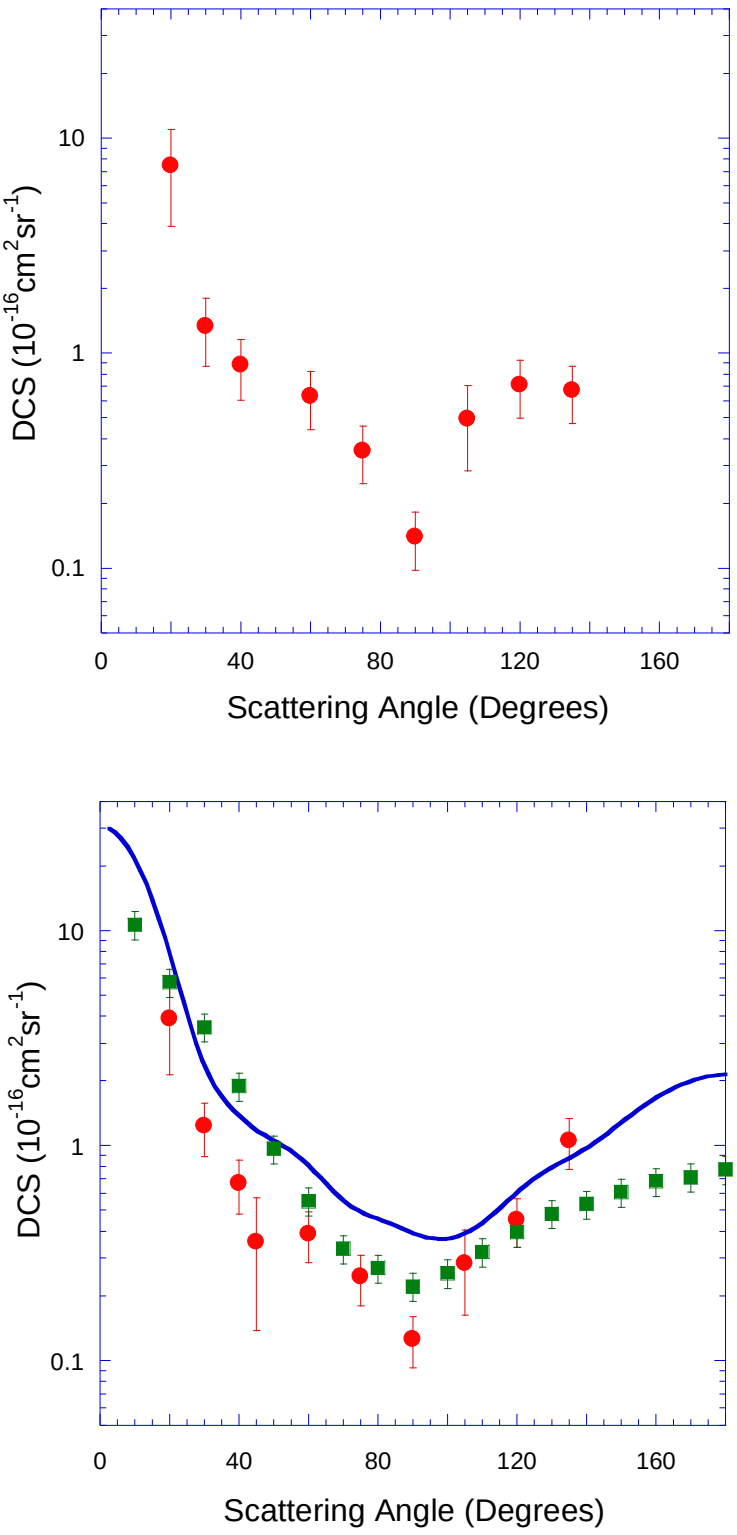

Figure 4.13: Elastic Differential Cross Sections of CF_3I for electron impact energies of 45eV (top) and 50eV (bottom). Present data [67](red ●) are compared against the experimental measurements of Cho *et al.*[36] (green ■) along with the theoretical SMC-SE(PP) level calculation of Bettega *et al.* [18, 68] (blue ——).

Energy (eV)	Scattering Angle									
	20°	30°	40°	45°	60°	75°	90. °	105°	120°	135°
10	-	61.92±6.95	16.59 ±4.57	9.64±2.73	2.51±0.69	1.90±0.48	3.87±0.98	3.85±1.09	3.64±1.38	11.27±6.28
12	-	35.38±12.92	11.69± 3.24	9.08 ±3.26	1.32±0.34	1.65±0.42	2.25±0.57	1.46±0.62	0.86±0.35	1.97±0.84
15	-	14.67±3.81	7.51±1.92	3.89±1.06	1.39±0.38	1.84±0.47	1.68±0.43	1.19±0.31	1.01±0.27	1.67±0.47
20	-	10.35±3.97	3.13±0.99	1.24±0.72	1.19±0.48	1.04±0.28	0.61±0.16	0.65±0.18	0.70±0.22	2.07±1.27
25	-	32.45± 9.85	2.54±0.76	2.47±0.85	1.70±0.58	0.49±0.15	0.70±0.21	0.47±0.14	0.74±0.27	1.34±0.42
30	-	3.79± 1.06	0.98±0.29	-	0.64±0.17	0.36±0.09	0.36±0.09	0.19±0.10	0.43±0.12	0.61±0.18
35	-	13.57±4.41	1.59±0.55	-	0.89 ±0.27	0.90±0.27	0.29±0.09	0.29±0.11	0.66±2 0.2	0.82±0.25
40	-	2.84± 0.79	3.33±1.01	-	0.67±0.18	0.72±0.19	0.26±0.07	0.46±0.13	0.68±0.19	0.73±0.19
45	7.45±3.54	1.34± 0.47	0.88±0.28	-	0.63±0.19	0.35±0.11	0.14±0.04	0.50±0.21	0.71±0.21	0.67±0.20
50	3.88±1.74	1.23± 0.34	0.67±0.19	0.36±0.22	0.39±0.10	0.25±0.07	0.13±0.03	0.28±0.12	0.45±0.12	1.06±0.28

Table 4.4: Experimental elastic differential cross sections of CF_3I for electron impact energies from 10-50eV in units of 10^{-16}c m^2sr^{-1}. [67].

4.2.2 Electron Impact Elastic Integral Cross Sections

The integral cross sections for the elastic electron scattering from CF_3I were determined from the present DCS data by first using a MPSA[73]procedure, to extend the angular range of the DCSs to 0° and 180°, followed by the standard integration. An alternative extrapolation, where we used Bettega *et al.*'s theoretical CF_3I DCSs as a guide[18], was also tried. The derived ICSs from these two procedures were consistent with each other to within the $\sim$ 40% uncertainty we conservatively cite for the present CF_3I ICS data[67].

The current ICS data appears in table 4.5 and is plotted in figure 4.14, where it is compared with the ICSs from Bettega *et al.*'s Schwinger Multichannel calculation in the static exchange approximation with pseudo-potentials SMC-SE(PP)[18] and the experimental measurements of Cho *et al*. [36]. Cho *et al.*'s group also extrapolated Kitajima *et al.'s* published DCS measurements to calculate their ICS of CF_3I. This data is also used for comparison in figure 4.14. Note that Cho *et al.* make no comment on how they actually extrapolated Kitajima et al.'s data from 130° to 180° or from 20° to 0°. The elastic continuum multiple-scattering method (CMS) theoretical electron scattering CF_3I cross section of Kawada *et al.* [31] is also included in our comparison plot, as is their grand total cross section (GTCS) measurement.

All the available CF_3I ICSs are consistent with each other (at all common energies) to within the experimental uncertainties that each data set contain. In particular, also note the exceptional agreement between the theories of Bettega *et al.*[18] and

Kawada *et al.* between 11-60eV[31]. In figure 4.14 it is interesting to consider the slight divergence of the present ICS data set and that of the other experimental groups, as they decrease below an energy of 20 eV. While all the data sets exhibit an enhancement in the elastic ICS with decreasing energy, showing that the dipole moment and polarisability of CF_3I does play an important role in the electron scattering dynamics, this effect is particularly prevalent in our ICS data set. Here the present experimental data set begins to more closely resemble the measured GTCS, while the other data sets remain somewhat lower. We note that at 10eV the vast majority of the GTCS is due to elastic scattering, with the ionisation cross section (at 10eV) reported to be only $0.039x10^{-16}cm^2$[29] and the vibrational and electronic excitation cross sections, although not specifically known for CF_3I at 10eV, being generally 1-2 or more orders of magnitude lower than the elastic cross section. Hence despite the agreement between the other ICS data at energies around 10eV, we interpret these elastic ICSs to be somewhat underestimated, as it is unlikely, even with the addition of all the open inelastic processes, that they would equal CF_3I's GTCS. This would also explain in part the difference seen between the present 10eV DCS data and that of the other groups.

Bettega *et al.*[18] detected two small resonances in CF_3I's ICS, one centred at ~ 7eV and the other centred at ~12 eV and both with widths of ~1 eV ; these were identified as being due to E symmetry and to A_1 symmetry respectively. As Bettega *et al.*'s SMC-SE(PP) calculation did not include a dipole or polarisation correction in their interaction potential, they acknowledge that their ICS would underestimate the true ICS[18]. This is also consistent with the present experimental data being

somewhat larger in magnitude then their calculated values, particularly below 20eV. As the inclusion of polarisation in the interaction potential also has the effect of shifting resonances to lower energies (as was clearly displayed in the case of the $^2B_1$ shape resonance of CF_2 that was discussed previously), it is likely that the peak energies of the E and A_1 symmetry resonances were over estimated by Bettega *et al.*

There is no strong evidence seen in any of the experimental ICS measurements in support for the existence of the two resonances detected by Bettega *et al*., but this is probably due to a combination of the energy grid used for the various measurements and the experimental uncertainties of between 20-40% attributed to the different measured data sets.

Table 4.5: Experimental elastic integral cross sections of CF_3I for electron impact energies from 10 to 50eV. Table reproduced from Francis-Staite *et al* [67].

Electron Impact Energy (eV)	ICS ($10^{-16}cm^2$)
10	58.20
12	52.90
15	44.55
20	33.78
25	32.68
30	20.46
35	25.77
40	21.59
45	20.27
50	14.43

Note: Uncertainties in the ICS measurements are in the order of 40%.

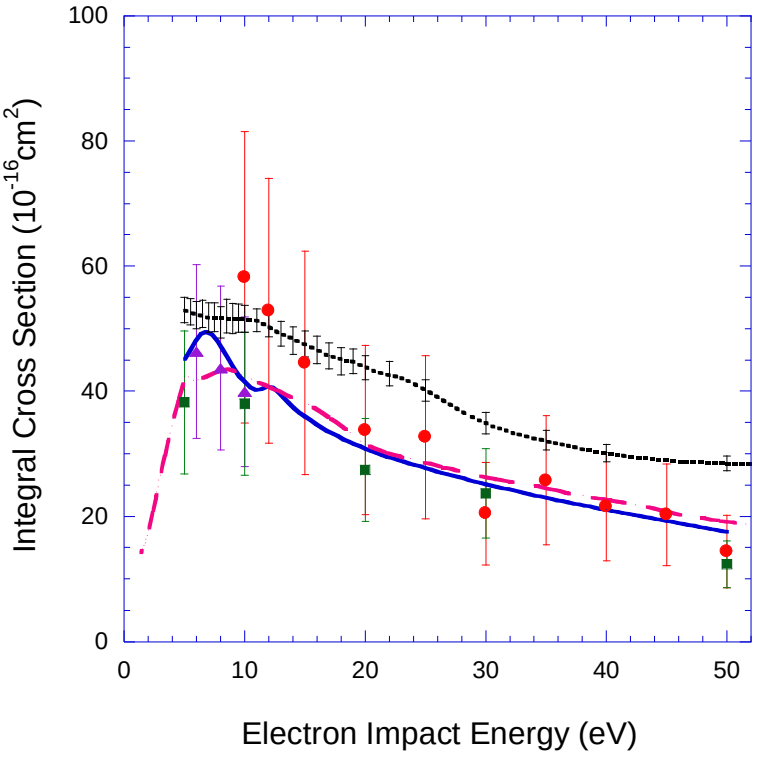

Figure 4.14: Elastic integral cross sections (10^{-16}cm^2) for electron scattering from CF_3I. The present data (red ●) are compared against Bettega *et al*.s' SMC-SE(PP) (blue ——) level calculation along with the experimental measurements of Cho *et al.* (green ■) and Kitajima *et al.* (purple ▲). Also included are the CF_3I CMS elastic cross section(pink — — —) and grand total cross section data (black ·····) both reported by Kawada *et al*.[31].

4.3 Elastic Differential and Integral Cross Sections for electrons scattering from a "mixed" molecular gas beam

This section details the recently published[69] results for elastic electron impact DCSs and ICSs measured using a "mixed" molecular beam. The electron impact energies ranged from 5eV to 50eV in this work. As discussed previously (in section 3.2.2), this multi-component "mixed" molecular beam was produced via the pyrolysis of CF_3I at 817°C, resulting in the following beam composition; I (30.03%), CF_3 (24.19%), C_2F_6 (11.32), I_2(8.34%), and CF_3I (25.68%). These pioneering "mixed" beam electron impact DCS measurements represent a vital stepping stone in our ultimate aim of investigating the e + CF_3 scattering process.

Due to the unique nature of these measurements, there are no data sets, either experimental or theoretical, against which a comparison can be made. Hence only a few of these "mixed-beam" DCSs are plotted in figures 4.15 and 4.16, for the specific electron impact energies of 7eV, 15eV, 30eV and 40eV, with the entire data set listed in table 4.6.

Qualitatively, these DCSs are moderately forward peaked at the lower incident electron energies (i.e. <15eV) which was anticipated considering the permanent dipole moments of both CF_3I ($\mu = 1.048\text{D}$ [18]) and CF_3 ($\mu = 0.43 \pm 0.07\text{D}$ [80]), along with the relatively large dipole polarisabilities of these species (CF_3I: $\alpha = 52.42a_0^3$ [94], CF_3: $\alpha \approx 9 - 15a_0^3$ [78]) and that of atomic iodine ($I(^2P_{3/2})$: $\alpha = 34.6a_0^3$ [135] and $I(^2P_{1/2})$: $\alpha = 31.5a_0^3$[135]). For the most part these DCSs do not exhibit any sharp angular features, that are typical of the atomic I cross sections (see section 3.4.2), suggesting that the molecular nature of the "mixed" beam dominates over that of the atomic constituent.

Some forward angle scattering points are clearly missing from our 5eV, 7eV and 10eV DCS data sets (see table 4.6), as there was some difficulty at those energies in resolving the true scattered electron counts from the background counts at the forward angles. Furthermore, during these measurements the CEM mounted at the 30° scattering angle experienced problems related to its signal gain, leading to a reduced sensitivity and hence fewer overall counts. As the 30° CEM shares a common high voltage power rail with all the other CEMs (except 20°), it was not possible to adjust its gain individually to overcome that problem, because of the risk

associated with damaging the other CEMS. However, despite the omission of some elastic DCS scattering data at 20° and 30° the "mixed-beam" cross section data set for electron impact energies from 5eV to 50eV remains comprehensive.

The ICSs were calculated in the usual way by first extrapolating the "mixed" beam DCSs at each energy to 0° and 180°, using the MPSA procedure[73], followed by a standard integration. These ICSs are plotted in figure 4.17 and are listed table 4.7.

The integral cross sections were observed to increase in magnitude with decreasing electron impact energy, as is generally the case for scattering systems dominated by dipole interactions. Within the limitation of our experimental uncertainties, we find no significant structural features in our ICS data that could indicate the existence of a resonance or resonances in this system.

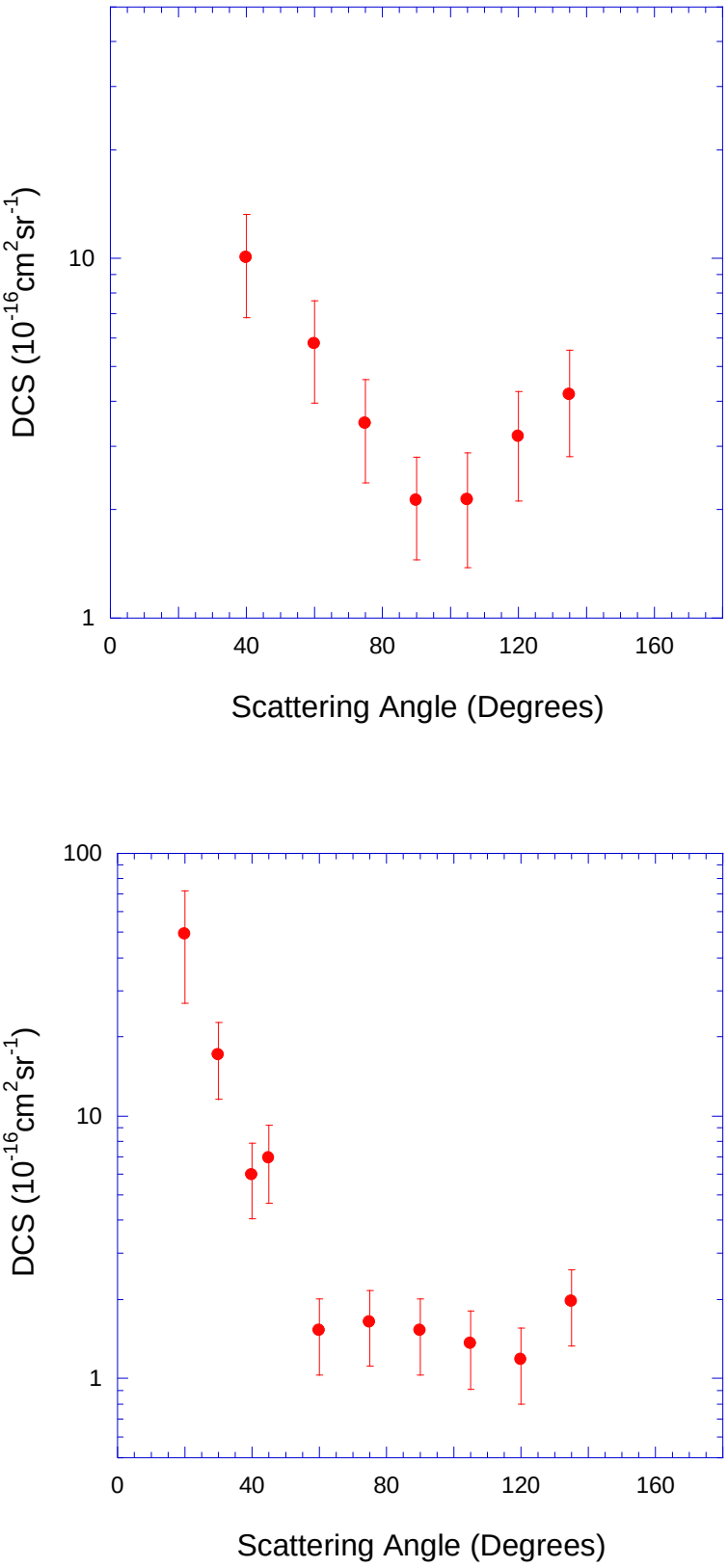

Figure 4.15: Elastic DCS in units of 10^{-16}cm^{2}sr^{-1} for electron impact from a "mixed" beam containing: I (30.03%), CF_3 (24.19%), C_2F_6 (11.32%), I_2(8.34%), and CF_3I (25.68%) at T=817°C. The present data (red ●)[69], for electron impact energies of 7eV(top) and 15eV(bottom) are shown.

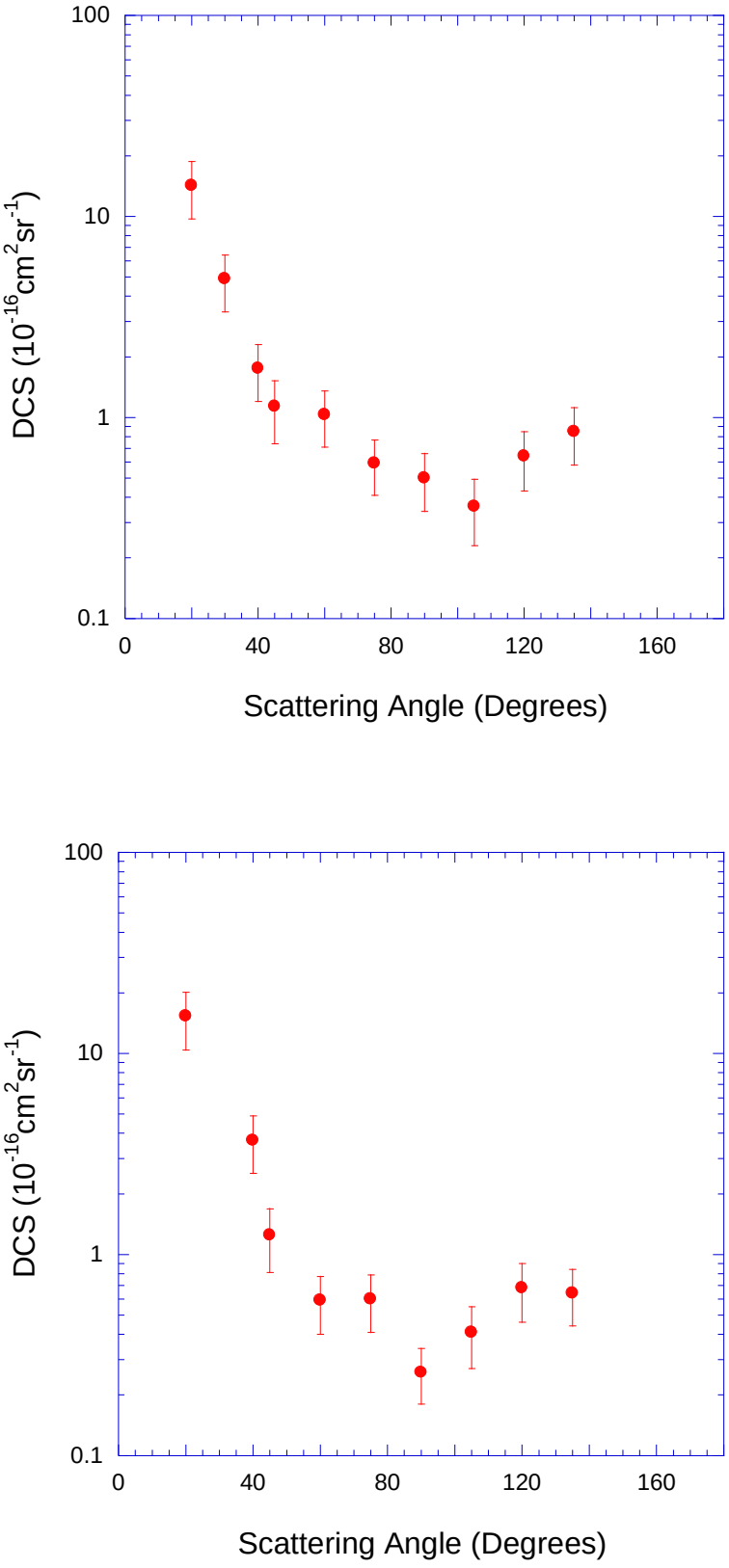

Figure 4.16: Elastic DCS in units of 10^{-16}cm^{2}sr^{-1} for electron impact from a "mixed" beam containing: I (30.03%), CF_3 (24.19%), C_2F_6 (11.32%), I_2(8.34%), and CF_3I (25.68%) at T=817°C. The present data (red ●)[69], for electron impact energies of 30eV(top) and 40eV(bottom) are shown.

Energy (eV)	Scattering Angle									
	20°	30°	40°	45°	60°	75°	90. °	105°	120°	135°
5	-	-	1.99 ± 0.51	1.10 ± 0.53	1.07 ± 0.28	0.61± 0.16	0.30± 0.08	0.18 ± 0.07	0.49 ± 0.21	0.31± 0.93
7	-	-	10.03 ± 3.19	-	5.78 ± 1.83	3.48 ± 1.11	2.12± 0.67	2.13 ± 0.75	3.19 ± 1.08	4.18 ± 1.37
10	-	-	15.48 ± 4.94	9.11 ± 2.93	2.01 ± 0.64	1.73 ± 0.55	2.28± 0.73	2.75 ± 1.03	1.73 ± 0.56	1.87 ± 0.59
15	49.40±22.55	17.10 ± 5.56	5.97 ± 1.91	6.93 ± 2.27	1.52 ± 0.49	1.64 ± 0.52	1.52± 0.49	1.36 ± 0.45	1.18 ± 0.38	1.96 ± 0.63
20	36.63± 16.69	20.67 ± 6.72	4.59 ± 1.47	7.83 ± 2.85	1.62 ± 0.52	1.17 ± 0.37	0.86± 0.28	-	3.27 ± 1.15	2.86 ± 0.93
25	9.06±3.34	-	1.76 ± 0.62	1.50 ± 0.57	0.89 ± 0.31	0.43 ± 0.15	0.48± 0.17	0.26 ± 0.12	0.68 ± 0.24	1.02 ± 0.36
30	14.20 ± 4.50	4.89 ± 1.54	1.75 ± 0.55	1.13 ± 0.39	1.03 ± 0.32	0.59 ± 0.18	0.50 ± 0.16	0.36 ± 0.13	0.64 ± 0.21	0.85 ± 0.27
35	6.29 ± 2.18	-	1.44 ± 0.50	1.21 ± 0.43	1.03 ± 0.36	0.97 ± 0.33	0.32± 0.11	0.45 ± 0.16	0.78 ± 0.27	0.76 ± 0.26
40	15.28 ± 4.88	-	3.70 ± 1.17	1.25 ± 0.44	0.59 ± 0.19	0.60 ± 0.19	0.26± 0.08	0.41 ± 0.14	0.68 ± 0.22	0.64 ± 0.20
45	6.83 ± 2.38	1.05 ± 0.37	0.72 ± 0.25	0.73 ± 0.26	0.39 ± 0.14	0.24 ± 0.08	0.09± 0.03	0.31 ± 0.11	0.68 ± 0.23	0.46 ± 0.16
50	10.47 ± 2.33	1.45±0.33	0.92 ± 0.21	0.80 ± 0.19	0.50 ± 0.11	0.31 ± 0.07	0.18 ± 0.04	0.63 ± 0.12	0.79 ± 0.15	1.25 ± 0.25

Table 4.6: Elastic DCS, in units of $10^{-16}cm^2sr^{-1}$, for electron impact energies in the range 5-50eV and for scattering from a "mixed" beam consisting of I (30.03%), CF_3 (24.19%), C_2F_6 (11.32%), I_2(8.34%), and CF_3I (25.68%) at T=817°C. [69].

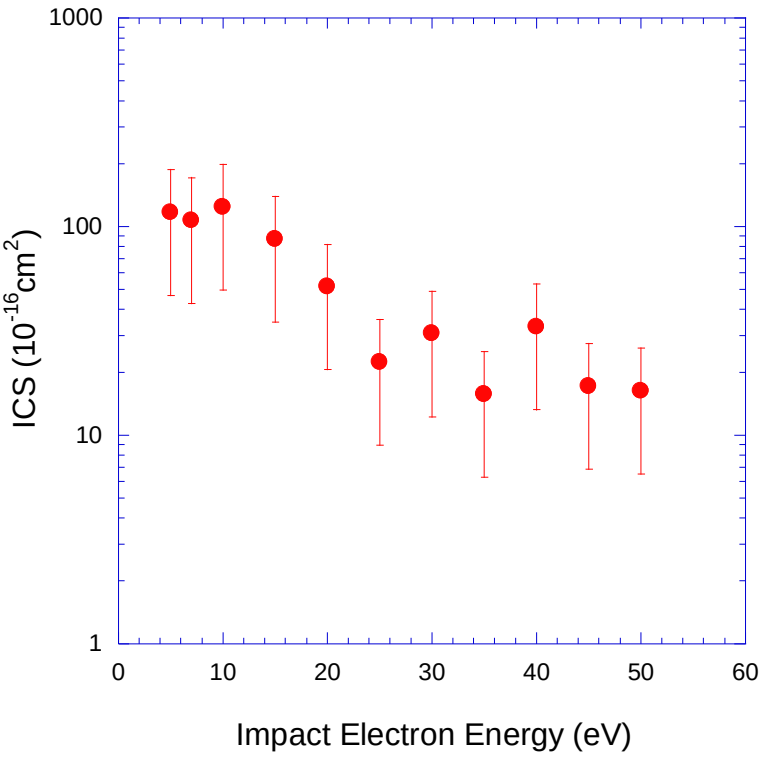

Figure 4.17: Elastic ICS in units of 10^{-16}cm^2, for electron scattering from our "mixed" beam containing: I (30.03%), CF_3 (24.19%), C_2F_6 (11.32), I_2(8.34%), and CF_3I (25.68%) at T=817°C. Present data (red ●)[69].

Table 4.7: Elastic ICS in units of 10^{-16}cm^2 for electron scattering from our "mixed" beam. The composition of the mixed beam is as stated previously.

Electron Impact Energy (eV)	ICS (10^{-16}cm^2)
5	117
7	107
10	124
15	86.8
20	51.4
25	22.4
30	30.6
35	15.7
40	33.1
45	17.2
50	16.3

Note: Uncertainties in the ICS measurements are in the order of 50%.

4.4 Differential and Integral Cross Sections for the CF_3 radical

4.4.1 Electron Impact Elastic Differential Cross Sections

Detailed in this section are the elastic e + CF_3 scattering DCSs for electron impact energies in the range 7-50eV. These cross sections were measured as part of a "mixed" molecular beam containing; CF_3, CF_3I, C_2F_6, I and I_2 that was produced in the manner detailed in section 3.3.2. The CF_3 scattering component from the mixed DCSs was extracted using the method previously described in section 3.4.1. We note that the cumulative effect of the experimental uncertainties attributed to the "mixed" beam DCS data, and to the composition of the mixed beam itself, has resulted in absolute uncertainties of the order of 100% for some of our CF_3 data. Large absolute uncertainties are always a problem when dealing with "difference-type" experiments, but they do not detract from the importance and usefulness of the present results. It must also be viewed in the context of how challenging these types of experiments are. The electron impact energies containing most of the data points with large uncertainties are 25eV and 35eV. Thus the discussion of our results will focus on the largely complete data sets, at the electron impact energies of 7eV, 10eV, 15eV, 20eV, 30eV, 40eV and 50eV. Our elastic DCSs for electron scattering from CF_3 are presented in figures 4.18-4.22, where they are compared against all the available theoretical calculations, namely those from Diniz *et al.*[58] and Rozum *et al.*[21], and the currently unpublished works of Blanco and García[72] and Winstead and McKoy[156]. The present DCSs are also listed in table 4.8.

Diniz *et al*.[58], a theoretical group based in Brazil, first published e + CF_3 elastic DCSs in 1999, for the electron impact energy range of 6.5eV-30eV. These calculations were made using the Schwinger Multichannel Method in the Static Exchange approximation (SMC-SE), with a corrected scattering amplitude designed to take into account both the initial and final spin states of the system. Their current code, a modified version of that from da Paixão *et al*. [157], for linear open shell species is the first such example of *ab initio* calculations from any open shell species with a non-linear geometry [58]. Diniz *et al.* sourced the geometry of CF_3 from Yamada and Hirota[45] (see figure 1.2), and used the Hartree-Fock Self Consistent Field (HF-SCF) method to describe the target bound orbitals and the continuum orbitals. In a similar fashion to the CF_3I calculations[18] from Bettega *et al.* (see section 4.2.1) pseudo-potentials were employed to mimic the CF_3 core electrons and thus reduce the computational difficulties associated with this 33 electron target.

In a similar fashion to that of Diniz *et al.*[58], Winstead and McKoy also used the SMC method in the static exchange approximation[156] in order to generate elastic CF_3 cross sections for incident electron energies in the range 10eV to 50eV. We note that they[156] also used the HF-SCF method to obtain their target bound orbitals and continuum orbitals. Diniz *et al.* and Winstead and McKoy used independently developed computer codes, and despite their respective calculations having similarities in terms of both the size and quality of the basis set employed for determining the wave function[156], there are some small but noticeable differences between their calculated cross sections. Those differences between the

calculated elastic CF_3 cross sections from these two groups are most prevalent at an electron impact energy of 10eV (see figure 4.18). On the other hand for the incident electron energy of 20eV (figure 4.19) both their cross sections are quite similar, while at 30eV (figure 4.20) the level agreement between the two calculations is very good.

Rozum *et al.*, as part of their extensive study into e + CF_x (x=1,2,3) collisions [7, 21, 25, 32, 59], published some elastic e + CF_3 DCSs[21]. They preformed their calculations using the UK Polyatomic R-matrix code and also sourced the geometry of CF_3 from the infra-red spectroscopy studies of Yamada and Hirota[45]. They included the six lowest lying electronic states of CF_3 in their calculations (that they had previously characterised [158]), resulting in them producing CF_3 elastic DCSs for electron impact energies below 10eV.

Rozum *et al.* considered using various basis sets to describe CF_3 for their compuations including: Sadlej pVTZ, aug-cc-pVDZ, aug-cc-pVTZ, 6-31G* and 6-311G* to describe CF_3[158]. Please refer to reference [158] for a description of these acronyms. Eventually they chose the 6-311G* basis set, as using it in conjunction with the CASSCF method[158] produced a ground state dipole moment of 0.55D[21, 158], which was nearest to the measured value of μ =0.43$\pm$0.07D[80] that they could obtain. As Diniz *et al*. did not give a value for the ground state dipole moment that their HF-SCF method produced, Rozum *et al.* attempted to predict it, by running their own HF-SCF test calculations using the 6-311G* Gaussian basis set. This resulted in a dipole moment of μ = 0.74D, which they noted "differs

significantly from the experimental value" [158]. Based on this prediction and taking into account the similarities between Diniz *et al.*'s[58] calculations and those of Winstead and McKoy[156], we tentatively consider the Winstead and McKoy ground state dipole moment to also be $\mu \approx 0.7\mathrm{D}$.

Blanco and García calculated two sets of elastic DCSs for e + CF_3 scattering data, for electron impact energies between 1-500eV, both with and without a correction for a ground state dipole moment of $\mu = 0.7\mathrm{D}$ [72]. They first calculated the scattering from each individual atom in CF_3 using their Optical Model Potential (OMP) method (see section 3.4.2), then, taking into account the geometry of CF_3[45], they combined the scattering from each individual atom using their Independent Atom Model (IAM) in conjunction with the additivity rule (AR) with a screening correction (SC)[72]. Note that a brief description of their OMP method and the IAM-SCAR approach, along with relevant references, has already been given previously in section 3.4.2 of this thesis. The effect of accounting for the ground state dipole moment in Blanco and García's IAM-SCAR results, can clearly be seen in figures 4.18-4.22. In particular we highlight that their dipole corrected data increases rapidly in magnitude for forward scattering angles ($\theta \leq 10°$), producing by far the largest cross sections at forward scattering angles of all of the theories available. For the lower electron impact energies, i.e. 7eV and 10eV, this dipole effect is even more pronounced, with their two data sets diverging from one another at scattering angles of $\theta \leq 40°$ and $\theta \leq 35°$ respectively.

Discounting scattering angles less than 10°, the general level of agreement (in terms of both the shape and magnitude of the DCSs), between the computation of Blanco and García's and those from Winstead and McKoy[156] and Diniz *et al.*[58], for electron impact energies of above 20eV, is quite good (see figures 4.19-4.22). This level of agreement is somewhat surprising, considering the Blanco and García calculations are computationally much more straightforward and require a greatly reduced amount of computing power. At 15eV, however, the elastic DCSs of Blanco and García begin to diverge from those of Winstead and McKoy and Diniz *et al.*, with considerable differences arising at 10eV and 7eV (see figure 4.18). However this is probably not overly surprising as Blanco and García cite 10eV as the absolute lower limit for the validity of the IAM-SCAR calculations[142, 143].

Before we move on to consider the level of agreement between our measured elastic e+CF_3 DCSs, and those from the various theories, we first return to address how the differences between our CF_3I elastic DCSs[67] and those from Cho *et al.* [36] affects our final CF_3 values. Note that we specifically address this at 10eV. In order to clearly investigate this potential influence we simply derived the 10eV CF_3 cross section twice, once using Cho *et al.*'s 10eV CF_3I elastic DCS data set[36] and once using the Flinders CF_3I elastic DCS data set[67]. These two sets of results are shown in red and blue, respectively, in figure 4.18. It is apparent from this figure that irrespective of which CF_3I data are used, the CF_3 cross sections are entirely consistent with each other, when taking into account their respective experimental uncertainties. This is a crucial result for the validity of the CF_3 cross sections we are

attempting to determine, particularly given the relatively large abundance of CF_3I in our "mixed" beam.

Thus we now turn our attention to the other atomic and molecular differential cross sections that were subtracted from the "mixed" DCS data sets in order to determine the CF_3 cross sections. Again we limit this specific comparison to 10eV. When comparing the two available 10eV elastic DCSs for atomic iodine, we note that Blanco and García[72] predict a "dip" in the cross sections' magnitude between 80°-120° and centred at 105°, that is three times larger than the corresponding "dip" predicted by Bartschat and Zatsarinny[71] (see section 3.4.2, specifically figure 3.11c). Note, as discussed earlier, we believe the atomic I results from Bartschat and Zatsarinny are inherently more exact that those from Blanco and García, although in many cases we reiterate that their level of accord is excellent. Nonetheless as Blanco and García's IAM-SCAR calculation for molecular iodine involves their OMP DCS of atomic iodine[72], it is likely that their underestimation in the magnitude of the elastic DCSs for e + I interactions in some cases, will also lead to an underestimation in some of their elastic e + I_2 DCSs. However, as the percentage abundance of I_2 in our "mixed" beam is only small, this effect is unlikely to cause a serious inaccuracy in the elastic e+CF_3 cross sections that we derive. Nonetheless it is important to reiterate that our CF_3 data sets are highly dependent on the quality of the other species (C_2F_6, I, I_2, CF_3I) DCSs, and are particularly sensitive to any angular features in those cross sections that coincide with our measured scattering angles.

So we can now discuss the level of agreement in figures 4.18-4.22, where we see a reasonable level of agreement between the shapes of our CF_3 cross sections and the shapes calculated by Diniz *et al.* [58], Winstead and McKoy[156] and Blanco and García[72], with only the odd exception at particular angles and impact energies (e.g. 45°at 20eV and 45° at 40eV). Specifically, we note particularly good agreement between the angular distribution of our 7eV elastic CF_3 DCS data and that of the corresponding R-matrix calculation and SMC-SE calculation (see figure 4.18). A similar level of agreement is also found at 10eV. However, at energies ≥15eV, where measured data are available at $\theta < 40°$, the forward angle shape of our DCSs appears to be more forward peaked than those predicted by the various theories. This is an interesting point to note because Blanco and García overestimated the ground state dipole moment of CF_3, and both Diniz *et al.* and Winstead and McKoy are also thought to have done the same thing. This being the case, one would usually expect that the calculated cross sections might be over-estimated at forward angles, in respect to the measured data, where the dipole effects pre-dominate. However, this is precisely the opposite to what we observe and could be an indication that these current theories do not provide an adequate description for the polarisation of the CF_3 radical.

We now move on to consider the overall magnitude of our elastic CF_3 DCSs, in comparison to the theoretically calculated results, and immediately note that ours appear to be much bigger for incident electron energies less than and equal to 20eV. In particular, we see our measured DCSs are approximately 10 times larger in magnitude than the theoretical cross sections at 7eV, and 5 times larger at 10eV,

15eV, and 20eV (see figures 4.18 and 4.19). This behaviour was not expected, as on the basis of our experience in CF_2 we had anticipated that an SMC-SE level calculation might provide a realistic description at least down to ~15eV. However for incident electron energies greater than 20eV, overall, with only a few exceptions, the level of agreement between the present measurements and the available calculations is quite fair (see figures 4.20-4.22). This is consistent with our previous experience with the CF_2 radical.

At this stage we simply observe that the theoretical calculations of open-shell radicals like CF_3, are significantly more complicated than those for closed shell species, with the treatment of spin coupling and unfilled orbitals being very different from the well established closed shell treatments[58]. Furthermore, the challenges associated with experimentally measuring DCSs for open-shell radicals has made all these current scattering theories difficult to benchmark[158], with the current results suggesting that something is in fact missing from them. Thus it seems possible that the unpaired bonding electron in CF_3, and the resultant unique physicochemical properties of CF_3, are producing an effect, enhanced at lower electron impact energies, that cannot be adequately accounted for using the standard quantum mechanical calculations currently available. If this is indeed the case then the magnitudes of our measured lower energy CF_3 DCSs could actually be the first indication for the true magnitude of the elastic interactions in electron scattering from open shell radicals.

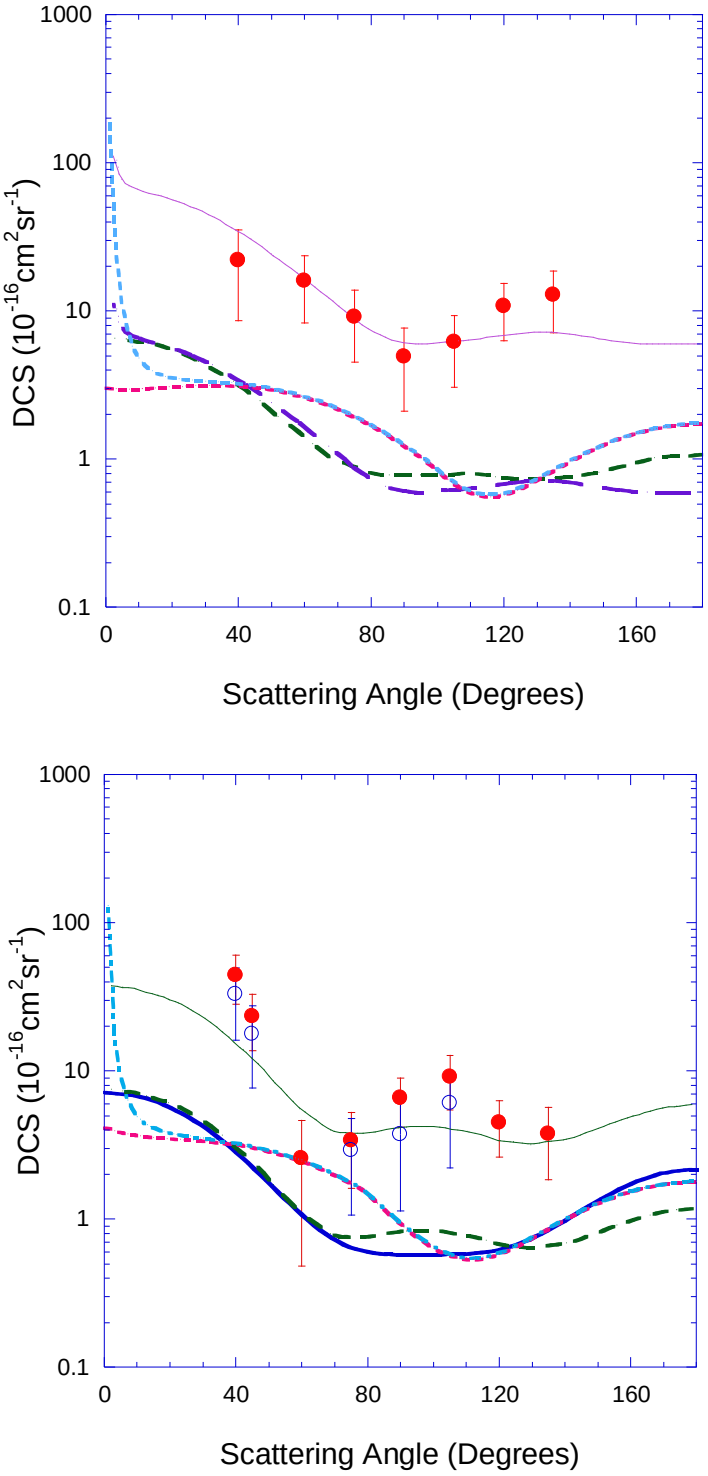

Figure 4.18: Elastic Differential Cross Sections for electron scattering from CF_3 (10^{-16}cm^{2}sr^{-1}) at electron impact energies of 7eV (top) and 10eV (bottom). Present data (red ●)calculated using the CF_3I elastic DCS of Cho *et al.*[36] are compared against the SMC-SE calculations of Winstead and McKoy [156] (blue ——), and Diniz *et al*[58]. (green – – –) along with 5*Diniz *et al.* (green— —) in the bottom figure. Shown also are the IAM-SCAR calculations of Blanco and García[72], both with (light blue ·····) and without (pink ·····) a ground state dipole correction. The R-matrix calculations of Rozum *et al.*[21](purple — — —) are also shown in the top figure along with 10*R-Matrix result (purple ———). Open circles (blue ○) are the present data calculated using our CF_3I elastic DCSs[67].

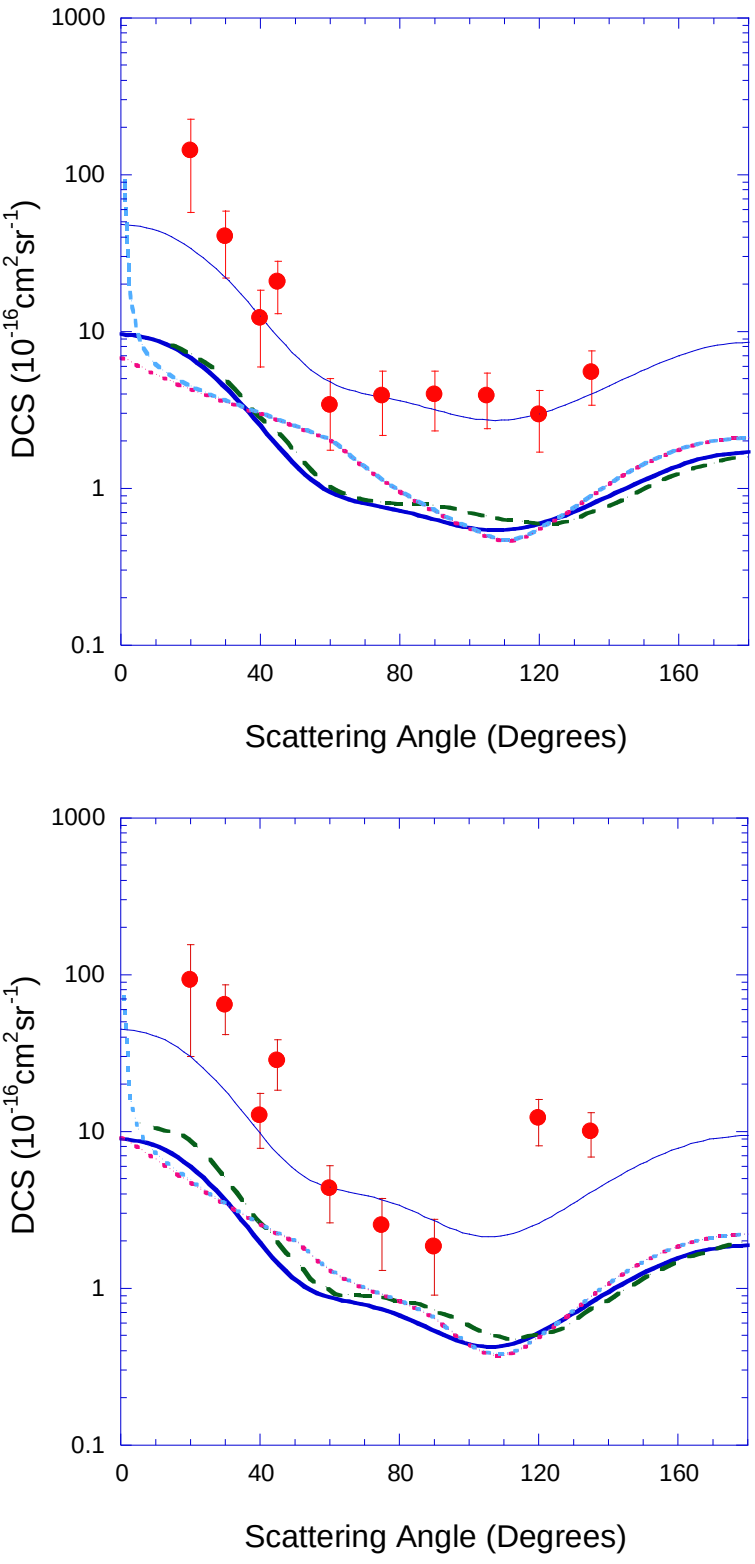

Figure 4.19: Elastic Differential Cross Sections for electrons scattering from CF_3 (10^{-16}cm^{2}sr^{-1}) at electron impact energies of 15eV (top) and 20eV (bottom). Present data (red ●) are compared against the SMC-SE calculations of Winstead and McKoy [156] (blue ——) and Diniz *et al.*[58] (green — — —), along with the IAM-SCAR calculations of Blanco and García[72], both with (light blue ••••••••••) and without (pink ••••••••••) a ground state dipole correction. Also shown are 5 times the SMC-SE calculations of Winstead and McKoy (blue ——), in the top figure and bottom plots.

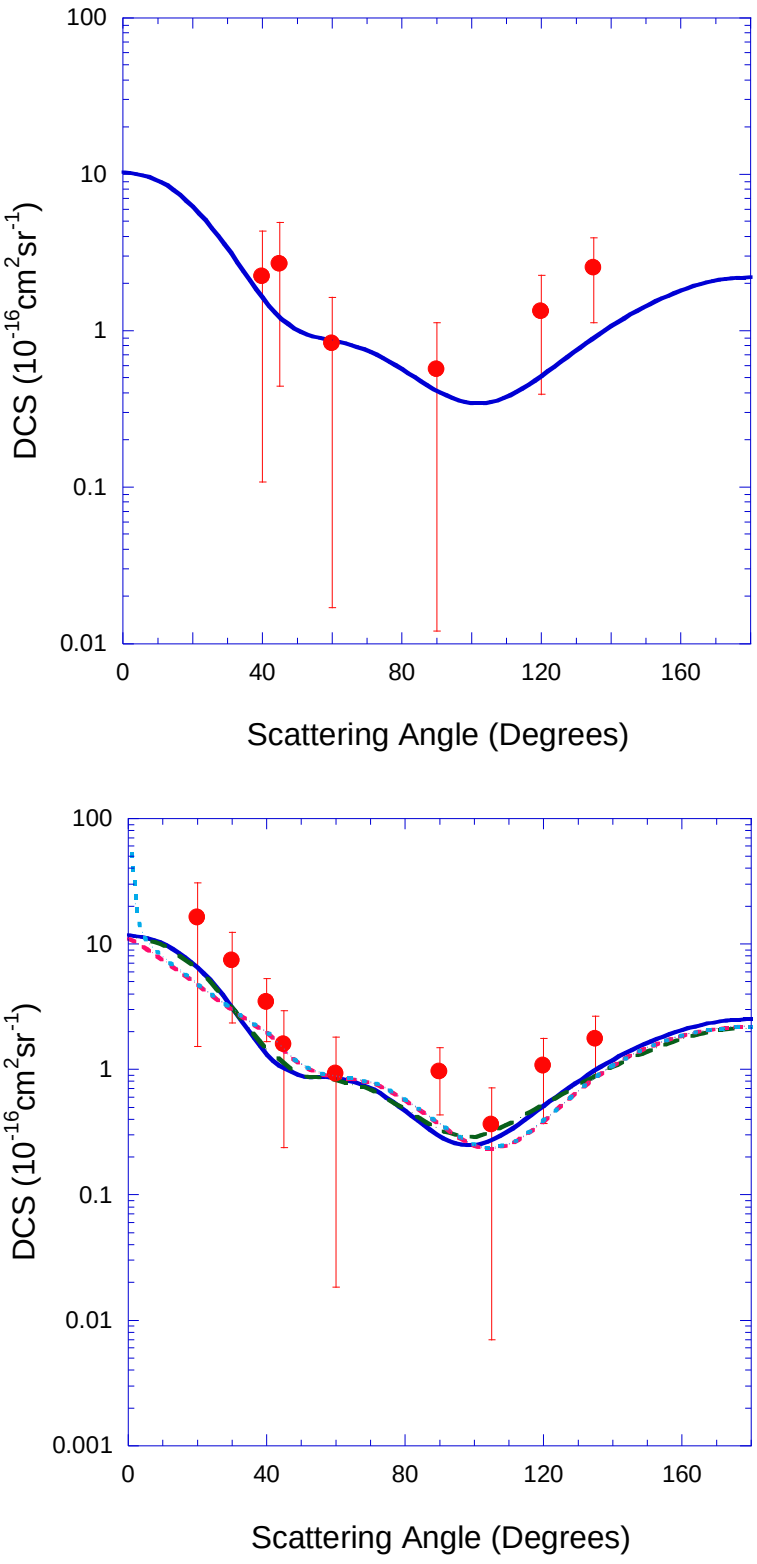

Figure 4.20: Elastic Differential Cross Sections for electrons scattering from CF_3 (10^{-16}cm^{2}sr^{-1}) at electron impact energies of 25eV (top) and 30eV (bottom). Present data (red ●) are compared against the SMC-SE calculations of Winstead and McKoy [156] (blue ——) and Diniz *et al*[58]. (green — — —), along with the IAM-SCAR calculations of Blanco and García[72], both with (light blue ·····) and without (pink ·····) a ground state dipole correction.

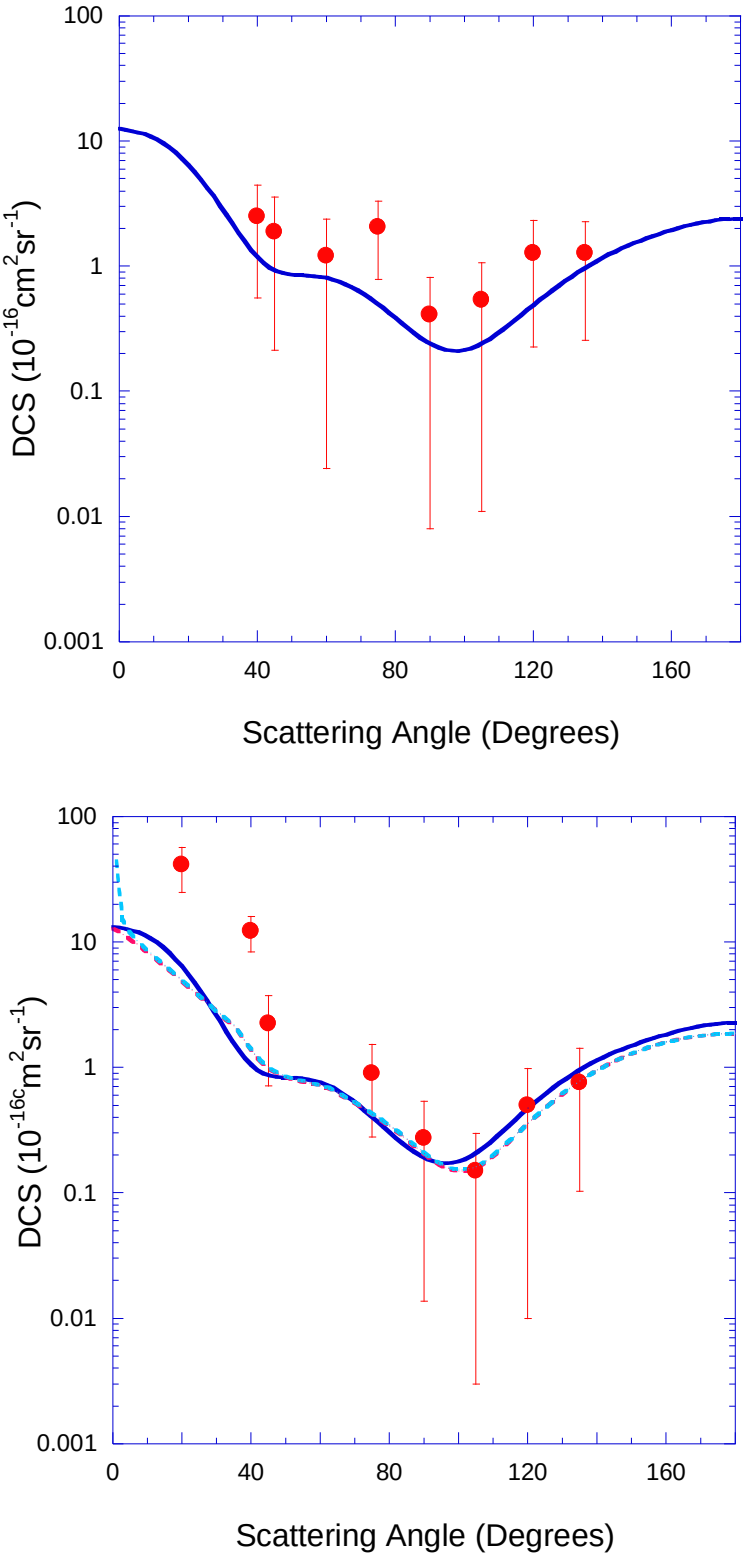

Figure 4.21: Elastic Differential Cross Sections for electrons scattering from CF_3 (10^{-16}cm^{2}sr^{-1}) at electron impact energies of 35eV (top) and 40eV (bottom). Present data (red ●) are compared against the SMC-SE calculations of Winstead and McKoy [156] (blue ——), along with the IAM-SCAR calculations of Blanco and García[72], both with (light blue ••••••••) and without (pink ••••••••) a ground state dipole correction.

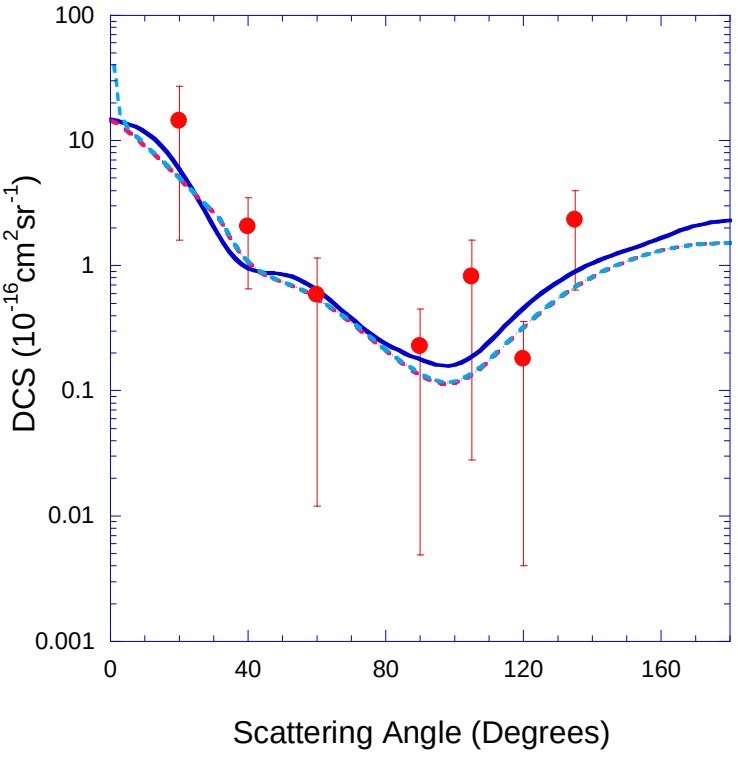

Figure 4.22: Elastic Differential Cross Sections for electrons scattering from CF_3 ($10^{-16}cm^2sr^{-1}$) at the electron impact energy of 50eV. Present data (red ●) are compared against the SMC-SE calculations of Winstead and McKoy [156] (blue ——), along with the IAM-SCAR calculations of Blanco and García[72], both with (light blue ••••••••••) and without (pink ••••••••••) a ground state dipole correction. Note that our experimentally measured iodine cross section was used for the extraction of the CF_3 DCS from the mixed DCS scatter data rather than a DBSR theoretical iodine DCS from Bartschat[71] as was the case at other electron impact energies.

Energy (eV)	Scattering Angle									
	20°	30°	40°	45°	60°	75°	90. °	105°	120°	135°
7	-	-	21.85 ± 13.29	-	15.97 ± 7.64	9.13 ± 4.63	4.91 ± 2.79	6.20 ± 3.13	10.79 ± 4.52	12.87 ± 5.73
10	-	-	44.32 ± 18.18	23.34 ± 11.16	2.56 ± 2.42	3.41 ± 2.09	6.58 ± 2.79	9.11 ± 4.03	4.47 ± 2.14	3.75 ± 2.24
15	142.20 ± 89.72	40.21 ± 21.19	12.19 ± 7.25	20.65 ± 8.70	3.37 ± 1.87	3.88 ± 1.98	3.96 ± 1.87	3.91 ± 1.73	2.95 ± 1.45	5.54 ± 2.41
20	92.58 ± 66.34	63.95 ± 22.30	12.65 ± 5.60	28.41 ± 11.13	4.33 ± 1.99	2.51 ± 1.41	1.84 ± 1.07	-	12.12 ± 4.48	10.00 ± 3.57
25	-	-	2.22 ± 2.17	2.67 ± 2.23	0.83 ± 0.81	-	0.57 ± 0.56	-	1.32 ± 0.93	2.52 ± 1.40
30	16.13 ± 14.61	7.33 ± 4.98	3.46 ± 1.79	1.58 ± 1.34	0.92 ± 0.90	-	0.96 ± 0.53	0.36 ± 0.35	1.07 ± 0.70	1.76 ± 0.89
35	-	-	2.49 ± 1.94	1.89 ± 1.68	1.20 ± 1.18	2.05 ± 1.27	0.41 ± 0.40	0.54 ± 0.53	1.26 ± 1.04	1.26 ± 1.01
40	41.04 ± 18.61	-	12.15 ± 4.47	2.24 ± 1.71	-	0.90 ± 0.72	0.27 ± 0.26	0.15 ± 0.14	0.50 ± 0.49	0.76 ± 0.74
50	14.39± 12.77	-	2.06 ± 1.41	-	0.58 ± 0.57	-	0.23 ± 0.21	0.82 ± 2.75	0.18 ± 1.95	2.31 ± 1.67

Table 4.8: Experimental elastic differential cross sections for electron scattering from CF_3, for electron impact energies from 7 - 50eV, in units of $10^{-16}cm^2sr^{-1}$. These cross sections were determined from a multi-component molecular beam, see text for further details.

4.4.2 Electron Impact Elastic Integral Cross Sections

Presented here are the current ICSs for elastic electron scattering from CF_3 (see table 4.9). These cross sections were again determined in the usual manner, by first extrapolating each elastic CF_3 DCS to 0° and 180°, using a MPSA procedure[73], followed by a standard integration. We note that the elastic DCSs for elastic electron scattering for CF_3 at 50eV were extracted from our mixed DCS data using our experimentally measured electron impact elastic atomic iodine DCS[133]. We cite a conservative 60% overall uncertainty on our ICS data from 7-40eV and an uncertainty of 80% on our 50eV ICS data, reflecting the level of experimental uncertainty in our DCS measurements, in addition to the uncertainty introduced by the extrapolation process.

In figures 4.23 we compare our elastic CF_3 ICSs with those from the IAM-SCAR results from Blanco and García, calculated both and without a correction for dipole scattering[72], and with the R-Matrix results (both with and without a Born correction) from Rozum *et al.*[158]. Also included for comparison are the ICSs produced from our integration of Winstead and McKoy's SMC-SE CF_3 elastic DCS data[156]. Diniz *et al.* reported only partial integral cross sections for singlet and triplet scattering from e + CF_3, but due to the similarity between their elastic CF_3 DCSs and those from Winstead and McKoy, we expect that their total elastic ICSs would also be essentially identical to one another.

When considering figure 4.23 we note immediately that the magnitude of our elastic CF_3 ICSs are much larger than the available theoretical values for the lower electron impact energies, while for incident electron energies of 25eV and above, our ICSs are consistent with the relevant theoretical ICSs to within our level of uncertainty. This result was not unexpected as we had already observed this same general trend in our DCS data (see previous section). We are not certain as to why our measured CF_3 elastic ICSs at energies less than 25eV are so much bigger than all of the present theoretical results. Although as before we speculate that it might be due to the unique physicochemical properties of CF_3 that are as a result of it's open shell nature. Certainly it is clear from figure 4.23 that this effect cannot currently be explained by using any of the standard quantum mechanical methods. One reason our ICSs are larger in magnitude than those from theory is the enhancement of our DCSs at forward scattering angles, likely a result of the ground state permanent dipole of CF_3 ($\mu = 0.43 \pm 0.07\mathrm{D}$ [80]), and its polarisability ($\alpha \approx 9 - 15a_0^3$ [78]) which is itself not a well understood quantity. Taking into account the magnitude of the difference between our lower energy ICSs and those from the various theories, we suspect that this could be a very important result for the low-temperature plasma modelling community.

A less surprising result, when considering figures 4.23, is that the calculations that include dipole scattering (IAM-SCAR and R-Matrix) sit above their non-dipole corrected counter parts. In addition, the anticipated results of this effect becoming more important as you go to lower energies are also seen in this figure.

Finally we note that in contrast to the quite rich resonance structures of CF_2 (see figure 4.8), we see no definitive evidence for any resonances in CF_3 from 7-50eV. Indeed the overall structure of the CF_3 ICS, as displayed by all of the data sets, appears to be almost completely featureless. The only exception to this is a small resonance predicted by Winstead and McKoy[156]. These authors attribute this resonance, occurring at around 11eV, to the combination of A_1 and E resonances as determined by the eigen phase-sum analysis as follows[156]:

$^3A_1$, E=10.89 eV, width=2.14 eV

$^1A_1$, E=11.61 eV, width=2.49 eV

^3E, E=10.43 eV, width=3.73 eV

^1E, E=14.10 eV, width=3.41 eV

Winstead and McKoy[156] note that SMC-SE calculations have a general tendency to predict resonances between 1-2 eV above their actual energy, and thus they expect, had they included polarisation effects, this resonance would have appeared at a lower energy. We did not find any definitive experimental evidence in support of the existence of this resonance, but considering its predicted magnitude, in conjunction with our experimental uncertainties, it is unlikely that our measurements would have been sensitive enough to detect it. Of course it thus follows that our data cannot rule out the existence of this resonance either.

Rozum *et al.* did not detect any energetically low lying electron resonances for CF_3, in either of their R-matrix calculations[158]. To check the consistency of their computations (both with and without a Born correction) they performed their calculations twice; once using an R-matrix sphere with a radius of $10a_0$ and once with a sphere of radius $13a_0$. They obtained essentially identical results[158]. They

also performed their R-matrix calculations using two different complete active space valence CI models, one that produced a ground state dipole moment of 0.51D (their preferred model) and another model(see [158] for details), that produced a ground state dipole moment of 0.68D. As expected, the model with the higher dipole moment resulted in a larger overall ICS, but no resonances were observed using either model.

This lack of any resonance structures, possibly implying an equal lack of low energy dissociative electron attachment (DEA), was suggested by Rozum *et al.* to be an important result. This follows as it could have some major consequences for the plasma processing industry[158]. Their result was the first to suggest that plasmas produced using a feedstock gas such as CF_3I, which would produce predominately CF_3 radicals, could be considerably less electro-negative than a plasma created with either C_2F_4 or C_4F_8, that would result in an abundance of CF and CF_2 radicals. This in turn could lead to a significant effect on the formation of polymers in plasma reactors, which is undesirable as their necessary removal leads to costly down time. In addition, Rozum *et al.* noted that the sheath that normally forms between the plasma, electrode and substrate, could be either reduced or completely absent in the case where there is a lack of anions[158], which would in turn directly affect the cation energies, and transport properties to the etching surface. Unfortunately, as our measurements did not extend below the electron impact energy of 7eV, we cannot test these hypotheses of Rozum *et al.* in relation to the ultimate effects on such plasmas.

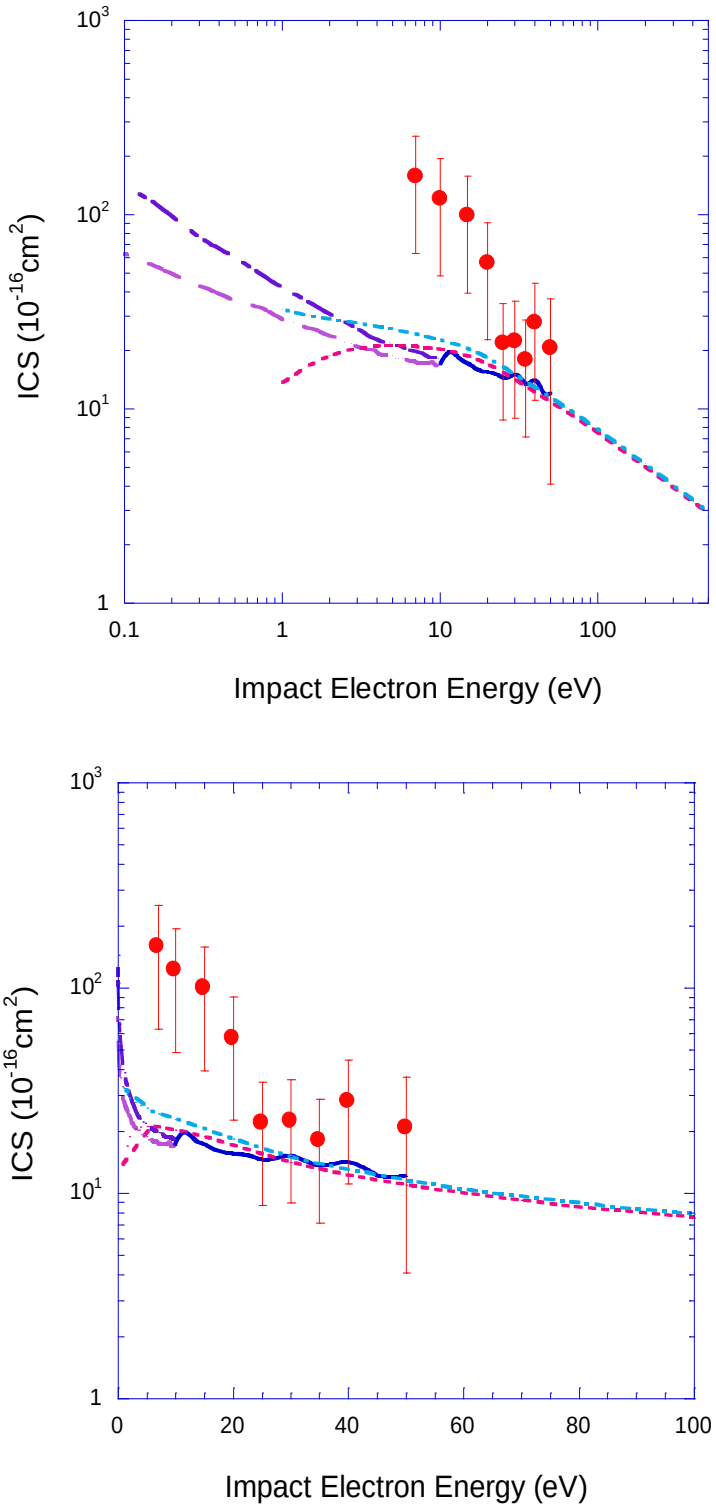

Figure 4.23: Elastic Integral Cross Sections, in units of 10^{-16}cm^2, for electrons scattering from CF_3. The top graph displays the data using a logarithmic scale on the x-axis while the bottom graph displays the same data using a linear scale on the x-axis. The present data (red ●) are compared against the SMC-SE calculations of Winstead and McKoy [156] (blue ——), and the IAM-SCAR calculations of Blanco and García[72], both with (light blue ·····) and without (pink ·····) a ground state dipole correction. Shown additionally are the R-matrix calculations of Rozum *et al.*[158], also both with (purple – — – —) and without (light purple — —) a Born correction.

Table 4.9: Present Integral cross sections ($10^{-16}cm^2$) for elastic e + CF_3 scattering.

Electron Impact Energy (eV)	ICS ($10^{-16}cm^2$)
7	157.9
10	121.2
15	98.9
20	56.8
25	21.8
30	22.4
35	17.9
40	27.8
50	20.5

Note: Uncertainties in the ICS measurements are in the order of 60% for 7-40eV, and in the order of 80% for 50eV.

Chapter 5 — Conclusions and Future Work

A unique apparatus for measuring elastic cross sections for electron scattering from radical species has been described in chapter 2. The measurement procedures and techniques that we developed specifically for this apparatus were also described in detail in chapter 3. Here we concentrate on reviewing the main findings of our investigations into the DCSs and ICSs due to elastic electron interactions with CF_2, CF_3I and CF_3. In addition, we also present in this chapter some of the possible future directions for this research.

5.1 Conclusions

In the case of CF_2(see section 4.1), the electron impact energy of the DCS measurements ranged from 2eV to 20eV, while the accompanying ICSs ranged over 3-20eV. These CF_2 cross sections were compared with the available theories, including the ISVM+DW approximation of Lee *et al*.[27, 145], the UK polyatomic R-matrix method of Rozum *et al*.[21, 25] and the SMC-SE[20] and SMC-SEP[20] computations of Winstead and McKoy. In general we found that the results from the SMC-SE calculations were best able to reproduce both the shapes and magnitudes of the measured DCSs, for incident electron energies from 12eV-20eV, although we highlight that the ISVM+DW calculations of Lee *et al.* also preformed quite well over this energy range. This result extended our earlier finding that SMC-SE level calculations satisfactorily described elastic electron scattering from CF_2 for incident energies between 25-50eV[19]. At lower electron impact energies, where dipole interactions dominate, the level of

agreement between our measured CF_2 data and the various theories became worse. Indeed the SMC-SEP calculations, representing the most sophisticated treatment of dipole interactions of all the calculations, produced the only DCSs whose magnitude agreed with our measured DCS for the more forward scattering angles ($\theta \leq 40°$).

On examination of our ICSs for elastic electron scattering from CF_2, we found some experimental evidence for the existence of a resonance in the energy range 8-20eV. Both Lee *et al*.[27] and Winstead and McKoy[20] predicted resonances would occur in this energy range. In particular Lee *et al*. predicted a $^2B_1$ shape resonance to occur at 15eV, while Winstead and McKoy attributed a peak in their SMC-SEP results to be a result of the overlap of an $^2A_1$ resonance centred at 12eV and the $^2B_2$ resonance centred at 13.5eV. Overall, the measured ICSs are largely consistent with the ICS results of the ISVM+DW[27], SMC-SE[19] and SMC-SEP[19] computations above about 14eV. However for the lower incident electron energies between 8-12eV, all of the theoretical ICSs sit a little above the measured ICSs, even when taking into account the 45% uncertainty attributed to the measured data. Finally, we note that for electron energies between 2eV and 8eV only the SMC-SEP ICSs are consistent with our measured data.

These CF_2 ICS results suggest that a SMC calculation, at the static exchange level, should be adequate for describing the elastic scattering cross sections for electron impact energies above $\sim$12eV in models attempting to describe plasma

reactor behaviour where CF_2 is a constituent. While for electron impact energies between 2-12eV the more computationally expensive SMC-SEP should be employed[20].

As a part of our ultimate investigation into elastic electron scattering from the CF_3 radical, we also measured elastic DCSs and ICSs for electron interactions with CF_3I from 10eV to 50eV(see section 4.2.1). These CF_3I cross sections[67] were compared against the available computational SMC-SE cross sections from Bettega *et al.*[18, 68], along with the experimental results of Kitajima *et al*.[60]. Subsequent to our CF_3I investigation, Cho *et al*.[36] published further CF_3I elastic DCSs and ICSs that were also used as a basis for comparison. Agreement between the various DCS measurements was typically satisfactory, with the exception of the data at 10eV where we were somewhat larger in magnitude at some scattering angles. Overall we also observed a slight divergence in the magnitude of our ICS from the others, for energies below 20eV, although we note that our results were largely consistent with all of the others to within the 45% uncertainty on our ICS data.

While our CF_3I elastic electron impact DCS results were largely consistent with the other available cross sections, in terms of both their shapes and magnitudes, we ultimately chose to use the CF_3I DCSs from Cho *et al*[36], in order to extract the CF_3 component of our "mixed" beam DCS measurements. We note that in the case of stable molecules the current effusive relative flow approaches, such as the one employed by Cho *et al.*[36]*,* are probably a preferable experimental

procedure. This follows simply because the reference gas cross sections are more accurately known for application with the effusive technique compared to those we have to use in our SSRDM approach.

We were able to extract elastic CF_3 DCSs from our measurements of electron scattering from a TOFMS characterised "mixed" beam, ultimately producing a set of CF_3 DCSs and ICSs from 7-50eV (see section 4.3). Those DCSs were compared against results from the SMC-SE level calculations of Diniz *et al*.[58] and the UK polyatomic R-matrix calculations of Rozum *et al*.[21], as well as the unpublished theoretical studies of Blanco and García (IAM-SCAR)[72] and Winstead and McKoy (SMC-SE)[156]. These comparisons were amongst the most notable results of this thesis. We observed that, in general, while the theoretical results clustered closely together, the magnitude of our 7eV CF_3 DCSs was approximately 10 times higher than theory with the difference at 10eV, 15eV and 20eV, being of the order of a factor of 5 higher. However, for larger electron impact energies the level of agreement between the present measurements and the available calculations is actually quite fair. We suggested that those mismatched magnitudes between our DCSs and the theoretical ones, could be an indication that the current theories do not adequately account for the open shell nature of CF_3 and its resultant unique physicochemical properties. If this is indeed the case, then the effect of low energy elastic electron scattering from CF_3 would be considerably greater than originally thought, which in turn could be an important result for the low temperature plasma community in systems where the CF_3 radical plays a role.

Not surprisingly, the elastic electron impact ICSs for CF_3 also proved to have significantly larger magnitudes than any of the theoretical cross sections at energies less than about 20eV. Indeed, if anything, this effect was even more prominent in our ICS data set compared to our DCS data set, due to the compounded effect of the enhanced dipole scattering that we observed at our more forward scattering angles in the DCS.

5.2 Future Directions

As the quality of our CF_3 DCSs is ultimately dependant on the quality of the cross sections we necessarily subtract from our "mixed" beam measurements, we plan to test the accuracy of the available atomic iodine theories by measuring corresponding experimental data. Note that these data sets will be of great interest to the ATMOP community as no such measurements currently exist in the literature. So far the electron impact elastic DCS for atomic iodine has been successfully measured at 50eV using a "mixed" beam from pyrolysis of a CH_3Isource. This "mixed" beam contained approximately 47% atomic iodine and was produced via flash pyrolysis at 1250°C. Once we have finished our current investigation of elastic electron scattering from atomic iodine, we plan to investigate the possibility of undertaking similar studies on Cl and Br (from the pyrolysis of CH_3Cl and CH_3Br). Again, to the best of our knowledge, no such experimental data exists in the literature for these atoms.

Perhaps the most obvious modification, to the present apparatus configuration, that would allow us to extend our studies to other radical species, is the addition of an electron impact ionisation source to our TOFMS. As discussed previously our current ionisation source is the ninth harmonic of an Nd:YAG laser, consequently all species with ionisation energies above 10.48eV are undetectable in this TOFMS. This restriction limits our ability to fully characterise the pyrolysis of any precursor molecule, if more than one possible product has an ionisation energy above 10.48eV. So far we have been able to work around this limitation by carefully choosing our precursor gases. However, this has restricted the species we have been able to study.

Another future possibility involves replacing the spectrometers' present retarding potential analyser array with one (or more) higher resolution detector(s), with the aim of enabling the detection of vibrational excitations. The CF_2 radical, where the vibrational excitation modes are relatively well separated and the molecular beam is pure CF_2, is an obvious starting point for such studies. Note that vibrational excitation, which represents an energy loss mechanism, might be more important to the modellers seeking to understand low temperature plasma behaviour than the elastic data we have provided. In addition, resonances are often easier to detect in vibrational modes than in the elastic channel. So this might well be a very fruitful avenue of research. It is hoped that a higher resolution detection system could also make the electron energy range below 2eV accessible, by discriminating more efficiently between scattered signal and the number of "background counts". This would enable us

to further investigate for the presence of any low lying energy resonances in fluorocarbon radicals.

Appendices

A. Electron impact elastic DCS for atomic iodine

This appendix lists the elastic electron impact DCS in units of $10^{-16}cm^2sr^{-1}$ for atomic iodine in table A, as determined by Bartschat and Zatsarinny[71], using the DBSR method.

Table A: Electron impact elastic DCSs ($10^{-16}cm^2sr^{-1}$) for atomic iodine as determined by Bartschat and Zatsarinny using the DBSR method. Note that this table continues over several pages.

Scattering	Incident Electron Energy (eV)						
Angle °	5	10	15	20	30	40	50
0	2.71E+01	4.91E+01	5.93E+01	7.04E+01	6.90E+01	4.52E+01	4.03E+01
1	2.70E+01	4.89E+01	5.90E+01	7.00E+01	6.85E+01	4.47E+01	3.98E+01
2	2.66E+01	4.82E+01	5.81E+01	6.87E+01	6.70E+01	4.33E+01	3.82E+01
3	2.61E+01	4.71E+01	5.67E+01	6.66E+01	6.46E+01	4.10E+01	3.57E+01
4	2.54E+01	4.57E+01	5.49E+01	6.40E+01	6.15E+01	3.81E+01	3.26E+01
5	2.45E+01	4.41E+01	5.27E+01	6.08E+01	5.78E+01	3.48E+01	2.90E+01
6	2.36E+01	4.22E+01	5.02E+01	5.73E+01	5.38E+01	3.12E+01	2.52E+01
7	2.26E+01	4.03E+01	4.77E+01	5.37E+01	4.96E+01	2.77E+01	2.14E+01
8	2.16E+01	3.84E+01	4.51E+01	5.00E+01	4.55E+01	2.43E+01	1.79E+01
9	2.06E+01	3.64E+01	4.25E+01	4.63E+01	4.14E+01	2.11E+01	1.48E+01
10	1.97E+01	3.46E+01	4.01E+01	4.28E+01	3.77E+01	1.83E+01	1.21E+01
11	1.88E+01	3.28E+01	3.77E+01	3.96E+01	3.41E+01	1.59E+01	9.81E+00
12	1.79E+01	3.12E+01	3.55E+01	3.65E+01	3.09E+01	1.37E+01	7.94E+00
13	1.71E+01	2.96E+01	3.35E+01	3.37E+01	2.80E+01	1.19E+01	6.43E+00
14	1.64E+01	2.82E+01	3.15E+01	3.11E+01	2.53E+01	1.03E+01	5.22E+00
15	1.57E+01	2.68E+01	2.97E+01	2.87E+01	2.29E+01	8.98E+00	4.25E+00
16	1.50E+01	2.55E+01	2.80E+01	2.65E+01	2.07E+01	7.82E+00	3.47E+00
17	1.43E+01	2.43E+01	2.64E+01	2.45E+01	1.87E+01	6.81E+00	2.84E+00
18	1.37E+01	2.31E+01	2.49E+01	2.26E+01	1.68E+01	5.93E+00	2.33E+00
19	1.31E+01	2.20E+01	2.34E+01	2.08E+01	1.51E+01	5.15E+00	1.91E+00
20	1.26E+01	2.10E+01	2.20E+01	1.91E+01	1.35E+01	4.47E+00	1.57E+00
21	1.21E+01	1.99E+01	2.07E+01	1.75E+01	1.21E+01	3.88E+00	1.28E+00
22	1.16E+01	1.90E+01	1.93E+01	1.60E+01	1.08E+01	3.35E+00	1.05E+00
23	1.11E+01	1.80E+01	1.81E+01	1.46E+01	9.52E+00	2.89E+00	8.55E-01
24	1.06E+01	1.71E+01	1.69E+01	1.33E+01	8.39E+00	2.49E+00	6.94E-01
25	1.02E+01	1.62E+01	1.57E+01	1.21E+01	7.35E+00	2.13E+00	5.62E-01
26	9.73E+00	1.54E+01	1.46E+01	1.09E+01	6.41E+00	1.82E+00	4.56E-01
27	9.32E+00	1.45E+01	1.36E+01	9.84E+00	5.55E+00	1.55E+00	3.71E-01
28	8.94E+00	1.38E+01	1.26E+01	8.85E+00	4.78E+00	1.32E+00	3.05E-01
29	8.57E+00	1.30E+01	1.16E+01	7.94E+00	4.10E+00	1.11E+00	2.53E-01

Note this table continues on to the next page

Scattering	Incident Electron Energy (eV)						
Angle °	5	10	15	20	30	40	50
30	8.22E+00	1.23E+01	1.07E+01	7.10E+00	3.48E+00	9.37E-01	2.12E-01
31	7.89E+00	1.17E+01	9.86E+00	6.34E+00	2.94E+00	7.82E-01	1.79E-01
32	7.57E+00	1.10E+01	9.05E+00	5.64E+00	2.46E+00	6.47E-01	1.51E-01
33	7.26E+00	1.04E+01	8.29E+00	5.00E+00	2.04E+00	5.29E-01	1.25E-01
34	6.97E+00	9.82E+00	7.58E+00	4.43E+00	1.67E+00	4.28E-01	1.03E-01
35	6.70E+00	9.27E+00	6.91E+00	3.90E+00	1.35E+00	3.43E-01	8.20E-02
36	6.44E+00	8.73E+00	6.27E+00	3.42E+00	1.08E+00	2.72E-01	6.41E-02
37	6.19E+00	8.23E+00	5.68E+00	2.99E+00	8.54E-01	2.15E-01	4.92E-02
38	5.96E+00	7.75E+00	5.13E+00	2.61E+00	6.63E-01	1.71E-01	3.73E-02
39	5.74E+00	7.29E+00	4.62E+00	2.26E+00	5.07E-01	1.38E-01	2.83E-02
40	5.53E+00	6.86E+00	4.14E+00	1.95E+00	3.81E-01	1.15E-01	2.15E-02
41	5.34E+00	6.45E+00	3.70E+00	1.68E+00	2.82E-01	9.89E-02	1.66E-02
42	5.16E+00	6.07E+00	3.30E+00	1.43E+00	2.08E-01	8.97E-02	1.31E-02
43	4.99E+00	5.70E+00	2.93E+00	1.22E+00	1.55E-01	8.64E-02	1.08E-02
44	4.84E+00	5.36E+00	2.59E+00	1.03E+00	1.21E-01	8.82E-02	9.65E-03
45	4.69E+00	5.04E+00	2.28E+00	8.73E-01	1.05E-01	9.48E-02	9.52E-03
46	4.56E+00	4.74E+00	2.00E+00	7.35E-01	1.03E-01	1.06E-01	1.04E-02
47	4.43E+00	4.45E+00	1.75E+00	6.17E-01	1.15E-01	1.21E-01	1.23E-02
48	4.32E+00	4.18E+00	1.53E+00	5.18E-01	1.37E-01	1.40E-01	1.50E-02
49	4.21E+00	3.93E+00	1.33E+00	4.35E-01	1.69E-01	1.63E-01	1.87E-02
50	4.11E+00	3.69E+00	1.15E+00	3.67E-01	2.09E-01	1.89E-01	2.34E-02
51	4.01E+00	3.47E+00	9.92E-01	3.12E-01	2.54E-01	2.18E-01	2.93E-02
52	3.92E+00	3.26E+00	8.55E-01	2.68E-01	3.03E-01	2.48E-01	3.64E-02
53	3.84E+00	3.06E+00	7.37E-01	2.34E-01	3.55E-01	2.80E-01	4.49E-02
54	3.77E+00	2.88E+00	6.37E-01	2.09E-01	4.08E-01	3.13E-01	5.47E-02
55	3.70E+00	2.71E+00	5.52E-01	1.91E-01	4.60E-01	3.45E-01	6.56E-02
56	3.64E+00	2.55E+00	4.82E-01	1.80E-01	5.11E-01	3.77E-01	7.72E-02
57	3.58E+00	2.40E+00	4.24E-01	1.75E-01	5.60E-01	4.07E-01	8.90E-02
58	3.53E+00	2.26E+00	3.79E-01	1.74E-01	6.05E-01	4.34E-01	1.01E-01
59	3.48E+00	2.13E+00	3.44E-01	1.76E-01	6.46E-01	4.58E-01	1.12E-01
60	3.43E+00	2.01E+00	3.18E-01	1.81E-01	6.83E-01	4.79E-01	1.22E-01
61	3.39E+00	1.89E+00	3.00E-01	1.88E-01	7.15E-01	4.97E-01	1.32E-01
62	3.35E+00	1.79E+00	2.90E-01	1.97E-01	7.42E-01	5.12E-01	1.42E-01
63	3.31E+00	1.69E+00	2.85E-01	2.07E-01	7.63E-01	5.24E-01	1.50E-01
64	3.27E+00	1.60E+00	2.85E-01	2.17E-01	7.80E-01	5.33E-01	1.58E-01
65	3.23E+00	1.52E+00	2.90E-01	2.27E-01	7.90E-01	5.39E-01	1.65E-01
66	3.20E+00	1.44E+00	2.98E-01	2.38E-01	7.95E-01	5.42E-01	1.71E-01
67	3.17E+00	1.37E+00	3.08E-01	2.48E-01	7.95E-01	5.41E-01	1.76E-01
68	3.13E+00	1.30E+00	3.21E-01	2.57E-01	7.89E-01	5.38E-01	1.80E-01
69	3.10E+00	1.24E+00	3.34E-01	2.65E-01	7.78E-01	5.31E-01	1.82E-01
70	3.07E+00	1.18E+00	3.48E-01	2.72E-01	7.63E-01	5.21E-01	1.82E-01
71	3.03E+00	1.13E+00	3.61E-01	2.78E-01	7.42E-01	5.09E-01	1.82E-01
72	3.00E+00	1.08E+00	3.74E-01	2.83E-01	7.18E-01	4.93E-01	1.79E-01

Note this table continues on the next page

Scattering	Incident Electron Energy (eV)						
Angle °	5	10	15	20	30	40	50
73	2.96E+00	1.03E+00	3.86E-01	2.86E-01	6.91E-01	4.76E-01	1.76E-01
74	2.93E+00	9.90E-01	3.97E-01	2.88E-01	6.61E-01	4.57E-01	1.70E-01
75	2.88E+00	9.48E-01	4.07E-01	2.89E-01	6.28E-01	4.35E-01	1.64E-01
76	2.84E+00	9.08E-01	4.15E-01	2.88E-01	5.93E-01	4.13E-01	1.56E-01
77	2.79E+00	8.71E-01	4.20E-01	2.85E-01	5.57E-01	3.89E-01	1.47E-01
78	2.75E+00	8.35E-01	4.24E-01	2.82E-01	5.20E-01	3.65E-01	1.37E-01
79	2.69E+00	8.02E-01	4.27E-01	2.78E-01	4.82E-01	3.41E-01	1.26E-01
80	2.64E+00	7.70E-01	4.27E-01	2.72E-01	4.44E-01	3.17E-01	1.15E-01
81	2.58E+00	7.41E-01	4.25E-01	2.66E-01	4.07E-01	2.93E-01	1.04E-01
82	2.52E+00	7.14E-01	4.22E-01	2.60E-01	3.70E-01	2.71E-01	9.23E-02
83	2.46E+00	6.89E-01	4.16E-01	2.52E-01	3.34E-01	2.49E-01	8.14E-02
84	2.40E+00	6.66E-01	4.09E-01	2.44E-01	2.99E-01	2.30E-01	7.11E-02
85	2.34E+00	6.44E-01	4.01E-01	2.36E-01	2.66E-01	2.12E-01	6.18E-02
86	2.27E+00	6.24E-01	3.90E-01	2.27E-01	2.36E-01	1.98E-01	5.37E-02
87	2.21E+00	6.06E-01	3.79E-01	2.18E-01	2.07E-01	1.85E-01	4.74E-02
88	2.14E+00	5.89E-01	3.66E-01	2.09E-01	1.82E-01	1.77E-01	4.31E-02
89	2.07E+00	5.73E-01	3.53E-01	2.00E-01	1.59E-01	1.71E-01	4.13E-02
90	1.99E+00	5.58E-01	3.39E-01	1.90E-01	1.40E-01	1.69E-01	4.20E-02
91	1.92E+00	5.44E-01	3.24E-01	1.81E-01	1.23E-01	1.71E-01	4.55E-02
92	1.84E+00	5.32E-01	3.10E-01	1.73E-01	1.10E-01	1.76E-01	5.17E-02
93	1.77E+00	5.20E-01	2.95E-01	1.64E-01	9.97E-02	1.85E-01	6.09E-02
94	1.69E+00	5.10E-01	2.81E-01	1.56E-01	9.22E-02	1.97E-01	7.29E-02
95	1.61E+00	5.01E-01	2.67E-01	1.49E-01	8.74E-02	2.13E-01	8.79E-02
96	1.52E+00	4.94E-01	2.53E-01	1.42E-01	8.52E-02	2.31E-01	1.06E-01
97	1.44E+00	4.88E-01	2.40E-01	1.36E-01	8.56E-02	2.53E-01	1.27E-01
98	1.36E+00	4.84E-01	2.28E-01	1.30E-01	8.82E-02	2.78E-01	1.51E-01
99	1.29E+00	4.81E-01	2.17E-01	1.24E-01	9.29E-02	3.05E-01	1.78E-01
100	1.21E+00	4.79E-01	2.06E-01	1.20E-01	9.96E-02	3.35E-01	2.08E-01
101	1.13E+00	4.79E-01	1.97E-01	1.15E-01	1.08E-01	3.68E-01	2.42E-01
102	1.06E+00	4.80E-01	1.88E-01	1.11E-01	1.18E-01	4.02E-01	2.77E-01
103	9.92E-01	4.82E-01	1.81E-01	1.07E-01	1.29E-01	4.38E-01	3.16E-01
104	9.25E-01	4.85E-01	1.74E-01	1.04E-01	1.41E-01	4.76E-01	3.56E-01
105	8.61E-01	4.90E-01	1.69E-01	1.01E-01	1.54E-01	5.14E-01	3.99E-01
106	8.01E-01	4.96E-01	1.65E-01	9.82E-02	1.66E-01	5.52E-01	4.42E-01
107	7.44E-01	5.03E-01	1.62E-01	9.62E-02	1.79E-01	5.89E-01	4.86E-01
108	6.90E-01	5.11E-01	1.61E-01	9.47E-02	1.91E-01	6.25E-01	5.29E-01
109	6.41E-01	5.21E-01	1.60E-01	9.37E-02	2.02E-01	6.58E-01	5.71E-01
110	5.97E-01	5.32E-01	1.62E-01	9.33E-02	2.11E-01	6.89E-01	6.12E-01
111	5.58E-01	5.45E-01	1.64E-01	9.33E-02	2.19E-01	7.16E-01	6.50E-01
112	5.24E-01	5.59E-01	1.68E-01	9.37E-02	2.26E-01	7.40E-01	6.86E-01
113	4.96E-01	5.75E-01	1.73E-01	9.45E-02	2.30E-01	7.59E-01	7.18E-01
114	4.75E-01	5.92E-01	1.79E-01	9.57E-02	2.32E-01	7.75E-01	7.47E-01
115	4.60E-01	6.11E-01	1.85E-01	9.71E-02	2.33E-01	7.86E-01	7.73E-01

Note this table continues on the next page

Scattering	Incident Electron Energy (eV)						
Angle °	5	10	15	20	30	40	50
116	4.53E-01	6.30E-01	1.93E-01	9.86E-02	2.32E-01	7.94E-01	7.95E-01
117	4.52E-01	6.51E-01	2.01E-01	1.00E-01	2.29E-01	7.97E-01	8.13E-01
118	4.59E-01	6.72E-01	2.09E-01	1.02E-01	2.25E-01	7.96E-01	8.27E-01
119	4.73E-01	6.94E-01	2.18E-01	1.04E-01	2.18E-01	7.91E-01	8.37E-01
120	4.94E-01	7.16E-01	2.27E-01	1.05E-01	2.10E-01	7.81E-01	8.42E-01
121	5.23E-01	7.40E-01	2.37E-01	1.07E-01	2.01E-01	7.67E-01	8.43E-01
122	5.60E-01	7.64E-01	2.46E-01	1.09E-01	1.90E-01	7.49E-01	8.38E-01
123	6.05E-01	7.89E-01	2.57E-01	1.10E-01	1.78E-01	7.26E-01	8.29E-01
124	6.57E-01	8.15E-01	2.68E-01	1.12E-01	1.65E-01	6.98E-01	8.13E-01
125	7.19E-01	8.42E-01	2.79E-01	1.14E-01	1.51E-01	6.65E-01	7.92E-01
126	7.88E-01	8.71E-01	2.91E-01	1.16E-01	1.36E-01	6.29E-01	7.65E-01
127	8.66E-01	9.00E-01	3.04E-01	1.18E-01	1.20E-01	5.88E-01	7.33E-01
128	9.52E-01	9.31E-01	3.17E-01	1.20E-01	1.04E-01	5.45E-01	6.96E-01
129	1.05E+00	9.62E-01	3.31E-01	1.22E-01	8.86E-02	4.98E-01	6.54E-01
130	1.15E+00	9.94E-01	3.46E-01	1.24E-01	7.37E-02	4.50E-01	6.08E-01
131	1.26E+00	1.03E+00	3.61E-01	1.27E-01	6.00E-02	4.01E-01	5.60E-01
132	1.38E+00	1.06E+00	3.76E-01	1.29E-01	4.78E-02	3.52E-01	5.09E-01
133	1.51E+00	1.09E+00	3.92E-01	1.32E-01	3.77E-02	3.04E-01	4.57E-01
134	1.64E+00	1.13E+00	4.09E-01	1.34E-01	3.01E-02	2.57E-01	4.05E-01
135	1.78E+00	1.16E+00	4.26E-01	1.37E-01	2.52E-02	2.13E-01	3.53E-01
136	1.93E+00	1.19E+00	4.43E-01	1.39E-01	2.35E-02	1.72E-01	3.02E-01
137	2.09E+00	1.22E+00	4.60E-01	1.42E-01	2.53E-02	1.34E-01	2.53E-01
138	2.25E+00	1.26E+00	4.78E-01	1.45E-01	3.10E-02	1.02E-01	2.07E-01
139	2.41E+00	1.29E+00	4.97E-01	1.47E-01	4.07E-02	7.41E-02	1.63E-01
140	2.58E+00	1.32E+00	5.17E-01	1.50E-01	5.48E-02	5.24E-02	1.24E-01
141	2.76E+00	1.36E+00	5.38E-01	1.53E-01	7.35E-02	3.72E-02	9.01E-02
142	2.94E+00	1.39E+00	5.60E-01	1.56E-01	9.71E-02	2.93E-02	6.14E-02
143	3.13E+00	1.43E+00	5.84E-01	1.59E-01	1.26E-01	2.92E-02	3.91E-02
144	3.32E+00	1.46E+00	6.09E-01	1.62E-01	1.59E-01	3.75E-02	2.38E-02
145	3.51E+00	1.50E+00	6.35E-01	1.65E-01	1.98E-01	5.46E-02	1.63E-02
146	3.71E+00	1.54E+00	6.64E-01	1.68E-01	2.42E-01	8.12E-02	1.72E-02
147	3.91E+00	1.57E+00	6.93E-01	1.72E-01	2.92E-01	1.17E-01	2.70E-02
148	4.11E+00	1.61E+00	7.25E-01	1.75E-01	3.46E-01	1.64E-01	4.63E-02
149	4.32E+00	1.64E+00	7.57E-01	1.79E-01	4.06E-01	2.20E-01	7.53E-02
150	4.52E+00	1.68E+00	7.91E-01	1.83E-01	4.71E-01	2.86E-01	1.14E-01
151	4.73E+00	1.71E+00	8.25E-01	1.87E-01	5.41E-01	3.63E-01	1.63E-01
152	4.93E+00	1.75E+00	8.61E-01	1.91E-01	6.16E-01	4.49E-01	2.22E-01
153	5.14E+00	1.78E+00	8.97E-01	1.95E-01	6.95E-01	5.43E-01	2.90E-01
154	5.34E+00	1.81E+00	9.33E-01	1.99E-01	7.78E-01	6.47E-01	3.68E-01
155	5.54E+00	1.84E+00	9.70E-01	2.04E-01	8.65E-01	7.59E-01	4.54E-01
156	5.74E+00	1.87E+00	1.01E+00	2.08E-01	9.55E-01	8.79E-01	5.49E-01
157	5.93E+00	1.90E+00	1.04E+00	2.13E-01	1.05E+00	1.01E+00	6.52E-01
158	6.12E+00	1.93E+00	1.08E+00	2.17E-01	1.14E+00	1.14E+00	7.62E-01

Note this table continues on the next page

Scattering	Incident Electron Energy (eV)						
Angle °	5	10	15	20	30	40	50
159	6.31E+00	1.96E+00	1.12E+00	2.22E-01	1.24E+00	1.28E+00	8.80E-01
160	6.49E+00	1.98E+00	1.16E+00	2.27E-01	1.34E+00	1.42E+00	1.00E+00
161	6.67E+00	2.01E+00	1.19E+00	2.31E-01	1.43E+00	1.57E+00	1.13E+00
162	6.84E+00	2.03E+00	1.23E+00	2.36E-01	1.53E+00	1.72E+00	1.26E+00
163	7.01E+00	2.06E+00	1.27E+00	2.40E-01	1.63E+00	1.87E+00	1.40E+00
164	7.17E+00	2.08E+00	1.30E+00	2.44E-01	1.72E+00	2.02E+00	1.53E+00
165	7.32E+00	2.11E+00	1.34E+00	2.48E-01	1.82E+00	2.17E+00	1.67E+00
166	7.47E+00	2.13E+00	1.37E+00	2.52E-01	1.91E+00	2.32E+00	1.81E+00
167	7.61E+00	2.15E+00	1.40E+00	2.56E-01	1.99E+00	2.46E+00	1.94E+00
168	7.74E+00	2.17E+00	1.43E+00	2.59E-01	2.08E+00	2.60E+00	2.07E+00
169	7.86E+00	2.18E+00	1.46E+00	2.63E-01	2.16E+00	2.73E+00	2.19E+00
170	7.97E+00	2.20E+00	1.49E+00	2.66E-01	2.23E+00	2.86E+00	2.31E+00
171	8.07E+00	2.21E+00	1.52E+00	2.69E-01	2.30E+00	2.98E+00	2.42E+00
172	8.16E+00	2.22E+00	1.54E+00	2.72E-01	2.37E+00	3.09E+00	2.53E+00
173	8.24E+00	2.24E+00	1.56E+00	2.74E-01	2.42E+00	3.18E+00	2.62E+00
174	8.31E+00	2.24E+00	1.58E+00	2.76E-01	2.48E+00	3.27E+00	2.70E+00
175	8.37E+00	2.25E+00	1.60E+00	2.78E-01	2.52E+00	3.35E+00	2.77E+00
176	8.41E+00	2.26E+00	1.61E+00	2.80E-01	2.56E+00	3.41E+00	2.83E+00
177	8.45E+00	2.26E+00	1.62E+00	2.81E-01	2.59E+00	3.46E+00	2.88E+00
178	8.48E+00	2.27E+00	1.63E+00	2.82E-01	2.61E+00	3.49E+00	2.91E+00
179	8.49E+00	2.27E+00	1.64E+00	2.83E-01	2.62E+00	3.51E+00	2.93E+00
180	8.50E+00	2.27E+00	1.64E+00	2.83E-01	2.63E+00	3.52E+00	2.94E+00

B. Electron impact elastic DCS for molecular iodine

This appendix lists the electron impact DCS in units of $10^{-16}cm^2sr^{-1}$ for molecular iodine in table B, as determined by Blanco and García[72], using the IAM model with a SCAR correction.

Table B: Electron impact elastic DCSs ($10^{-16}cm^2sr^{-1}$) for molecular iodine as determined by Blanco and García[72] using the IAM model with a SCAR correction. Note that this table continues over several pages.

Scattering	Incident Electron Energy (eV)						
Angle °	5	7	10	20	30	40	50
0	4.48E+01	5.77E+01	8.29E+01	1.11E+02	1.23E+02	1.01E+02	6.10E+01
1	4.43E+01	5.66E+01	8.12E+01	1.09E+02	1.20E+02	9.80E+01	5.82E+01
2	4.30E+01	5.48E+01	7.78E+01	1.04E+02	1.14E+02	9.24E+01	5.25E+01
3	4.14E+01	5.25E+01	7.45E+01	9.91E+01	1.09E+02	8.74E+01	4.79E+01
4	3.99E+01	5.04E+01	7.17E+01	9.52E+01	1.03E+02	8.29E+01	4.34E+01
5	3.85E+01	4.85E+01	6.89E+01	9.07E+01	9.80E+01	7.84E+01	3.94E+01
6	3.72E+01	4.66E+01	6.55E+01	8.62E+01	9.30E+01	7.39E+01	3.56E+01
7	3.59E+01	4.49E+01	6.27E+01	8.18E+01	8.85E+01	7.00E+01	3.21E+01
8	3.46E+01	4.31E+01	6.05E+01	7.78E+01	8.34E+01	6.55E+01	2.89E+01
9	3.33E+01	4.14E+01	5.77E+01	7.39E+01	7.90E+01	6.16E+01	2.59E+01
10	3.22E+01	3.99E+01	5.53E+01	7.06E+01	7.45E+01	5.77E+01	2.31E+01
11	3.10E+01	3.84E+01	5.29E+01	6.66E+01	7.06E+01	5.39E+01	2.06E+01
12	2.99E+01	3.68E+01	5.06E+01	6.33E+01	6.61E+01	5.02E+01	1.82E+01
13	2.88E+01	3.54E+01	4.84E+01	5.99E+01	6.22E+01	4.67E+01	1.60E+01
14	2.78E+01	3.41E+01	4.63E+01	5.66E+01	5.82E+01	4.33E+01	1.41E+01
15	2.68E+01	3.28E+01	4.42E+01	5.34E+01	5.47E+01	4.00E+01	1.22E+01
16	2.59E+01	3.16E+01	4.23E+01	5.03E+01	5.12E+01	3.69E+01	1.06E+01
17	2.49E+01	3.04E+01	4.04E+01	4.74E+01	4.77E+01	3.39E+01	9.13E+00
18	2.40E+01	2.92E+01	3.85E+01	4.46E+01	4.44E+01	3.11E+01	7.78E+00
19	2.32E+01	2.81E+01	3.67E+01	4.19E+01	4.13E+01	2.83E+01	6.61E+00
20	2.23E+01	2.70E+01	3.51E+01	3.94E+01	3.82E+01	2.58E+01	5.57E+00
21	2.15E+01	2.60E+01	3.34E+01	3.69E+01	3.53E+01	2.34E+01	4.66E+00
22	2.07E+01	2.50E+01	3.19E+01	3.45E+01	3.26E+01	2.11E+01	3.86E+00
23	2.00E+01	2.40E+01	3.04E+01	3.23E+01	3.00E+01	1.89E+01	3.16E+00
24	1.93E+01	2.31E+01	2.89E+01	3.01E+01	2.76E+01	1.69E+01	2.56E+00
25	1.85E+01	2.22E+01	2.75E+01	2.81E+01	2.52E+01	1.51E+01	2.06E+00
26	1.79E+01	2.14E+01	2.62E+01	2.61E+01	2.30E+01	1.33E+01	1.63E+00
27	1.72E+01	2.06E+01	2.49E+01	2.42E+01	2.09E+01	1.17E+01	1.27E+00
28	1.66E+01	1.98E+01	2.36E+01	2.25E+01	1.90E+01	1.02E+01	9.69E-01
29	1.60E+01	1.90E+01	2.25E+01	2.08E+01	1.71E+01	8.90E+00	7.28E-01
30	1.55E+01	1.83E+01	2.13E+01	1.92E+01	1.54E+01	7.67E+00	5.31E-01
31	1.49E+01	1.76E+01	2.02E+01	1.77E+01	1.38E+01	6.55E+00	3.76E-01

Note this table continues on the next page

Scattering	Incident Electron Energy (eV)						
Angle °	5	7	10	20	30	40	50
32	1.44E+01	1.69E+01	1.92E+01	1.63E+01	1.23E+01	5.53E+00	2.57E-01
33	1.39E+01	1.63E+01	1.81E+01	1.50E+01	1.10E+01	4.63E+00	1.69E-01
34	1.34E+01	1.57E+01	1.72E+01	1.38E+01	9.69E+00	3.83E+00	1.05E-01
35	1.29E+01	1.51E+01	1.63E+01	1.26E+01	8.51E+00	3.12E+00	6.22E-02
36	1.25E+01	1.45E+01	1.55E+01	1.15E+01	7.45E+00	2.50E+00	3.67E-02
37	1.21E+01	1.39E+01	1.46E+01	1.05E+01	6.50E+00	1.97E+00	2.55E-02
38	1.17E+01	1.34E+01	1.38E+01	9.58E+00	5.58E+00	1.52E+00	2.52E-02
39	1.13E+01	1.29E+01	1.30E+01	8.68E+00	4.78E+00	1.14E+00	3.35E-02
40	1.10E+01	1.24E+01	1.24E+01	7.90E+00	4.07E+00	8.23E-01	4.79E-02
41	1.06E+01	1.20E+01	1.17E+01	7.17E+00	3.43E+00	5.77E-01	6.66E-02
42	1.04E+01	1.16E+01	1.10E+01	6.50E+00	2.86E+00	3.82E-01	8.85E-02
43	1.00E+01	1.11E+01	1.04E+01	5.82E+00	2.37E+00	2.42E-01	1.11E-01
44	9.74E+00	1.08E+01	9.86E+00	5.28E+00	1.94E+00	1.49E-01	1.36E-01
45	9.52E+00	1.04E+01	9.30E+00	4.76E+00	1.57E+00	9.69E-02	1.59E-01
46	9.24E+00	1.00E+01	8.79E+00	4.30E+00	1.25E+00	8.12E-02	1.81E-01
47	9.02E+00	9.69E+00	8.29E+00	3.88E+00	9.91E-01	9.63E-02	2.03E-01
48	8.79E+00	9.35E+00	7.84E+00	3.49E+00	7.78E-01	1.38E-01	2.22E-01
49	8.62E+00	9.02E+00	7.39E+00	3.15E+00	6.10E-01	2.01E-01	2.40E-01
50	8.40E+00	8.74E+00	7.00E+00	2.86E+00	4.76E-01	2.81E-01	2.56E-01
51	8.23E+00	8.46E+00	6.61E+00	2.59E+00	3.77E-01	3.74E-01	2.71E-01
52	8.06E+00	8.18E+00	6.27E+00	2.35E+00	3.09E-01	4.76E-01	2.84E-01
53	7.95E+00	7.90E+00	5.94E+00	2.14E+00	2.66E-01	5.82E-01	2.96E-01
54	7.78E+00	7.67E+00	5.60E+00	1.97E+00	2.46E-01	6.94E-01	3.05E-01
55	7.67E+00	7.45E+00	5.31E+00	1.81E+00	2.45E-01	8.06E-01	3.14E-01
56	7.56E+00	7.17E+00	5.03E+00	1.67E+00	2.58E-01	9.07E-01	3.21E-01
57	7.39E+00	6.94E+00	4.77E+00	1.56E+00	2.85E-01	1.01E+00	3.28E-01
58	7.28E+00	6.78E+00	4.52E+00	1.46E+00	3.21E-01	1.10E+00	3.32E-01
59	7.22E+00	6.55E+00	4.29E+00	1.37E+00	3.65E-01	1.19E+00	3.35E-01
60	7.11E+00	6.33E+00	4.07E+00	1.29E+00	4.13E-01	1.27E+00	3.37E-01
61	7.00E+00	6.16E+00	3.86E+00	1.23E+00	4.63E-01	1.33E+00	3.37E-01
62	6.89E+00	5.99E+00	3.67E+00	1.18E+00	5.15E-01	1.38E+00	3.35E-01
63	6.83E+00	5.77E+00	3.49E+00	1.13E+00	5.66E-01	1.43E+00	3.32E-01
64	6.72E+00	5.60E+00	3.32E+00	1.09E+00	6.16E-01	1.46E+00	3.27E-01
65	6.66E+00	5.45E+00	3.16E+00	1.06E+00	6.61E-01	1.47E+00	3.20E-01
66	6.55E+00	5.28E+00	3.01E+00	1.02E+00	7.06E-01	1.48E+00	3.11E-01
67	6.50E+00	5.11E+00	2.86E+00	9.97E-01	7.39E-01	1.47E+00	3.01E-01
68	6.38E+00	4.95E+00	2.72E+00	9.74E-01	7.73E-01	1.46E+00	2.88E-01
69	6.27E+00	4.78E+00	2.59E+00	9.46E-01	7.95E-01	1.43E+00	2.73E-01
70	6.22E+00	4.63E+00	2.46E+00	9.24E-01	8.18E-01	1.39E+00	2.57E-01
71	6.10E+00	4.47E+00	2.34E+00	8.96E-01	8.29E-01	1.35E+00	2.40E-01
72	5.99E+00	4.31E+00	2.22E+00	8.74E-01	8.34E-01	1.29E+00	2.21E-01
73	5.88E+00	4.16E+00	2.11E+00	8.51E-01	8.34E-01	1.23E+00	2.02E-01
74	5.77E+00	4.00E+00	2.00E+00	8.23E-01	8.29E-01	1.16E+00	1.81E-01

Note this table continues on the next page

Scattering	Incident Electron Energy (eV)						
Angle °	5	7	10	20	30	40	50
75	5.66E+00	3.85E+00	1.90E+00	7.95E-01	8.18E-01	1.10E+00	1.60E-01
76	5.56E+00	3.70E+00	1.80E+00	7.67E-01	7.95E-01	1.02E+00	1.39E-01
77	5.43E+00	3.54E+00	1.71E+00	7.39E-01	7.73E-01	9.41E-01	1.19E-01
78	5.30E+00	3.39E+00	1.61E+00	7.11E-01	7.45E-01	8.57E-01	9.86E-02
79	5.17E+00	3.24E+00	1.52E+00	6.78E-01	7.11E-01	7.73E-01	7.95E-02
80	5.03E+00	3.10E+00	1.44E+00	6.44E-01	6.78E-01	6.94E-01	6.16E-02
81	4.89E+00	2.95E+00	1.36E+00	6.10E-01	6.38E-01	6.10E-01	4.53E-02
82	4.74E+00	2.80E+00	1.27E+00	5.82E-01	5.99E-01	5.36E-01	3.12E-02
83	4.59E+00	2.65E+00	1.19E+00	5.47E-01	5.54E-01	4.62E-01	1.95E-02
84	4.44E+00	2.51E+00	1.11E+00	5.15E-01	5.11E-01	3.92E-01	1.06E-02
85	4.27E+00	2.37E+00	1.04E+00	4.83E-01	4.66E-01	3.28E-01	4.76E-03
86	4.11E+00	2.23E+00	9.69E-01	4.51E-01	4.22E-01	2.70E-01	2.37E-03
87	3.94E+00	2.09E+00	9.02E-01	4.21E-01	3.79E-01	2.18E-01	3.72E-03
88	3.76E+00	1.95E+00	8.34E-01	3.92E-01	3.37E-01	1.74E-01	9.02E-03
89	3.59E+00	1.81E+00	7.73E-01	3.65E-01	2.96E-01	1.37E-01	1.85E-02
90	3.41E+00	1.69E+00	7.11E-01	3.39E-01	2.58E-01	1.08E-01	3.23E-02
91	3.23E+00	1.56E+00	6.55E-01	3.16E-01	2.22E-01	8.68E-02	5.06E-02
92	3.05E+00	1.43E+00	6.05E-01	2.96E-01	1.89E-01	7.34E-02	7.34E-02
93	2.87E+00	1.31E+00	5.56E-01	2.77E-01	1.60E-01	6.78E-02	1.01E-01
94	2.68E+00	1.19E+00	5.11E-01	2.62E-01	1.33E-01	7.00E-02	1.32E-01
95	2.50E+00	1.08E+00	4.69E-01	2.50E-01	1.10E-01	7.95E-02	1.67E-01
96	2.32E+00	9.69E-01	4.31E-01	2.40E-01	9.02E-02	9.58E-02	2.07E-01
97	2.14E+00	8.68E-01	3.98E-01	2.34E-01	7.39E-02	1.19E-01	2.50E-01
98	1.96E+00	7.67E-01	3.68E-01	2.31E-01	6.10E-02	1.47E-01	2.97E-01
99	1.79E+00	6.78E-01	3.43E-01	2.31E-01	5.15E-02	1.81E-01	3.46E-01
100	1.61E+00	5.88E-01	3.22E-01	2.34E-01	4.52E-02	2.19E-01	3.98E-01
101	1.45E+00	5.10E-01	3.06E-01	2.39E-01	4.22E-02	2.60E-01	4.51E-01
102	1.29E+00	4.36E-01	2.93E-01	2.48E-01	4.19E-02	3.05E-01	5.06E-01
103	1.13E+00	3.69E-01	2.86E-01	2.60E-01	4.44E-02	3.51E-01	5.60E-01
104	9.86E-01	3.09E-01	2.82E-01	2.74E-01	4.93E-02	3.98E-01	6.16E-01
105	8.46E-01	2.56E-01	2.83E-01	2.91E-01	5.66E-02	4.46E-01	6.72E-01
106	7.11E-01	2.11E-01	2.88E-01	3.10E-01	6.55E-02	4.93E-01	7.28E-01
107	5.94E-01	1.73E-01	2.98E-01	3.31E-01	7.62E-02	5.39E-01	7.78E-01
108	4.79E-01	1.43E-01	3.12E-01	3.54E-01	8.79E-02	5.82E-01	8.29E-01
109	3.77E-01	1.22E-01	3.31E-01	3.79E-01	1.01E-01	6.22E-01	8.79E-01
110	2.87E-01	1.08E-01	3.53E-01	4.05E-01	1.15E-01	6.61E-01	9.18E-01
111	2.09E-01	1.02E-01	3.80E-01	4.33E-01	1.29E-01	6.94E-01	9.63E-01
112	1.44E-01	1.05E-01	4.10E-01	4.61E-01	1.44E-01	7.17E-01	9.97E-01
113	9.18E-02	1.17E-01	4.45E-01	4.91E-01	1.58E-01	7.39E-01	1.03E+00
114	5.36E-02	1.37E-01	4.83E-01	5.20E-01	1.72E-01	7.56E-01	1.05E+00
115	2.96E-02	1.66E-01	5.25E-01	5.50E-01	1.86E-01	7.67E-01	1.08E+00
116	2.05E-02	2.03E-01	5.71E-01	5.82E-01	1.99E-01	7.73E-01	1.09E+00
117	2.67E-02	2.49E-01	6.16E-01	6.10E-01	2.11E-01	7.67E-01	1.10E+00

Note this table continues on the next page

Scattering	Incident Electron Energy (eV)						
Angle °	5	7	10	20	30	40	50
118	4.86E-02	3.04E-01	6.72E-01	6.38E-01	2.21E-01	7.56E-01	1.10E+00
119	8.62E-02	3.66E-01	7.22E-01	6.66E-01	2.30E-01	7.39E-01	1.10E+00
120	1.41E-01	4.37E-01	7.84E-01	6.94E-01	2.38E-01	7.17E-01	1.09E+00
121	2.11E-01	5.17E-01	8.40E-01	7.22E-01	2.45E-01	6.89E-01	1.07E+00
122	2.99E-01	6.05E-01	9.02E-01	7.45E-01	2.50E-01	6.55E-01	1.05E+00
123	4.03E-01	7.00E-01	9.69E-01	7.67E-01	2.54E-01	6.16E-01	1.01E+00
124	5.25E-01	8.06E-01	1.04E+00	7.90E-01	2.56E-01	5.71E-01	9.80E-01
125	6.61E-01	9.13E-01	1.10E+00	8.12E-01	2.58E-01	5.26E-01	9.35E-01
126	8.18E-01	1.04E+00	1.17E+00	8.29E-01	2.59E-01	4.76E-01	8.90E-01
127	9.91E-01	1.16E+00	1.24E+00	8.46E-01	2.58E-01	4.24E-01	8.40E-01
128	1.18E+00	1.29E+00	1.32E+00	8.57E-01	2.58E-01	3.71E-01	7.84E-01
129	1.38E+00	1.43E+00	1.39E+00	8.74E-01	2.56E-01	3.19E-01	7.22E-01
130	1.61E+00	1.58E+00	1.46E+00	8.79E-01	2.55E-01	2.68E-01	6.61E-01
131	1.84E+00	1.73E+00	1.54E+00	8.90E-01	2.54E-01	2.20E-01	5.99E-01
132	2.10E+00	1.89E+00	1.61E+00	8.96E-01	2.54E-01	1.75E-01	5.34E-01
133	2.37E+00	2.05E+00	1.69E+00	8.96E-01	2.54E-01	1.34E-01	4.70E-01
134	2.65E+00	2.22E+00	1.76E+00	9.02E-01	2.55E-01	1.00E-01	4.06E-01
135	2.95E+00	2.39E+00	1.84E+00	9.02E-01	2.59E-01	7.28E-02	3.44E-01
136	3.26E+00	2.56E+00	1.92E+00	8.96E-01	2.63E-01	5.42E-02	2.86E-01
137	3.58E+00	2.74E+00	1.99E+00	8.96E-01	2.70E-01	4.47E-02	2.30E-01
138	3.92E+00	2.93E+00	2.06E+00	8.90E-01	2.79E-01	4.56E-02	1.80E-01
139	4.27E+00	3.12E+00	2.13E+00	8.79E-01	2.91E-01	5.77E-02	1.34E-01
140	4.63E+00	3.31E+00	2.21E+00	8.74E-01	3.06E-01	8.23E-02	9.41E-02
141	5.00E+00	3.51E+00	2.28E+00	8.62E-01	3.24E-01	1.20E-01	6.10E-02
142	5.38E+00	3.70E+00	2.35E+00	8.51E-01	3.44E-01	1.71E-01	3.57E-02
143	5.77E+00	3.89E+00	2.42E+00	8.46E-01	3.69E-01	2.36E-01	1.79E-02
144	6.16E+00	4.09E+00	2.49E+00	8.34E-01	3.98E-01	3.16E-01	8.51E-03
145	6.55E+00	4.29E+00	2.55E+00	8.18E-01	4.30E-01	4.12E-01	7.95E-03
146	6.94E+00	4.49E+00	2.62E+00	8.06E-01	4.66E-01	5.23E-01	1.66E-02
147	7.39E+00	4.69E+00	2.68E+00	7.90E-01	5.06E-01	6.50E-01	3.47E-02
148	7.78E+00	4.88E+00	2.75E+00	7.73E-01	5.50E-01	7.90E-01	6.27E-02
149	8.18E+00	5.08E+00	2.81E+00	7.62E-01	5.99E-01	9.46E-01	1.00E-01
150	8.62E+00	5.28E+00	2.87E+00	7.45E-01	6.50E-01	1.12E+00	1.48E-01
151	9.02E+00	5.47E+00	2.92E+00	7.34E-01	7.06E-01	1.31E+00	2.05E-01
152	9.46E+00	5.66E+00	2.98E+00	7.17E-01	7.67E-01	1.51E+00	2.72E-01
153	9.86E+00	5.82E+00	3.04E+00	7.06E-01	8.29E-01	1.72E+00	3.48E-01
154	1.02E+01	6.05E+00	3.09E+00	6.89E-01	8.96E-01	1.95E+00	4.34E-01
155	1.07E+01	6.22E+00	3.14E+00	6.78E-01	9.63E-01	2.18E+00	5.28E-01
156	1.11E+01	6.38E+00	3.19E+00	6.61E-01	1.04E+00	2.43E+00	6.33E-01
157	1.15E+01	6.55E+00	3.23E+00	6.50E-01	1.11E+00	2.69E+00	7.39E-01
158	1.19E+01	6.72E+00	3.28E+00	6.38E-01	1.19E+00	2.95E+00	8.57E-01
159	1.22E+01	6.89E+00	3.32E+00	6.27E-01	1.27E+00	3.21E+00	9.74E-01
160	1.26E+01	7.06E+00	3.35E+00	6.16E-01	1.34E+00	3.48E+00	1.10E+00

Note this table continues on the next page

Scattering	Incident Electron Energy (eV)						
Angle °	5	7	10	20	30	40	50
161	1.29E+01	7.22E+00	3.39E+00	6.05E-01	1.43E+00	3.76E+00	1.23E+00
162	1.33E+01	7.39E+00	3.43E+00	5.99E-01	1.51E+00	4.03E+00	1.36E+00
163	1.36E+01	7.50E+00	3.47E+00	5.88E-01	1.58E+00	4.30E+00	1.50E+00
164	1.39E+01	7.67E+00	3.49E+00	5.82E-01	1.66E+00	4.57E+00	1.63E+00
165	1.43E+01	7.78E+00	3.53E+00	5.71E-01	1.74E+00	4.83E+00	1.76E+00
166	1.46E+01	7.90E+00	3.56E+00	5.66E-01	1.81E+00	5.08E+00	1.89E+00
167	1.48E+01	8.01E+00	3.58E+00	5.60E-01	1.88E+00	5.33E+00	2.02E+00
168	1.51E+01	8.12E+00	3.60E+00	5.56E-01	1.95E+00	5.57E+00	2.13E+00
169	1.53E+01	8.23E+00	3.62E+00	5.51E-01	2.01E+00	5.77E+00	2.25E+00
170	1.56E+01	8.29E+00	3.65E+00	5.47E-01	2.07E+00	5.99E+00	2.36E+00
171	1.57E+01	8.40E+00	3.66E+00	5.43E-01	2.13E+00	6.16E+00	2.46E+00
172	1.59E+01	8.46E+00	3.67E+00	5.40E-01	2.17E+00	6.38E+00	2.55E+00
173	1.61E+01	8.51E+00	3.69E+00	5.37E-01	2.22E+00	6.50E+00	2.63E+00
174	1.62E+01	8.57E+00	3.71E+00	5.35E-01	2.26E+00	6.66E+00	2.70E+00
175	1.64E+01	8.62E+00	3.71E+00	5.33E-01	2.30E+00	6.78E+00	2.77E+00
176	1.65E+01	8.68E+00	3.72E+00	5.31E-01	2.32E+00	6.89E+00	2.82E+00
177	1.65E+01	8.74E+00	3.73E+00	5.30E-01	2.35E+00	6.94E+00	2.86E+00
178	1.66E+01	8.74E+00	3.73E+00	5.29E-01	2.36E+00	7.00E+00	2.89E+00
179	1.66E+01	8.74E+00	3.74E+00	5.29E-01	2.37E+00	7.06E+00	2.91E+00
180	1.66E+01	8.74E+00	3.74E+00	5.29E-01	2.37E+00	7.06E+00	2.91E+00

References

1. J. W. McConkey, *Electron Collisions - Past Present and Future*, in *Proceedings of the XXIV International Conference on Photonic, Electronic and Atomic Collisions*. 2006, World Scientific Publishing Co. Pty. Ltd.: Singapore. p. 3-15.

2. M. J. Brunger, L. Campbell, and D. C. Cartwright, *Studying the effects of electron-impact excitation in the upper atmosphere.* Trends in Applied Spectroscopy, 2004. **5**: p. 39-54.

3. L. Campbell, et al., *Prediction of electron-driven VUV emission in the earth's atmosphere.* J. Electron. Spectrosc. Relat. Phenom., 2005. **144-147**: p. 119-122.

4. L. Campbell, M. J. Brunger, and P. J. O. Teubner, *Electron Driven Processes in Atmospheric Behaviour*, in *Proceedings of the XXIV International Conference on Photonic, Electronic and Atomic Collisions*. 2006, World Scientific Publishing Co. Pty. Ltd: Singapore. p. 305-312.

5. L. Campbell and M. J. Brunger, *Electron cooling by carbon monoxide in the atmospheres of Mars and Venus.* PMC Physics B, 2008. **1**(3).

6. L. Campbell, M. J. Brunger, and T. N. Rescigno, *Carbon dioxide electron cooling rates in the atmospheres of Mars and Venus.* J. Geophys. Res., 2008. **113**: p. E08008 (7 pages).

7. I. Rozum, N. J. Mason, and J. Tennyson, *Electron collisions with the CF radicals using the R-matrix method.* J. Phys. B. At. Mol. Opt. Phys., 2003. **36**: p. 2419-2432.

8. D. B. Graves, et al., *Database Needs for Modeling and Simulation of Plasma Processing*. 1996 National Research Council, National Academy Press: Washington D.C.

9. F. L Arnot, *The Diffraction of Electrons in Gases.* Proc. R. Soc. Lond. A., 1931. **133**: p. 615-636.

10. M. J. Brunger and S. J. Buckman, *Developments in techniques for cross-section determination in electron scattering experiments: from Lenard to the present day.* The Nucleus, 1997. **34**(3-4): p. 201-213.

11. J. C. Nickel, et al., *Principles and procedures for determining absolute differential electron-molecule (atom) scattering cross sections.* J. Phys. E: Sci. Instrum., 1989. **22**: p. 730-738.

12. M. J. Brunger and S. J. Buckman, *Electron–molecule scattering cross-sections. I. Experimental techniques and data for diatomic molecules* Phys. Rep., 2002. **357**: p. 215-458.

13. N. J. Mason, *The status of the database for plasma processing.* J. Phys. D: Appl. Phys., 2009. **42**: p. 11.

14. M. Hoshino, et al., *Elastic Differential Cross Sections for Electron Collisions with Polyatomic Molecules*, in *National Institute for Fusion Science Data Series 101*. 2008: Toki, Japan.

15. T. Underwood-Lemons, et al., *Low-energy electron scattering cross sections of halofluorocarbons.* Chem. Phys., 1994. **100**: p. 9117-9122.

16. S. J. Buckman and C.W. Clark, *Atomic negative-open resonances.* Rev. Mod. Phys., 1994. **66**(2): p. 539-655.

17. G. J. Schulz, *Resonances in Electron Impact on Atoms and Diatomic Molecules.* Rev. Mod. Phys., 1973. **45**(3): p. 378-486.

18. M. H. F. Bettega, et al., *Elastic scattering of low-energy electrons by CF_3Cl, CF_3Br and CF_3I.* J. Phys. B. At. Mol. Opt. Phys., 2003. **36**: p. 1263-1272.

19*. T. M. Maddern, et al., *Absolute Electron Scattering Cross Sections for the CF_2 Radical.* Phys. Rev. Lett., 2008. **100**: p. 063202-063205.

20* J. R. Francis-Staite, et al., *Differential and Integral Cross Sections for Elastic Electron Scattering from CF_2.* Phys. Rev. A, 2009. **79**: p. 052705 (9 pages).

21. I. Rozum and J. Tennyson, *Elastic differential cross sections for the CF_x (x = 1, 2, 3) radicals.* J. Phys. B. At. Mol. Opt. Phys., 2004. **37**: p. 957-966.

22. J. V. DiCarlo and M. J. Kushner, *Solving the spatially dependent Boltzmann's equation for the electron-velocity distribution using flux corrected transport.* J. Appl. Phys., 1989. **66**(12): p. 5763-5774.

23. M. Kushner, *Controlling the Properties of Low Temperature Plasmas: The Role of Modelling in Investigating the Science and Developing the Technology*, in *Allis Prize Lecture at the 63rd Gaseous Electronics Conference and the 7th International Conference on Reactive Plasmas*. 2010: Paris, France.

24. J. Proud, R. Gottscho, and J. Bondur, *Plasma Processing of Materials: Scientific Opportunities and Technological Challenges*. Commission on Physical Sciences, Mathematics, Applications 1991, Washington, D.C.: National Academy Press.

25. I. Rozum, N. J. Mason, and J. Tennyson, *Electron collisions with the CF_2 radical using the R-matrix method.* J. Phys. B. At. Mol. Opt. Phys., 2002. **35**: p. 1583-1591.

26. S. Raoux, et al., *Remote microwave plasma source for cleaning chemical vapour deposition chambers: Technology for reducing global warming gas emissions.* J. Vac. Sci. Technol. B, 1999. **17**: p. 477-486.

27. M.-T. Lee, et al., *Theoretical study of electron collisions with the CF_2 radical.* Phys. Rev. A, 2006. **74**: p. 052716 (7 pages).

28. P. Chabert, et al., *Radical dynamics in unstable CF_4 inductive discharges.* J. Appl. Phys., 2003. **94**(1): p. 76-84.

29. L. G. Christophorou and J. K. Olthoff, *Electron Interactions with CF_3I.* J. Phys. Chem. Ref. Data, 2000. **29**(4): p. 553-569.

30. S. Marienfeld, et al., *High resolution low-energy electron attachment to CF_3I.* J. Phys. B. At. Mol. Opt. Phys., 2006. **39**: p. 105-126.

31. M. K. Kawada, O. Sueoka, and M. Kimura, *Electron and positron scattering from CF_3I molecules below 600 eV: a comparison with CF_3H.* Chem. Phys. Lett., 2000. **330**: p. 34-40.

32. I. Rozum, et al., *Electron Interaction Cross Sections for CF_3I, C_2F_4, and CF_x (x=1-3) Radicals.* J. Phys. Chem. Ref. Data, 2006. **35**(1): p. 267-284.

33. S. Samukawa, T. Mukai, and K. Tsuda, *New radical control method for high-performance dielectric etching with nonperfluorocompound gas chemistries in ultrahigh-frequency plasma.* J. Vac. Sci. Technol. A, 1999. **17**: p. 2551-2557.

34. T. Oster, et al., *Anion formation from gaseous and condensed CF_3I on low energy electron impact.* J. Chem. Phys., 1993. **99**: p. 5141-5151.

35. Y. Li, et al., *Potential impacts of CF_3I on ozone as a replacement for CF_3Br in aircraft applications.* Atmos. Chem. Phys, 2006. **6**: p. 4559–4568.

36. H. Cho, et al., *Elastic electron scattering from CF_3H and CF_3I.* J. Phys. B. At. Mol. Opt. Phys., 2010. **43**: p. 135205-135213.

37. T. Tanaka, et al., *Photoabsorption spectra of CF_3I and thermally dissociated CF_3I near the C 1s, I 3d and F 1s ionisation thresholds.* J. Electron. Spectrosc. Relat. Phenom., 2008. **164**: p. 24-27.

38. M. Haverlag, et al., *High-resolution infrared spectroscopy of etching plasmas* Plasma Sources Sci. Technol., 1995. **4**: p. 260.

39. M. Cameron, S. H. Kable, and G. B. Bacskay, *The electronic spectroscopy of jet-cooled difluorocarbene (CF_2): The missing Ã-state stretching frequencies.* J. Chem. Phys., 1995. **103**(11): p. 4476-4483.

40. M. Cameron and S. Kable, *Rotational State Dependent Fluorescence Lifetimes in CF_2.* J. Mol. Spectrosc., 1998. **192**: p. 449-451.

41. D. E. Milligan, D. E. Mann, and M. E. Jacox, *Infrared Spectrum of CF_2.* J. Chem. Phys., 1964. **41**(5): p. 1199-1203.

42. Venkateswarlu, P., *On the Emission Bands of CF_2.* Phys. Rev. , 1950. **77**(5): p. 676-680.

43. D. E. Milligan, M. E. Jacox, and J. J. Comeford, *Infrared Spectrum of the Free Radical CF_3 Isolated in Inert Matrices.* J. Chem. Phys., 1966. **44**: p. 4058-4059.

44. K. Maruyamat, A. Sakai, and T. Gotot, *Measurement of the CF_3, radical using infrared diode laser absorption spectroscopy.* J. Phys. D: Appl. Phys., 1993. **26**: p. 199-202.

45. C. Yamada and E. Hirota, *Infrared diode laser spectroscopy of the CF_3 ν_3 band.* J. Chem. Phys., 1983. **78**(4): p. 1703-1712.

46. G. A. Carlson and G.C. Pimentel, *Infrared Detection of Gaseous Trifluoromethyl Radical.* J. Chem. Phys., 1996. **44**: p. 4053-4054.

47. F. Aguirre and S. T. Pratt, *Photoionization of vibrationally hot CH_3 and CF_3.* J. Chem. Phys., 2005. **122**(23): p. 234303 (13 Pages).

48. M. Suto and L. C. Lee, *Emission spectra of CF_3 radicals. V. Photodissociation of CF_3H, CF_3Cl, and CF_3Br by vacuum ultraviolet.* J. Chem. Phys., 1979. **79**: p. 1127-1133.

49. M. Suto and N. Washida, *Emission spectra of CF_3 radicals. I. UV and visible emission spectra of CF_3 observed in the VUV photolysis and the metastable argon atom reaction of CF_3H.* J. Chem. Phys., 1983. **78**(3): p. 1007-1011.

50. M. Suto and N. Washida, *Emission spectra of CF_3 radicals. II. Analysis of the UV emission spectrum of CF_3 radicals.* J. Chem. Phys., 1983. **78**(3): p. 1012-1018.

51. M. Suto, et al., *Emission spectra of CF_3 radicals. III. Spectra and quenching of CF_3 emission bands produced in the VUV photolyses of CF_3Cl and CF_3Br.* J. Chem. Phys., 1983. **78**(3): p. 1019-1024.

52. N. Washida, et al., *Emission spectra of CF_3 radicals. IV. Excitation spectra, quantum yields, and potential energy surfaces of the CF_3 fluorescences.* J. Chem. Phys., 1983. **78**(3): p. 1025-1032.

53. Y. Endo, et al., *The microwave spectrum of the trifluoromethyl radical.* J. Chem. Phys., 1982. **77**: p. 3376-3382.

54. T. M. Maddern, et al., *An apparatus for measuring absolute electron scattering cross sections for molecular radicals.* Meas. Sci. Technol., 2008. **19**: p. 085801 (8 Pages).

55. V. Tarnovsky and K. Becker, *Absolute partial cross sections for the parent ionization of the CF_x (x= 1-3) free radicals by electron impact.* J. Chem. Phys., 1993. **98**: p. 7868-7874.

56. H. Deutsch, et al., *Theoretical determination of absolute electron-impact ionization cross sections of molecules.* Int. J. Mass Spectrom., 2000. **197**: p. 37-69.

57. W. M. Huo, V. Tarnovsky, and K. Becker, *Total electron-impact ionization cross-sections of CF_x and NF_x (x=1-3).* Chem. Phys. Lett., 2002. **358**: p. 328-336.

58. R. B. Diniz, M. A. P. Lima, and F. J. da Paixão, *Elastic differential cross sections for electron collision with CF_3 and CF_3H.* J. Phys. B. At. Mol. Opt. Phys., 1999. **32**: p. L539-L545.

59. J. Tennyson, et al., *Electron molecule collisions calculations using the R-matrix method.* Radiat. Phys. Chem., 2003. **68**: p. 65-72.

60. M. Kitajima, et al., *Low-energy electron impact elastic and inelastic scattering from CF_3I.* J. Phys. B. At. Mol. Opt. Phys., 2002. **35**: p. 3257-3263.

61. K. N. Joshipura, et al., *Calculated total cross sections of electron-impact ionization and excitations in tetrahedral (XY_4) and SF_6 molecules.* Phys. Rev. A, 2004. **69**: p. 022705 (6 pages).

62. C. Q. Jiao, et al., *Comparisons of electron impact ionization and ion chemistries of CF_3Br and CF_3I.* Int. J. Mass Spectrom., 2001. **208**: p. 127-133.

63. U. Onthong, et al., *Calculated absolute electron impact ionization cross-section for the molecules CF_3X (X=H, Br, I)* Int. J. Mass Spectrom., 2002. **214**: p. 53-56.

64. K. N. Joshipura, et al., *Theoretical total ionization cross-sections of CH_x, CF_x, SiH_x, SiF_x (x=1-4) and CCl_4 targets by electron impact.* Eur. Phys. J. D, 2003. **23**(1): p. 81-90.

65. L. R. Hargreaves, *Absolute Electron Scattering Cross Sections for the CF_2 radical*, in *Faculty of Science and Engineering*. PhD Thesis, 2008, Flinders University: Adelaide.

66*. S J Buckman, et al., *Low energy lepton scattering: recent results for electron and positron interactions.* J. Phys.: Conf. Ser., 2008. **133**: p. 012001 (8 pages).

67*. J. R. Francis-Staite, et al., *Elastic electron scattering from CF_3I.* Phys. Rev. A, 2010. **81**: p. 022704 (7 Pages).

68. M. H. F. Bettega, *Personal Correspondence*. 2009.

69*. L. R. Hargreaves, et al., *Electron interaction cross sections for a low temperature 'plasma-like' gas mixture.* Plasma Sources Sci. Technol., 2010. **19**: p. 065021-065027.

70. T. Takagi, et al., *Elastic scattering and vibrational excitation cross sections for electron collisions with C_2F_6.* J. Phys. B. At. Mol. Opt. Phys., 1994. **27**(21): p. 5389-5404.

71. K. Bartschat and O. Zatsarinny, *Personal Correspondence*. 2010.

72. F. Blanco and G. García, *Personal Correspondence*. 2010.

73. L. Campbell, et al., *Integral cross sections for electron impact excitation of electronic states of N_2.* J. Phys. B. At. Mol. Opt. Phys., 2001. **34**(7): p. 1185-1199.

74. C. Winstead and V. McKoy, *Personal Correspondence*. 2008.

75. N. Russo, E. Sicilia, and M. Toscano, *Geometries, singlet-triplet separations, dipole moments, ionization potentials, and vibrational frequencies in methylene (CH_2) and halocarbenes (CHF, CF_2, CCl_2, CBr_2, and Cl_2).* J. Chem. Phys., 1992. **97**(7): p. 5031-5036.

76. Z.-L. Cai, *Ab Initio Study of Several Electronic States of the CF_2 Radical.* J. Phys. Chem., 1993. **97**: p. 8399-8404.

77. W. H. Kirchhoff, D. R. Lide Jr, and F. X. Powell, *The microwave spectrum, force field and dipole moment of CF_2.* J. Mol. Spectrosc., 1973. **47**(3): p. 491-498.

78. *Computational Chemistry Comparison and Benchmark Data Base*, in *NIST Standard Reference Database 101 Release 15a*. 2010, National Institute of Standards and Technology.

79. C. Millot and B. J. Costa Cabral, *Electronic properties of liquid water by sequential molecular dynamics density functional theory.* Chem. Phys. Lett., 2008. **460**: p. 466-469.

80. N. I. Butkovskaya, et al., *Mass-spectrometric analysis of a beam of polar molecules. Measurements of the dipole moment of the CF_3 radical* Chem. Phys. Lett., 1979. **63**(2): p. 375-377.

81. M. Tsuji, M. Aizawa, and Y. Nishimura, *Mass spectroscopic studies on ion-molecule reactions of CF_3^+ with benzene and toluene at near-thermal energy.* Chem. Lett., 1995. **3**: p. 211.

82. M. Goto, et al., *Cross section measurements for electron-impact dissociation of CHF_3 into neutral and ionic fragments.* Jpn. J. Appl. Phys. Part 1 1994. **33**: p. 3602.

83. E. R. Fisher and P.B. Armentrout, *The appearance energy of CF_3^+ from CF_4: Ion/molecule reactions related to the thermochemistry of CF_3^+.* Int. J. Mass Spectrom. Ion Processes, 1991. **101**(1): p. R1-R6.

84. Y. J. Kime, D.C. Driscoll, and P.A. Dowben, *The stability of the carbon tetrahalide ions.* J. Chem. Soc. Faraday Trans. 2, 1987. **83**: p. 403.

85. Y. Loguinov, V.V. Takhistov, and L.P. Vatlina, *Photoionization studies of substituted trimethylamines.* Org. Mass Spectrom., 1981. **16**: p. 239.

86. D. W. Berman, J. L. Beauchamp, and L.R. Thorne, *Ion cyclotron resonance and photoionization investigations of the thermochemistry and reactions of ions derived from CF_3I.* Int. J. Mass Spectrom. Ion Phys., 1981. **39**: p. 47-54.

87. D. H. Uae, ed. *Chapter 9. Stabilities of positive ions from equilibrium gas phase basicity measurements*. Ions Chemistry, ed. M.T. Bowers. 1979, Academic Press: New York.

88. B.G. Syrvatka, M. M. Gil'burd, and A.L. Bel'ferman, *Ion-dissociative processes of some halogen containing butadienes and particles structure.* Zh. Org. Khim., 1973. **9**: p. 1117.

89. T. A. Walter, et al., *Mass-Spectrometric Study of the Photoionization of C_2F_4 and CF_4.* J. Chem. Phys., 1969. **51**(8): p. 3531-3536.

90. C. Lifshitz and W.A. Chupka, *Photoionization of the CF_3 free radical.* J. Chem. Phys., 1967. **47**(9): p. 3439-3443.

91. T. C. Ehlert, *Bonding in C_1 and C_2 fluorides.* J. Phys. Chem., 1969. **73**: p. 949-953.

92. D. Ajitha, et al., *Spin–orbit ab initio study of alkyl halide dissociation via electronic curve crossing.* J. Chem. Phys., 2004. **121**(12): p. 5761-5766.

93. S. Marienfeld, et al., *High resolution low-energy electron attachment to CF_3I.* J. Phys. B. At. Mol. Opt. Phys., 2006. **39**: p. 105-126.

94. K. M. Swift, L. A. Schile, and R.D. Rathage, *Dispersion of gases in atomic iodine lasers at 1.315 µm.* Appl. Opt., 1988. **27**(21): p. 4377-4384.

95. B. K. Antony, K. N. Joshipura, and N. J. Mason, *Total and ionization cross sections of electron scattering by fluorocarbons.* J. Phys. B. At. Mol. Opt. Phys., 2005. **38**: p. 189-205.

96. G. M. Bancroft, et al., *High resolution gas phase photoelectron spectra using synchrotron radiation: selective enhancement of the I 5p cross section in CF_3I due to photoexcitation of I 4d electrons.* J. Chem. Soc., Chem. Commun., 1984: p. 1613-1614.

97. J. Cvitas, et al., *Photoelectron spectra of bromo- iodotrifluoromethane.* Z. Naturforsch. A, 1977. **32**: p. 1528.

98. F. C.-Y. Wang and G.E. Leroi, *Photoionization and fragmentation of halogenated methanes.* Ann. Isr. Phys. Soc. , 1983. **6**: p. 210.

99. C. J. Noutary, *Mass spectrometric study of some fluorocarbons and trifluoromethyl halides.* J.Res. NBS, 1968. **72A**: p. 479.

100. F. H. Dorman, *Appearance potentials of the fragment ions from CF_3I.* J. Chem. Phys., 1964. **41**: p. 2857-2859.

101. J. Marriott and J.D. Craggs, *Ionization and dissociation by electron impact. I. Trifluoromethyl halides.* J. Electron., 1956. **1**: p. 405.

102. V. H. Dibeler, R. M. Reese, and F.L. Mohler, *Ionization and dissociation of the trifluoromethyl halides by electron impact.* J. Res. NBS, 1956. **57**: p. 113.

103. *National Institute of Science and Technology Chemistry WebBook*. NIST Standard Reference Database Number 69 2010; Available from: http://webbook.nist.gov/chemistry/.

104. I. Martín, E. Mayor, and A.M. Velasco, *Molecular Quantum Defect Orbital (MQDO) Calculation of the Photoionization of CF_3X (X=Br,I): Study of Ligand Substitution Effects.* J. Quant. Chem., 2005. **104**: p. 522-529.

105. H. Clauberg, D. Minsek, and P. Chen, *Mass and Photoelectron Spectroscopy of C_3H_2. ΔH_f of Singlet Carbenes Deviate from Additivity by Their Singlet-Triplet Gaps* J. Am. Chem. Soc., 1992. **114**: p. 99-107.

106. E. Harting and F. Read, *Electrostatic Lenses*. 1976, Amsterdam: Elsevier Scientific Publishing.

107. Scientific Instrument Services, I., *CPO - Charged Particle Optics Software*. 2010.

108. J. N. H. Brunt, F. H. Read, and G. C. King, *The realisation of high energy resolution using the hemispherical electrostatic energy selector in electron impact spectroscopy.* J. Phys. E: Sci. Instrum., 1977. **10**: p. 134-139.

109. F. Read, et al., *The optimization of electrostatic energy selection systems for low energy electrons.* J. Electron. Spectrosc. Relat. Phenom., 1974. **4**(4): p. 293-312.

110. S. K. Howell, N.J. Bowering, and T.D.S. Hamilton, *The real-time optimisation of electron spectrometers.* J. Phys. E: Sci. Instrum., 1987. **20**: p. 7.

111. W.C Wiley and I. H McLaren, *Time-of-Flight Mass Spectrometer with Improved Resolution.* Rev. Sci. Instrum., 1955. **26**(12): p. 1150-1157.

112. D. A. Kleinman, *Theory of Second Harmonic Generation of Light.* Phys. Rev., 1962. **128**: p. 1761-1775.

113. R. W. Boyd, *Nonlinear Optics*. 3rd ed. Vol. 1. 2008, Burlington MA, USA: Academic Press.

114. R. T. Brinkmann and S. Trajmar., *Effective path length corrections in beam-beam scattering experiments.* J. Phys. E: Sci. Instrum., 1981. **14**: p. 245-254.

115. D. F. Register, S. Trajmar, and S.K. Srivastava, *Absolute elastic differential electron scattering cross section for He: A proposed calibration standard from 5 to 200 eV.* Phys. Rev. A, 1980. **21**(4): p. 1134-1151.

116. S. K. Srivastava, A. Chutjian, and S. Trajmar, *Absolute elastic differential electron scattering cross section in the intermediate energy region. I. H_2*.* J. Chem. Phys., 1975. **63**(6): p. 2659-2665.

117*. L. R. Hargreaves, et al., *A new normalization method for electron collision cross sections measured using skimmed supersonic jet beams.* Meas. Sci. Technol., 2007. **18**: p. 2783-2790.

118. R. K. Nesbet, *Accurate e^--He cross sections below 19 eV.* J. Phys. B. At. Molec. Phys., 1979. **12**(7): p. L243-L248.

119. L. Boesten and H. Tanaka, *Rational function fits to the nonresonant elastic differential cross sections (DCS) for e + He collisions, 0°–180°, 0.1 to 1000 eV* At. Data Nucl. Data Tables, 1992. **52**(1): p. 25-42.

120. D. R. Miller, ed. *Atomic and Molecular Beam Methods*. Free Jet Sources, ed. P. Scholes. Vol. 1. 1988, Oxford University Press: Oxford.

121. G. S. Sikora, *Analysis of asymptotic behavior of free jets: prediction of molecular beam intensity and velocity distributions*. PhD Thesis, 1973, Princeton University.

122. S. Götte, et al., *A triply differentially pumped supersonic beam target for high-resolution collision studies.* Rev. Sci. Instrum., 2000. **71**(11): p. 4070-4077.

123. L. Boesten, et al., *Crossed-beam experiment for the scattering of low energy electrons from CF_4.* J. Phys. B. At. Mol. Opt. Phys., 1992. **25**(7): p. 1607-1620.

124. W. M. Huo, *Electron-CF_4 elastic scattering in the static-exchange approximation.* Phys. Rev. A, 1988. **38**(7): p. 3303-3309.

125. M. T. N. Varella, et al., *Low-energy electron scattering by CF_4 , CCl_4 , $SiCl_4$, $SiBr_4$, and SiI_4.* Phys. Rev. A, 1999. **60**(5): p. 3684-3693.

126. M. A. Ali and Y-K Kim, *Ionization cross sections by electron impact on halogen atoms, diatomic halogen and hydrogen halide molecules.* J. Phys. B. At. Mol. Opt. Phys., 2008. **41**: p. 145202 (12 pages).

127. A. Snelson, *Matrix Isolation of CF_2 and CF_3 from Pyrolysis of C_2F_4 and CF_3I.* High Temperature Science, 1970. **2**: p. 70-79.

128. R. F. Pottie, *Ionization Potential and Heat of Formation of the Difluoromethylene Radical.* J. Chem. Phys., 1965. **42**(7): p. 2607.

129. M. Cameron and S. Kable, *A new design for a simple and effective pyrolysis nozzle in a supersonic free jet.* Rev. Sci. Instrum., 1996. **67**(1): p. 283-287.

130. B. Gans, et al., *Determination of the Absolute Photoionization Cross Sections of CH_3 and I Produced from a Pyrolysis Source, by Combined Synchrotron and Vacuum Ultraviolet Laser Studies.* J. Phys. Chem. A, 2010. **114**: p. 3237-3246.

131. P. Sauvageau, et al., *Vacuum ultraviolet and photoelectron spectra of fluoroethanes.* J. Chem. Phys., 1974. **61**(1): p. 391-395.

132. W. Radloff, et al., *Ultrafast photodissociation dynamics of electronically excited CF_2I_2.* Chem. Phys. Lett., 1998. **291**: p. 173-178.

133*. O. Zatsarinny, et al., *Electron-collsion cross sections for iodine.* Phys. Rev. A, 2011. **83**: p. 042702 (11 Pages).

134. O. Zatsarinny and K. Bartschat, *Relativistic B-spline R-Matrix method for electron collisions with atoms and ions: Application to low-energy electron scattering from Cs.* Phys. Rev. A, 2008. **77**: p. 062701(8 Pages).

135. T. Fleig and A. J. Sadlej, *Electric dipole polarizabilities of the halogen atoms in $^2P_{1/2}$ and $^2P_{3/2}$ states: Scalar relativistic and two-component configuration-interaction calculations.* Phys. Rev. A, 2002. **65**(3): p. 032506(8 Pages).

136. M. E. Riley and G. Truhlar, *Approximations for the exchange potential in electron scattering.* J. Chem. Phys., 1975. **63**: p. 2182-2192.

137. X. Zhang, J. Sun, and Y. Liu, *A new approach to the correlation polarization potential-low-energy electron elastic scattering by He atoms.* J. Phys. B. At. Mol. Opt. Phys., 1992. **25**(8): p. 1893-1897.

138. F. Blanco and G. García, *Improvements on the quasifree absorption model for electron scattering.* Phys. Rev. A, 2003. **67**: p. 022701(9 Pages).

139. A. Muñoz, et al., *Energy Deposition Models at the Molecular Level in Biological Systems.* Adv. Quantum Chem., 2007. **52**: p. 21-57.

140. H. Kato, et al., *Absolute elastic differential cross sections for electron scattering by $C_6H_5CH_3$ and $C_6H_5CF_3$ at 1.5–200 eV: A comparative*

experimental and theoretical study with C_6H_6. Phys. Rev. A, 2009. **79**: p. 062703(7 pages).

141*. L. R. Hargreaves, et al., *Elastic cross sections for electron scattering from iodomethane.* J. Phys. B. At. Mol. Opt. Phys., 2011. **44**: p. 045207 (7 pages).

142. F. Blanco and G. García, *Screening corrections for calculation of electron scattering from polyatomic molecules.* Phys. Lett. A, 2003. **317**: p. 458-462.

143. F. Blanco and G. García, *Screening corrections for calculation of electron scattering differential cross sections from polyatomic molecules.* Phys. Lett. A, 2004. **330**: p. 230-237.

144. S. L. Shostak, W. L. Ebenstein, and J. S. Muenter, *The dipole moment of water. I. Dipole moments and hyperfine properties of H_2O and HDO in the ground and excited vibrational states.* J. Chem. Phys., 1991. **94**(9): p. 5875-5882.

145. M-T Lee, *Personal Correspondence*. 2008.

146. M. A. Morrison, *The Physics of Low-energy Electron-Molecule Collisions: A Guide for the Perplexed and the Uninitiated.* Aust. J. Phys., 1983. **36**: p. 239-286.

147. B. A. Lippmann and J. Schwinger, *Variational Principles for Scattering Processes. I.* Phys. Rev., 1950. **79**(3): p. 469-480.

148. R. R. Lucchese, G. Raseev, and V. McKoy, *Studies of differential and total photoionisation cross sections of molecular nitrogen.* Phys. Rev. A, 1982. **25**(5): p. 2572-2587.

149. N. T Padial and D. W. Norcross, *Parameter-free model of the correlation-polarisation potential for electron-molecule collisions.* Phys. Rev. A, 1984. **29**: p. 1742-1748.

150. K. Takatsuka and V. McKoy, *Extension of the Schwinger variational principle beyond the static-exchange approximation.* Phys. Rev. A, 1981. **24**(5): p. 2473-2480.

151. K. Takatsuka and V. McKoy, *Theory of electronically inelastic scattering of electrons by molecules.* Phys. Rev. A, 1984. **30**(4): p. 1734-1740.

152. R. L. Schwartz, et al., *Singlet-Triplet Splittings in CX_2 (X = F, Cl, Br, I) Dihalocarbenes via Negative Ion Photoelectron Spectroscopy.* J. Phys. Chem. A, 1999. **103**: p. 8213-8221.

153. F. H. Read and J. M. Channing, *Production and optical properties of an unscreened but localized magnetic field.* Rev. Sci. Instrum., 1996. **67**(6): p. 2372-2377.

154. M. H. F. Bettega, L. G. Ferreira, and M. A. P. Lima, *Transferability of local-density norm-conserving pseudopotentials to electron-molecule-collision calculations.* Phys. Rev. A, 1993. **47**(2): p. 1111-1118.

155. G. B. Bachelet, D. R. Hamann, and M. Schluter, *Pseudopotentials that work: From H to Pu.* Phys. Rev. B, 1982. **26**(8): p. 4199-4228.

156. C. Winstead and V. McKoy, *Personal Correspondence*. 2010.

157. F. J. da Paixão, M. A. P. Lima, and V. McKoy, *Spin Exchange in Elastic e-O_2 Collisions.* Phys. Rev. Lett., 1992. **68**(11): p. 1698-1701.

158. I. Rozum, N. J. Mason, and J. Tennyson, *Electron collisions with the CF_3 radicals using the R-matrix method.* New. J. Phys., 2003. **5**: p. 155.1-155.12.

*References marked with an asterisk indicate papers on which Jessica Brunton is an author, either under her current name or under her maiden name Jessica Francis-Staite.